UNIVERSITÀ DEGLI STUDI DI PALERMO

PhD programme in *Chemical, Environmental, Biomedical, Hydraulic and Materials Engineering*

Characterisation and performance optimisation of Fiber Metal Laminates with thermoplastic matrix composite for aerospace applications

PhD candidate:

RICCARDO MIRANDA

Tutor:

PROF. ANTONINO VALENZA

Co-Tutor:

PROF. MONICA SANTAMARIA

PROF. GIUSEPPE CATALANOTTI

PhD Course Coordinator:

PROF. GIORGIO MICALE

CYCLE XXXVI

GRADUATION YEAR 2024

Acknowledgements

Now that I have come to the end of this journey, I feel I must strongly thank all those who have supported me during these years of intense work.

First, I would like to thank Professor Antonino Valenza, my tutor, who gave me the opportunity to pursue my research work and follow my interests during this complex path that is the PhD.

Next, I would like to sincerely thank Professor Monica Santamaria and Professor Francesco Di Franco for having always supported and helped me throughout the experimental course of my thesis and the various laboratory activities. Thanks to their teachings and experience, my cultural background has grown enormously.

I would also like to thank Professor Vincenzo Fiore for his direct support in the day-to-day activities of research and laboratory work; it is also thanks to him that I can say that I have experienced a complete and rich PhD program.

Special thanks go to Professor Giuseppe Catalanotti, thanks to whom I had a wonderful research experience abroad where I learnt so much. And a further special thanks goes to Professor Alejandro J. Müller who, thanks to his immense experience in calorimetry, allowed me, during my work in his laboratory in San Sebastian, to overcome many doubts that had occurred during my PhD.

I continue by thanking my two fantastic lab mates, with whom I shared most of my days, Carmelo Sanfilippo and Dionisio Badagliacco. Thank you for all the time you spent with me and the important physical and moral support you gave me. I also thank all the guys who helped me during these years through the experimental phase, especially Marco Luciano, to whom I wish a prosperous future for his new PhD.

I would like to end by thanking my family and friends, both Italian and Spanish, who have always supported me throughout these years, experiencing happy moments but also moments of discouragement, supporting me and always giving me words of comfort.

Abstract

The aim of this research is to improve the performance of thermoplastic fibre metal laminates (FML) for aerospace applications. For this purpose, the work was divided into two parts. The first part studied the composite substrate in depth, considering the crystallization process of the matrix and how this is affected by the presence of the fibres. Furthermore, the crystallization process was studied to assess how it affected the mechanical properties of the material. From the experimental results, a numerical model was developed in Abaqus to predict the crystallinity value of the matrix.

The results of this first part of the thesis, accurately showed that the presence of the carbon fibres negatively affects the kinetics of the crystallization process, slowing it down. The results demonstrated that carbon fibres act as antinucleating agent.

In addition, the kinetics curves were used in the Abaqus model to predict the performance of the material as the crystallinity value changes.

The second part of the thesis focused on the interface between the composite and the metal substrates. The objective was to use different chemical and electrochemical treatments to modify the morphology and improve the mechanical strength of the FMLs. Two metal types (aluminium and titanium alloy) were evaluated to gain a greater understanding of materials for aerospace applications.

The results of this second part showed that electrochemical treatments, for both metal alloys, generate a strong increase in mechanical performance of the FMLs, a sign of the effectiveness of the treatments.

List of Figures

List of Tables

Table of contents

Chapter 1: General Introduction and Objectives

1.1 Introduction

The aerospace industry has historically been the driving force in the field of materials research and innovation, given the need to use materials with the best performance but low weight. In this context, composite materials play a fundamental role, thanks to the peculiarity of tailoring, i.e., the possibility of shaping the material according to its final application. Precisely because of this typical characteristic, research on how best to combine the components of these materials is still open and growing.

The best combination for the aerospace industry is composed by a material with excellent characteristics in terms of strength, but at the same time lightweight. This last characteristic, lightness, is fundamental for all materials applied to aircraft, because many factors depend on the weight of the aircraft, including fuel consumption and therefore also CO_2 emissions into the atmosphere. As reported by Grave et al. [1] emissions from civil aviation have increased by 35% from 2013 to 2018 and will continue year on year, contrary to the desired trend, which, in relation to environmental protection, sets the goal of reducing carbon dioxide emissions in the coming decades.

To observe the mechanical properties of a material in relation to its specific weight, a very useful graph is the Ashby diagrams (Fig. 1).

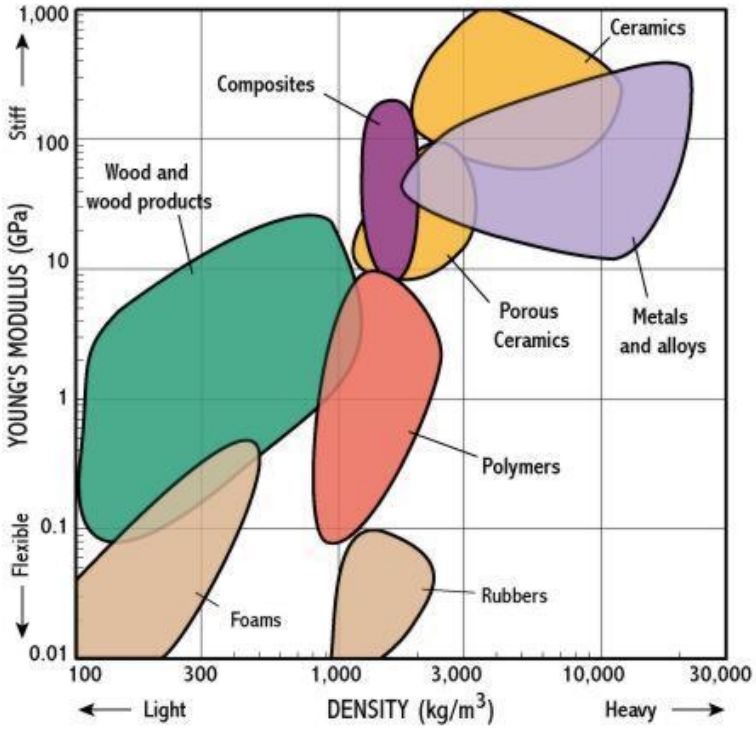

Fig. 1: Ashby diagram for different materials – Young's modulus vs Density [adopted from website - http://www-materials.eng.cam.ac.uk/mpsite/interactive_charts/].

The materials historically used for aviation are metals, in particular aluminium alloys, which belong to the group of materials characterised by high density. In recent decades, there has been a move towards the application of composites, which, as can be seen in Fig. 1, have mechanical properties comparable to metals, but with a much lower density, and therefore lower weight.

Nowadays, there are several examples of aircraft that use composite materials for more than half of their weight, such as the Boeing 787 and the Airbus A350 [2].

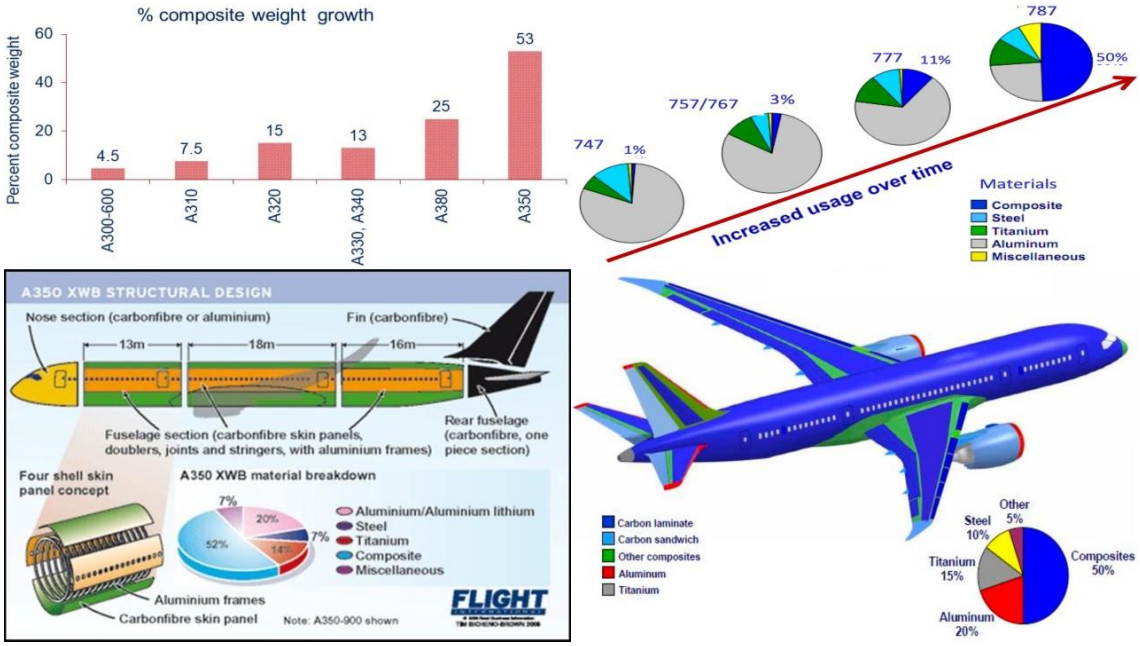

Fig. 2: Evolution of composite use in Boeing and Airbus airplane trough years [3].

The most used composite materials are those with a polymer matrix, in particular epoxy reinforced with long carbon or glass fibres (Fig. 2). However, composite materials are not always able to meet the strength requirements of the specific application and therefore traditional metals must be used. Precisely for this reason, in the 1980s, a research group at *Delft University* developed an innovative material formed by combining fibre-reinforced polymer matrix composites and metals, and so Fibre Metal Laminates or FML was born. [4]. The latter is formed by a succession of alternating layers of composite and metal, creating a material that overall possesses all the advantages of the individual components, such as the excellent plasticity of metal and the high strength and specific modulus of composite materials (Fig. 3). From their invention to the present day, several types of FML have been commercialised, but the three main ones are [4-7]:

- GLARE: composed of aluminium alloys and glass fibre-reinforced epoxy composite.
- ARALL: which uses composites reinforced with aramid fibres.
- CARALL: which employs carbon fibre reinforcement.

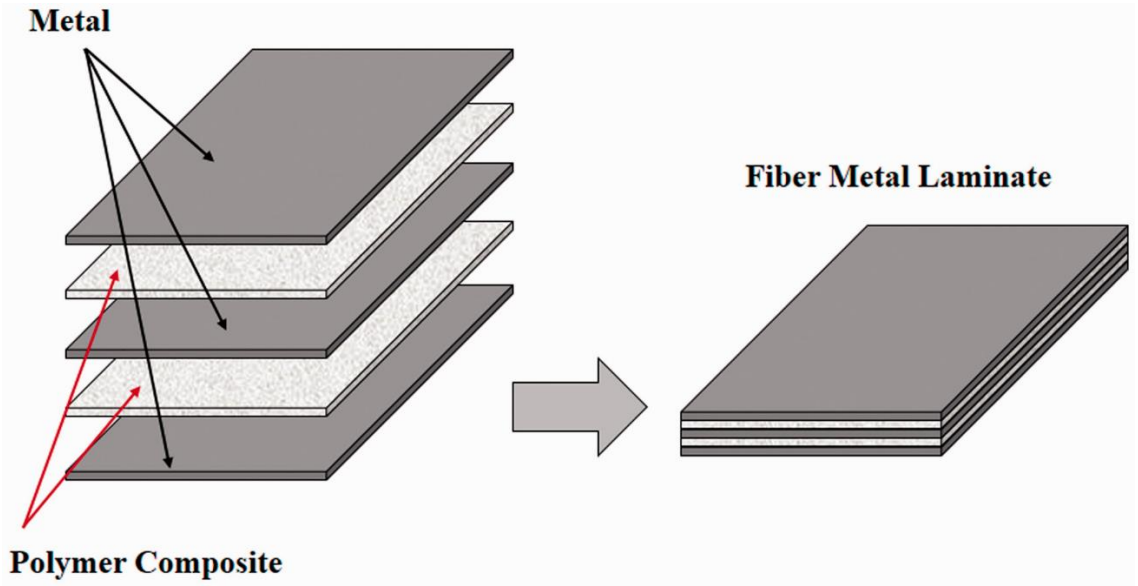

Fig. 3: Stacking sequence of fibre metal laminates [9].

So far, carbon reinforced FMLs are receiving increasing research interest, particularly in their use with thermoplastic matrix composites. Due to the environmental problems associated with the disposal of epoxy matrix composites, the aviation industry is shifting its interest towards more environmentally sustainable and recyclable products. From this point of view, thermoplastic matrix composites possess considerable advantages over thermoset composites, due to the possibility of being cast and reused and possessing greater resistance to impact and fatigue [10]. In addition, high performance is required in the aerospace industry, so suitable polymeric materials for this purpose are techno-polymers. This particular group of thermoplastics is characterised by high strength and elastic modulus, maintaining their values even at high operating temperatures, thanks to their high glass transition temperature T_g [11,12]. Among these, the most interesting is certainly polyether ether ketone (PEEK). It is a semi-crystalline polymer with a T_g of about 143°C, a melting temperature of 343°C, an elastic modulus between 2 and 4 GPa and a tensile strength of up to 120 MPa.

Thanks to these properties, PEEK can also be used at up to 250 °C without any loss of performance and would therefore allow the creation of components whose range of use is greater than epoxy, which is limited by the poor resistance to high temperatures [11-15].

The biggest problem with these materials is their high viscosity, which causes problems at the interface with reinforcement fibres or even metal surfaces in the case of FML. For example, Sarasini et al. [18] investigated the effect of temperature, fibre type and various surface treatments on the properties of FMLs produced using polypropylene (PP) composite reinforced with glass or basalt fabrics and aluminium 2024. The impact

resistance was evaluated by varying the treatments on the matrix (adding silane coupling agents) and substituting basalt fabrics for glass fabrics. The results showed that the use of thermoplastic matrices (such as PP) in the composite substrate of FMLs produces an effective increase in impact resistance, when compared to that of aluminium alloy alone. In addition, PP treated with silane coupling agents and basalt fabric as reinforcement resulted in the best performance of all types evaluated.

When considering the adhesive coupling between thermoplastic matrix composites and metals, the most important thing to improve adhesion is surface treatment, which is a very current research topic. In this regard, much work has been carried out precisely with the aim of improving the quality of the interface between the metal and the polymer composite, using different types of surface treatment: mechanical (abrasion or sandblasting); chemical (erosion with acids or coupling agents); electrochemical (anodising) [17-22].

Ji et al. [25] investigated the influence of process parameters, such as temperature, solution concentration and immersion time, in the application of a silane coupling agent on the surface of a grade 5 titanium alloy to improve adhesion with a PEEK-carbon fibre composite. Through mechanical tests, it was observed that the best performance was obtained when the silane concentration was 10%, the process temperature 130°C and the consolidation time on the metal surface 1 hour.

From these examples, it can be deduced that research is very interested in the application of thermoplastics as possible replacements for thermoset matrices, and in addition, techno-polymers, such as PEEK, are suitable for combining with metals that resist high temperatures well, such as titanium alloys. In this context, it can be seen how the application of such materials could enable the development of applications in supersonic aircraft, as the temperatures to which they would be subjected would be higher than in subsonic aircraft [24-27].

Thermoplastics, in addition to resisting high temperatures well, have a special characteristic that makes them even more unique. They can be defined as semi-crystalline, i.e., certain types of thermoplastic polymers show an alignment of the polymer chains in a specific direction, making the material more resistant. This characteristic can be controlled and studied through studies of crystallisation kinetics, which follow the various changes in the polymer chains during the material formation process. For thermoplastics, the term semi-crystalline derives from the fact that not all its polymer chains align, making it necessary to calculate a degree of crystallinity, i.e., the percentage of mass or volume of crystalline material, and depending on this, the material properties vary. The

degree of crystallinity depends on various factors, one of which is certainly the rate at which the polymer is cooled from a molten state [28-30]. For example, Batista et al. [33] studied the effect of varying the degree of crystallinity on the mechanical performance of a carbon-fibre reinforced polyphenylene sulphide (PPS) matrix composite. Three different degrees of crystallinity were obtained by varying the cooling rate (which they indicate as: fast, slow and in air). The various measurements of the degree of crystallinity were performed with DSC, while DMA and short beam shear were used to assess the mechanical performance at varying degrees of crystallinity. The results show that the slowest cooling of all, i.e., cooling in air, correlated with the highest degree of crystallinity, produces the highest mechanical performance.

Due to the influence of the degree of crystallinity on mechanical properties, research has focused on the study of this particular property of thermoplastic materials, and on its modelling, i.e., the study of crystallisation kinetics. Various works related to the study of kinetics can be found in the literature [32-35]. Historically, the first model to be developed to reproduce the kinetics of crystallisation is the Avrami model [38]. This model is widely used in literature to study the kinetics of isothermal crystallisation, although it leads to a less than accurate approximation. Based on this model, more accurate ones have also been developed, such as the Dual Avrami model, modified by Seo et Al. [39] who extended Avrami model by considering two different indices for primary and secondary crystallisation.

When it comes to non-isothermal crystallisation, however, another type of model can be used, such as the Nakamura model, which is formed by an infinitesimal approximation of as many Avrami equations as the temperature varies, as if each infinitesimal temperature change were an infinitesimal isothermal step. Also, Seo et Al. [40] applied the modification of the Dual Avrami, to the Nakamura model, thus creating the Dual Nakamura model that better approximates the kinetics of crystallisation during non-isothermal crystallisation.

With these models, it is therefore possible to follow the entire crystallisation process of the polymer and predict the degree of crystallinity depending on the temperature and the process by which the crystalline phase is being formed, i.e., whether it is isothermal or non-isothermal.

1.2 Aim of the work

The purpose of this research work is the study of fibre metal laminates with a thermoplastic matrix. In particular, the main objective is to optimise the mechanical

performance of the latter by acting on several factors. The FML used consists of a polyether ether ketone (PEEK) composite part reinforced with carbon fibre fabrics, and a metal part using two different alloys widely used in aerospace: either the aluminium alloy 7075 T6 or the titanium alloy grade 5 Ti6Al4V, to assess the adhesion of the thermoplastic matrix composite with one alloy or the other.

It can be said that the aim of this research project is to find alternative ways to improve the performance of a thermoplastic matrix FML. For the composite part, the kinetics of matrix crystallisation and how carbon fibres influence it, were analysed in depth. On the metal interaction side, electrochemical surface treatments will be applied to improve adhesion and, in the case of aluminium alloy, the corrosion resistance.

1.3 Structure of the thesis

The work was divided into two parts. In the first, the composite substrate was analysed in detail, studying the entire crystallisation process of the matrix, to observe how it changes in the presence of the fibres and how it influences the mechanical properties. The data from this study were used to develop a model in Abaqus and Python to predict the material's properties from its degree of crystallinity. In this way, at the end of the study, it was possible to simulate a composite material consisting of PEEK reinforced with carbon fibres with associated engineering constants depending on the degree of crystallinity of the material, so that it can be used in micro and macro mechanics simulations in the future.

The second part was focused on the study of the interface between the composite and the metal. In fact, the aim in this part was the study of possible surface treatments to carry out on the metal substrate to improve adhesion with the FML composite substrate.

As already mentioned, the metal substrates analysed are different in nature, but both are of enormous interest in the aerospace industry. Regarding the aluminium alloy 7075, the innovative technique chosen was that of a special anodising process. In detail, research was focused on obtaining an anodising technique that would form an oxide layer on the material that would produce good adhesion with the composite and at the same time generate good corrosion resistance. For this reason, it was decided to create a two-step anodising process consisting of one part tartaric-sulphuric acid anodising and one part phosphoric-sulphuric acid anodising. The oxide layer thus created has the peculiarity of having pores of variable geometry, with a small diameter outside and a larger diameter inside. This treatment has been compared with others in terms of mechanical strength and corrosion resistance.

In relation to the use of the titanium alloy, an electrochemical technique was again chosen to improve adhesion with the thermoplastic matrix composite. However, the focus was only on the mechanical improvement of the interface, since the titanium oxide formed on the surface has excellent corrosion resistance. In this part of the work, the technique mainly analysed is an anodising of the titanium alloy to obtain a layer of titanium oxide nanotubes. To optimise their shape, various process parameters were analysed: modifying the applied potential, the anodising time, and the composition of the electrolyte solution.

Chapter 2: First Part - Composite Substrate

2.1 Literature analysis of the first part

2.1.1 Composite materials

Composite materials are heterogeneous materials defined as a system consisting of two or more micro- or macro-constituents, which differ in shape and chemical composition and are insoluble in each other. They are obtained from the combination of two or more materials with different characteristics with the aim of enhancing the qualities of each constituent: specifically, they are intended to confer an improvement in terms of strength and stiffness compared to the base material. The constituents of composite materials take on different nomenclatures according to the role they play, thus distinguishing matrix and reinforcement [41,42].

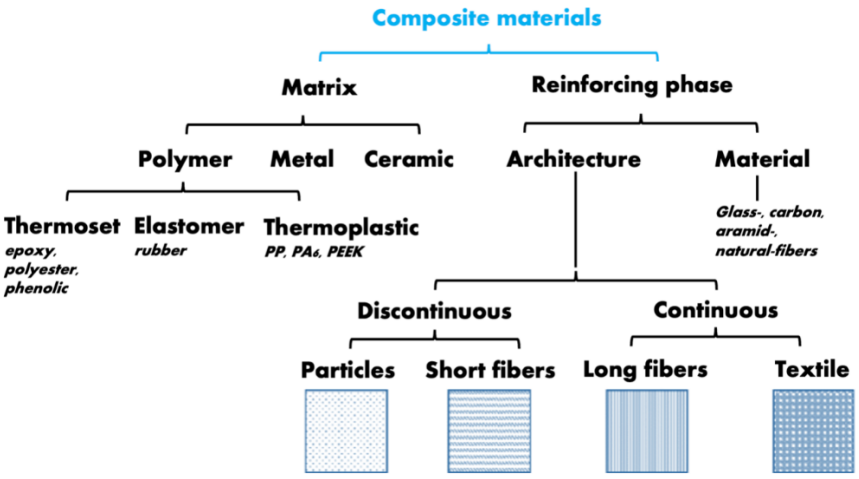

Fig. 4: Classification of composite materials based on type of matrix or reinforcements [adopted from website - https://www.milanpolymerdays.org/blog/what-are-polymer-matrix-composites].

The matrix plays a minor role in load-bearing capacity, but influences interlaminar shear strength, thus having an indirect effect. In addition, it provides lateral support, which does not allow the fibres to flex transverse to the load of compression. For applications requiring high performance, matrices with a high tensile modulus and high tensile strength are preferred. These characteristics influence the torsional, flexural, and compressive properties of the composite. Another relevant parameter is high fracture toughness, which enables the composite to resist crack propagation and delamination. Finally, the matrix must possess a thermal expansion coefficient that ensures dimensional stability at high temperatures.

Matrices can be differentiated into three types: ceramic, metallic and polymeric. Ceramic and metal matrices are preferred when the application involves high temperatures. On the other hand, polymer matrices are preferred for structural applications, where lightness and specific chemical-physical properties are required [43].

The latter are formed from polymers, i.e., substances consisting of large molecules, which are obtained by chain-joining smaller molecules, the monomers.

Polymer matrices include thermoplastic polymers and thermosetting polymers, which will be discussed in detail in this work.

As for the reinforcement, it plays a fundamental role in a composite. It has the task of carrying most of the load and often occupies most of the volume. Reinforcement can come in different forms: fibrous, particle or skeletal.

For structural applications, fibre reinforcement is preferred. Therefore, the fibres have the task of resisting stress, and the strength value of the material depends significantly on the cross-sectional area of the fibres. If the material is made from thin fibres, there is an increase in overall strength. In addition, this tends to reduce the possibility of defects such as blowholes, inclusions, or cracks. In polymeric materials, the use of fibre reinforcement is useful when the type of stress to which they are subjected is known. The positioning of the fibres, i.e., their orientation, influences the strength characteristics [44].

Commercially, four types of fibres can be distinguished [45]:

- Strands: these are commonly referred to as fibres but appear as a set of filaments. The strands can be parallel or twisted, joined together using special binders. The strands can be subsequently cut to obtain filaments from 3.2 mm to 12.7 mm, called chopped strands. These are then used for production techniques such as injection moulding. Chopped mat strands can also be obtained by cutting the strands into longer fibres from 50.8 mm upwards. They are then blended with resins to form a two-dimensional fabric, which exhibits isotropic properties in the plane. They are used in production techniques such as hand lay-up or vacuum bagging.
- Yarns (rovings): consist of groups of parallel strands, which are wound into cylindrical spools. They are used to produce filaments. The yarns are impregnated with a polymer resin and left to partially cure. This results in pre-pregs, which are used in production techniques such as compression moulding or autoclaving. However, they have high operating costs, as their storage requires a low and constant temperature, which is necessary so that the curing process does not advance too quickly.

- Woven fabrics: consist of continuous rovings woven in two directions orthogonal to each other. They are used in all production techniques and, in addition, are often combined with mats to form the combined.
- Powders (milled): these are obtained by grinding strands. Their size ranges from 0.79 to 3.22 mm and their application are mainly for particle composites.

The main types of fibres currently used in the field of composites, subdivided according to the nature of the material, are:

- Glass fibres
- Carbon fibres
- Aramid fibres

Regardless of the shape of the fibres used to develop the composite, they are responsible for reacting to the load transmitted to the composite and are characterised by high mechanical performance, excellent tensile strength, and strong dependence on the production process [46].

2.1.2 Polymers

The main objective of this first part of the thesis is to study the properties of a particular polymer used as a matrix in a composite material, so it is necessary to explain what a polymer is and in particular the nature of semi-crystalline types, which differ from amorphous types.

Polymers are defined as a succession of long polymer chains, i.e., macromolecules; in fact, the word polymer is derived from the Greek 'poly' meaning many and 'mer' being the main part. According to the IUPAC definition: "a polymer is a molecule of high relative molecular mass, whose structure essentially comprises multiple repetition of units derived, effectively or conceptually, from molecules of low molecular mass." [47]. Each polymer is composed of a monomer and the process that converts the monomer into a polymer is called polymerisation.

Polymers can be divided into two large families: amorphous or semi-crystalline. Of these, the fundamental property is the glass transition temperature or T_g, i.e., a particular temperature value that divides two state regions of the polymer material: the glassy state (below T_g) and the rubbery state (above T_g). Amorphous polymers possess only the value of T_g as their characteristic temperature, whereas semi-crystalline materials, in addition to T_g, are also characterised by the melting temperature of the semi-crystalline phase, T_m [48]. Observing the shape of the long polymer chains that constitute these materials,

amorphous polymers always present a random and disorganised structure, whereas for semi-crystalline polymers the morphology is different. In these materials, it is observed that the long polymer chains are randomly arranged above the T_m, thus having a so-called amorphous structure; but when the material is cooled, the long polymer chains begin to reorganise, aligning themselves in certain preferred directions, thus creating the lamella. Not all the chains of the material reorganise, thus leaving a portion of the polymer in its amorphous state, which is why the name is semi-crystalline material, or why exist the degree or percentage of crystallinity. Looking at the graph in Fig. 5, for amorphous polymers, T_g is the point at which the specific volume as a function of temperature changes slope. For semi-crystalline polymers, there are not just two regions in the graph, but three: the first above T_m where the material can be defined as amorphous; between T_m and T_g where crystallisation processes take place and below T_g where the material is in its glassy state [49].

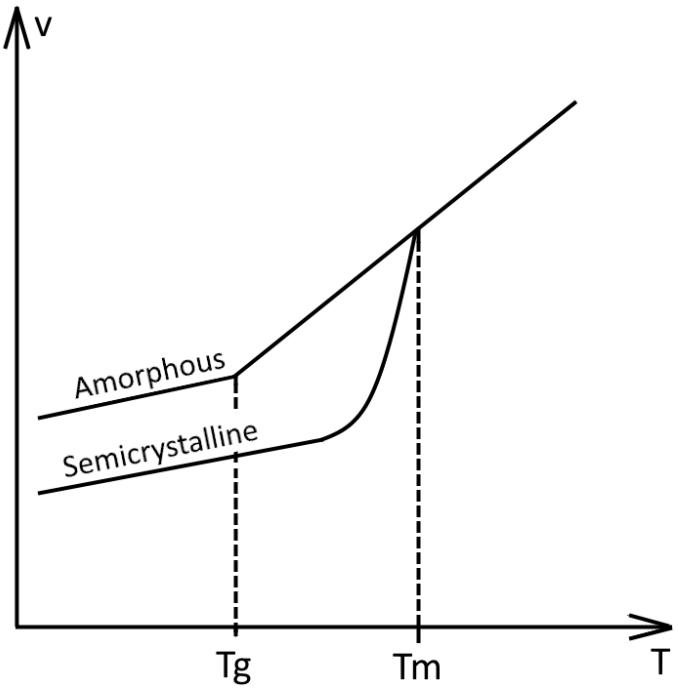

Fig. 5: Development of specific volume with temperature in an amorphous or semi-crystalline polymer [50].

It is often possible to obtain the amorphous version of a semi-crystalline polymer by cooling from above melting temperature to room temperature very quickly, for example using liquid nitrogen. In this way, the polymer chains do not have time to reorganise themselves and remain in their amorphous state.

When speaking of matrices for composite materials, two large families are always distinguished: thermosets and thermoplastics. Noting the definitions of amorphous and semi-crystalline, thermosetting matrices are always amorphous polymers, due to their

peculiar way of forming polymer chains through a curing process between the monomer and the cross-linking agent. In fact, the chains formed from the curing reaction (cross link*)* are very stable three-dimensional covalent bonds that do not allow the chains to order themselves. An example of such materials are epoxy resins, which are extremely widely used in various areas of modern industry as a matrix for composite materials.

Considering thermoplastic matrices, they can be subdivided into amorphous and semi-crystalline, as the long polymer chains are held together by weaker bonds. The most common examples for these materials are certainly polyethylene (PE), a semi-crystalline material that can reach very high degrees of crystallinity (70-90%), PEEK, PPS, etc... As far as amorphous thermoplastic polymers are concerned, one example is polyimide (PI), known commercially as Kapton, produced by DuPont^{TM}. This amorphous techno-polymer is extremely interesting because its high melting temperature of over 400°C allows it to be used in large temperature ranges.

The mechanical behaviour of a polymer is closely linked to its morphology.

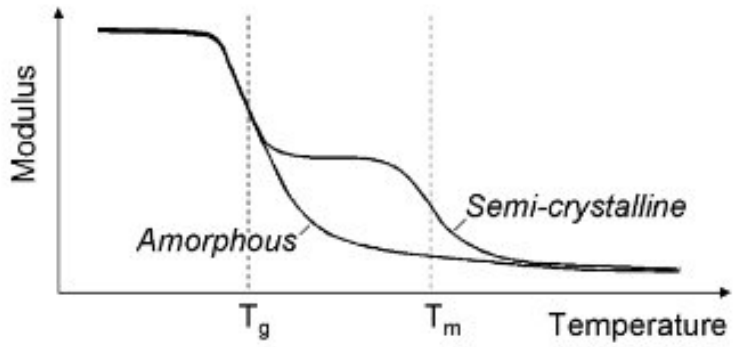

Fig. 6: Young modulus -temperature diagram of a semi-crystalline polymer vs amorphous [51].

Referring to Fig. 6 it can be seen that, plotting Young's modulus as a function of temperature, at the glass transition temperature (T_g) in the graph there is a 'step' and this step is all the more accentuated as the polymer tends to be amorphous. In fact, in the case of an amorphous polymer, the maximum gap occurs at the glass transition temperature and this is an indication of the fact that an amorphous material (or a semi-crystalline material with a low degree of crystallinity) is strongly affected by temperature variations above the T_g, which is an excellent condition from the point of view of the material's processing but counterproductive from the point of view of its stiffness and thus its strength.

In Tab. 1 glass transition temperature and melting temperature values of common thermoplastic polymers are shown:

Tab. 1: Glass transition temperature (T_g), melt temperature (T_m) of main plastics [52].

Polymers	T_g [°C]	T_m [°C]
PET	70 to 80	250 to 260
LDPE	<-100	100 to 110
PVC	80 to 84	-
PP	-30 to -20	160 to 165
PS	90 to 105	-
HDPE	<-100	125 to 135
PC	145	-
PMMA	100 to 115	-
PA6	50 to 80	190 to 230
PA66	70 to 90	185
PA610	50 to 80	117 to 227
POM	-85 to -75	316 to 335
PBT	40 to 60	142

It can be noted that some thermoplastics can even have a glass transition temperature that lies below 0 °C, which implies that at room temperature these materials possess medium viscous behaviour and have a rubber-like (rubbery) consistency.

2.1.3 Semi-crystalline polymers and their models

Crystallisation of polymers is a behaviour that is attributed to the shape of the long polymer chains, which, precisely because of this size, are difficult to untangle and therefore prefer to align, creating long parallel chains, i.e., the so-called lamella. Polymers never reach 100% crystallinity; hence they are called semi-crystalline. To describe the nature of semi-crystalline polymers, several models have been developed and the most important are the fringed micelle model and the chain fold model.

2.1.3.1 Fringe-micelle model

This model was among the first to be developed and is based on a two-phase system, amorphous and crystalline. The crystalline region is composed of a set of short macromolecular chains that are aligned and parallel to each other. On the other hand, the amorphous region is composed of a disordered sequence of chains that lie between the various crystalline regions. The key part of this model is that a single long polymer chain participates in multiple crystal regions, as the chain length is more than 10 times longer (approximately 100nm) than the experimentally measured crystal length (Fig. 7). This

model also explains the mechanical properties of semi-crystalline polymers, based on the physical bonds (called fringes) that exist between the ordered regions. However, the model is inadequate to explain complex shapes, such as the three-dimensional spherulites that can be observed experimentally by crystallising a polymer from the molten state [42-44].

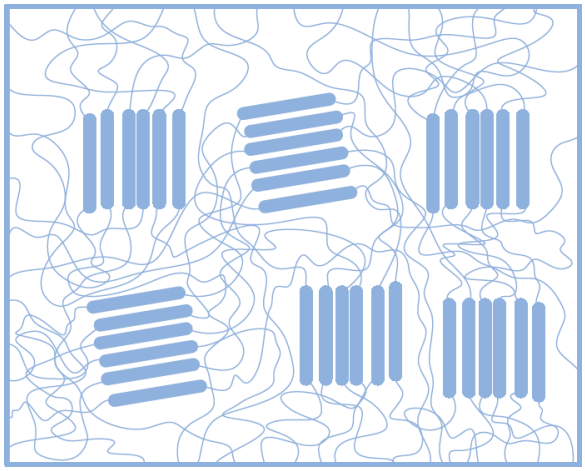

Fig. 7: Schematic illustration of the fringe micelle model [55].

2.1.3.2 Chain folded model

The chain folded model was introduced by Stocks but became famous after Keller's studies in 1957. He formulated this model because he observed that the lamellae that form inside the polymer have a thickness that is not compatible with the lengths of the polymer chains that are found inside and develop along the thickness. Therefore, he assumed that the polymer chains would fold to remain contained within the lamella. Thus, the model is based on the polymer chain re-entering a zone adjacent to the exit zone and so on, forming a loop of chains aligned with each other (Fig. 8a).

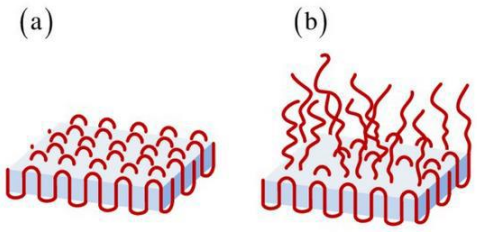

Fig. 8: Schematic representation of the chain folded model - a) model with adjacent chain indentation, b) switchboard model [55].

The switchboard model is a version proposed immediately after the adjacent return model (Fig. 8b). In this case, re-entry is not always guaranteed and therefore considers the possibility of polymer chains escaping from the crystal without folding. Although the

model involving totally random re-entry would be physically impossible as it would lead to unrealisable densities in the interfacial zone.

When it comes to crystallisation from the melt, the folding model prevails, although it is not as ordered as in Fig. 8a and there are often chains that escape and move until they reach a neighbouring lamella, binding to it.

Lamellae growth can be achieved in two ways, one starting from a solution containing very small amounts of polymer and one starting from the melted polymer. In the first case, the lamella being grown will not feel the presence of neighbouring lamellae as the solution is very dilute. Therefore, a single lamella can be grown. On the other hand, when crystallisation takes place from the molten polymer as it cools, all the polymer chains are very close to each other and can enter and leave several different lamellae. In this condition, parallel stacking of the lamellae occurs with the amorphous part of the polymer contained between the lamellae and, in addition, there is growth of the lamellae in a radial direction, creating so-called spherulites [49,54,56].

2.1.4 Crystallisation process

Polymer crystallisation is an extremely interesting subject of research for both academia and industry, since approximately 75% of commercial polymers are semi-crystalline and their properties depend on the degree of crystallinity, melting point, and polymer crystal morphology. For this reason, polymer crystallisation has been the subject of several books and reviews since the phenomenon was discovered [57]. There are many factors that influence the crystallisation process such as, for example, the cooling rate, the presence of chain orientation in the melt and the melting temperature, as well as the molecular mass or the presence of additives that favour the process, i.e., nucleating agents.

Why the crystallisation phenomenon occurs has not been fully explained, but certainly the most plausible interpretation follows thermodynamic laws. Considering the Gibbs free energy equation (Eq. (1)), the system can be defined as being in equilibrium when the free energy is minimal.

$$G = H - TS \tag{1}$$

H is the enthalpy while S is the entropy. When the polymer is above the melting temperature, T_m, it is in a very disorganised state with groupings of random polymer chains and therefore the entropy values, S, are very high and G low. Subsequently, when the polymer starts to cool, the crystallisation process begins, the system switches to a more ordered state and the entropy is lowered, but likewise the enthalpy, H, of the system is lowered, leading to lower G values, which means that the crystallisation process is

thermodynamically favoured. The problem with this approach is that it can be applied to quasi-static processes, whereas the production of polymers, especially at an industrial level, is very rapid, and so in these cases it is better to speak of crystallisation kinetics, using the rate at which polymer crystals are nucleated and grow as a subject [57,58]

2.1.5 Crystallisation kinetics

The crystallisation kinetics can be divided into two phases: primary and secondary crystallisation. Primary crystallisation is further subdivided into two phases: nucleation and growth, or also called primary and secondary nucleation respectively. The most common crystallisation process occurs from a temperature above the melting temperature. When the material is in that temperature range, all the chains are randomly distributed, but when the temperature starts to drop and the actual T_m value is reached, the nucleation process begins, which is part of the primary crystallisation phase. The first nuclei of the crystalline phase are thus formed, which in this case are called spherulites. The latter are three-dimensional formations composed of a set of lamellae, i.e., groupings of long polymer chains aligned and folded within the thickness of the lamella itself. The second step within primary crystallisation is growth. The nuclei or spherulites formed begin their growth process by increasing in volume until they reach a size where they meet other nearby spherulites. At this point, the primary crystallisation process (i.e., nucleation and growth) can be considered complete and the secondary crystallisation process begins. In this phase, the present and grown spherulites have little space to move because they are in contact with the neighbouring ones. For this reason, this phase is considered more as a crystal refinement phase, creating changes within the spherulite, such as an increase in thickness [58,59]. All phases are illustrated in Fig. 9 to best highlight the process.

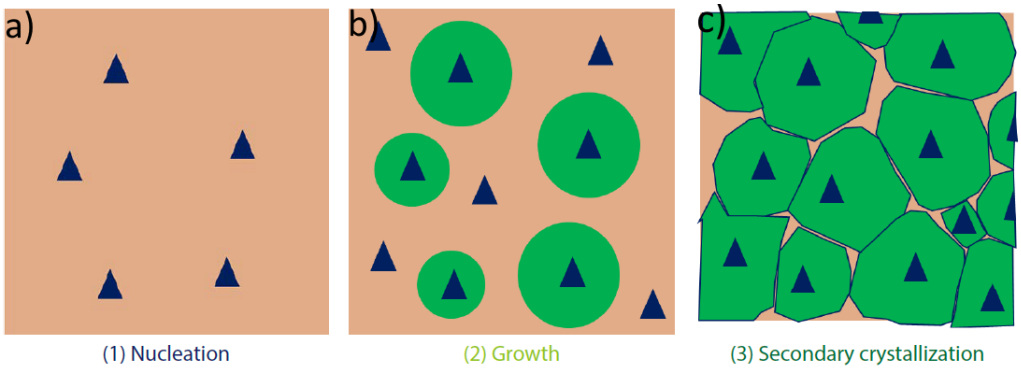

Fig. 9: Phases of crystallisation - primary crystallisation: a) nucleation and b) growth); c) secondary crystallisation [59].

2.1.5.1 Primary crystallisation: nucleation or primary nucleation

Nucleation is the process during which the first nuclei of crystalline lamellae begin to form; it is the beginning of the crystallisation process. There are two types of nucleation that can be classified into: homogeneous nucleation and heterogeneous nucleation.

Homogeneous nucleation is a spontaneous development of the lamella independently of external factors, so it is not possible to predict when or if it will occur. It is a type of nucleation that is very difficult to obtain, since it is very difficult to obtain molten polymer that does not contain any impurities inside. One method to obtain this nucleation is to study crystallisation from a solution in which small drops of polymer are released, i.e., an almost infinitesimal volume of polymer in relation to the volume of the solution, which in any case must be very pure. In this case it is therefore possible to study the homogeneous formation of the lamella from solution, a very useful method for observing the single lamella with the polymer chains folded inside [59].

A special mechanism that can be considered homogeneous nucleation is "self-nucleation (SN)". This nucleation involves a polymeric crystal birth from a "memory" of its morphology that has survived the melting process. This process is still not fully explained by the scientific community. The SN is subdivided into three domains: domain I, consisting of the completely melted material without the presence of SN; domain II where only SN is present; domain III where SN and annealing phenomena coexist, i.e., crystal refinement phenomena. Between domain II and domain III is the lowest self-nucleation temperature, $T_{s,ideal}$. At this temperature, the highest number of crystals are formed all at the same time, and thus having reached the polymer's maximum crystal density, studying crystallisation from that temperature, how crystal growth phenomena vary can be observed, since nucleation will no longer be possible.

On the other hand, heterogeneous crystallisation occurs on the surface of impurities present within the polymer. This is the most common crystallisation phenomenon, and it often occurs. The presence of impurities of any kind within the polymer, generates a surface on which the crystal can thermodynamically arise. These impurities can also be purposely inserted, such as nucleation agents, i.e., substances that promote crystal nucleation, increasing the degree of crystallinity of the polymer [57,59].

2.1.5.2 Primary crystallisation: growth or secondary nucleation

Following the nucleation of new crystals, they begin to grow in a preferential direction. Considering a spherulite, i.e., the crystal form created by the three-dimensional union of several lamellae, it grows radially until its size is such that it meets another growing

spherulite. At that point, the two come into contact and stop their growth because they no longer have the space to further increase their volume. Usually, the process continues until the time corresponding to 50% crystallised volume is reached, this very important parameter is called $\tau_{50\%}$, i.e., the half-crystallisation time. These two paragraphs together form primary crystallisation, i.e., the combination of nucleation (or primary nucleation) and growth (or secondary nucleation) [59].

2.1.5.3 Secondary crystallisation

This phase begins when the crystals start to encounter each other. This occurs on average after passing the half-crystallisation time ($\tau_{50\%}$) and marks the end of the primary crystallisation phase. Even if all the spherulites have stopped growing because they have met their neighbours, remains space between one spherulite and another, so this refinement process begins. This can be a densification of the lamellae within the spherulite, or a thickening of the lamellae or a refinement in the crystal shape. This process is very slow compared to the speed of primary crystallisation.

2.1.6 Avrami classic model: isothermal crystallisation

The Avrami equation was one of the first models to analyse the entire crystallisation process during an isothermal process [38]. In particular, the model follows the approximation of the free growth of nuclei, so it approximates well the behaviour during primary crystallisation, nucleation and growth, i.e., up to the half-crystallisation time, $\tau_{50\%}$, i.e., until the volume fraction of crystalline phase (V_c) is equal to 50%. In its simplest form, the Avrami equation considers a constant nucleation rate and growth rate (Eq.(2)).

$$1 - V_c = e^{-kt^n} \tag{2}$$

Where V_c is the volumetric fraction of crystallised material at time t, k is the general crystallisation rate, i.e., considering both nucleation and growth, and n is the Avrami index. The latter can be written as the sum of two contributions (Eq.(3)):

$$n = n_{gD} + n_n \tag{3}$$

Where n_{gD} represents the shape of the crystal and can be 1 if one-dimensional, 2 if two-dimensional, 3 if three-dimensional. In polymers, the most common values obtained are 2 or 3, because the structures often obtained are lamellae (two-dimensional) or spherulites (three-dimensional). On the other hand, n_n considers the time dependence of nucleation and can vary between 0 and 1. A value of 0 corresponds to instantaneous nucleation, while 1 is completely sporadic nucleation. Thus, Avrami's index can have values between 1 and 4 as can be seen from the diagram in Fig. 10. This equation is widely used in literature to

analyse the overall isothermal crystallisation process obtained by differential scanning calorimeter measurements or more simply DSC [59,60].

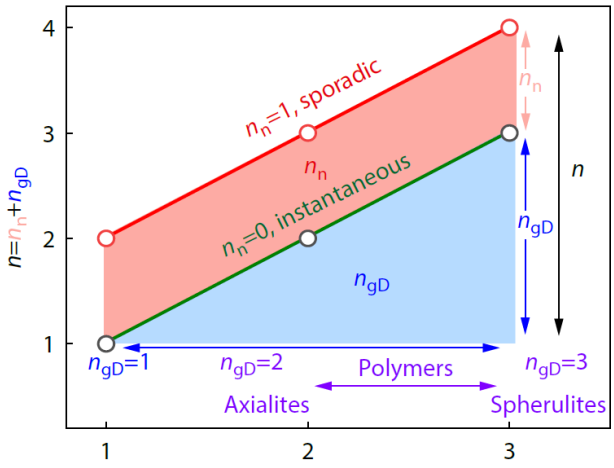

Fig. 10: Avrami index variation [59].

For practical purposes Eq.(2) was modified by Lorenzo et al. [61] by introducing the term induction time, t_0. This term indicates the time that must elapse at the given isothermal crystallisation temperature T_c for the crystallisation process to begin. Because once the material is brought to T_c, the crystallisation process does not begin instantaneously, but must wait for this time for primary nucleation to begin. So, considering the induction time, Eq.(2) becomes Eq.(4):

$$1 - V_c = e^{-k(t-t_0)^n} \tag{4}$$

And thus, the volume fraction V_c will be a function of the term $t-t_0$.

Performing the Napierian logarithm (ln) to both terms of Eq.(4) and then apply the log in base 10 (log) to them, we obtain Eq.(5):

$$\log[-\ln(1 - V_c)] = \log(k) + n\log(t - t_0) \tag{5}$$

Eq.(5) is called the Avrami plot and is the linear form of the Avrami equation, from which k and n can easily be derived from the experimental data, n being the angular coefficient and k the intercept.

By switching from the volume fraction to the mass fraction, it is possible to rewrite V_c according to Eq.(6):

$$V_c = \frac{W_c}{W_c + \left(\frac{\rho_c}{\rho_a}\right)(1 - W_c)} \tag{6}$$

Where ρ_c is the density of the theoretically 100% crystalline material and ρ_a is the density of the 100% amorphous material.

W_c can be calculated by DSC tests according to Eq.(7):

$$W_c = \frac{\Delta H}{\Delta H_{tot}} \tag{7}$$

Where ΔH is the enthalpy change recorded over time during an isothermal crystallisation at the crystallisation temperature T_c, while ΔH_{tot} is the maximum crystallisation enthalpy obtained at the end of the isothermal crystallisation process.

Finally, again from the Avrami equation, a theoretical expression of the half-crystallisation time $\tau_{50\%}$, where V_c =0.5, can be obtained (Eq.(8)):

$$\tau_{50\%} = \left(\frac{\ln 2}{k}\right)^{\frac{1}{n}} \tag{8}$$

The difference between $\tau_{50\%}$ theoretical and experimental is an indication of the goodness of fitting the experimental data. The experimental value can be obtained from the specific heat versus time graph, by measuring the time corresponding to the peak of isothermal crystallisation.

2.1.7 Theory of Lauritzen and Hoffman

Secondary nucleation or growth, described in the previous paragraphs, can be modelled according to an equation developed by Lauritzen and Hoffman, or also called the LH equation [62]. This equation correlates the growth rate (G) with supercooling. The latter parameter is defined as the temperature gap between the crystallisation temperature and the melting temperature at equilibrium, i.e.: $\Delta T = T_m^0 - T_c$. This model is mainly used to fit DSC data during the polymer crystallisation process.

In addition to the LH theory, which the scientific community criticises to date, there are various models describing the crystallisation process [63]. For example, the Sadler and Gilmer model [64] based on the concept of barrier entropy; the intermolecular nucleation model of Hu et al. [65]; Strobl's multi-stage [66] or even the continuum model of Muthukumar et al. [67]. In contrast to the LH model, all those listed here are more accurate, but do not have an easy-to-use analytical form and require simulations. The LH model, on the other hand, has an easy-to-apply analytical form and is therefore the most widely used model in the literature for fitting experimental data from DSC tests.

Talking about the growth velocity (G) of spherulites, this is the velocity that can be observed experimentally under a polarised light optical microscope or also known by the

acronym PLOM (Polarised Light Optical Microscopy). Growth speed is measured by taking several photos over time during the crystallisation process.
The LH theory predicts the growth of a stem from a nucleation surface, as can be seen in Fig. 11.

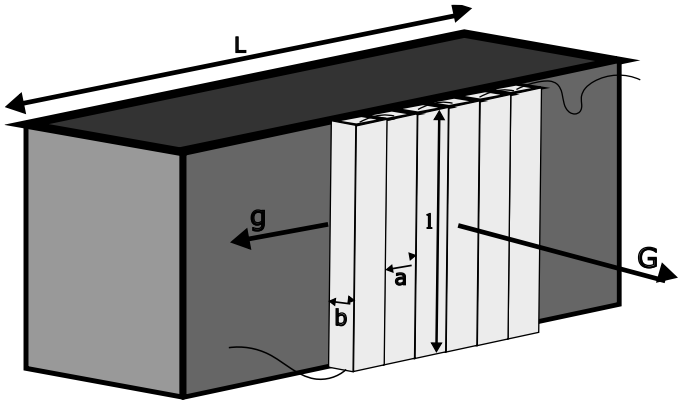

Fig. 11: Schematic representation of crystal growth according to the Lauritzen-Hoffman theory – redesigned by [68].

Stems are characterised by their length l, thickness b along the direction G and width a along the direction g. G and g are not only the growth directions, but also the growth velocities in that direction. The velocity along the G direction is constant for given T_c. A further important parameter to consider is the nucleation velocity, called i, i.e., the speed at which new nuclei are formed. According to LH theory, there are three possible regimes during the crystallisation process:

- Regime I: In this case g >> i and thus stem growth in the g-direction is predominant, resulting in a structure that will complete the surface of length L before advancing in the g-direction, as shown in Fig. 12a
- Regime II: g ≤ i, in this case the nucleation rate is greater than regime I and comparable to g, a separation between the stems, i.e., niches, is created as growth follows both the g and the G direction. These niches can also be larger than the width, a, of the stem (Fig. 12b)
- Regime III: i >> g, in this case the growth corresponds to increased nucleation and the niches are the same size as the stem width (Fig. 12c).

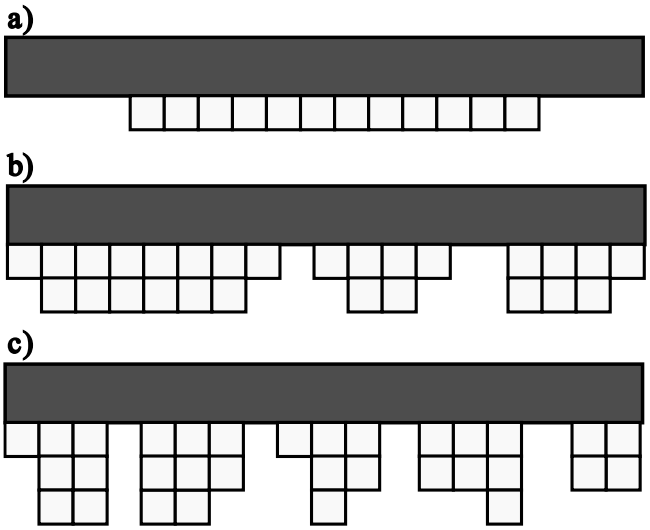

Fig. 12: Lauritzen-Hoffman theory schematisation - a) regime I; b) regime II; c) regime III – redesigned by [69].

According to the most general form, the LH equation has the following expression (Eq. (9)):

$$A = A_0 e^{\left(-\frac{U^*}{R(T_c - T_\infty)}\right)} e^{\left(-\frac{K_g^A}{T_c \Delta T f}\right)} \tag{9}$$

It is referred to as a generic formula since A can vary depending on how it is used. If Eq.(9) is applied to fit data from the PLOM, where crystal growth was observed, then the A becomes G and what is being analysed is the actual crystal growth, i.e., secondary nucleation. On the other hand, if the same equation is used to fit data from DSC tests, A will be the total crystallisation rate, i.e., $1/\tau_{50\%}$ and what is being analysed will be the total crystallisation process, nucleation plus growth. In what follows, it will utilize only the version where A=$1/\tau_{50\%}$, so Eq.(9) can be rewritten as follows (Eq.(10)):

$$\frac{1}{\tau_{50\%}} = \frac{1}{\tau_0} e^{\left(-\frac{U^*}{R(T_c - T_\infty)}\right)} e^{\left(-\frac{K_g^\tau}{T_c \Delta T f}\right)} \tag{10}$$

In Eq.(10) the term $1/\tau_0$ is constant and considers the constant total crystallisation rate, this term includes all temperature-independent parameters.

It can be seen from the expression in Eq.(10) that it is divided into two contributions. The first exponential term is called "diffusive" and expresses the temperature dependence of the transport velocity of the crystalline segments. Whereas the second term is called “nucleation” and expresses the temperature dependence of the nucleation velocity. Within these two terms it can be found:

- U* is defined as the activation energy for the transport of the chains on the crystallisation surface. It is a constant value and as a first approximation can be taken as 1500 cal/mol unless the exact value is known, which can be obtained by rheological tests.
- R is the universal gas constant ($8.314\ \frac{J}{mol\ K}$).
- T_c is the isothermal crystallisation temperature.
- $T_\infty = T_g - 30\ K$ this is a hypothetical temperature at which it is certain that the mobility of the chains is interrupted.
- ΔT is supercooling defined as $\Delta T = T_m^0 - T_c$ where T_m^0 is the melting temperature at equilibrium.
- f is a temperature correction factor that considers changes in enthalpy of fusion with crystallisation temperature and is equal to: $f = \frac{2T_c}{T_c + T_m^0}$
- K_g^τ is a constant proportional to the barrier energy for the entire crystallisation process. It can be expressed according to the following expression (Eq.(11)):

$$K_g^\tau = \frac{jb_0\sigma\sigma_e T_m^0}{\kappa \Delta H_f} \tag{11}$$

Where j is a constant depending on the regime, it takes the value 4 when considering regime I or III, or it is worth 2 when considering regime II; b_0 is the width of the stem (Fig. 11); σ is the lateral surface free energy; σ_e is the fold free energy; κ is the Boltzmann constant $\left(1.23 * 10^{-23}\ \frac{J}{K}\right)$; ΔH_f is the enthalpy of fusion of the 100% crystalline material. The equation of LH expressed in logarithmic terms is a straight line of angular coefficient K_g^τ and intercept $\ln\frac{1}{\tau_0}$ (Eq. (12)):

$$\ln\frac{1}{\tau_{50\%}} + \frac{U^*}{R(T_c - T_\infty)} = -K_g^\tau\left(\frac{1}{T_c \Delta T f}\right) + \ln\left(\frac{1}{\tau_0}\right) \tag{12}$$

In this form, considering $y = \left(\ln\frac{1}{\tau_{50\%}} + \frac{U^*}{R(T_c - T_\infty)}\right)$ and $x = \left(\frac{1}{T_c \Delta T f}\right)$, linear fitting can be performed from the experimental data of $1/\tau_{50\%}$ and T_c , to derive K_g^τ e $1/\tau_0$.
Via the Thomas-Stavely equation [70] it is possible to calculate σ (Eq.(13)):

$$\sigma = 0.1\Delta H_f\sqrt{a_0 b_0} \tag{13}$$

Where $a_0 b_0$ is the cross-sectional area of the stem. To this equation is added that of q, i.e., the work done by the chain to form a fold (Eq.(14)):

$$q = 2a_0 b_0 \sigma_e \tag{14}$$

Therefore, known K_g^τ from fitting the experimental data via the LH equation (Eq.(12)), using Eq.(11) e (13) it is possible to obtain σ_e and subsequently, using Eq.(14) the parameter q can be derived.

Finally, it is possible to state that Eq.(10), in the two contributions of nucleation and diffusion, has a contrasting trend, because as the temperature increases, the first term related to diffusion increases, since the transport of molecules increases with temperature; on the other hand, the nucleation term decreases with increasing temperature. For this reason, the graph of $\frac{1}{\tau_{50\%}}$ as a function of crystallisation temperature shows a bell shape with a maximum value [49,58,59,68].

2.1.8 Modified model of Avrami: The Dual Avrami

The Avrami model, as explained in the previous paragraphs, is not always adequately accurate in modelling relative crystallinity. Indeed, it fails to approximate secondary crystallisation and thus loses accuracy after the value of V_c has exceeded 50%. Consequently, models were developed, still based on the Avrami equation, but considering secondary crystallisation. One of these is the model of Velisaris and Seferis [71] who suggested a model consisting of two Avrami equations in parallel, considering the competition between two growth processes (Eq.(15)):

$$V_c = \omega_p\left[1 - e^{-k_p(t)^{np}}\right] + \omega_s\left[1 - e^{-k_s(t)^{ns}}\right] \quad (15)$$

Where ω_p e ω_s are the critical constants of the primary and secondary crystallisation process. In fact, the subscript p and s stand for primary and secondary respectively. In the specific case of PEEK, it is commonly accepted that secondary crystallisation corresponds to the formation of thin lamellae within liquid pockets contained between the thicker lamellae of primary crystallisation [72]. Whereas primary crystallisation occurs in the amorphous phase, secondary crystallisation occurs when the material is already crystalline and has crystals from the primary crystallisation trying to grow. Therefore, the secondary Avrami exponent will have to be smaller than the primary one, because it is only related to the growth in crystal size [73]. Seo et al. [74] modified Eq.(15) by replacing the percentage by weight of crystalline and amorphous fraction (i.e. ω_p e ω_s) with the probability of primary and secondary crystallisation occurring, since these two occur simultaneously during the crystallisation process (Eq.(16)):

$$V_c = P_p\left[1 - e^{-k_p(t)^{np}}\right] + P_s\left[1 - e^{-k_s(t)^{ns}}\right] \quad (16)$$

Where the two P are proportional to the volume fraction of crystalline and amorphous phase:

$$P_s = V_c \tag{17}$$

$$P_p = 1 - V_c \tag{18}$$

The sum of the two probabilities will always give 1. Combining Eq. (16), (17), (18) we obtain the modified Avrami equation (Eq. (19)):

$$V_c = \frac{\left[1 - e^{-k_p(t)^{n_p}}\right]}{\left[1 - e^{-k_p(t)^{n_p}}\right] + \left[e^{-k_s(t)^{n_s}}\right]} \tag{19}$$

It can also be assumed that the crystallisation process changes from primary to secondary when V_c =0.5. At this point the time is equal to $\tau_{50\%}$. If V_c =0.5 then both primary and secondary crystallisation refer to the same crystal volume value and thus it can be written that (Eq. (20)):

$$1 - e^{-k_p(\tau_{50\%})^{n_p}} = 1 - e^{-k_s(\tau_{50\%})^{n_s}} \tag{20}$$

And thus, it can be able to derive k_s as a function of the coefficients of primary crystallisation (Eq.(21)):

$$k_s = k_p \tau_{50\%}^{n_p - n_s} \tag{21}$$

Using Eq.(8) to derive $\tau_{50\%}$ as a function of k_p and n_p, the following Eq.(22) can be derived:

$$k_s = k_p \left[\frac{\ln(2)}{k_p}\right]^{1-\frac{n_s}{n_p}} \tag{22}$$

By inserting Eq.(22) into Eq.(19) we obtain the expression of the Dual Avrami model (Eq.(23)):

$$V_c = \frac{\left[1 - e^{-k_p(t)^{n_p}}\right]}{\left[1 - e^{-k_p(t)^{n_p}}\right] + \left[e^{-k_p(t)^{n_s}\left(\frac{\ln(2)}{k_p}\right)^{1-\frac{n_s}{n_p}}}\right]} \tag{23}$$

In Eq. (23) the numerator is the classical Avrami equation, while the denominator is the correction function to account for the phenomenon of secondary crystallisation. This equation allows the fitting of the isothermal crystallisation process considering the dual nature of crystallisation kinetics and depending on only three fitting parameters: k_p; n_p; n_s.

In this thesis work, Eq. (23) will be used to better approximate the entire PEEK crystallisation curve, so that an equation can be easily fitted within an Abaqus model.

2.1.9 Self-nucleation (SN)

Self-nucleation is a thermal procedure to produce self-nuclei in the molten polymer. Theoretically, the best nucleating agent for any polymer is its own crystal fragments or polymer chains that are found in the melt and maintain the "memory" of the crystal state shape [63-65]. The SN technique was originally studied by Blundell et al. [78] to improve single crystal preparation from a solution. Fillon et al. [77] were the first to study the SN phenomenon using DSC and identified three domains that can be described as follows:

- Domain I or melting domain: the polymer is in domain I when it is completely melted, and the crystalline history completely erased.
- Domain II or SN exclusive domain: in this domain the polymer is heated sufficiently to melt most of the crystals but is low enough to create self-nuclei. In Domain II the T_c is shifted to higher values as it depends on the density of the self-nuclei and there is no trace of annealing.
- Domain III or domain with SN and annealing: when the temperature of SN, T_s, is too low, during the time required for self-nucleation, usually about 5 minutes, in addition to the formation of self-nuclei, there is also an annealing phenomenon of the crystals that had not fully fused. In this case, two endothermic peaks can be observed in the DSC scan, one related to SN and one to annealing.

The SN phenomenon may be important because, when considering the T_s that delimits domain II from domain III, the material almost instantaneously produces the maximum crystalline phase density. This temperature is identified as $T_{s,ideal}$ and is used as an indirect form to assess crystal growth alone, without any nucleation phenomenon (because all the crystalline phase that could be formed has already formed). Using $T_{s,ideal}$ and performing isothermal crystallisation tests, with a particular temperature protocol, it is possible to follow the crystal growth-only phase using the Lauritzen-Hoffmann equation.

2.1.9.1 Nucleation efficiency

One of the best ways to quantitatively calculate the efficiency of an additive on the crystallisation of a polymer is to use SN.

The nucleation efficiency (NE) can be calculated according to Eq. (24):

$$NE = \frac{T_{c,NA} - T_{c,pol}}{T_{c,max} - T_{c,pol}} \quad (24)$$

Where $T_{c,NA}$ is the crystallisation temperature measured from the non-isothermal cooling peak of the polymer with a nucleating agent (NA); $T_{c,pol}$ is that of the base polymer; $T_{c,max}$ is the maximum crystallisation temperature of the polymer that has undergone the

SN cycle at temperature $T_{s,ideal}$ [77,79]. When, for example, the presence of a reinforcement (fibrous or particle) within a composite is considered as NA, the nucleation efficiency that the fibres create to the polymer matrix of the composite can be calculated.

2.1.10 Subsequent self-nucleation and annealing (SSA)

Polymers are not always composed of a succession of the same monomer, but sometimes couplings are created to generate a polymer containing different properties. This is the case, for example, with comonomers that are added to the monomer, forming the copolymer by polymerisation. A practical example is polyolefins, which can be used with ethylene to create the ethylene/α-olefin copolymer. This example is appropriate in this paragraph since these materials are often studied by fractionation. Fractionation involves dividing the material, physically or otherwise, so that its components can be studied and how they interact with each other. Fractionation can be performed in solution or thermally. Solution fractionation generates a physical separation of the components but is complicated and time-consuming. Among the most widely used solution fractionation techniques are Temperature Rising Elution Fractionation (TREF) and Crystallisation Analysis Fractionation (CRYSTAF) [80]. Alternatively, thermal fractionation uses thermal protocols at the DSC, through which it is possible to obtain information regarding the various components or otherwise through simple thermal cycles. Thus, these are much simpler and more efficient techniques. Conversely, a physical separation between the components is not achieved and therefore measurements can be affected by imperfections or defects in the bonds established between the different chemical species. The successive self-nucleation and annealing (SSA) technique is a thermal fractionation technique that was developed by Müller et Al. [81]. It involves applying the thermal protocol of self-nucleation, outlined in the previous section, in several steps, decreasing the T_s with a defined interval. In this way, at the end of all the steps, a final heating up to above the melting temperature of the material is carried out, resulting in a succession of melting peaks, which refer to the melting of crystals of different thicknesses, formed and grown during the various steps. An example of the SSA technique applied to the HPB polymer is shown in Fig. 13 [82].

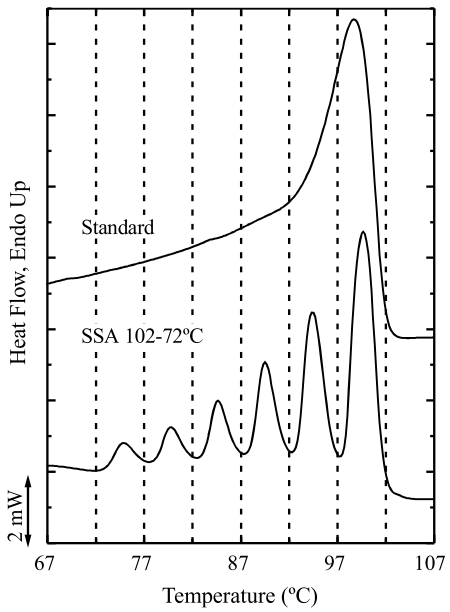

Fig. 13: DSC analysis with 10 °C/min heating of HPB before (standard) and after SSA fractionation [82].

This technique can be used not only to study the fractionation of copolymers, but also to analyse the nucleating effect of chemical species inserted in the polymer, such as when considering composites whose matrix has carbon nanotubes or others. By applying the same SSA thermal protocol to the polymer with and without the addition of elements, it is possible to assess, from the variation that occurs in the peaks, whether the added element interacts with the crystallisation process. For example, this technique was used by Pérez-Camargo et al. [83] to assess the nucleating effect of lignin in a PCL matrix.

To obtain truthful information from the material, the technique must be applied following rules [84]. Usually, it always starts with the $T_{s,ideal}$ and therefore the first thermal protocol to be applied is that linked to the identification of this particular temperature. From that, it goes on to identify the peaks corresponding to T_s lower than $T_{s,ideal}$ by 5 °C at a time, this is the ΔT_s called the "fractioning window". This quantity ensures a balance between good resolution and spacing between fractionations and must never be less than 2.5 °C. As it starts at $T_{s,ideal}$ and decreases in steps of 5 °C, it moves from domain II to domain III, where *annealing* phenomena exist. During the process, when T_s is reached, there is only partial melting of some crystals, during a time that is usually 5 minutes. This time is a key parameter and is the same as that used in the determination of $T_{s,ideal}$. Similar results are obtained if this time varies between 5 and 15 minutes, so it is always preferable to use the shorter time. In the case of polymers that show degradation phenomena in that time, it can be decreased to 1 minute. The important thing is, as mentioned, that this time must be the same in both $T_{s,ideal}$ and SSA. Being in regime III, during this time there is not only a partial melting of the crystals, but also a thickening of those that do not melt (the

annealing phenomenon). Therefore, as the T_s varies, there will be different thicknesses, which can be observed in the final heating by all the peaks presents. Each peak corresponds to the chosen T_s. Since the first peak corresponds to $T_{s,ideal}$, there will be no annealing phenomenon, whereas for all other peaks there will be.

2.2 Experimental of the first part

2.2.1 Materials

During this phase of the research project, the materials studied are polyether ether ketone (PEEK) and carbon fibre-reinforced fabric. The polymer is produced by Solvay in pellet form and is called Ketaspire®. It has a melting temperature (T_m) of 340°C and a glass transition temperature (T_g) of 150°C. The carbon fibre fabric is bi-directional plain with a weight of 200 g/m^2 and is produced by Hexcel. The fibres that make up the fabric are HexTow® AS4 3k.

In Tab. 2 shows the main properties of these materials.

Tab. 2: Mechanical and thermal properties of the matrix and reinforcement.

Properties from data sheet	PEEK Ketaspire®	HexTow® AS4 3k
Young's modulus [GPa].	3.5	231
Tension at break [MPa].	95	4620
Strain at break [%].	20-30	1.8
Specific heat [cal/g°C]	0.238	0.27
Thermal conductivity [W/mK]	0.24	6.83

2.2.2 Manufacture

To use differential scanning calorimetry (DSC) as a method of study, polymer foils were produced from the pellet. To recreate a DSC sample of the correct weight, it is necessary that the specimen is between 3 and 5 mg in order not to create problems with the proper heating or cooling of the material. For this reason, it was decided to create the foils with a thickness of 0.5 mm. In this way, considering the base area of the DSC crucible, a weight of between 3 and 5 mg can be obtained by almost filling the base. The technological process used is compression moulding in a CARVER Autofour/3012-PLH hot press following the thermal cycle observed in Fig. 14.

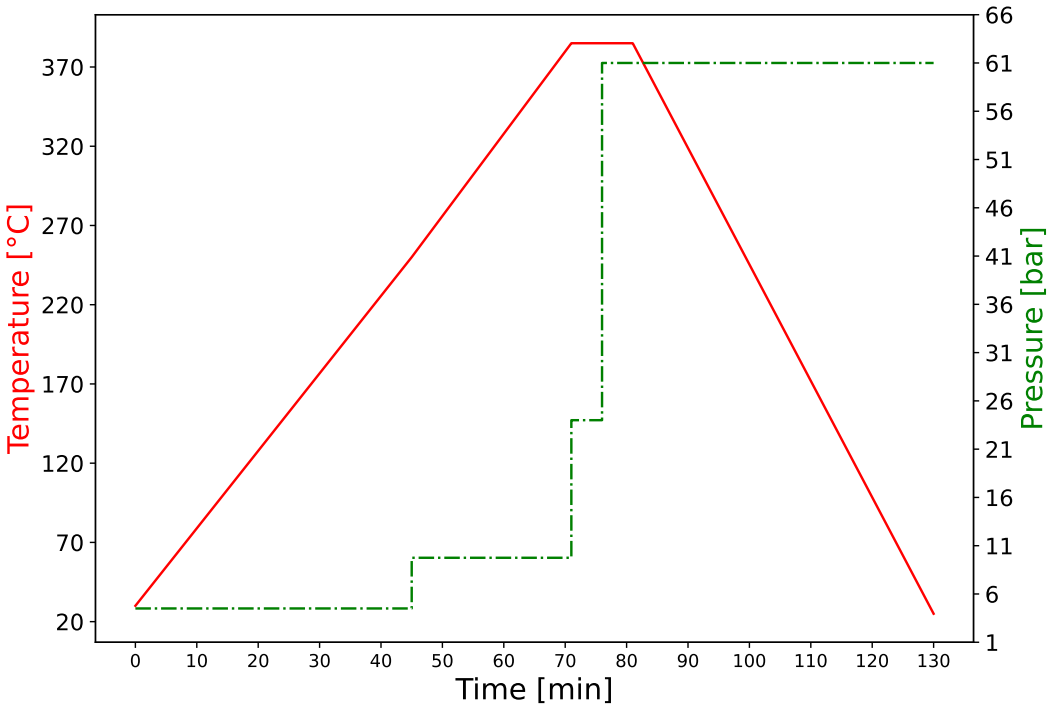

Fig. 14: Temperature-pressure cycle for the manufacture of PEEK and PEEK/carbon films for the crystallinity study.

Specifically, for PEEK neat foils, 6g of pellets were spread on a mould measuring 100x100x0.5 mm, heated to a temperature of 385°C and held for 20 minutes. The pressure was gradually increased to a maximum value of 61 bar, which was maintained until the material had completely cooled down. For the PEEK/carbon composite, initially, following the same procedure as above, two films of 0.25 mm thickness and 100x100 mm^2 surface area were formed, using 6 mg pellets for each. The composite was then created with the two PEEK foils and the carbon fabric foil, with the carbon foil placed between the two polymer foils. Approximating from the weight of the reinforcement and matrix contained in the composite after fabrication, it can be stated that the mass percentage content of the reinforcement is approximately 20%.

The test specimens for the tensile test were prepared using the same hot press. First, 18 g pellets were used to create a 150x100x0.9 mm panel by applying the same pressure-temperature cycle as in Fig. 14. Secondly, the same panels were heated up to 385°C with a pressure of 7 bar. Finally, each panel was cooled down to a specific crystallinity-related temperature, following the non-isothermal cooling curve in Fig. 15. The cooling rate of 40 °C/min is the value given by the hot-press. The cooling rate of 40 °C/min is the value given by the hot press. While cooling the material at 40 °C/min, having reached the temperature relative to a specific crystallinity value, the sample was taken out of the hot press and immediately immersed in fresh water to freeze the crystallinity value obtained.

From each panel, varying the crystallinity value, five specimens of 17x150x0.9 mm were cut to perform tensile test.

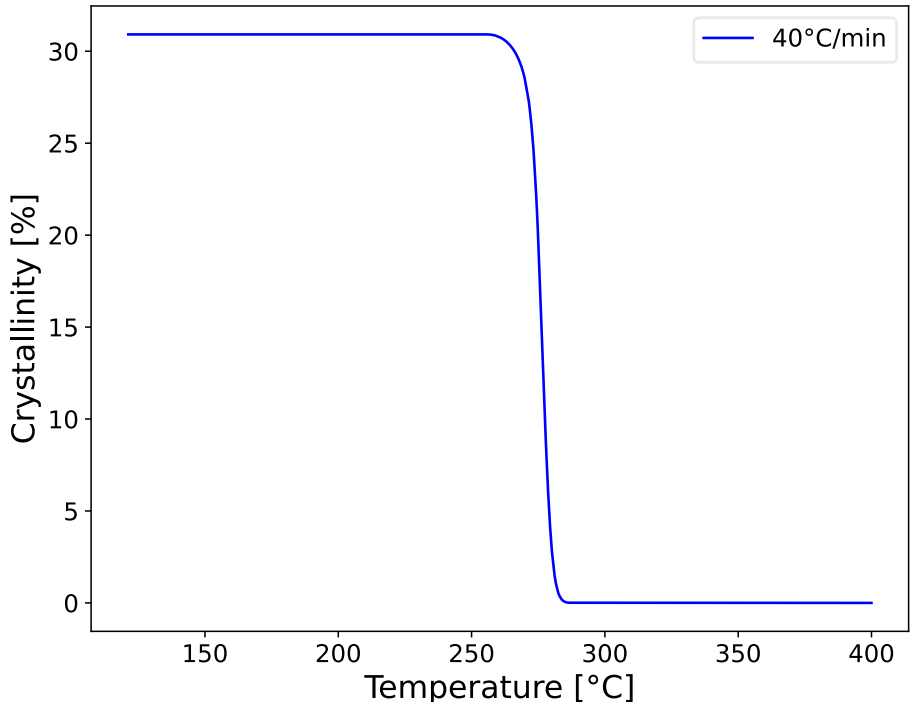

Fig. 15: Crystallinity-temperature during non-isothermal crystallization at 40°C/min in PEEK neat.

2.2.3 Differential scanning calorimetry (DSC)

Differential scanning calorimetry or DSC is the main thermal analysis technique that can be used to characterise a polymeric, metallic, or ceramic material.

The basic principle of this technique is to obtain information about the material by heating or cooling it in a controlled manner, i.e., by imposing so-called temperature profiles. Specifically, DSC is based on measuring the difference in heat flux between the sample under test and a reference sample while the two are constrained to undergo a time-varying but equal temperature cycle.

In this work, DSC is used to study the crystallisation kinetics of PEEK and how it is influenced by the presence of carbon fibres. In addition, with the data from the crystallisation kinetics, by applying theoretical models, it will be possible to use this information to input it into Abaqus simulations.

All measurements were carried out at the POLYMAT laboratories, located in San Sebastian, Spain, under the supervision of Prof. Alejandro J. Müller.

The instrument used is the DSC Perkin Elmer 8000 characterised by two separate furnaces for the sample and the reference, obviously subjected to the same thermal cycle.

In the following, when the term “PEEK neat” is written, it will refer to PEEK without the addition of anything, while if the term “PEEK CF” is displayed, it will refer to PEEK reinforced with carbon fibre fabric.

The entire experimental campaign related to the study of crystallisation kinetics can be divided into two groups of measurements:

- Analysis of isothermal crystallisation kinetics from the melt of both PEEK neat and PEEK CF to obtain the data set to apply the theoretical models.
- Analysis of crystal growth kinetics, studying isothermal crystallisation from the ideal self-nucleation temperature ($T_{s,\,ideal}$).

2.2.3.1 Thermal protocol $T_{c,\,min}$ PEEK from melt

The kinetics of isothermal crystallisation from the melt is studied by starting with the identification of the minimum crystallisation temperature, i.e., that temperature above which no crystallisation phenomena are observed following rapid cooling at the desired speed. For this work, the speed used for rapid cooling is 50 °C/min. The thermal protocol applied is as follows:

1. Bringing the material to equilibrium at 400 °C
2. Cooling down to assumed T_c at 50 °C/min
3. Heating from the assumed T_c up to 400 °C at 20 °C/min
4. Keep at 400°C for 3 minutes (to eliminate thermal history)
5. Repeat steps 2 to 4 for another T_c

The assumed T_c ranges from 296 °C to 300 °C for PEEK neat, and 295 °C to 300 °C for PEEK CF.

2.2.3.2 Thermal protocol for PEEK isothermal crystallisation from melt

Once the $T_{c,min}$ has been identified, a protocol can be created from this to investigate isothermal crystallisation as the T_c varies. From here it is easy to see why it is necessary to obtain a $T_{c,min}$, because if measurements of isothermal crystallisation were carried out below the $T_{c,min}$, there would be a double action on the formation of the crystalline phase, i.e. the component coming from non-isothermal cooling and that coming from isothermal maintenance at the desired T_c . This is why the entire study of isothermal crystallisation is carried out with T_c values greater than $T_{c,min}$. The protocol followed for the study is listed below:

1. Bringing the material to equilibrium at 400 °C
2. Cooling the material to a specific T_c ($\geq T_{c,min}$) at 50 °C/min

3. Keep at T_c for a certain time (varying between 10 and 60 minutes)
4. Heating the material from T_c to 400 °C at 20 °C/min
5. Keep at 400 °C for 3 minutes (to eliminate thermal history)
6. Repeat steps 2 to 5 for another T_c

For PEEK neat, the T_c chosen ranged from 300 to 309 °C with a variation of 1 °C at a time and from 312 to 322 with a variation of 2 °C at a time. For PEEK CF from 298 to 307 °C with a variation of 1 °C; the maximum value in PEEK CF was not passed because due to the higher temperatures, crystallization peaks during measurements were difficult to detect.

In addition, the choice of time during the isothermal step is not random. It must be at least 3 to 5 times longer than the time it takes the material to reach the maximum exothermic peak. Since as T_c increases, the material takes longer and longer to crystallise, then the total time must increase to follow the increase in crystallisation time.

2.2.3.3 Thermal protocol for temperature of self-nucleation ideal PEEK

The ideal SN temperature was identified to obtain the transition temperature between domain II and domain III. Repeating what has already been set out in the previous paragraphs, at this temperature, following the protocol that will be set out below, it is possible to obtain the maximum crystal density that the polymer can offer. In this way, since the maximum quantity of crystals is produced instantaneously, from this $T_{s,ideal}$, during the study of isothermal crystallisation, only the crystal growth phase is observed and not its nucleation, phases which are impossible to separate when measurements are made from the melt. In this way, an indirect evaluation of crystal growth alone is obtained, and it is possible to verify how the presence of the fibres influences it. Furthermore, it is useful to calculate the crystallisation efficiency.

The protocol used for the detection of $T_{s,ideal}$ is as follows:

1. Bringing the material to equilibrium at 400 °C
2. Cool the material from 400 °C down to below T_g, then 120 °C, at 20 °C/min.
3. Keep at 120 °C for 1 minute to stabilise
4. Heating from 120 °C to assumed $T_{s,ideal}$ at 20 °C/min
5. Keep at assumed $T_{s,ideal}$ for 5 minutes, to nuclearize the entire crystalline phase
6. Cooling from assumed $T_{s,ideal}$ to 120 °C at 20 °C/min
7. Keep at 120 °C for 1 minute
8. Heating from 120 °C to 400 °C at 20 °C/min
9. Hold for 3 minutes at 400 °C to eliminate thermal history

10. Repeat all steps 2 to 9 by varying the assumed $T_{s,ideal}$

For PEEK neat the investigated $T_{s,ideal}$ vary between 337 and 348 °C, while for PEEK CF between 343 and 348 °C.

2.2.3.4 Thermal protocol $T_{c,min,SN}$ PEEK from $T_{s,ideal}$

Identified the $T_{s,ideal,}$ the study of isothermal crystallisation is carried out from this, in the same way as observed in the previous paragraphs, then a protocol must be applied to measure the $T_{c,min,SN}$ again. This must be recalculated because the $T_{c,min,SN}$ of the material, starting from $T_{s,ideal}$, is always greater than that obtained when the material is cooled by the melt. For this reason, the following protocol is applied:

1. Bringing the material to equilibrium at 400 °C
2. Cool the material from 400 °C down to below T_g, then 120 °C, at 20 °C/min.
3. Keep at 120 °C for 1 minute to stabilise
4. Heating from 120 °C to the previously calculated $T_{s,ideal}$ at 20 °C/min
5. Keep at $T_{s,ideal}$ for 5 minutes, to nucleare the entire crystalline phase
6. Cooling from $T_{s,ideal}$ to assumed $T_{c,SN}$ at 50 °C/min
7. Heating from the assumed $T_{c,SN}$ up to 400 °C at 20 °C/min
8. Hold for 3 minutes at 400 °C to eliminate thermal history
9. Repeat steps 2 to 8, changing the assumed $T_{c,SN}$

For PEEK neat the assumed $T_{c,SN}$ ranged from 303 to 316 °C. For PEEK CF, the assumed $T_{c,SN}$ ranges from 300 to 310 °C.

2.2.3.5 Thermal protocol for PEEK isothermal crystallisation from SN

Obtained the $T_{s,ideal}$ and the $T_{c,min,SN}$ it can proceed with the study of isothermal crystallisation from the SN phenomenon. The protocol is similar to the previous one, with the addition that for each step it is necessary to recreate the maximum crystal density and then grow the crystalline phase at $T_{s,ideal}$. The protocol to be followed is as follows:

1. Bringing the material to equilibrium at 400 °C
2. Cool the material from 400 °C down to below T_g, then 120 °C, at 20 °C/min.
3. Keep at 120 °C for 1 minute to stabilise
4. Heating from 120 °C to the previously calculated $T_{s,ideal}$ at 20 °C/min
5. Keep at $T_{s,ideal}$ for 5 minutes, to nucleare the entire crystalline phase
6. Cooling the material to a specific $T_{c,SN}$ ($\geq T_{c,min,SN}$) at 50 °C/min
7. Keep at $T_{c,SN}$ for a certain time (varying between 45 and 120 minutes)
8. Heating the material from $T_{c,SN}$ to 400 °C at 20 °C/min

9. Hold at 400 °C for 3 minutes (to eliminate thermal history)
10. Repeat steps 2 to 9 for another $T_{c,SN}$

For PEEK neat, the $T_{c,SN}$ chosen ranged from 316 to 319.5 °C with a variation of 0.5 °C each time. For PEEK CF, on the other hand, 308 to 311.5 °C were chosen, again with a variation of 0.5 °C.

2.2.3.6 Thermal protocol successive self-nucleation and annealing (SSA)

The protocol followed here is intended to make a comparison between PEEK neat and PEEK CF, so it will be identical for both specimens. As already stated in the guidelines of Müller et Al. [84] it will have to start from the $T_{s,ideal}$ protocol and follow particular rules already stated in the previous paragraphs. The protocol followed specifically for PEEK is shown below:

1. Bringing the material to equilibrium at 400 °C
2. Cool the material from 400 °C down to below T_g, then 120 °C, at 20 °C/min.
3. Keep at 120 °C for 1 minute to stabilise
4. Heating from 120 °C to the previously calculated $T_{s,ideal}$ at 20 °C/min
5. Hold at $T_{s,ideal}$ for 5 minutes
6. Cooling from $T_{s,ideal}$ to 120 °C at 20 °C/min
7. Keep at 120 °C for 1 minute
8. Heating from 120 to new T_s (which for the first will be$T_{s,ideal}$ minus 5°C) at 20 °C/min
9. Repeat steps 5 to 8 but each new T_s must always be 5 °C smaller than the previous one
10. After repeating all the necessary steps, the last step must be a heating from 120 °C to 400 °C at 20 °C/min, which is useful for observing the succession of peaks formed throughout the protocol.

In the present case, nine T_s were observed starting from $T_{s,ideal}$, decreasing by 5 °C at a time.

2.2.3.7 Thermal self-nucleation protocol: identification of domains

Identified $T_{s,ideal,}$ which separates domain II from III, a further thermal history was applied to identify all domains of self-nucleation in the material. To achieve this, various temperatures T_s were investigated and compared with standard crystallisation temperatures obtained from non-isothermal cooling starting from the melt.

1. Bringing the material to equilibrium at 400 °C

2. Cool the material from 400 °C down to below T_g, then 120 °C, at 20 °C/min (to create the non-isothermal reference cooling curve)
3. Keep at 120 °C for 1 minute to stabilise
4. Heating from 120 °C to 400 °C at 20 °C/min (to obtain the non-isothermal reference heating curve)
5. Keep at 400°C for 3 minutes
6. Cooling the material from 400 °C to 120 °C, at 20 °C/min.
7. Keep at 120 °C for 1 minute to stabilise
8. Heating from 120 °C to assumed T_s at 20 °C/min
9. Maintain at the assumed T_s for 5 minutes, to nuclearize the entire crystalline phase
10. Cooling from assumed T_s to 120 °C at 20 °C/min
11. Keep at 120 °C for 1 minute
12. Heating from 120 °C to 400 °C at 20 °C/min
13. Repeat steps 5 to 12 for all assumed T_s

For both PEEK neat and PEEK CF, a wide temperature range was analysed, as the aim at this stage is to identify all material domains. Thus, the T_s range from 342 °C to 388 °C.

2.2.4 Mechanical tests

The tensile test was chosen as the mechanical test to evaluate the properties of the PEEK matrix when varying the crystallinity value. A WANCE universal testing machine model ETM-C equipped with a 50 kN load cell was used to perform the test. In addition, the samples were equipped with the YYU-10/50 extensometer with a gauge length of 50 mm to evaluate the displacements. The crosshead speed was set at 2 mm/min. Five samples were tested for each crystallinity value and the tensile strength and Young's modulus were compared between all sample types.

The crystallinity value of all samples was measured prior to the tensile test by means of a DSC measurement using the Linseis DSC-10 with a single heating from room temperature to 400 °C and a heating rate of 20 °C/min.

2.3 Results and discussions of the first part

2.3.1 $T_{c,min}$ from the melt

From the study of the $T_{c,min}$ of the PEEK neat shown in Fig. 16 it can be observed that the endothermic melting peak of the crystalline phase is present for all temperatures except 300 °C. Following the protocol outlined in 2.2.3.1 the result shown in Fig. 16 is the melting of the crystalline phase formed during cooling from the molten phase at the

chosen T_c . For this reason, all temperatures, less than 300 °C, show crystalline phase formation during cooling at 50 °C/min and therefore cannot be used in the subsequent isothermal study, where the crystalline phase only must grow due to maintenance at that specific T_c. Thus, the $T_{c,min}$ of the PEEK neat, starting from the melt, is 300 °C.

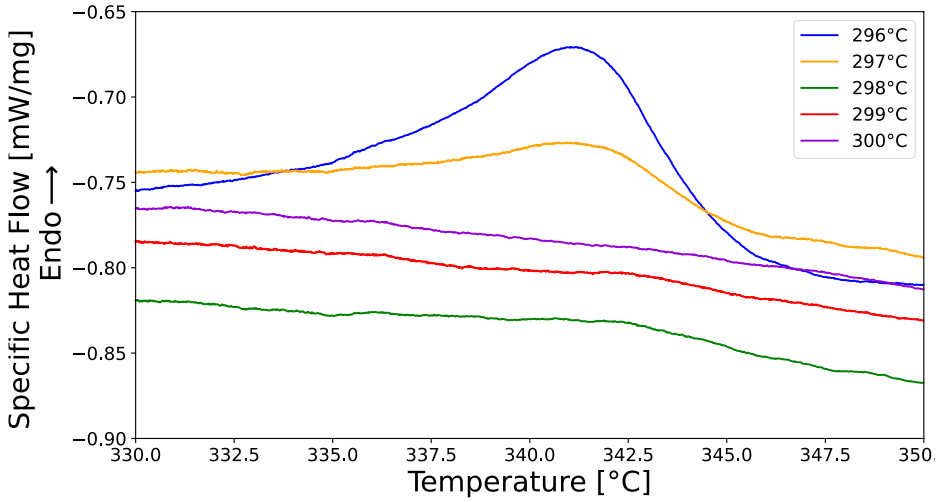

Fig. 16: Specific heat flow of the heating phase following cooling at 50 °C/min for PEEK neat.

Considering PEEK CF, i.e. with the addition of carbon fibres, the curves shown in Fig. 17 show less pronounced peaks, but with a detailed visual analysis it can be stated that the first T_c to show no peak is 298 °C, so the $T_{c,min}$ of PEEK CF is 298 °C. Comparing the two images, it is possible to see that the presence of the carbon fibres does indeed affect the crystallisation of the matrix.

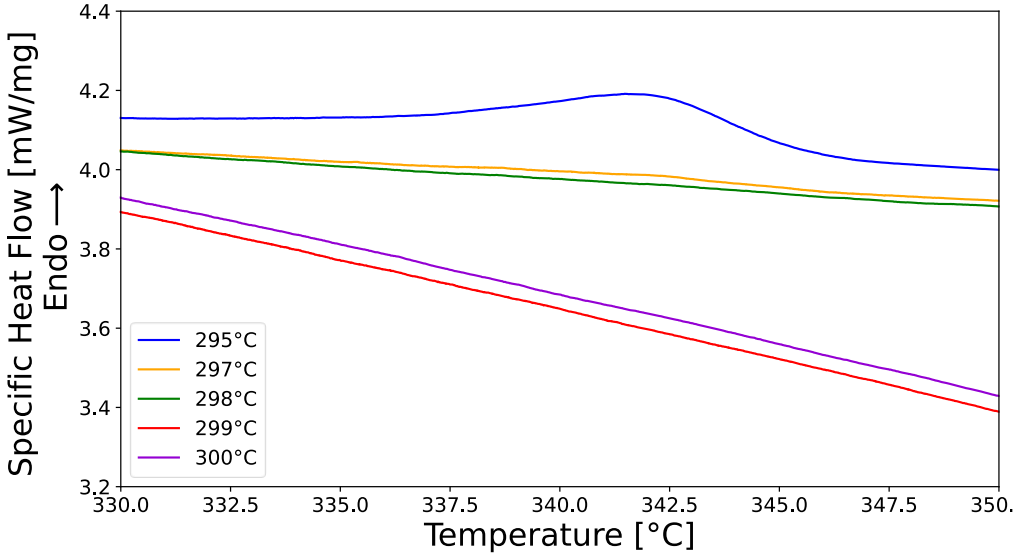

Fig. 17: Specific heat flow of the heating phase following cooling at 50 °C/min for PEEK CF.

2.3.2 Kinetics of isothermal crystallisation of PEEK neat from the melt: Avrami model

Following the protocol in section 2.2.3.2, as the T_c ($\geq T_{c,min}$) varies, different curves of the specific heat measured by the DSC are obtained as a function of the maintaining time at the specific T_c . This simple curve can be analysed by applying the theoretical model of Avrami, to calculate all those theoretical parameters that best explain the kinetics of crystallisation of this material; for simplicity's sake, the complete procedure for applying Avrami to a single temperature will be shown in this paragraph, while comparison graphs will be shown for all the others.

First, the raw data from the DSC is imported into a Python script written specifically by the author to process this data. In this work, these Python scripts were used, but there are also other programs that have already been developed that enable the application of Avrami model. One of these was written by Prof. Alejandro J. Müller as an app for Origin. Once the raw data has been imported into Python, a linear baseline is created with two points around the crystallinity peak. The first point is very important because it determines the induction time t_0. This parameter was added by Lorenzo et. al. [61] because, if the curve were fitted with Avrami model as it is, it would give totally unreal index values (>> 4). For this reason, this t_0 must be subtracted from the time, which indicates the time required for the material to begin the crystallisation process. A criterion for choosing this time is to evaluate the value of Avrami index to obtain a realistic value and then apply the same criterion to all other T_c. On the other hand, the second point, is chosen far enough from the crystallinity peak to be sure that the entire crystallisation process is contained within the baseline. Fig. 18 is an example of this first phase. Also, another two points are shown in the image indicating the beginning and end of the curve. These are only needed for construction in the Python script but have no physical meaning; the only two useful points are those before and after the peak.

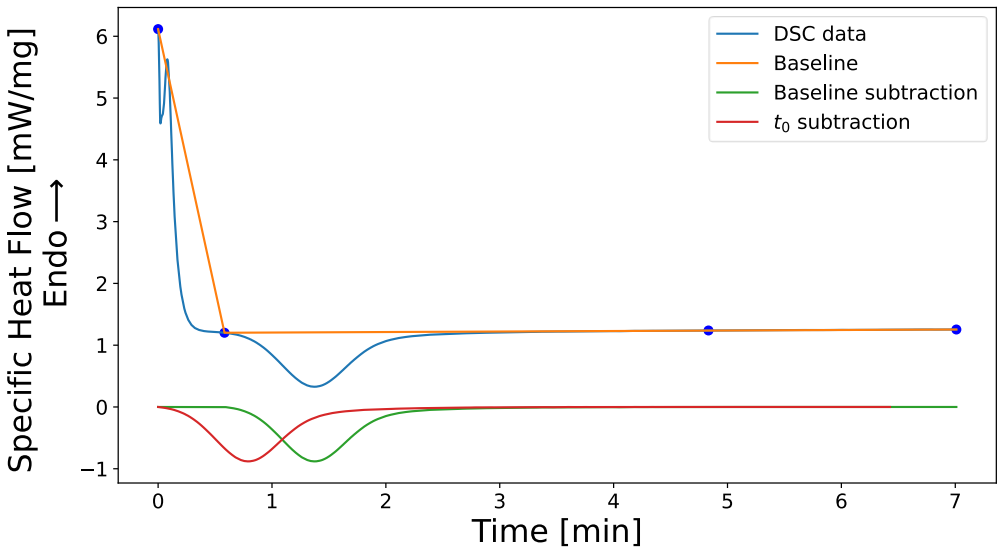

Fig. 18: Subtraction of the baseline from the DSC data to derive the experimental data for fitting in the Avrami - PEEK neat model.

The relative crystallinity can be calculated from the curve by subtracting the induction time. This is calculated by performing the point-by-point integral of the area subtended by the peak, divided by the total area (Eq. (25)).

$$X_{rel} = \frac{\int_{T_0}^{T} \frac{dH}{dT} dT}{\int_{T_0}^{T_{end}} \frac{dH}{dT} dT} \tag{25}$$

The script performs the calculation by dividing the consecutive sum of the areas of the trapezoids point by point by the total area, so the result will be between 0 and 1, where 0 corresponds to the total absence of crystalline phase (amorphous material) and 1 to complete crystallisation (which does not mean that the material has reached 100% crystallinity, which is not possible for polymers, but that it has reached the maximum crystalline phase it could reach).

When the total area, i.e., the total ΔH, is divided by the theoretical value of the 100% crystalline material, which for PEEK is 130 J/g [85,86], the absolute crystallinity percentage of the material is obtained. In the case under study, for PEEK neat during isothermal crystallisation at varying T_c an almost constant value of 31.4% is obtained on average.

The value calculated experimentally and denoted by X_{rel} is none other than W_c in Eq. (7). Avrami model in its logarithmic form (Eq. (5)) is written as a function of relative volumetric crystallinity, i.e. V_c , so Eq. (6) is needed to go from X_{rel} (as well as W_c) to V_c. To use Eq. (6) it is necessary to know the values of ρ_a and ρ_c of PEEK, which from the literature [87] are 1.262 g/cm^3 and 1.378 g/cm^3, respectively.

By plotting Eq. (5) with the experimental data, yields a curve that is not quite linear, this is because the Avrami equation can only follow the primary crystallisation, i.e., V_c < 40-50%. So, it is important to find an interval of V_c where it is sure linear, so that the linear equation of Avrami (Eq. (5)) can be used. Lorenzo et al. [61] identified this range in V_c between 3% and 20%. The 3% was chosen to eliminate the initial points that are always affected by measurement errors related to the stabilisation of the instrument. Fig. 19 shows Avrami total plot with the range chosen for fitting.

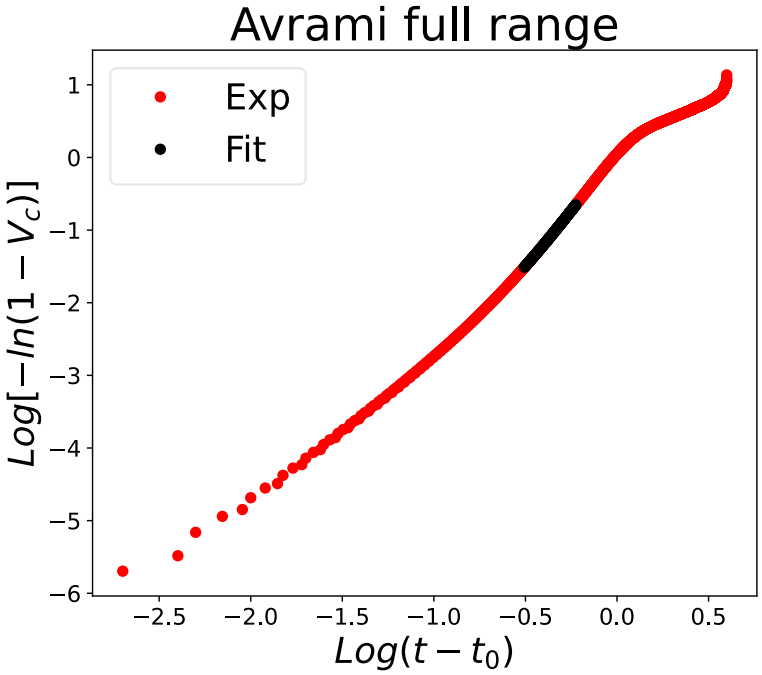

Fig. 19: Complete Avrami plot with detail in black on the interval in which to fit the data - PEEK neat.

With the range of V_c known, linear fitting can be performed using Eq. (5) to derive the values of k and n, i.e. the total crystallisation rate and Avrami index respectively (Fig. 20).

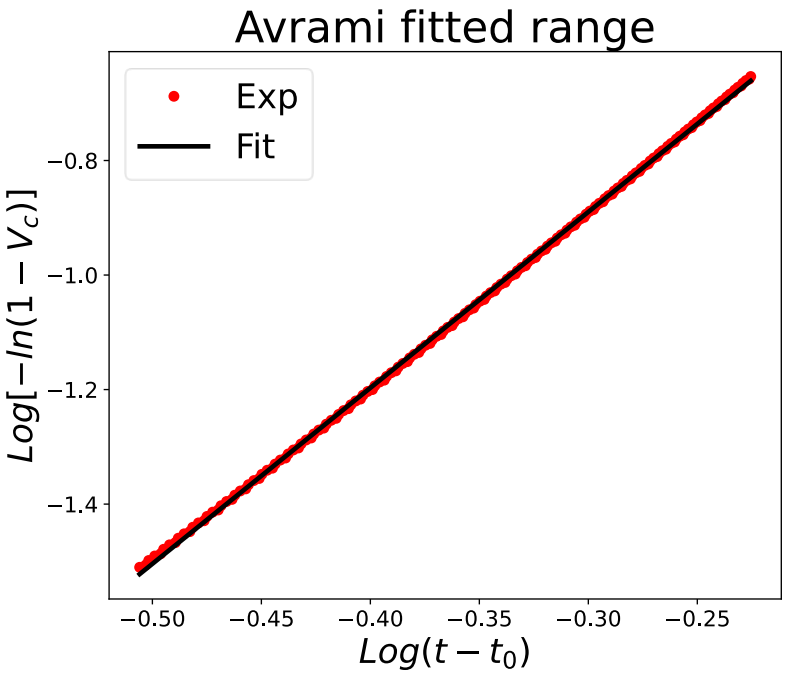

Fig. 20: Avrami plot of the linear fitting area only (3% <V_c < 20%) - PEEK neat.

As can be seen from Fig. 20 the linear fitting follows the experimental data perfectly; in fact, calculating the R^2 of the fitting yields 0.9997, which proves the goodness of the approximation. Avrami equation fittings with R^2 below 0.97 are not acceptable.

Calculated the coefficients k and n, it is possible to estimate $V_{c,fit}$, i.e., the volumetric relative crystallinity value calculated using Avrami equation. Moving from volumetric to mass-related, i.e. $X_{rel,fit}$, using Eq. (6), a comparison can be made between the experimental relative crystallinity and that calculated with the Avrami equation (Fig. 21).

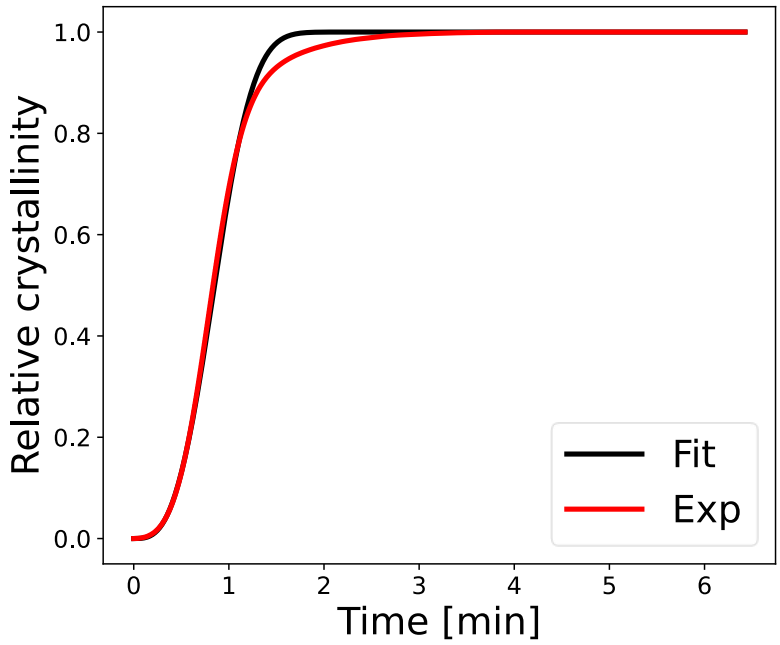

Fig. 21: Experimental relative crystallinity vs. relative crystallinity calculated using the Avrami equation (fit) - PEEK neat.

As can be seen from Fig. 21 the Avrami equation follows the curve perfectly up to the value of V_c =50%, after that, secondary crystallisation phenomena begin, and the equation loses its accuracy.

So far, only one example has been shown of how to apply the Avrami equation to obtain data useful for the study of crystallisation kinetics. By carrying out the various steps set out above for all the crystallisation temperatures chosen, a comparison of the various characteristic parameters of polymer crystallisation kinetics can be made.

First, the fundamental parameters of the Avrami equation are analysed, namely the Avrami index n and k. As can be seen from Fig. 22 for PEEK neat, the trend of Avrami index is almost constant and equal to 3.18 on average.

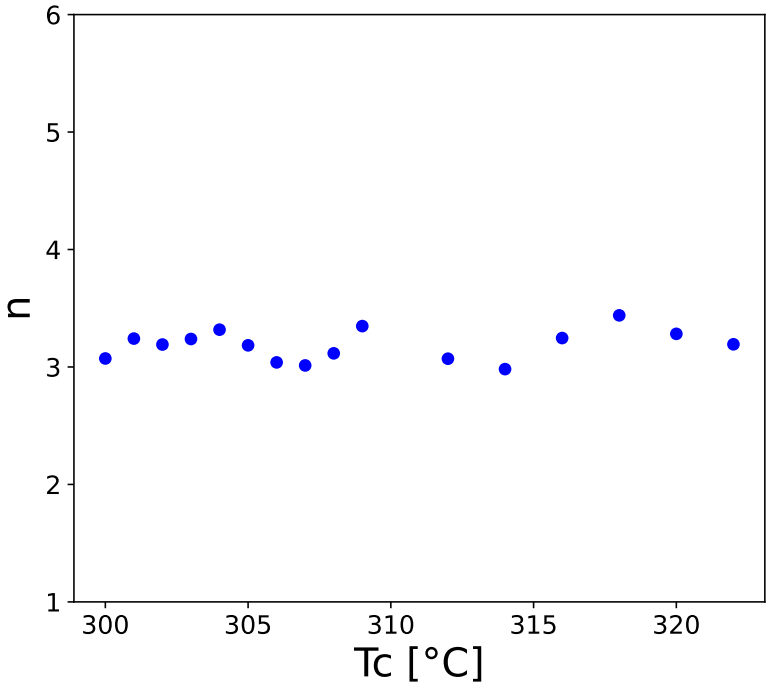

Fig. 22: Avrami n index trend for PEEK neat.

The value of Avrami index, following Eq. (3) shows that PEEK neat has a three-dimensional crystal shape, i.e., spherulites, and that nucleation is very rapid.

The two data that instead consider the total crystallisation rate, i.e., k and $\tau_{50\%}$ have the same trend since they both give information about the crystallisation rate. The parameter τ being a time, to be considered as a velocity is expressed as $1/\tau$; while the parameter k has the unit of measurement min^{-n} which, unless n is an integer, has no physical meaning, so it is always expressed as $k^{1/n}$ so that the unit of measurement is min^{-1} (Fig. 23). In Fig. 23a can also be seen the difference between the theoretical $\tau_{50\%}$, calculated using Eq.(8) using the coefficients of Avrami equation, and the experimental $\tau_{50\%}$ calculated by taking the time corresponding to the maximum of the exothermic peak measured by the DSC.

Thanks to a good fitting approximation, it can be observed that the two values are practically equal.

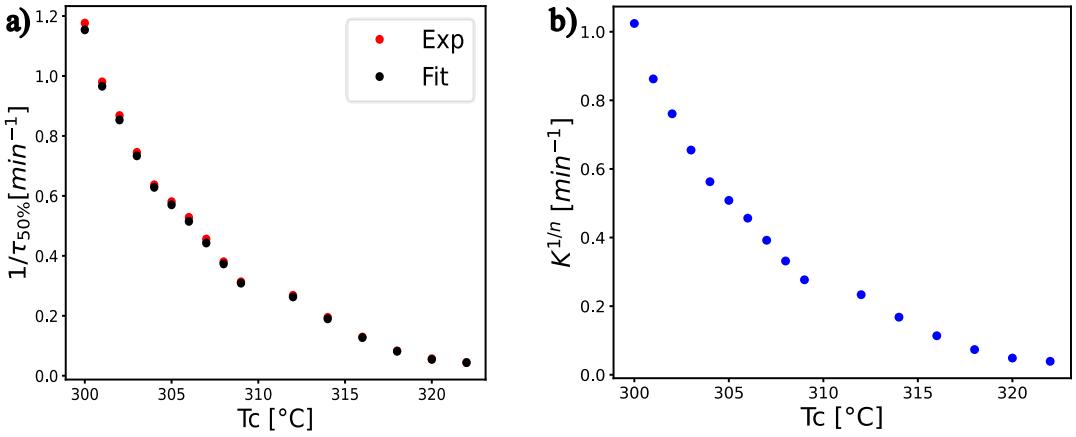

Fig. 23: Trend of a) $1/\tau_{50\%}$ (in black that calculated with Eq.(8) and in red the experimental one) and b) $k^{1/n}$ for PEEK neat.

The last parameter giving information about the kinetics of crystallisation is the induction time (t_0) which, when expressed as $1/t_0$, indicates the speed of nucleation (Fig. 24).

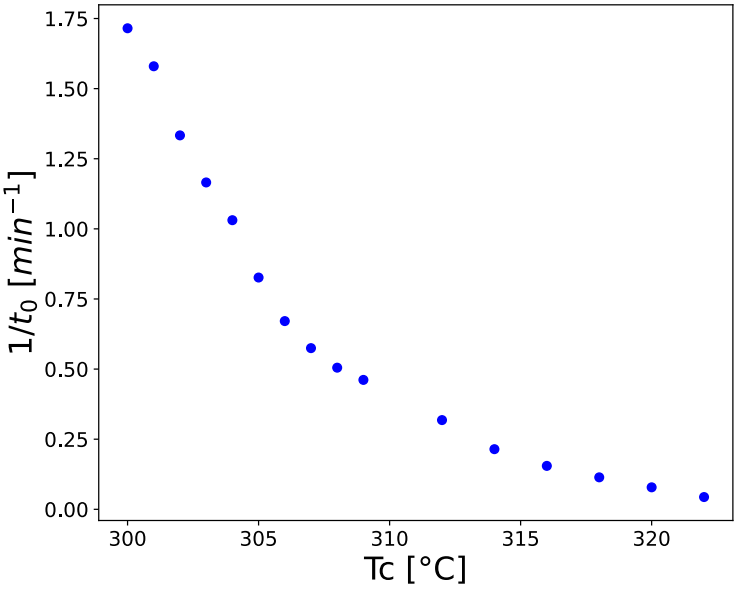

Fig. 24: Development of nucleation rate $1/t_0$ in PEEK neat.

For both the nucleation rate and the total crystallisation rate, the trend is decreasing with increasing T_c, because the higher the crystallisation temperature, the lower the rate at which the crystalline phase forms and grows.

Calculated all the parameters of Avrami equation and their trends, it is also possible to compare all the trends in relative crystallinity as T_c changes experimental and theoretical (Fig. 25).

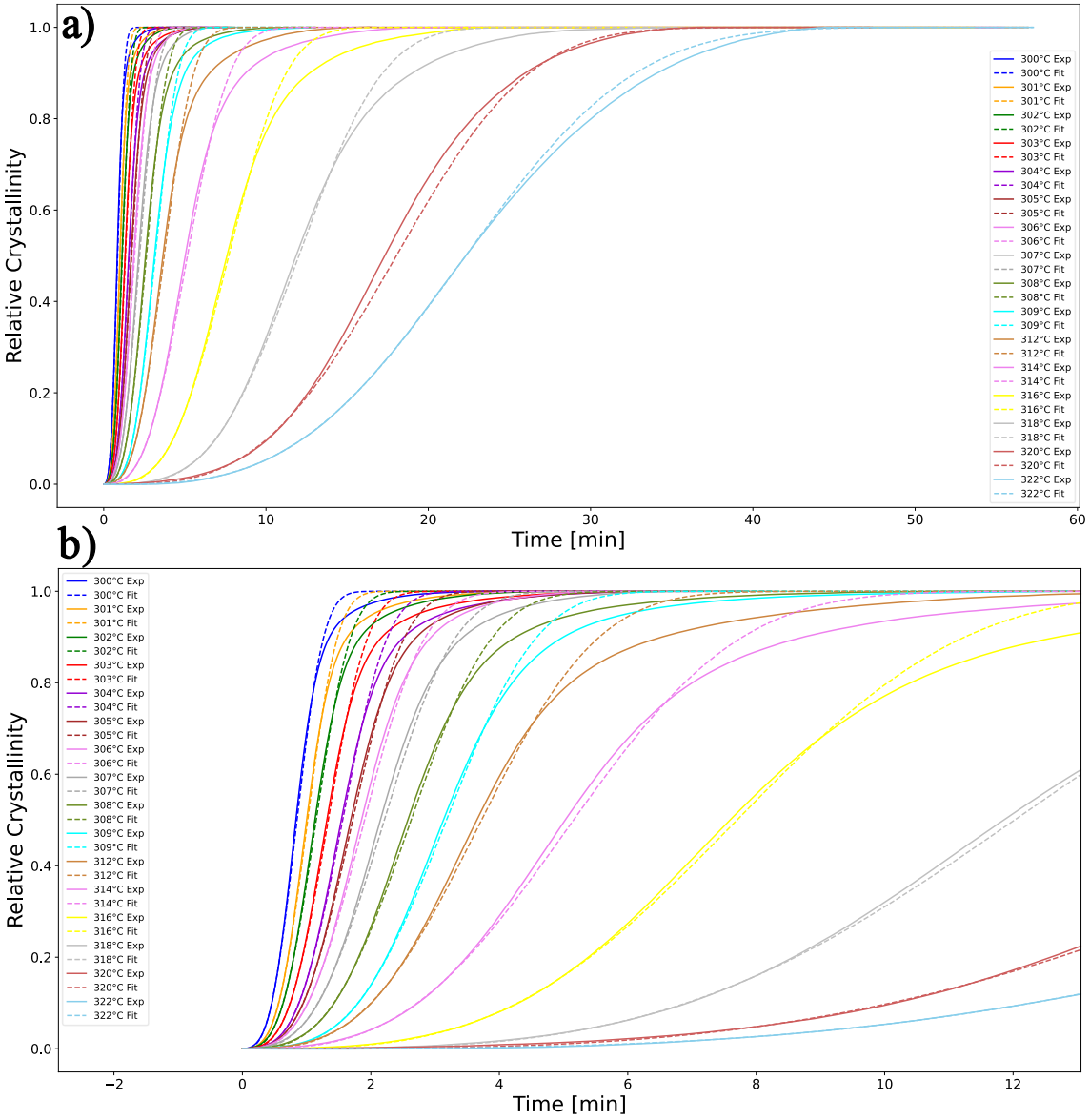

Fig. 25: Development of the relative crystallinity of PEEK neat - a) all values of T_c; b) zoom with only values between 300 °C and 309 °C.

As can be seen from Fig. 25 and as mentioned earlier, Avrami model does not perfectly follow the crystallinity trend as it varies with time. These curves will have to be the ones to be included in the Abaqus model to create a model capable of predicting the degree of crystallinity of the material for given T_c and given time. For the Abaqus model, the relative crystallinity trend is certainly not sufficient, but it is better to use the total crystallinity, i.e., the relative crystallinity multiplied by the maximum crystallinity value that the PEEK neat can reach.

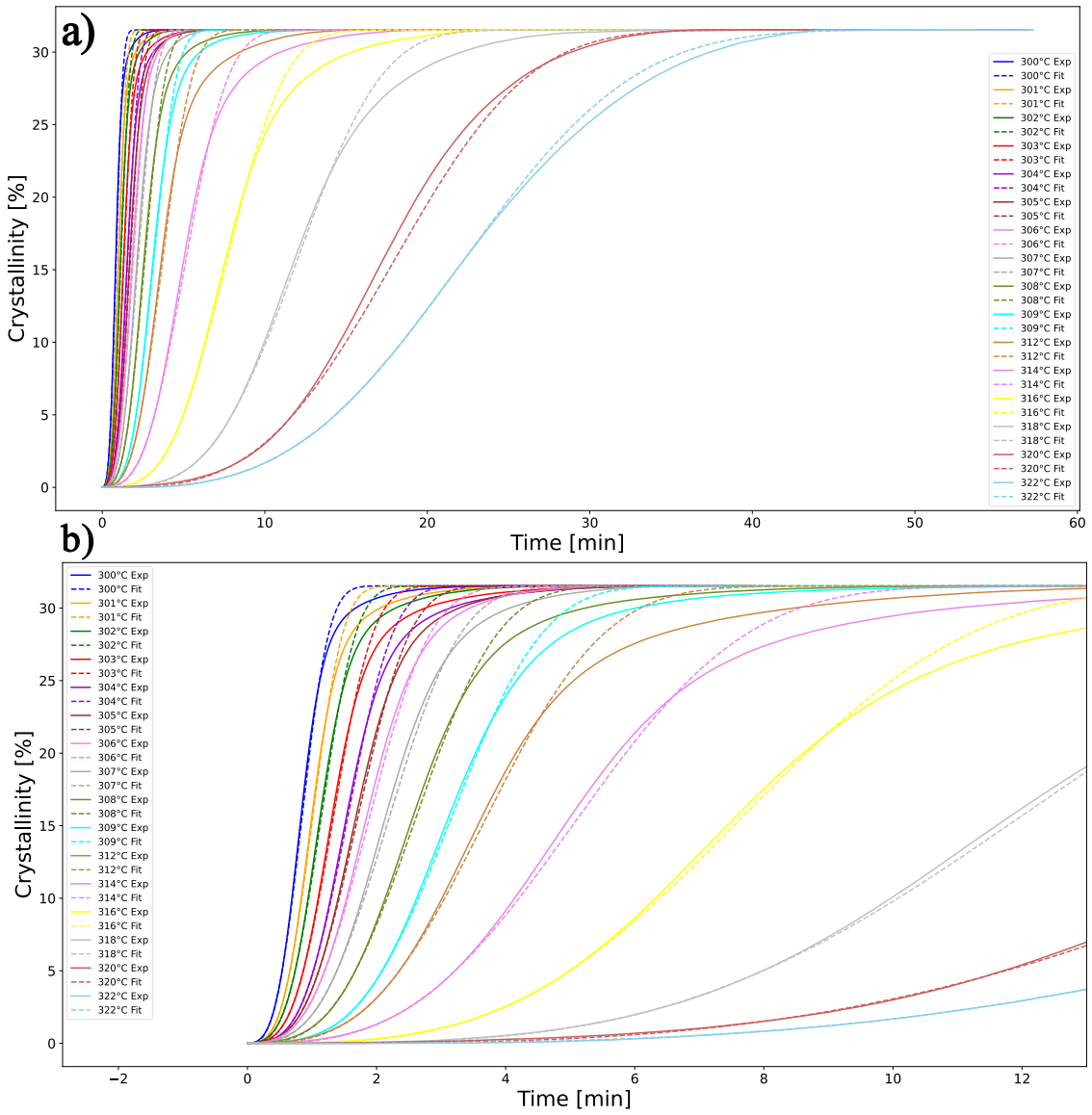

Fig. 26: Development of the total crystallinity of PEEK neat - a) all values of T_c; b) zoom with only values between 300 °C and 309 °C.

The trend is identical to that of relative crystallinity, but the values change, in fact in the Fig. 26 are the actual crystallinity values achieved by the material over time. This is the fundamental data for the Abaqus model because it recreates via an equation the crystallinity trend over time as the chosen T_c varies. It can also be seen that the time to reach the same crystallinity value is much greater as T_c increases, ranging from the order of tenths of a minute at crystallisation temperatures of 300 °C to the order of tens of minutes above 312 °C.

2.3.3 Kinetics of isothermal PEEK neat crystallisation from the melt: Lauritzen and Hoffman model

Up to now, the kinetic of crystallisation has been analysed according to the Avrami model. Approaching the problem from an energetic point of view, it is possible to use the Lauritzen and Hoffman model to find additional information that adds further detail to the kinetic of PEEK neat. The method finds its importance because, using the DSC data, it is possible to reconstruct the trend of the overall crystallisation rate (nucleation + growth) with temperature, varying from T_∞ to T_m^0. In addition, another fundamental thing that will be explained in detail in the following paragraphs, is the possibility of comparing parameters from theory (i.e., K_g^τ, σ_e, q) of PEEK neat and PEEK CF, to assess the effect of the fibres on the crystallisation of the material.

All coefficients must be calculated to the fit the data with Eq.(10). The glass transition temperature was obtained by heating the PEEK neat with a non-isothermal ramp at 20 °C/min and is equal to T_g = 150 °C (Fig. 27).

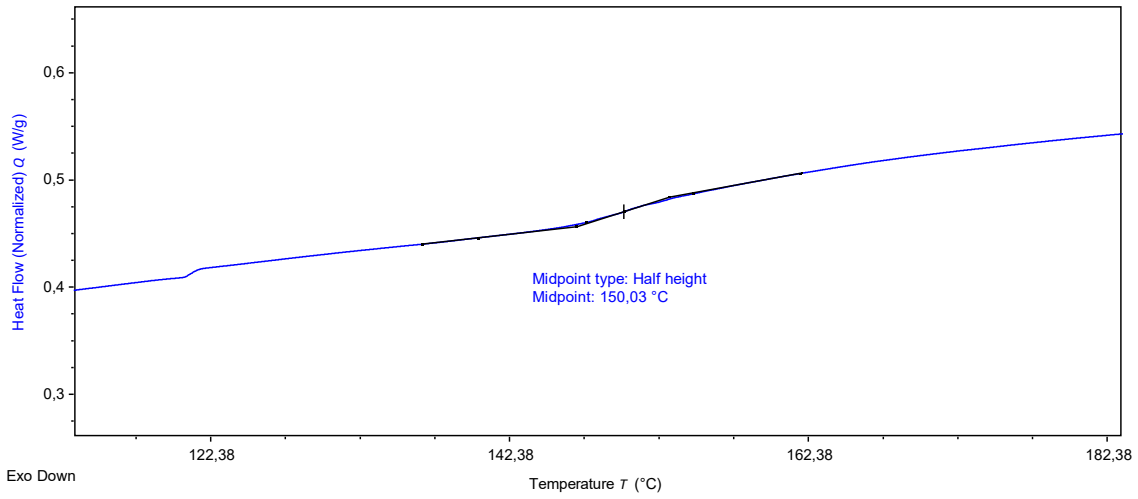

Fig. 27: Glass transition temperature analysis for PEEK neat.

The T_m^0 can be obtained experimentally by applying the linear Hoffman-Weeks equation or the non-linear Marand-Herve equation [88,89]. these two methods lead to a difference in the T_m^0 of about 20 °C, where the non-linear method is always about 20 °C greater than the linear method. In this work, both methods were applied to make a comparison with the literature. The Hoffman-Weeks linear method is based on fitting the experimental data of T_m to the T_c measured in the heating ramp after isothermal crystallisation varying T_c. By plotting T_c vs T_m in a graph, a linear fitting can be made. The point at which this line intersects the line $T_c = T_m$, identifies the T_m^0. Furthermore, from the literature [74] it is inferred that to get a more accurate figure, it is better to use T_c that are above 310 °C,

which is why only points from 312 °C onwards were used in this work. The result is shown in Fig. 28.

The intersection shows that the T_m^0 experimental is 360 °C.

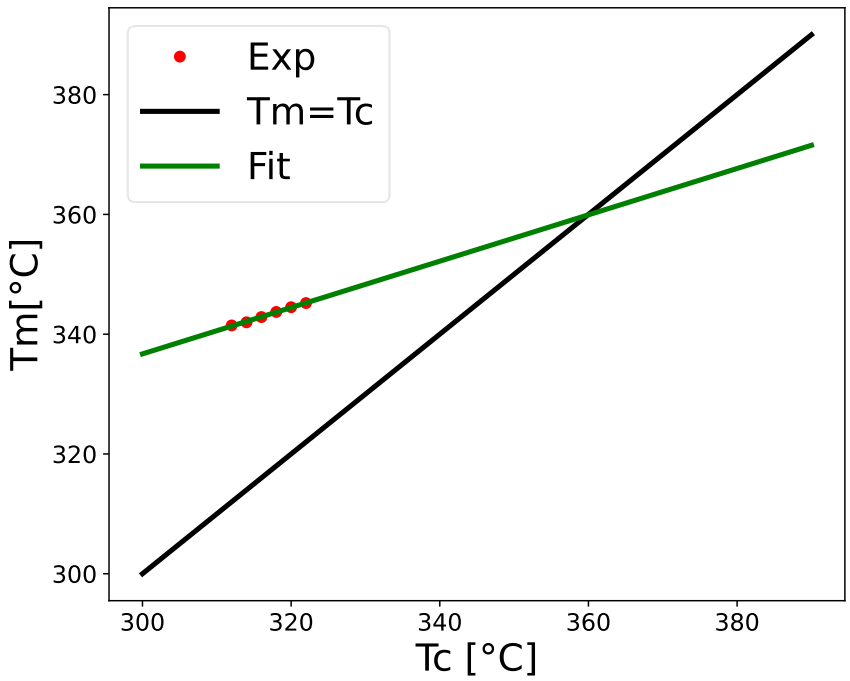

Fig. 28: Equilibrium melting temperature, T_m^0, obtained by the Hoffman-Weeks method, for PEEK neat.

When applying the non-linear method, the coefficients of the equation must first be calculated. The Marand-Herve equation is also called M-X because it necessary first calculates these two terms assuming hypothetic melting temperatures T_m.

In the present case, the $T_{m,hy}$ varies from 352 °C to 408 °C in steps of 1 °C. Therefore, M and X were calculated according to Eq.(26) e (27):

$$M = \frac{T_{m,hy}}{T_{m,hy} - T_{m,exp}} \tag{26}$$

$$X = \frac{T_{m,hy}}{T_{m,hy} - T_{c,exp}} \tag{27}$$

So, for given $T_{m,hy}$ it will have several M and X equal to the number of $T_{m,exp}$ and $T_{c,exp}$.

In a graph M-X these points are lines whose equation is as follows (Eq.(28)):

$$M = \beta(X + \alpha) \tag{28}$$

Where β is the coefficient of thickening of the crystalline lamellae and α a dimensionless constant.

Linear fitting of these pairs of values yields the graph in Fig. 29 and all values of β and α.

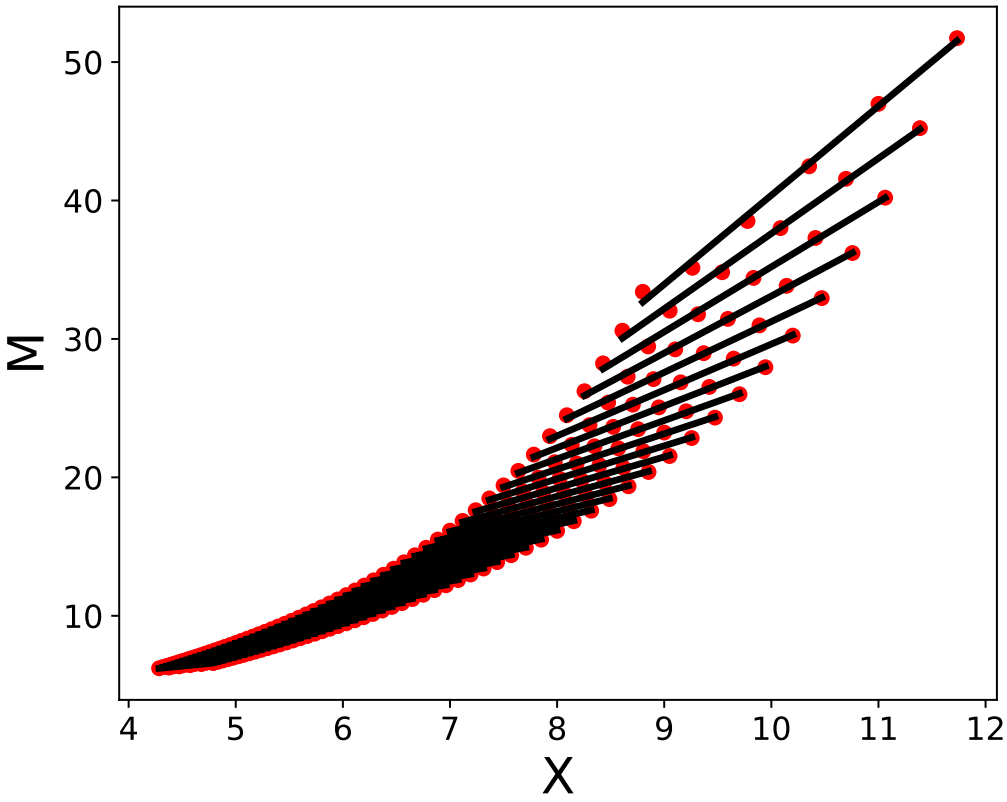

Fig. 29: M-X graph to obtain the β and α coefficients from the fitting - PEEK neat.

Plotting the β and α data further as a function of the $T_{m,ip}$ it is possible to obtain the graph in Fig. 30. From this graph, it is derived the T_m^0 since, according to Marand-Herve theory, this temperature corresponds to that of β=1.

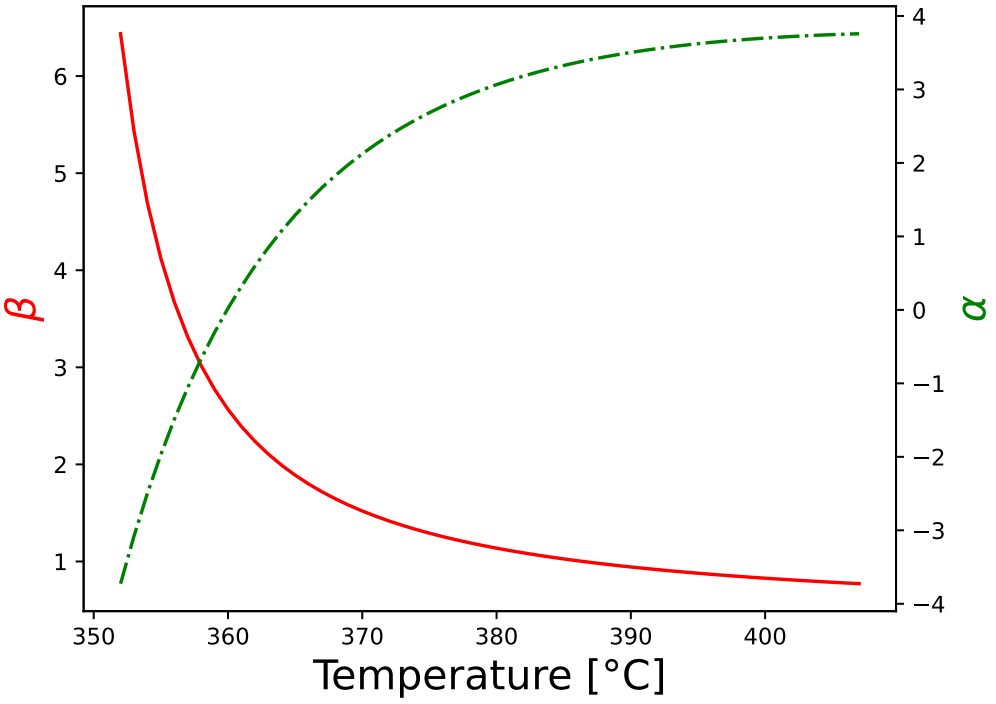

Fig. 30: β and α graph to derive the T_m^0 - PEEK neat.

Selecting the temperature at β=1 gives a $T_m^0 = 386\ °C$. So, in this case, the difference in values between the two methods has been proven to be true, which is about 20 °C. However, more extensive studies in the literature, which consider a much larger range of T_c than that considered in this work, state that the T_m^0 is equal to 380.8 °C [74]. The aim of this section was to demonstrate the possibility of calculating the T_m^0 with both linear and non-linear methods. Considering that the focus of this work is not the calculation of the T_m^0, it was preferred, for the application of the LH method, to use the value obtained from the literature, which is certainly more accurate than the one measured here.

Please note that all temperatures stated here in °C in the application of the model must be expressed in K.

Continuing with the other coefficients of the LH equation, the U* parameter was obtained from literature data and is 2800 J/mol [90]. R, the universal gas constant, equals 8.314 $\frac{J}{mol\ K}$. For the terms ΔT, T_∞ and f, please refer to section 2.1.7.

Applying Eq.(12) and performing linear fitting of the experimental data, the values of K_G^τ and $\frac{1}{\tau_0}$ were calculated (Fig. 31). Consider that the experimental data of 1/τ must be expressed in sec^{-1}.

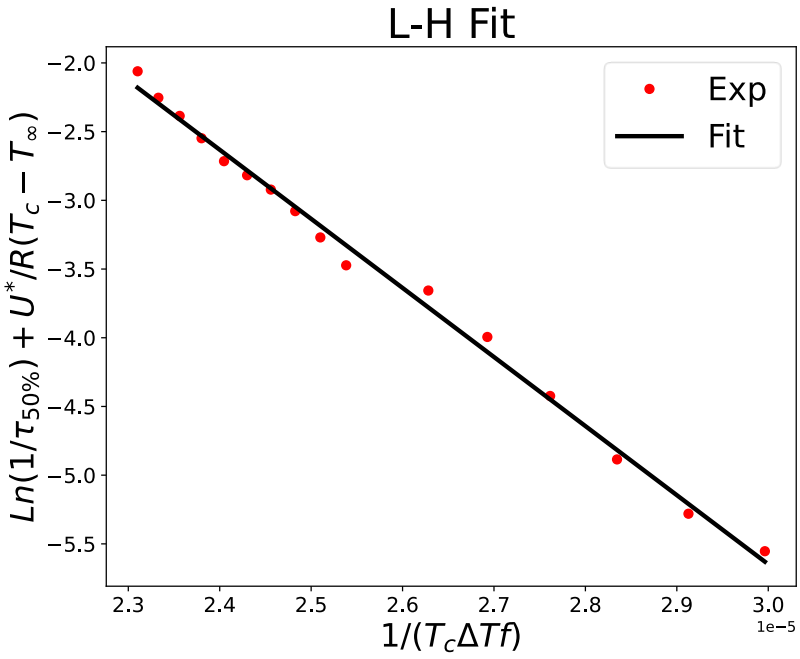

Fig. 31: Lauritzen Hoffman linear fitting for PEEK neat.

Another parameter that must be calculated to continue LH is σ. It is calculated using Eq. (13) Knowing both the geometrical parameters of the PEEK crystals, i.e., a_0 and b_0 and the melting enthalpy of the 100% crystalline material ΔH_f. The latter is equal to $130\ J/g$; while a_0 and b_0 are respectively equal to $7.78 \cdot 10^{-8}$ cm e $5.92 \cdot 10^{-8}$ cm [91].

The calculated value of σ is $8.82 \cdot 10^{-7}\ \frac{Jcm}{g}$. This parameter is often expressed in erg/cm^2. To obtain this unit of measurement, it is necessary to change J to erg and multiply σ by a density, specifically by ρ_c. the final value is $12.157\ \frac{erg}{cm^2}$.

Calculated the value of K_G^{τ} (via fitting) equal to 5.027·10^5 K^2 (R^2 =0.995) and knowing the value of σ, it is possible to use Eq.(11) to calculate σ_e. To utilize Eq. (11) it is necessary to assume in which regimes the growth of the crystalline phase will occur. As a first attempt, regime II has usually used to see whether in the LH graph the line approximates the experimental points well. To use regime II, in Eq. (11) j will be equal to 2. Also, it is required the Boltzmann constant $\kappa = 1.23 \cdot 10^{-23}\ \frac{J}{K}$. The calculation shows that σ_e is equal to $1.32 \cdot 10^{-5}\ \frac{J}{cm^2}$, this term, like σ, is often expressed in erg/cm^2 so that the converted value is equal to $132.011\ \frac{erg}{cm^2}$. Given all the above terms, it is possible to calculate q through Eq. (14). It is equal to $1.216 \cdot 10^{-12}\ erg$. Finally, the second coefficient obtained from the fitting, i.e., the intercept $1/\tau_0$ which is equal to $1.25 \cdot 10^4\ sec^{-1}$

Tab. 3 below shows a summary of all parameter values used in the LH equation and all results obtained.

Tab. 3: Parameters and results of the Lauritzen and Hoffman fitting for PEEK neat.

Parameters		Results	
T_g [°C]	150	σ [erg/cm^2]	12.157
T_m^0 [°C]	380.85	K_G^{τ} [K^2]	5.027-10^5
U* [J/mol].	2800	$1/\tau_0$ [sec^{-1}]	$1.25 \cdot 10^4$
R [J/molK].	8.314	σ_e [erg/cm^2]	132.011
ΔH_f [J/g]	130	q [erg]	$1.216 \cdot 10^{-12}$
ρ_c [g/cm^3]	1.378		
a_0 [cm]	$7.78 \cdot 10^{-8}$		
b_0 [cm]	$5.92 \cdot 10^{-8}$		
J (II)	2		
κ [J/K].	$1.23 \cdot 10^{-23}$		

Obtained all the parameters of the LH equation, they can be applied to Eq. (10) to obtain the overall crystallisation trend from T_∞ to T_m^0. The result is shown in Fig. 32.

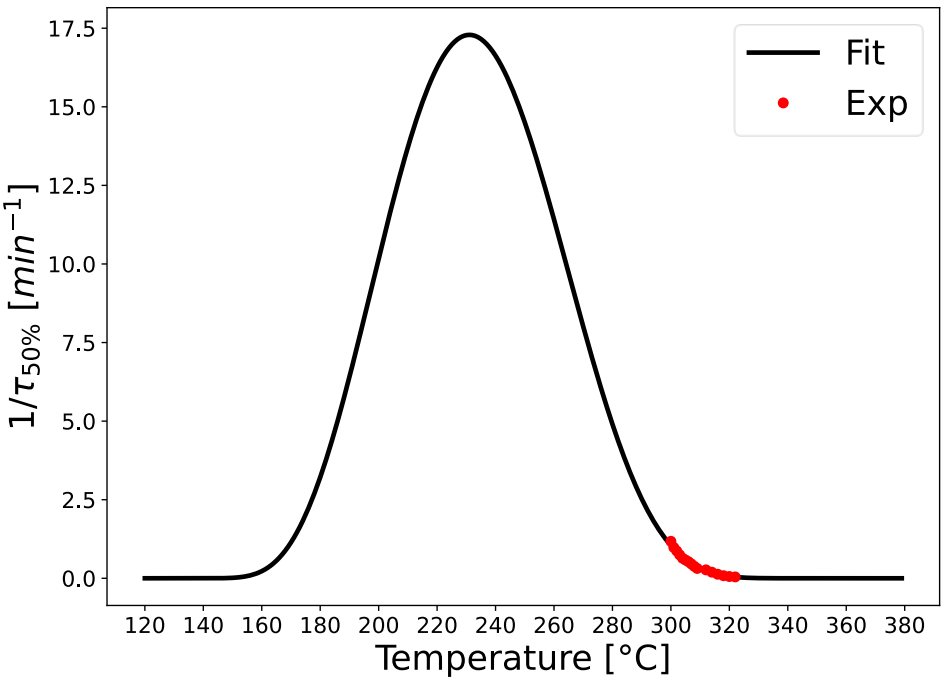

Fig. 32: Global crystallisation of PEEK neat.

As already mentioned in the previous paragraphs, the crystallisation rate follows a bell-shaped trend with a maximum. The latter is the crystallisation temperature that divides the material's behaviour in two. To the left of this value are the diffusive phenomena because the crystalline phase formed now occupies almost all the space and therefore the movement of the molecules is mainly controlled by diffusive phenomena. The closer it gets to T_∞ the lower the mobility of the molecules and thus the lower the crystallisation rate, which tends to 0. On the other side, to the right of the maximum, nucleation phenomena occur. The closer it gets to T_m^0 the lower the speed because the energy present in the molten material is so great that it only allows the existence of the amorphous phase and does not give the material the possibility of organising itself into the ordered nuclei of the crystalline phase. As can be seen from Fig. 32 the experimental points only fall in the nucleation part, because with conventional DSC, the cooling rates that the instrument can offer are not large enough to consider low T_c values without the creation of crystalline phase during cooling. To obtain other points, or the whole curve experimentally, it would use so-called fast scanning calorimetry or fast DSC, which allows cooling rates even of the order of $5\text{-}10^5$ K/sec [59].

2.3.4 Kinetics of isothermal crystallisation in PEEK neat from the melt: Dual Avrami

Avrami model is the most widely used equation to clarify which parameters influence the kinetics of polymer crystallisation. Despite this, the model does not approximate the

entire crystallisation process well, because it does not consider the phenomena of secondary crystallisation. In this thesis work, as already explained in the previous paragraphs, the aim of the project is not only to investigate the crystallisation kinetics of PEEK, but to create an Abaqus model that can best approximate the crystallisation trend over time after an isothermal process. To do this, the classic Avrami model is not sufficient, and so it was decided to use a modified version, which would also consider secondary crystallisation and thus be able to better approximate the entire crystallisation process. In this discussion, the Eq. (23) will be used. This equation was further modified by considering the induction time t_0 as was done in Avrami classical model. Thus, the time parameter t will always be $t-t_0$. The procedure is identical to that of Avrami classical model, except that the equation will not be linearised, but will be directly fitted by non-linear fitting, to identify the 3 fundamental parameters, i.e., k_p, n_p, n_s. Then, once the baseline has been subtracted by identifying the two points around the crystallinity peak following isothermal testing, the area, relative crystallinity, and relative volumetric crystallinity are calculated, and finally the non-linear fitting of the curve is performed. To show an example of the result, the fitting corresponding to the temperature T_c of 300 °C is shown below (Fig. 33), the same temperature as shown in Fig. 21 for the classical Avrami (or Single Avrami) model.

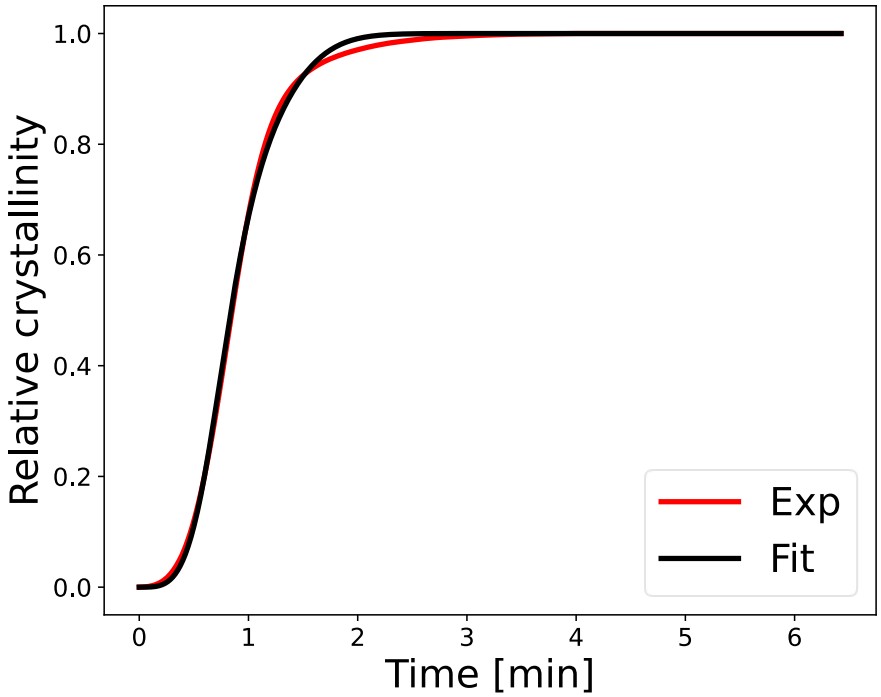

Fig. 33: Relative crystallinity fit with the Dual Avrami model for PEEK neat.

As can be seen, comparing the Fig. 21 with Fig. 33, a very good approximation is possible with the *Dual* Avrami model even for $V_c > 50\%$. The R^2 calculated for this non-linear

fitting is 0.999, a sign of a very good approximation. Thanks to this model, it is therefore possible to have an equation to import into Abaqus to simulate the crystallinity behaviour during the isothermal process.

In the application of the model, the induction time t_0 is the same between Single Avrami and Dual Avrami. What certainly changes between the two models is the Avrami index, which this time will be divided into two, considering both primary and secondary crystallisation. The values are shown in Fig. 34.

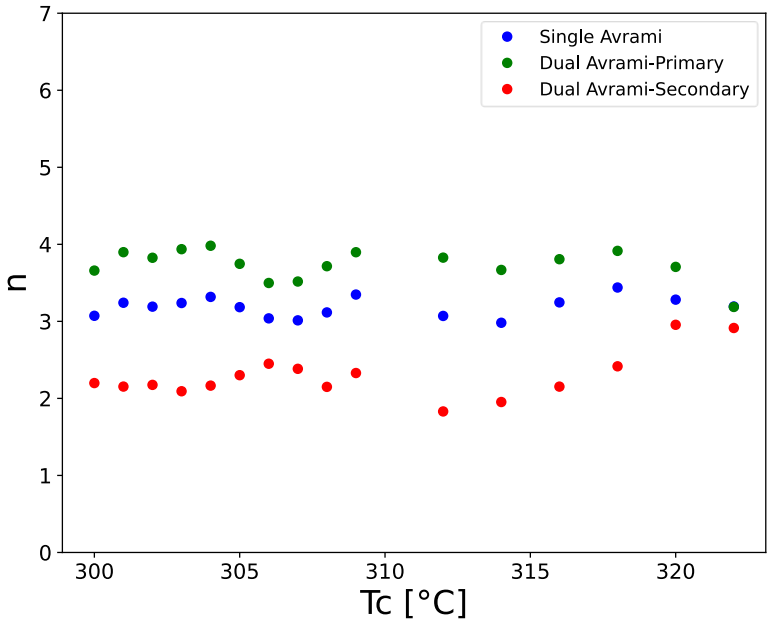

Fig. 34: Comparison of Avrami indices between the classical model (Single Avrami) and the Dual Avrami model for PEEK neat.

As expected from the model and as it has already been observed in the literature [74] the Avrami indices divide into a value close to the maximum, 4, for primary crystallisation and around 2 for secondary crystallisation.

Regarding the total speed of crystallisation, i.e., the term $1/\tau_{50\%}$, it can be stated that it does not change when considering the dual or single model, as shown in Fig. 35. For this reason, the treatment of LH is not carried out again.

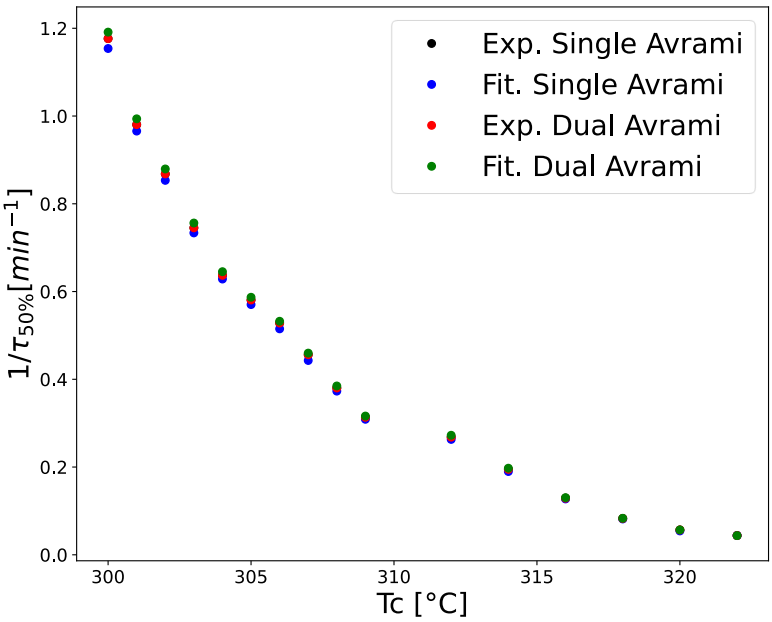

Fig. 35: Differences in overall crystallisation speed between the Single and Dual Avrami model for PEEK neat.

What certainly change is the way the crystallinity curve is approximated over time, which is fundamental information for the application of the model in Abaqus. Looking at the absolute crystallinity curves (Fig. 36) it is possible to see, especially at high values of T_c, the almost perfect approximation of the theoretical curves to the experimental curve.

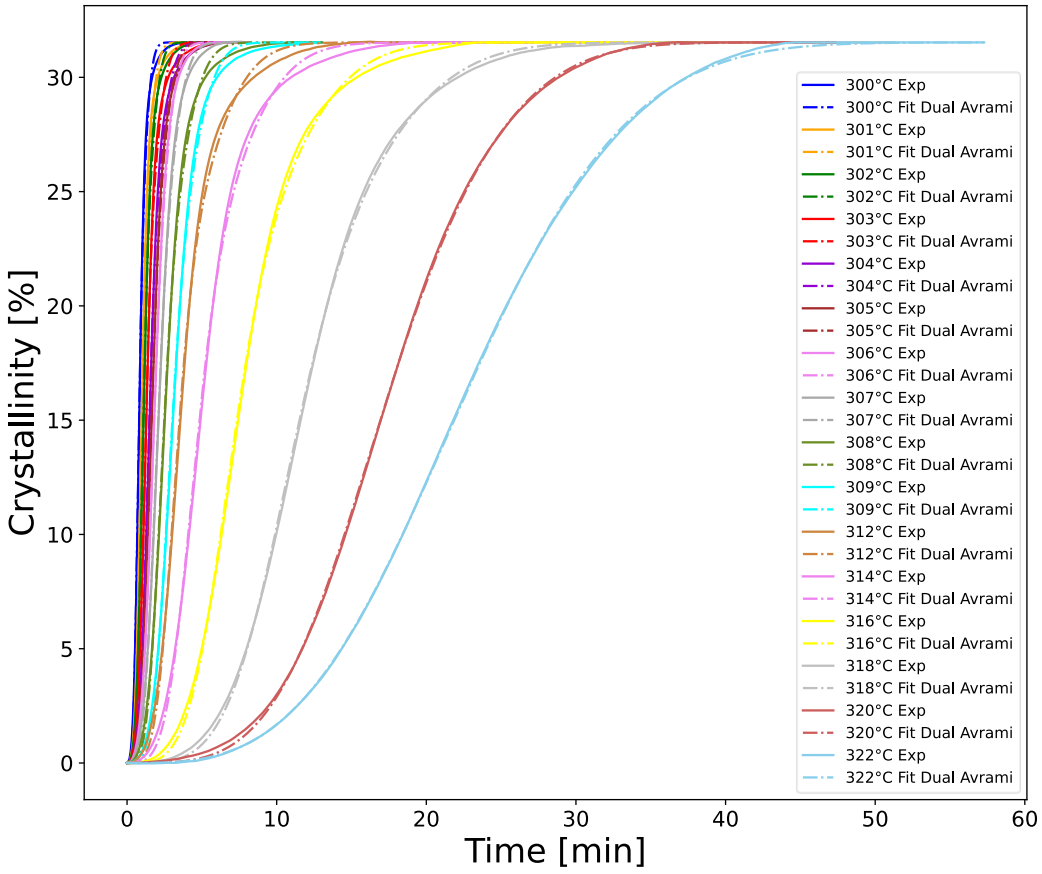

Fig. 36: Total crystallinity with the Dual Avrami model fitting for PEEK neat.

The fitted curves in Fig. 36, are those that will be used in the Abaqus model to simulate and calculate, for given T_c and time, the crystallinity value formed in the polymer.

2.3.4.1 Abaqus model: PEEK neat crystallisation

The model in Abaqus was created from data processed in Python. In fact, all calculations were carried out in Python scripts and then fed into Abaqus via a subroutine written in Fortran.

First, the parameters required in the Dual Avrami model were calculated in Python, i.e., t_0, K_p, n_p, n_s. Once calculated, a linear interpolation was performed to obtain all values in the range of T_c between 300 °C and 322 °C. To be as detailed as possible, the T_c was varied in steps of 0.1 °C. Then starting from the experimental data of the four parameters, interpolating curves were calculated by linear interpolation (from Fig. 37 to Fig. 40).

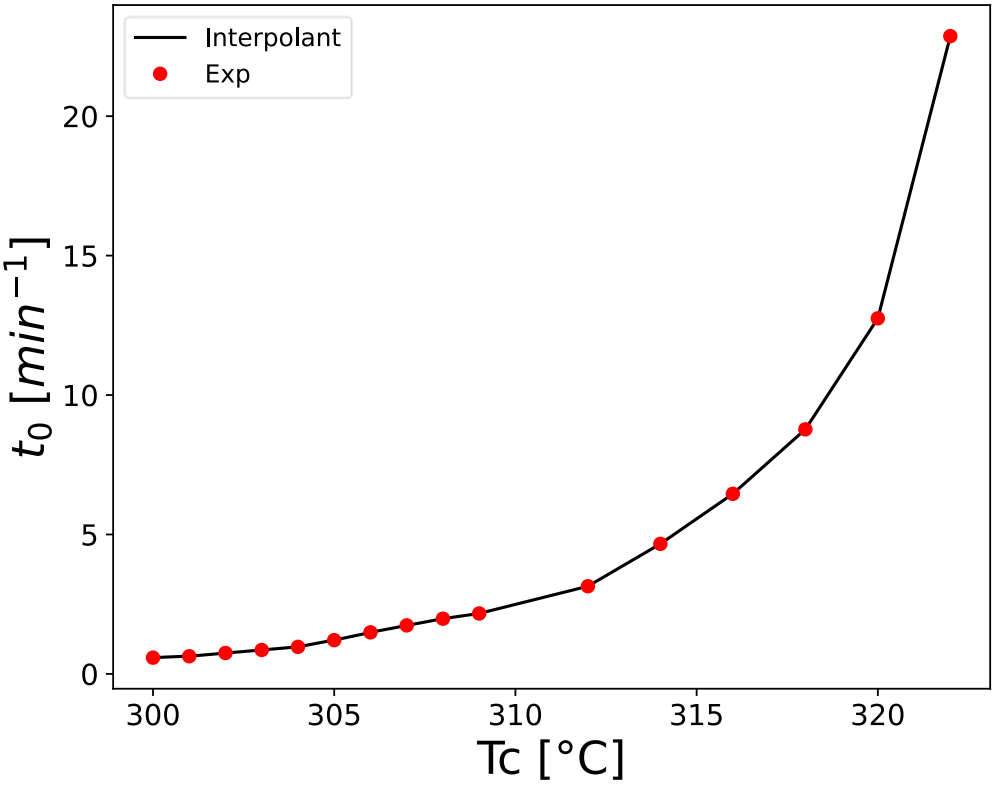

Fig. 37: Interpolation of experimental data of t_0 for PEEK neat.

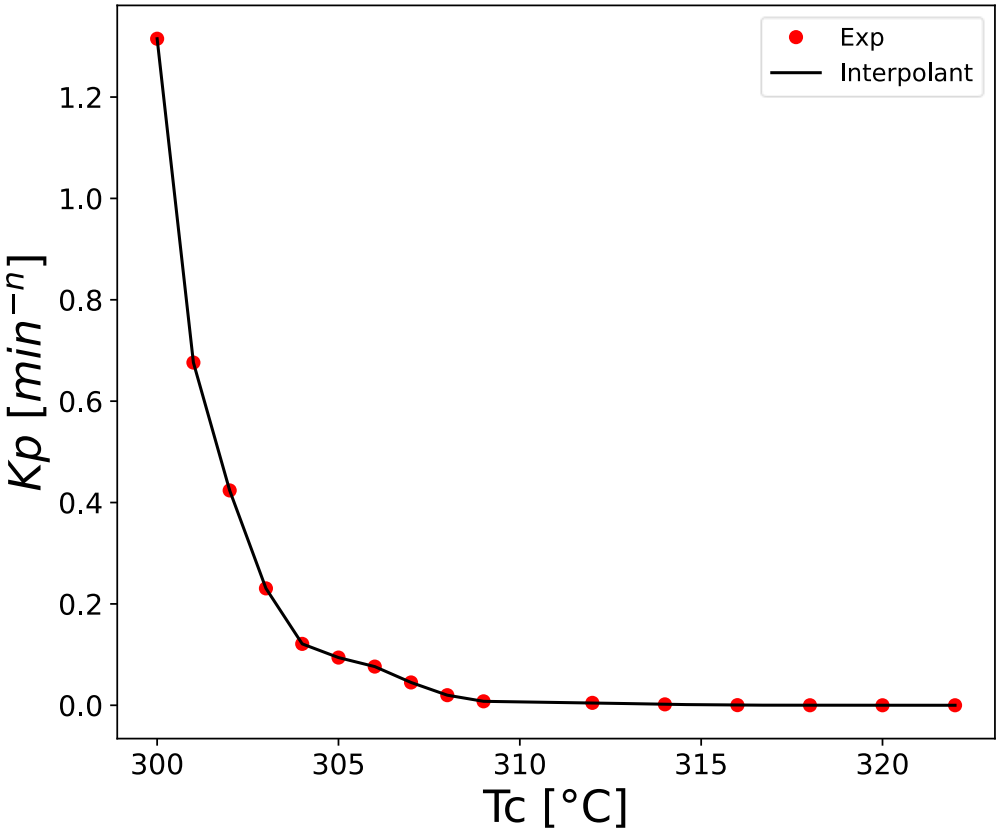

Fig. 38: Interpolation of experimental data of K_p for PEEK neat.

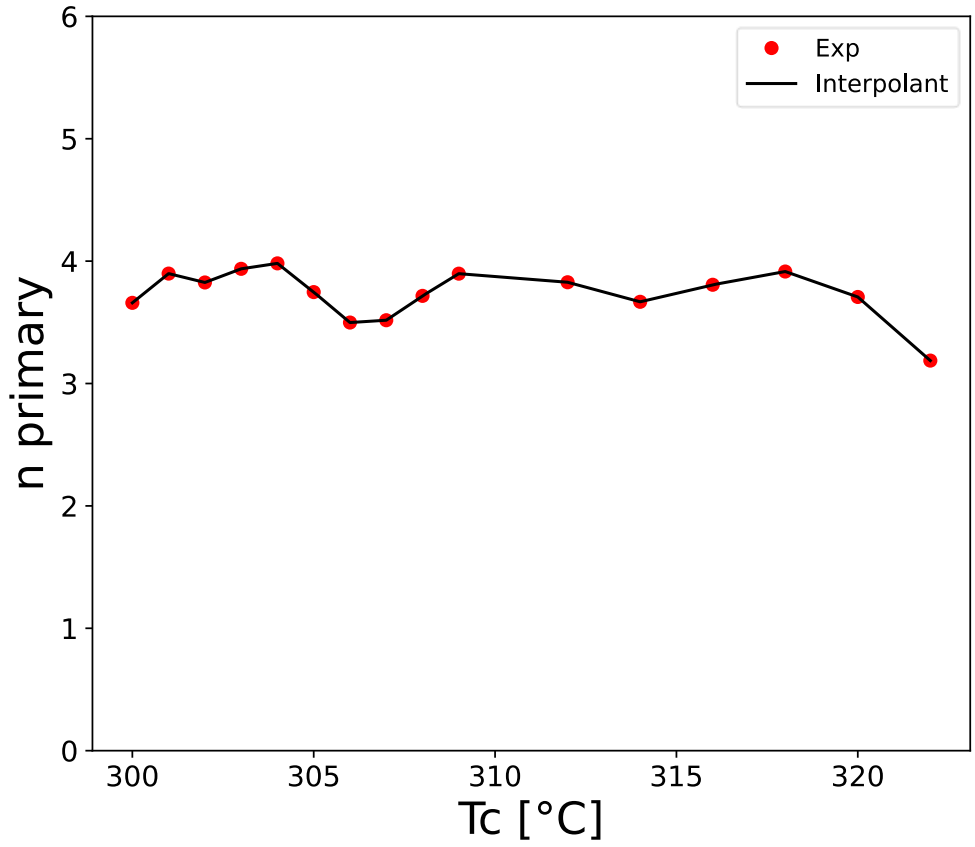

Fig. 39: Interpolation of experimental data of n_p for PEEK neat.

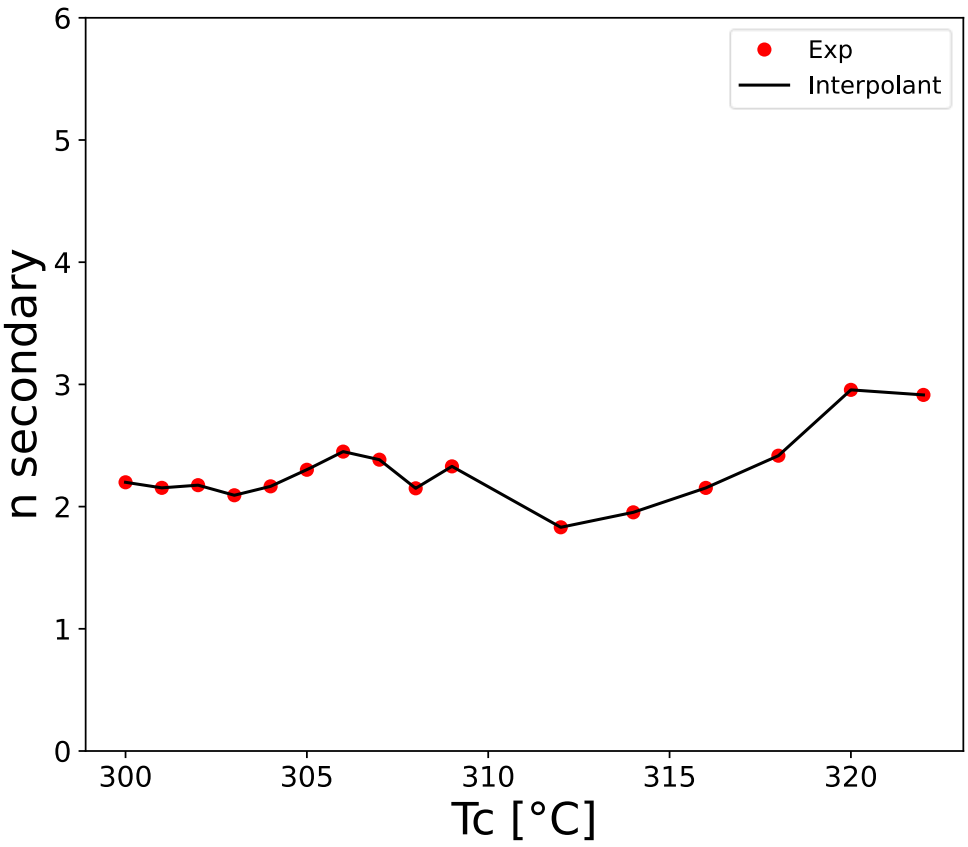

Fig. 40: Interpolation of experimental data of n_s for PEEK neat.

Thanks to these curves, for data T_c between 300°C and 322°C with a maximum interval of 0.1 °C, it is possible to know the exact value of the four parameters. All these values are entered in matrices, exported in text files that can be used in Fortran script.

The Fortran subroutine reads the data matrices from the interpolation. The file is set up in such a way that for given T_c chosen in the Abaqus model, the subroutine calculates the minimum distance between the set T_c and the T_c present in the databases to which the values of the three fundamental parameters correspond.

At this point for the date T_c, the subroutine identifies the value of the four parameters to be entered into the Dual Avrami model, which is written into the Fortran subroutine to calculate V_c and then X_{rel}. The calculation is repeated step by step during the Abaqus simulation, to have the trend of X_{rel} over time. Multiplying X_{rel} by the maximum measured crystallinity value yields the simulated absolute crystallinity trend. The geometry of the sample is rectangular and equal to 100x150x0.5 mm. The simulation time is 70 minutes with steps of 0.1 minutes (Fig. 41).

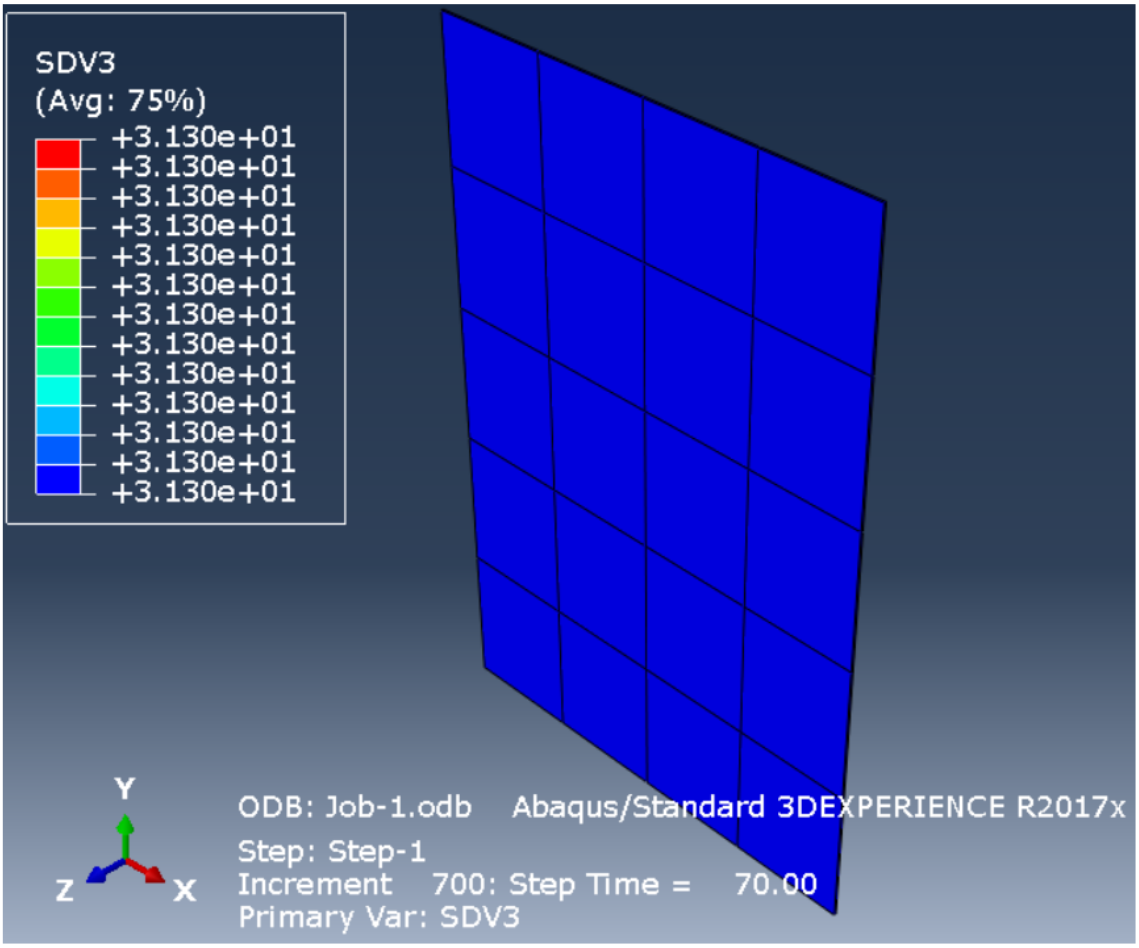

Fig. 41: Abaqus model, example at temperature 322°C, total crystallinity results at the end of the simulation for PEEK neat.

For comparison purposes, three temperatures were chosen to simulate isothermal crystallisation: 302 °C, 313 °C and 322 °C.

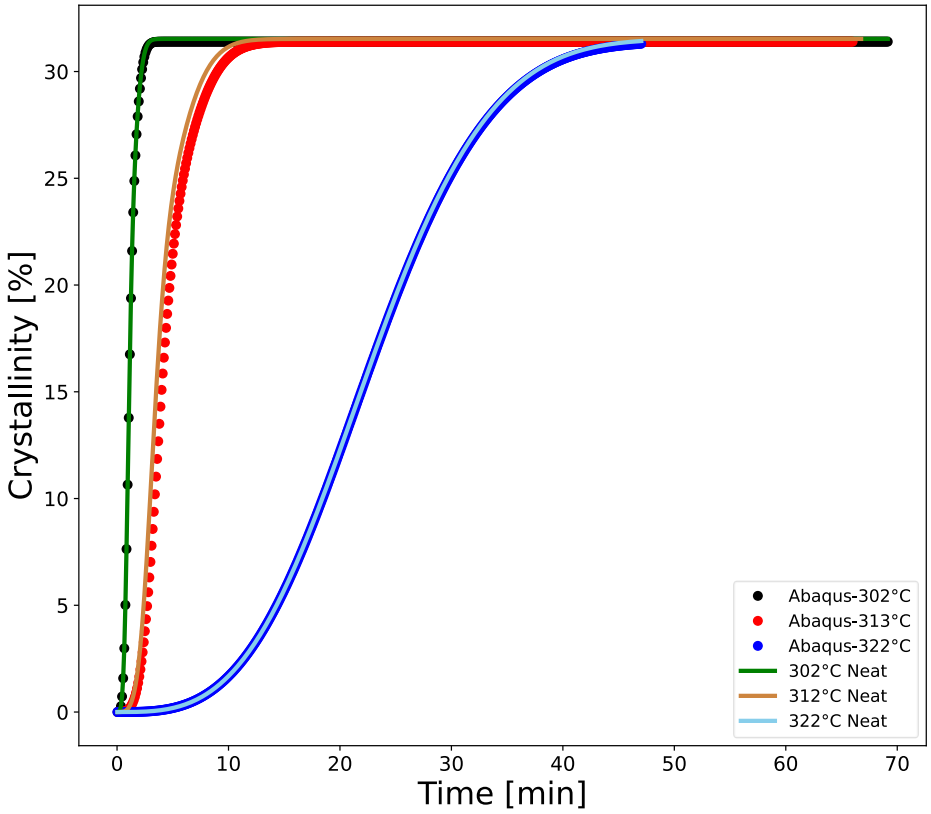

Fig. 42: Simulation results in Abaqus and comparison with experimental data for PEEK neat.

In Fig. 42 a comparison between the results of the Abaqus simulations and the experimental results can be observed. The temperatures T_c of 302 °C and 322 °C were chosen to demonstrate how the simulation perfectly follows the experimental data. While the temperature of 313 °C was chosen to demonstrate that with the Abaqus model, it is possible to recreate the absolute crystallinity trend for any temperature T_c in the range 300-322 °C and with a maximum resolution of 0.1 °C. In fact, the 313 °C trend is slightly later than the experimental 312 °C figure, a sign that the simulated figure follows the trend as T_c varies.

2.3.5 Kinetics of isothermal PEEK crystallisation from the melt: influence of carbon fibres in Single Avrami

The study carried out so far for PEEK neat was repeated for samples produced with carbon fabric (PEEK CF). All values that will be reported refer to samples analysed at DSC where the mass of the polymer alone within the composite is considered. Therefore, the mass of the fibres occupying 20% of the total volume will be subtracted from the total mass of the sample.

As already explained in section 2.3.1 in contrast to PEEK neat, the minimum crystallisation temperature is less than 2 °C, so that all isothermal crystallisation curves

will start from 298 °C, this temperature being the first one that does not crystallise during cooling at 50 °C/min.

The analysed temperature range is from 298 °C to 307 °C, since for higher temperatures it is difficult to detect the crystallinity peak and therefore it could be easy to make mistakes in the evaluation. This is already a first difference to PEEK neat, i.e., that with a conventional DSC it is complex to analyse PEEK CF at high crystallisation temperatures.

By analysing all the parameters from Avrami classical model, it can be made an effective comparison in terms of differences in kinetics.

Avrami index, n, between PEEK neat and CF is shown in Fig. 43.

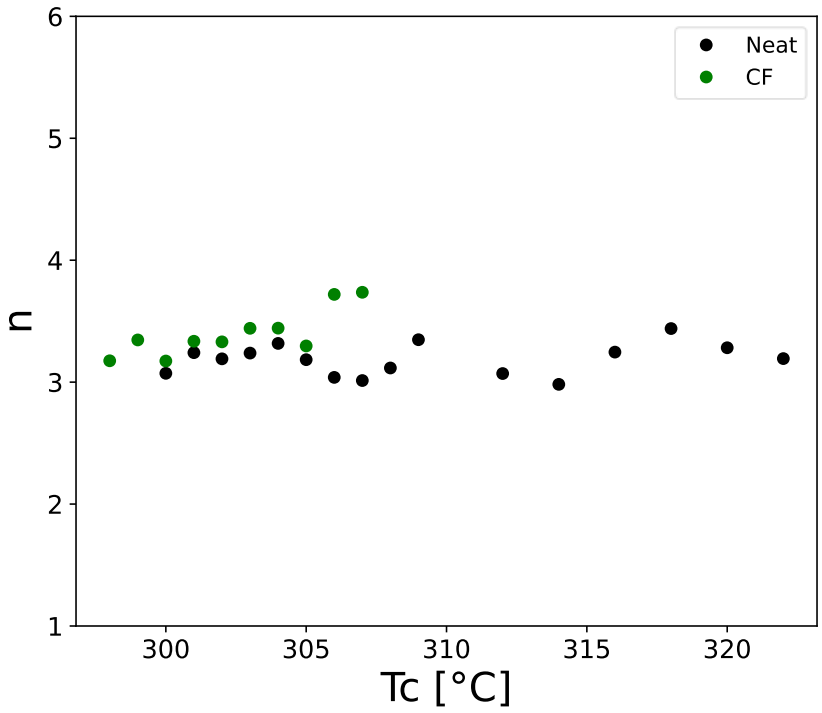

Fig. 43: Avrami index comparison between PEEK neat and PEEK CF.

The n-values do not vary much between PEEK neat and PEEK CF, a sign that the carbon fibres do not interfere in the shape of the crystalline phase, there are always three-dimensional spherulites forming more or less quickly.

However, things change when the terms related to the nucleation velocity are evaluated, in particular $k^{1/n}$ and $1/\tau_{50\%}$, which have the same trend.

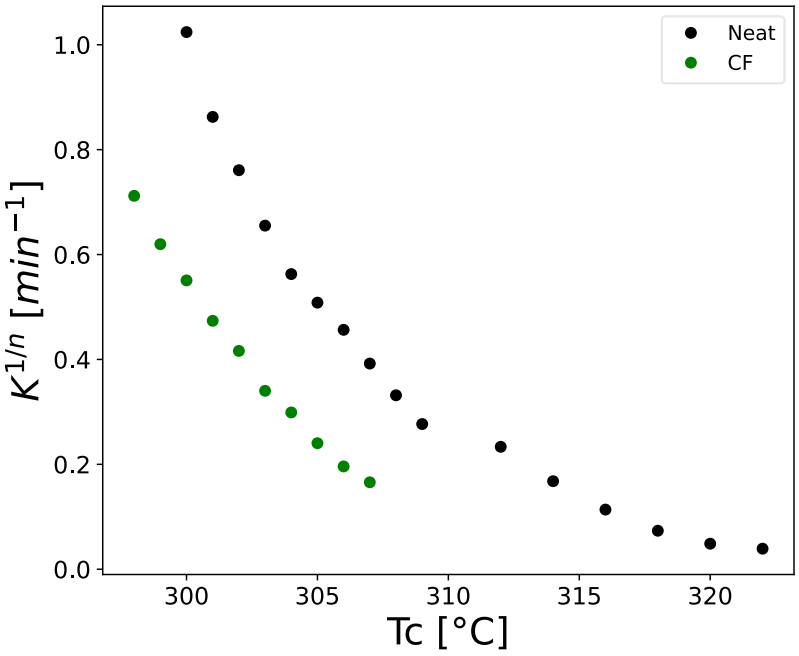

Fig. 44: Comparison of the coefficient $k^{1/n}$ of PEEK neat and PEEK CF.

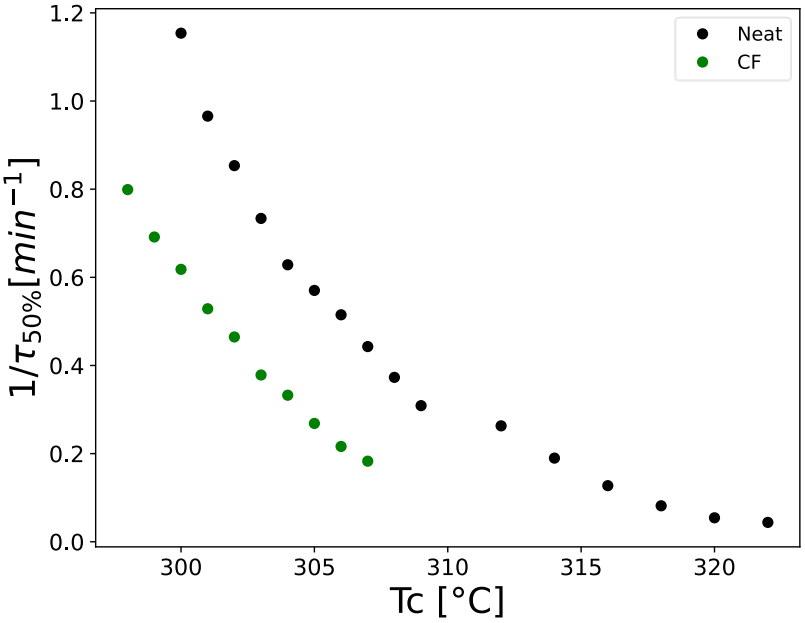

Fig. 45: Comparison in the $1/\tau$ coefficient$_{50\%}$ of PEEK neat and PEEK CF.

In Fig. 44 e Fig. 45 the trends related to the total crystallisation speed for PEEK neat and PEEK CF are shown. As can be seen from the two figures, the specimens containing the carbon fibres crystallise much more slowly at the same crystallisation temperature. So, this is a very important effect to consider, namely that the presence of the carbon fibre reinforcement slows down the crystallisation process of the matrix. This is also observed in the trend of the nucleation rate $1/t_0$.

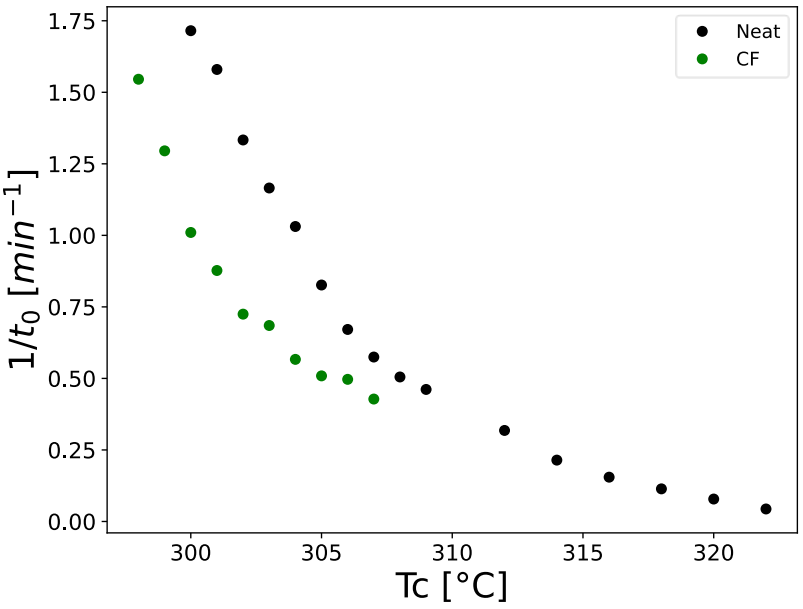

Fig. 46: Comparison in nucleation speed, $1/t_0$, between PEEK neat and PEEK CF.

Also shown in Fig. 46 at the same crystallisation temperature, a slowdown in nucleation is observed due to the presence of the fibres.

This slowdown is clearly observable when comparing the relative crystallinity trend.

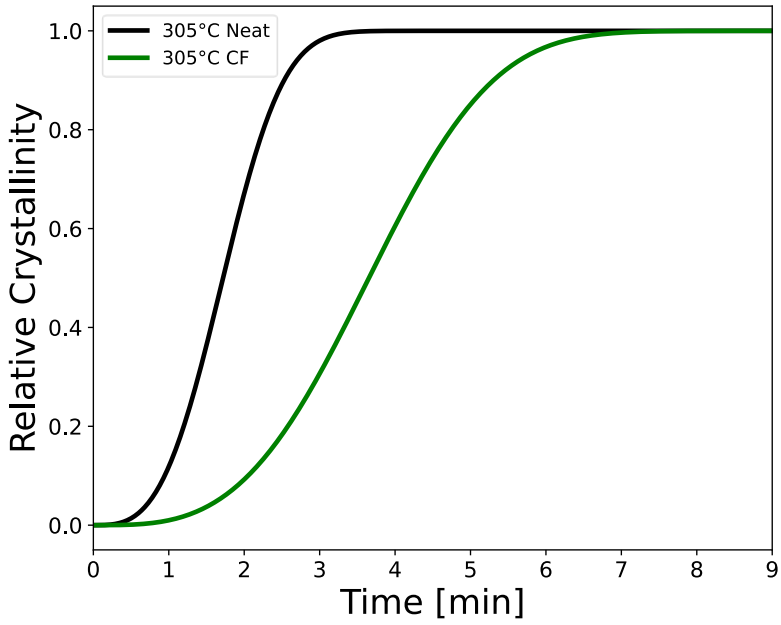

Fig. 47: Comparison of relative crystallinity between PEEK neat and PEEK CF.

In Fig. 47 the actual slowing down caused by the presence of the fibres can be observed in an example between two equal T_c. To obtain the same crystallinity value in the case of samples containing carbon fibres, the sample must be kept at the given T_c for a longer time. That shown in Fig. 47 is an example, but from the analysis of all temperatures, the gap between the curves is present in all curves. In addition, the higher the crystallisation

temperature, the greater the detachment. Another interesting variation is seen when looking at the total crystallinity trend.

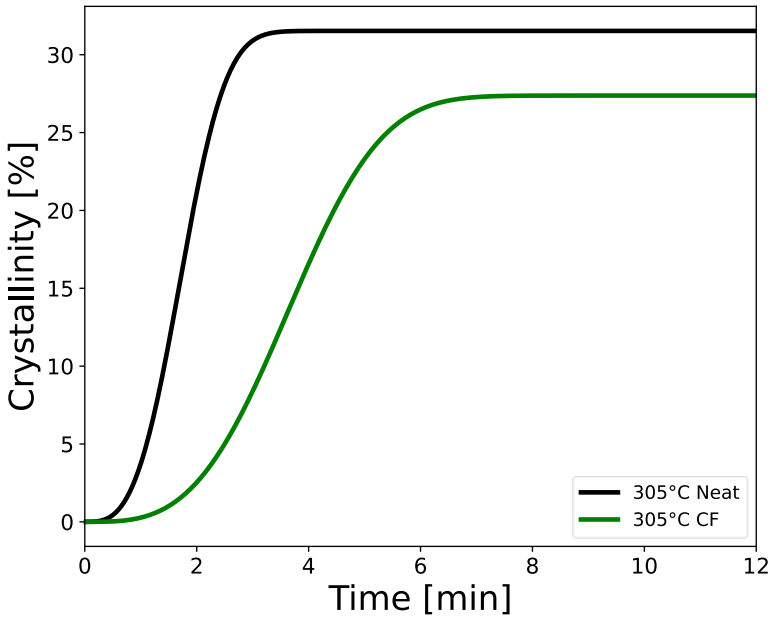

Fig. 48: Comparison of total crystallinity between PEEK neat and PEEK CF.

As can be seen from Fig. 48 in addition to the slowdown already observed due to the different parameters of the Single Avrami model, in the case of total crystallinity, a decrease in the maximum crystallinity value is also observed. Whereas in the case of PEEK neat the maximum value was 31% on average, in the case of PEEK CF it is 27%. Thus, the presence of the fibres not only slows down the crystallisation process of the matrix, but also lowers the maximum attainable crystallinity value.

In the *Single* Avrami fitting shows in Fig. 49 it can be seen that the model does not best approximate the trend, and although this defect was already generally known, in the case of PEEK CF it is more pronounced than in PEEK neat, i.e. the model is less accurate in PEEK CF than in PEEK neat.

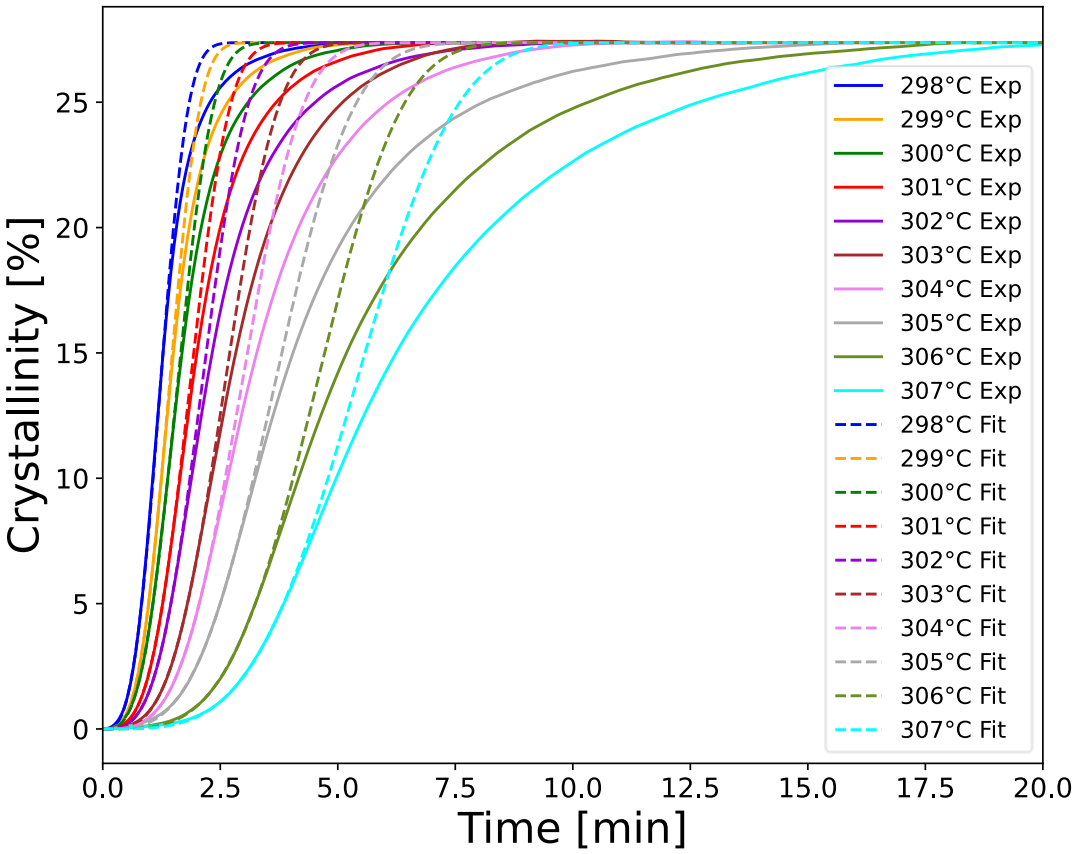

Fig. 49: Fitting model Single Avrami in PEEK CF.

2.3.6 Comparison of PEEK neat and CF in global crystallisation: the Lauritzen and Hoffman model

To obtain further confirmation of the effect of carbon fibres on the overall crystallisation of the polymer, the LH model was applied to the DSC data analysed by Avrami method from the PEEK CF samples. In the same way as in the previous paragraphs, the parameters of the LH model were calculated, i.e., K_G^{τ}, σ_e, σ and q.

Since it is still PEEK, the parameters used in the model are the same as for PEEK neat, so reference can be made to Tab. 3. Again, only regime II was considered. The only difference in the parameters is the T_g, which from the data of the non-isothermal test at DSC is 152.7 °C, as opposed to 150 °C for PEEK neat.

Tab. 4: Lauritzen and Hoffman fitting results for PEEK CF and comparison with PEEK neat.

	PEEK neat	**PEEK CF**
σ [erg/cm²]	12.157	12.157
K_G^τ *[K²]*	$5.027\text{-}10^5$	$7.724\text{-}10^5$
$1/\tau_0$ [sec^{-1}]	$1.25 \cdot 10^4$	$3.75 \cdot 10^6$
σ_e [erg/cm²]	132.011	202.83
q *[erg]*	$1.216 \cdot 10^{-12}$	$1.868 \cdot 10^{-12}$

From the results in Tab. 4 the values of K_G^τ, σ_e and q are greater in PEEK CF than in PEEK neat. The value of σ remains the same because being always PEEK, a_0, b_0 and ΔH_f do not vary. The fact that those three parameters are greater in PEEK CF than in PEEK neat confirms that carbon fibres slow down the crystallisation process. In fact, when a nucleating agent, i.e., a chemical species that promotes nucleation of the crystalline phase, is added, these three parameters decrease in the polymer with the nucleating agent compared to the pure polymer [59]. In this case, the parameters are higher in PEEK CF, an indication that the carbon fibres act as an anti-nucleating agent, i.e., they behave the opposite of a nucleating agent. This is further confirmation that the presence of the carbon fibres slows down the nucleation process by generating an anti-nucleating effect.

2.3.7 Kinetics of isothermal PEEK crystallisation from the melt: influence of carbon fibres in Dual Avrami

It has been observed in the previous paragraphs that the presence of carbon fibres within the PEEK matrix produces a slowdown in the nucleation and crystallisation of the material. As already mentioned, several times, the aim of this work is to develop a model to predict the degree of crystallinity of the material after processing, such as holding it at a certain temperature (isothermal crystallisation). To produce this, the Single Avrami model is not sufficiently accurate, so it was necessary to adopt a modification of it, the Dual Avrami. In this section, the results of applying the Dual Avrami model to specimens containing carbon fibres will be presented, since, as the kinetics change, if the matrix behaviour is to be simulated in the presence of carbon fibres, then the model must be calibrated with the new data.

First, the difference between Single and Dual Avrami with PEEK CF specimens is analysed. Then the difference between PEEK neat and PEEK CF will be assessed within the Dual Avrami.

When comparing the two models, one must consider how the fundamental parameters vary, which for the Dual Avrami are divided into primary and secondary.

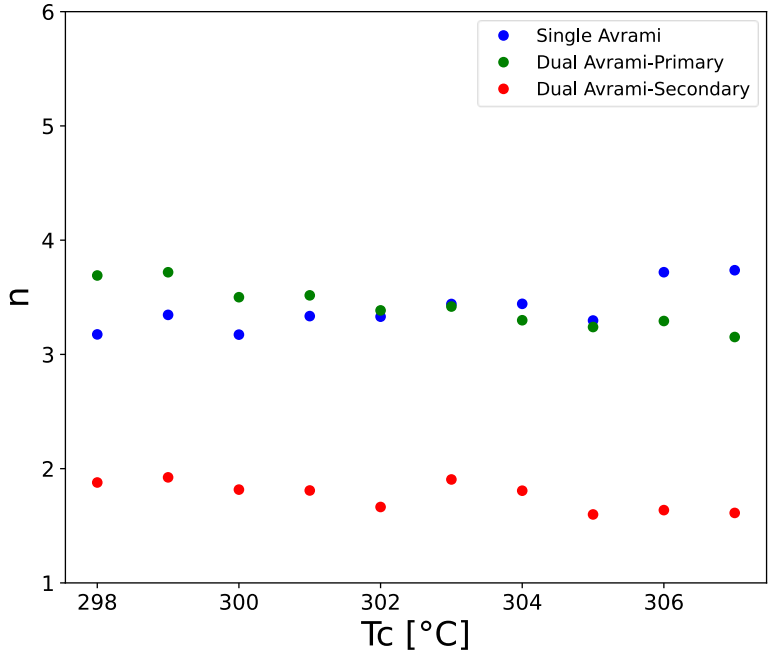

Fig. 50: Avrami index trend for both the Single and Dual models for PEEK CF.

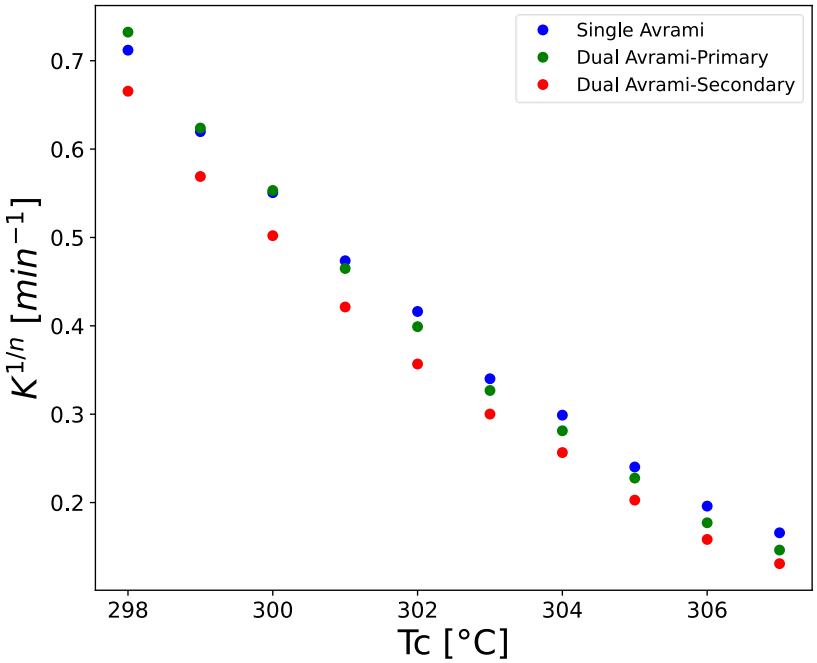

Fig. 51: Development of parameter $K^{1/n}$ of both the Single and Dual Avrami models for PEEK CF.

As can be seen from Fig. 50 e Fig. 51 there is a variation, considering the fact that the parameters are divided into two contributions, in the case of the Avrami index, the primary value is larger than the secondary, as already explained in the previous paragraphs for the PEEK neat, and it can also be observed that the value of the primary follows that of the

Single, as they both refer to primary crystallisation. The same concept applies to the velocity parameter K.

As far as the parameter $1/\tau_{50\%}$ is concerned, it does not vary much between *Single* and *Dual*, so the calculations with the LH model will not be repeated (Fig. 52).

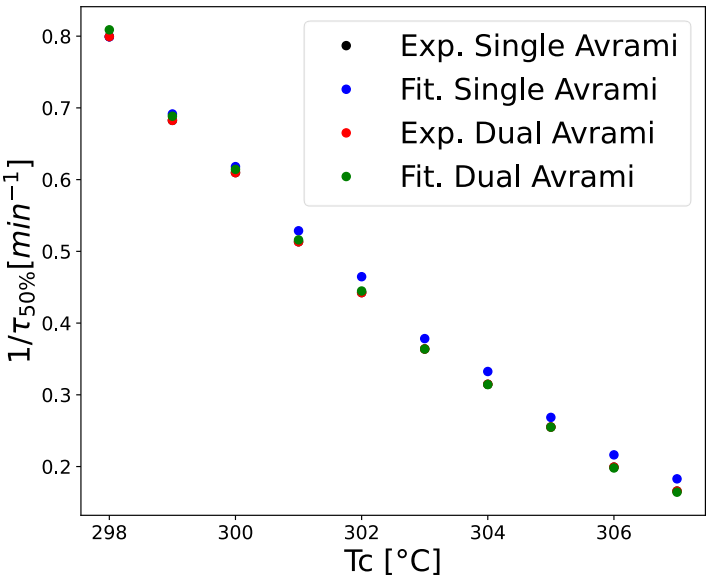

Fig. 52: Development of parameter $1/\tau_{50\%}$ of both the Single and Dual Avrami models for PEEK CF.

Finally, the fitting of total crystallinity is shown, curves that are necessary when applying the model in Abaqus (Fig. 53).

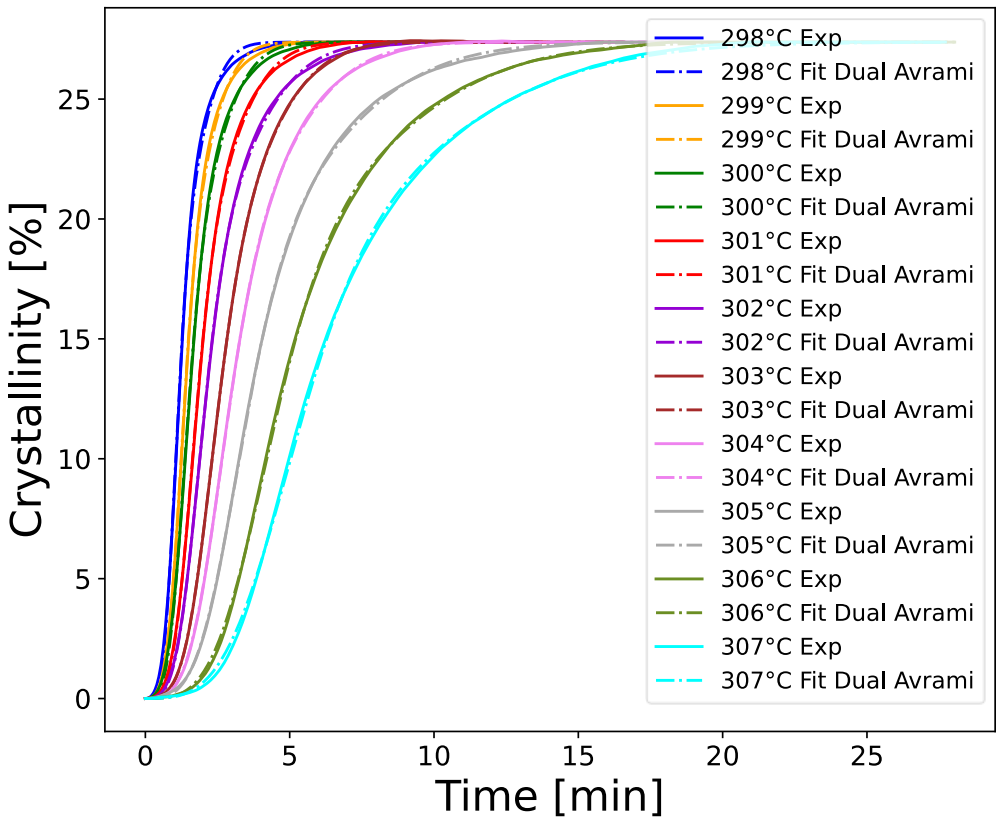

Fig. 53: Fitting the crystallinity with Dual Avrami in PEEK CF.

From Fig. 53 it can be seen that, even in the case of PEEK CF, the model perfectly approximates the crystallinity trend, unlike the Single Avrami model.

The difference between PEEK neat and PEEK CF within the Dual Avrami will be shown below.

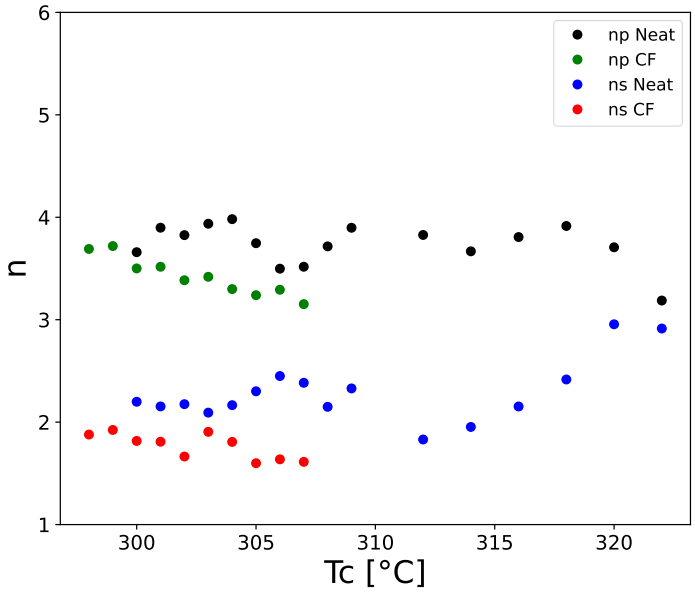

Fig. 54: Primary and secondary Dual Avrami index trend for PEEK CF.

Fig. 54 shows the development of both primary and secondary PEEK CF Avrami indices. As in the case of Single Avrami, the difference between PEEK neat and PEEK CF is not great in the case of the indexes, because three-dimensional spherulites are always created. Even in the case of nucleation velocity, the same difference occurs as in the case of Single Avrami. In fact, as shown in Fig. 52 the parameter $1/\tau_{50\%}$ does not change, so that even in the difference between PEEK CF and PEEK neat, it is possible to refer to the trend shown in paragraph 2.3.5. The same happen in $1/t_0$, as the value does not change between Single and Dual Avrami. Another parameter that varies because it is divided into two, like the Avrami index, is K, which is displayed in Fig. 55.

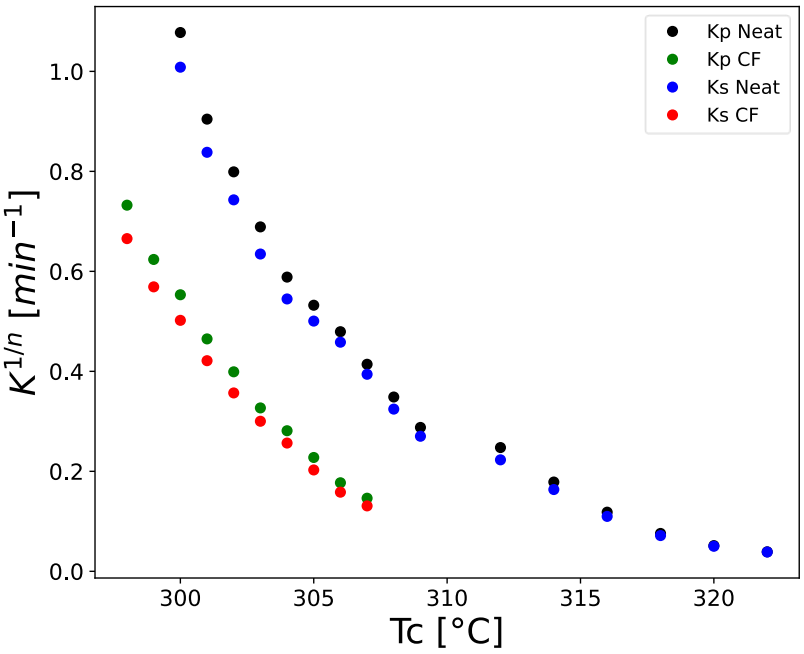

Fig. 55: Development of $K^{1/n}$ in the Dual Avrami model for PEEK CF.

As with Single Avrami, there is a difference in the speed of crystallisation, which is also reflected in the coefficients associated with secondary crystallisation.

2.3.7.1 Abaqus model: PEEK CF crystallisation

The model in Abaqus for PEEK CF is the same for PEEK neat, as the same Dual Avrami model is used. Obviously, the values change, as explained in the previous paragraph. So, in this paragraph the parameters needed to adapt the model written for PEEK *neat* will be explained to use them with PEEK CF. This is useful, for example, when considering a micromechanical model, which has the fibres embedded in the PEEK matrix. In this case, the crystallisation law, i.e., the Dual Avrami model, which must follow the matrix must consider the interpolating equations of PEEK CF and not PEEK neat. The functions are set out below.

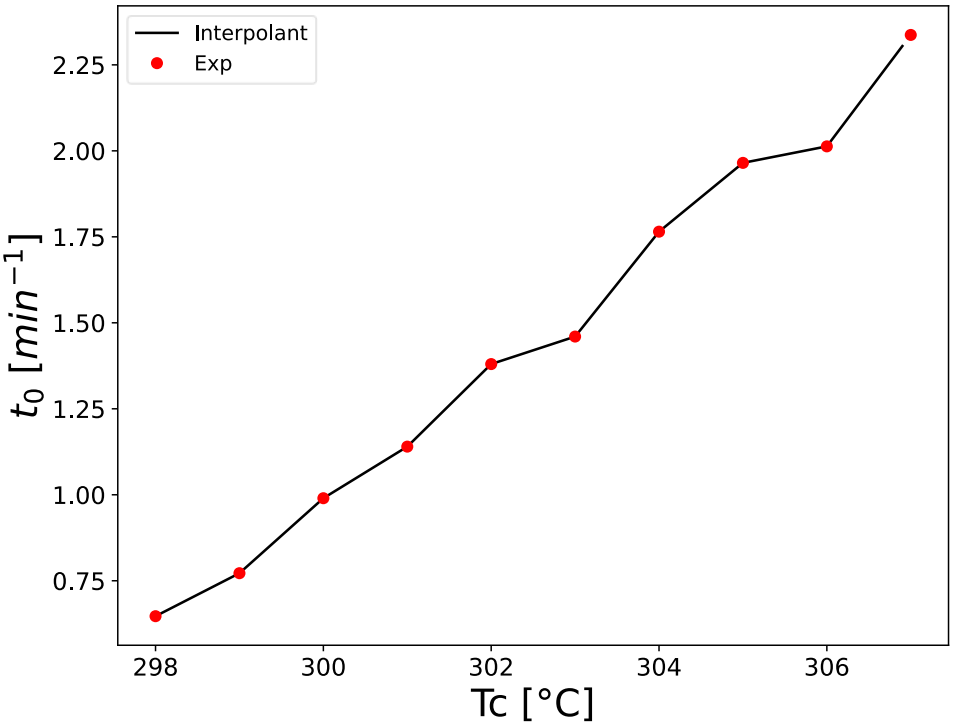

Fig. 56: Interpolation of experimental data of t_0 for PEEK CF.

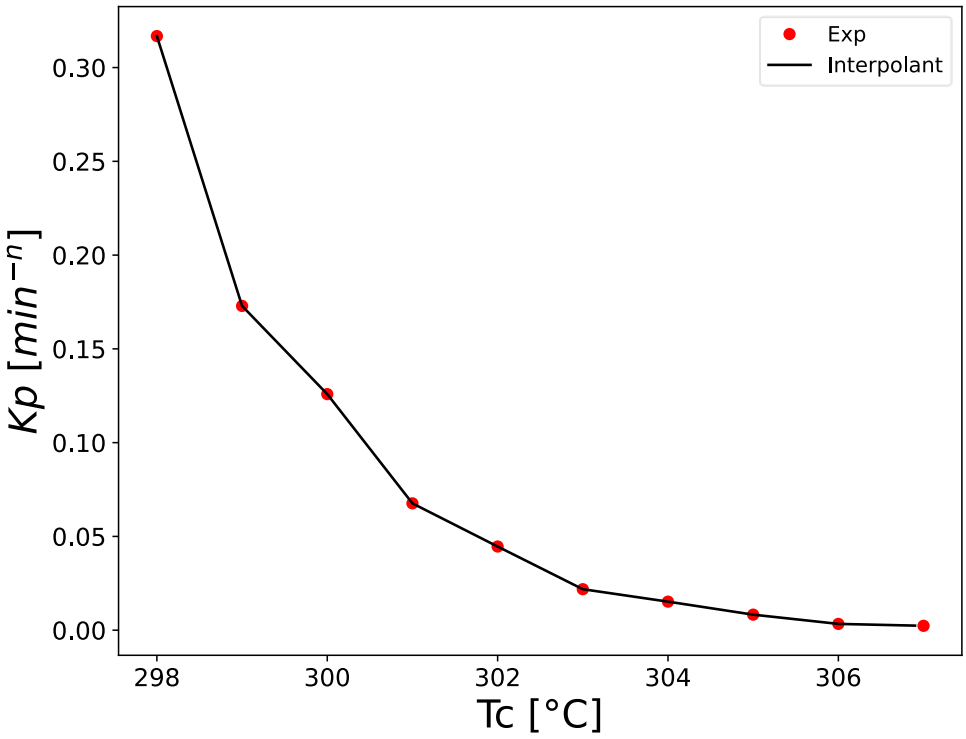

Fig. 57: Interpolation of experimental data of K_p for PEEK CF.

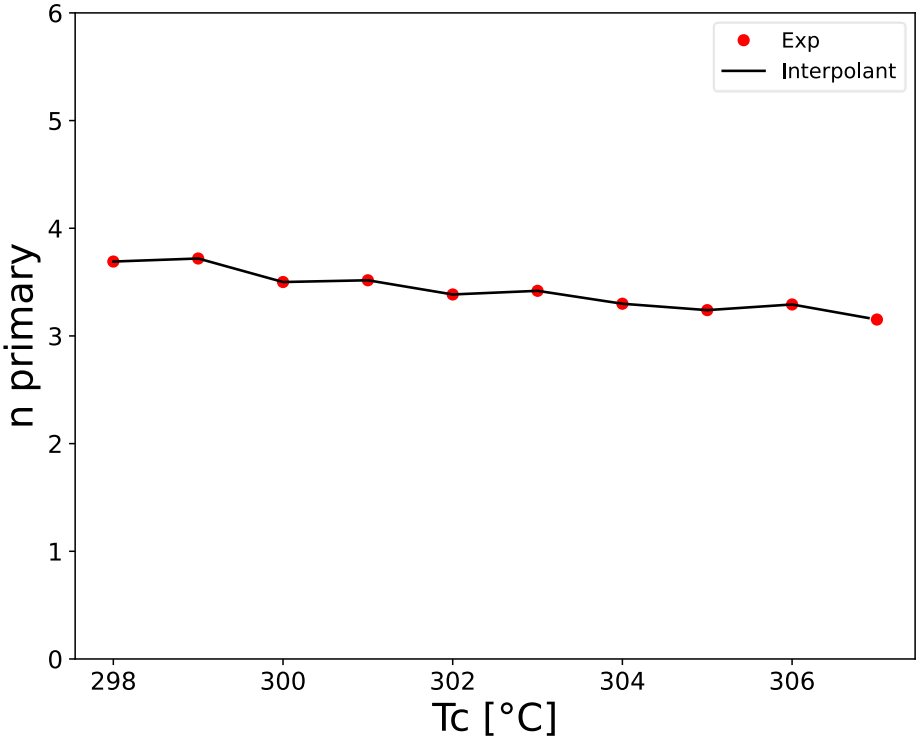

Fig. 58: Interpolation of experimental data from n_p for PEEK CF.

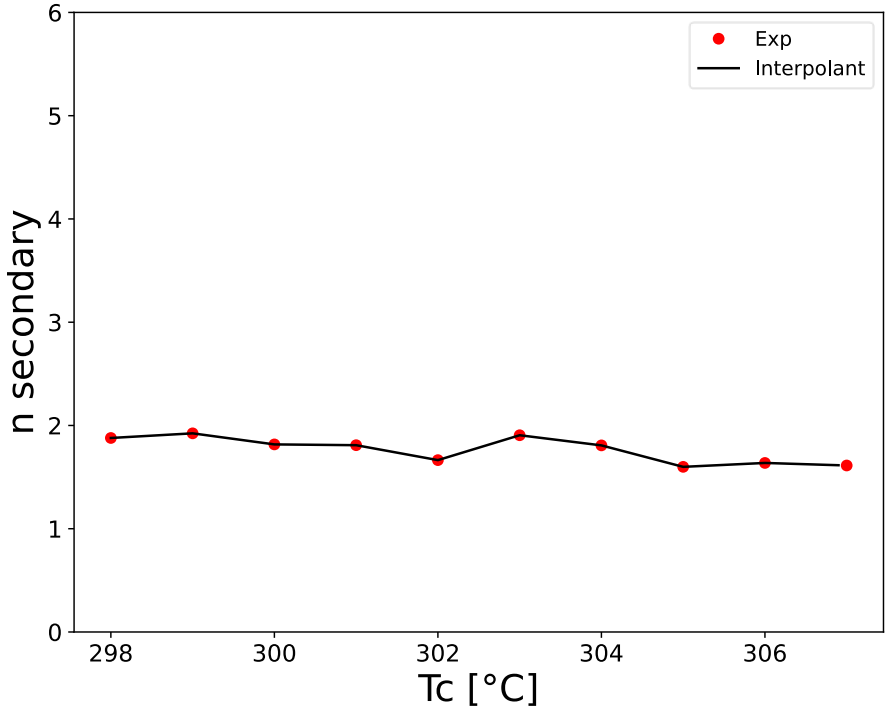

Fig. 59: Interpolation of experimental data from n_s for PEEK CF.

All curves exposed by Fig. 56 a Fig. 59 replace those of PEEK neat, so the Abaqus model for PEEK is obtained when carbon fibres are present.

2.3.8 Analysis of crystalline phase growth: self-nucleation (SN) and $T_{s,ideal}$

All the data shown in the previous paragraphs concerning the comparison between neat and CF, confirm the effect of carbon fibres as an anti-nucleating agent; thus, they slow down the nucleation process by interfering in the overall crystallisation. However, it is not certain that they also affect the crystal growth process alone. To better analyse this process and isolate it from the nucleation phase, one method can be used, as explained in the previous sections, namely self-nucleation at the ideal self-nucleation temperature. Before the growth of the lamellae alone will be studied, the $T_{s,ideal}$ should be found in both PEEK neat and PEEK CF, i.e., that temperature dividing the domain II from domain III. At this temperature, the almost instantaneous nucleation of all possible nuclei takes place, and then the subsequent maintenance at a crystallisation temperature considers only the growth phase of the crystal, because there can be no further nucleation, since the maximum has already been produced. The identification of $T_{s,ideal}$ is carried out by applying the protocol seen in section 2.2.3.3.

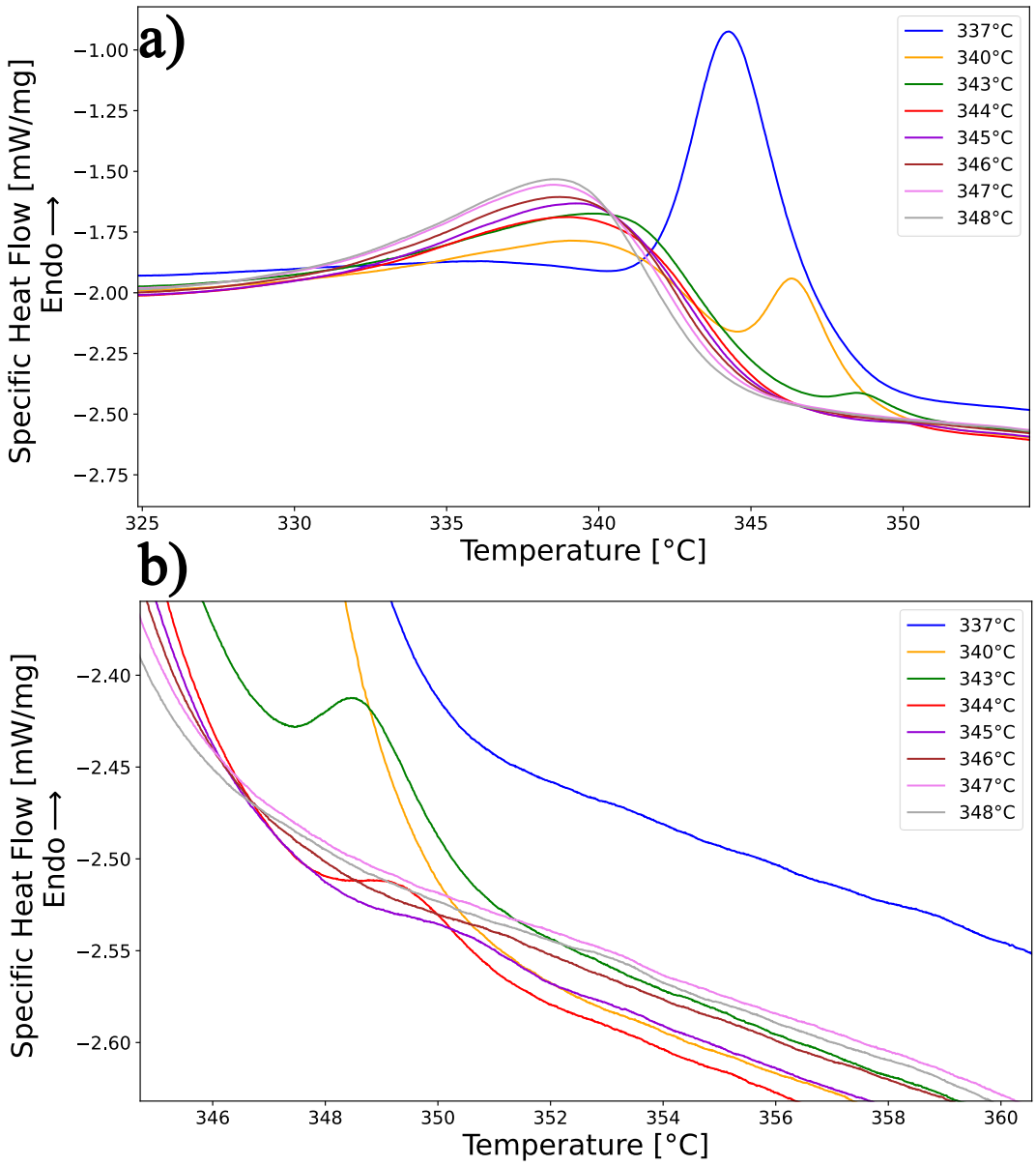

Fig. 60: Results of the heating phase after cooling following the reaching of the assumed T_s of the PEEK neat - a) full data; b) zoom to better identify peaks.

From Fig. 60 the results of applying this protocol can be observed. $T_{s,ideal}$ being the temperature between domain II and domain III, it can be observed from the Fig. 60a that certainly the temperatures 337 °C, 340 °C, 343 °C are part of domain III where annealing is present, in fact in the figure the double peak can be observed, which is typical of the annealing phase. In order to identify $T_{s,ideal}$ the first temperature which has not the double peak need to be evaluated. By analysing the graph more closely in Fig. 60b, it can be observed that this first temperature is 347 °C. Therefore the latter can be identified as the transition temperature between domain II and domain III, i.e., $T_{s,ideal}$ for PEEK neat.

The same procedure was repeated for the PEEK CF samples.

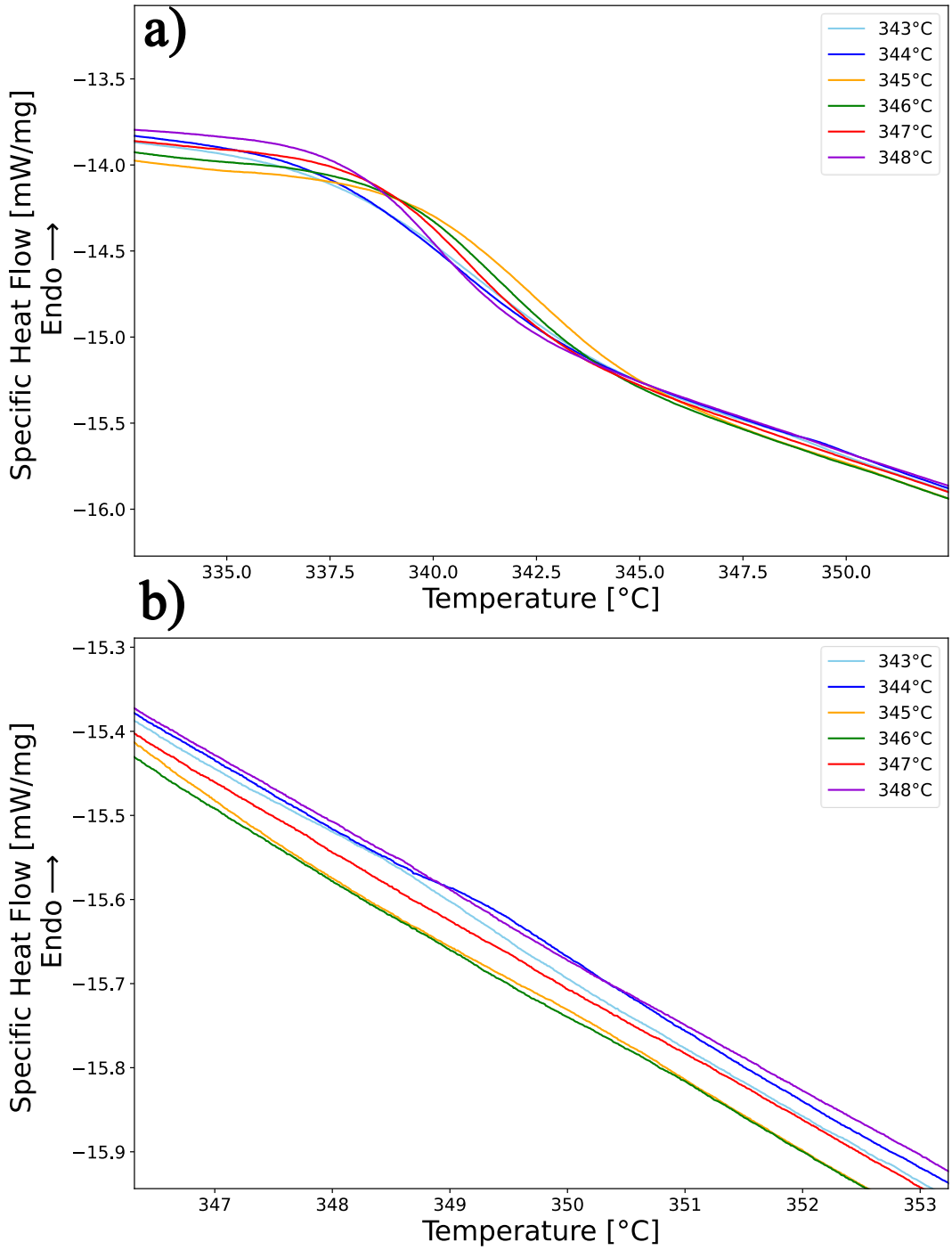

Fig. 61: Results of the heating phase after cooling following the reaching of the assumed T_s of the PEEK CF - a) full data; b) zoom to better identify peaks.

For PEEK CF, the results of the DSC test are shown in Fig. 61. In contrast to PEEK neat, the annealing peaks are not very pronounced and are very difficult to detect. Only by zooming in Fig. 61b, even if with difficulty, it can be notice that the temperatures 343 °C, 344 °C, 345 °C show a small hint of annealing peak, as early as 346 °C the second peak is probably no longer noticeable, but since for PEEK neat the temperature $T_{s,ideal}$ was easily discernible at 347 °C, this value was again taken as $T_{s,ideal}$ for PEEK CF. In conclusion, the $T_{s,ideal}$ for both PEEK neat and PEEK CF was considered to be 347 °C.

2.3.9 Analysis of crystalline phase growth: minimum crystallisation temperature from SN ($T_{c,min,SN}$)

When switching from crystallisation from the melt to crystallisation from self-nucleation, the $T_{c,min}$ changes, moving to higher values, precisely because of the physical difference between the two processes, self-nucleation promotes crystallisation with less supercooling (supercooling is the ΔT between T_m^0 and T_c). Therefore, the detection of a $T_{c,min,SN}$ greater than the $T_{c,min}$ from the melt is a sign that the self-nucleation process has been carried out correctly.

To calculate the $T_{c,min,SN}$ of PEEK neat, the protocol in section 2.2.3.4 will be followed using the $T_{s,ideal}$.

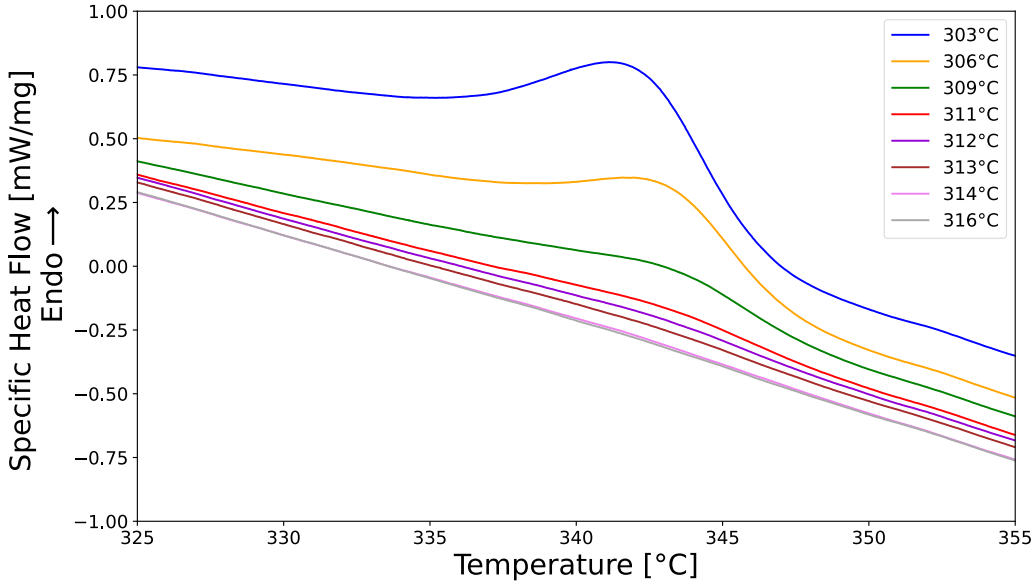

Fig. 62: DSC test results on PEEK neat for $T_{c,min,SN}$.

From Fig. 62 it can easily be seen that heating, following cooling at 50 °C/min, from $T_{s,ideal}$ produces a peak at all the temperatures analysed except 316 °C. This is why this is defined as the $T_{c,min,SN}$ for PEEK *neat*, since it is the first temperature to show no crystallisation following cooling, this time not from the melt (i.e., 400 °C), but from $T_{s,ideal}$. As can be seen from the value, comparing it with that from melt, is much higher. In fact, $T_{c,min}$ from melt was 300 °C, whereas $Tc_{,min,SN}$ is 316 °C.

For PEEK CF, the procedure was the same, applying the protocol to the samples containing the carbon fibres.

As can be seen from Fig. 63 several peaks are present relative to the crystalline phase formed because of the 50 °C/min cooling in the protocol. From a detailed visual analysis of the curves, it can be stated that the first curve that definitely has no crystallinity peaks is the one corresponding to 308 °C, so the $T_{c,min,SN}$ for PEEK CF is 308 °C. This is a

higher temperature than the $T_{c,min}$ from the melt, in agreement with the self-nucleation theory.

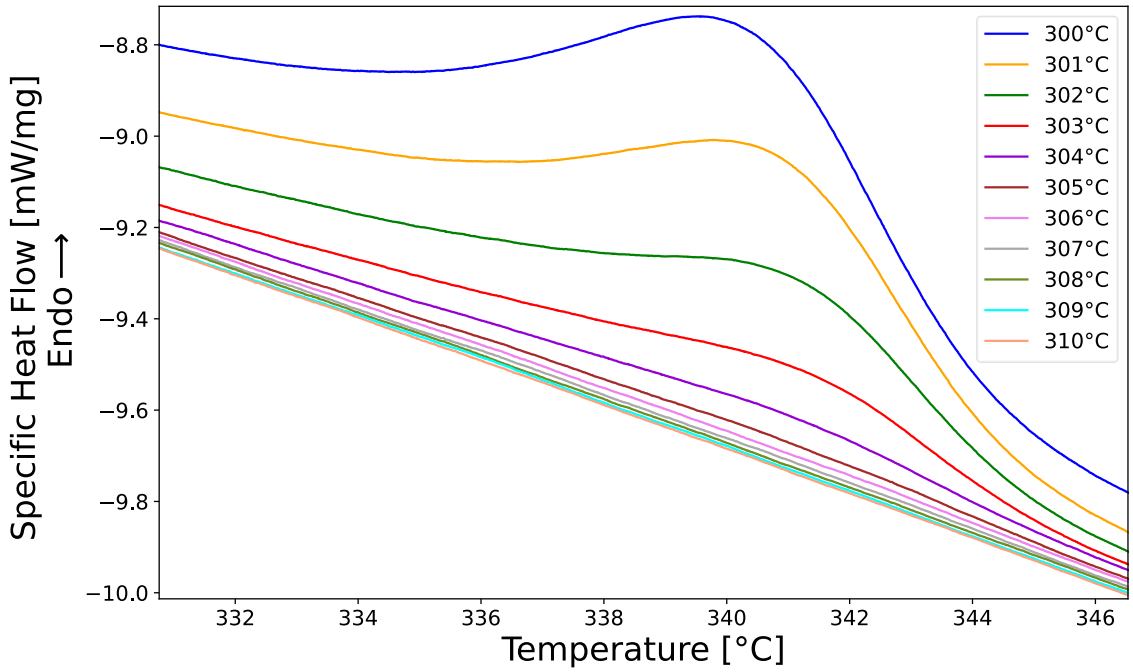

Fig. 63: DSC test results on PEEK CF for $T_{c,min,SN}$.

2.3.10 Growth analysis of the crystalline phase of PEEK neat: Single Avrami and Lauritzen Hoffman model from SN

The growth of the crystalline phase analysed by self-nucleation follows the same procedure for analysing the kinetics of crystallisation as seen so far. Once the $T_{s,ideal}$ and $T_{c,min,SN}$ have been calculated, the thermal protocol seen in section 2.2.3.5 could be applied. From this set of steps, the isothermal crystallisation at the specific T_c is analysed, which this time will be larger than the one analysed previously, as it starts from the value of 316 °C. For this reason, to have enough points to apply the LH model, the measurements proceed in steps of 0.5 °C, from 316 °C to 319.5 °C. The steps are equivalent to those observed in the previous sections and are shown in Fig. 64 e Fig. 65.

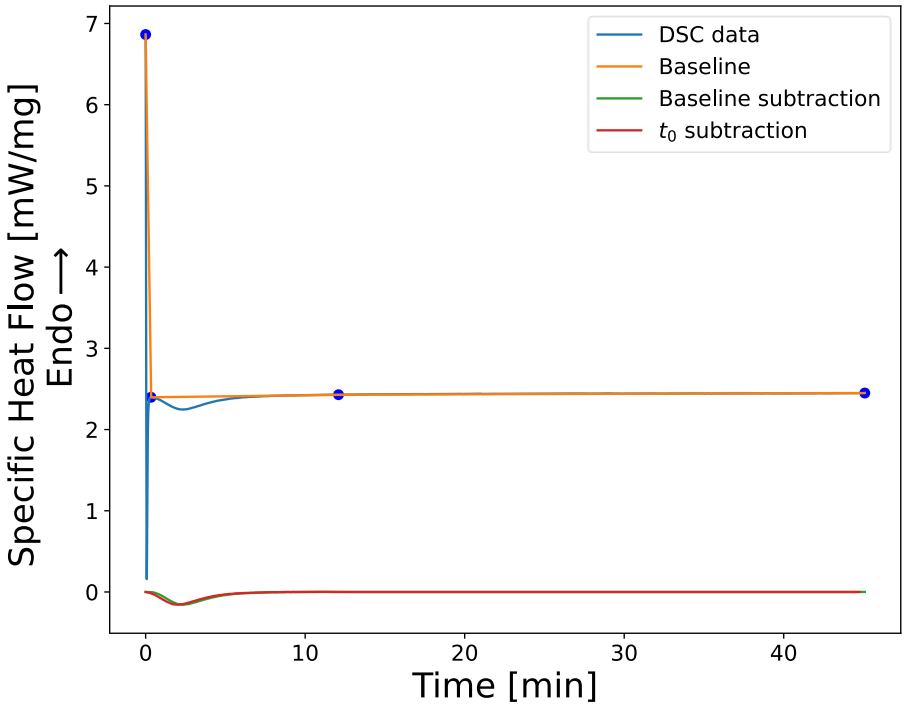

Fig. 64: Subtraction of the baseline and analysis of the crystallisation peak following an isothermal process from SN for PEEK neat.

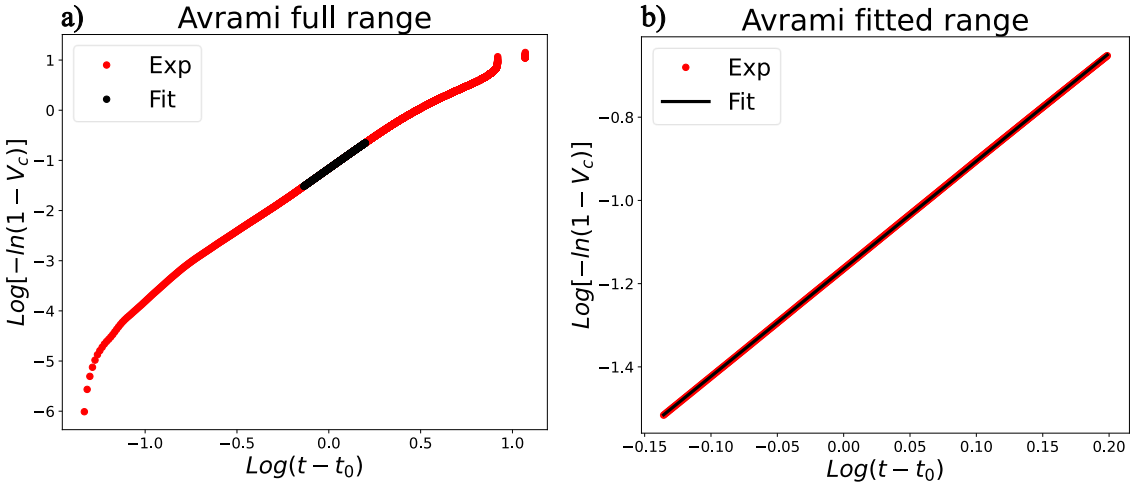

Fig. 65: a) complete Avrami and b) fitted for isothermal PEEK neat from SN.

In this specific case, Avrami analysis aims to identify those same parameters related to the overall crystallisation of the crystalline phase (nucleation + growth), only that, since everything starts from SN, they will only refer to the growth phase. This is why a G is placed in the nomenclature of the crystallisation rate, a sign that the parameter considered refers only to the growth phase. One parameter that loses its significance is the t_0 since nucleation occurs instantaneously. Surely the most important parameter is $1/\tau_{50\%}^{G}$ since it is fundamental to the application of the LH model.

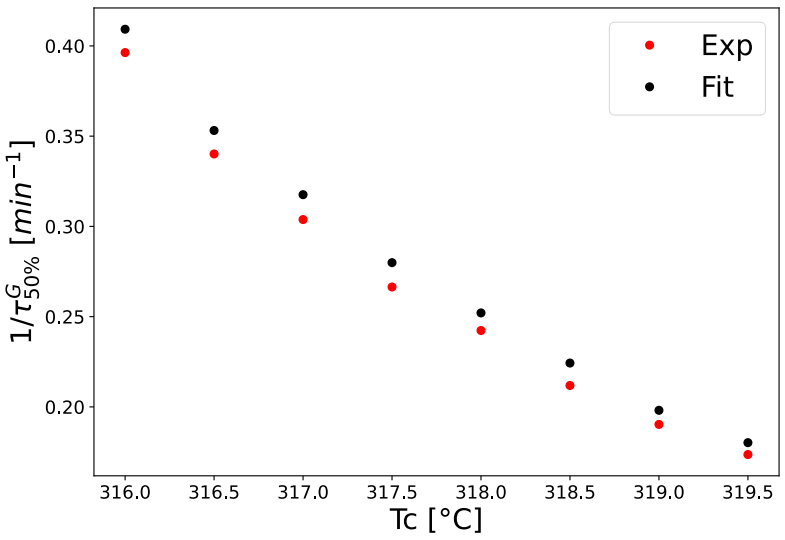

Fig. 66: Experimental and calculated trend with Avrami model for the term $1/\tau^{G}_{50\%}$ from SN for PEEK neat.

In Fig. 66 the development of the growth rate of the lamellae is shown. It is through the application of that model that it is possible to assess the difference in lamella growth between PEEK neat and PEEK CF, to get the full picture of the influence of the carbon fibres.

Avrami index is also given for completeness. The value is close to 3, precisely because nucleation is almost instantaneous and always has a three-dimensional shape, the spherulite.

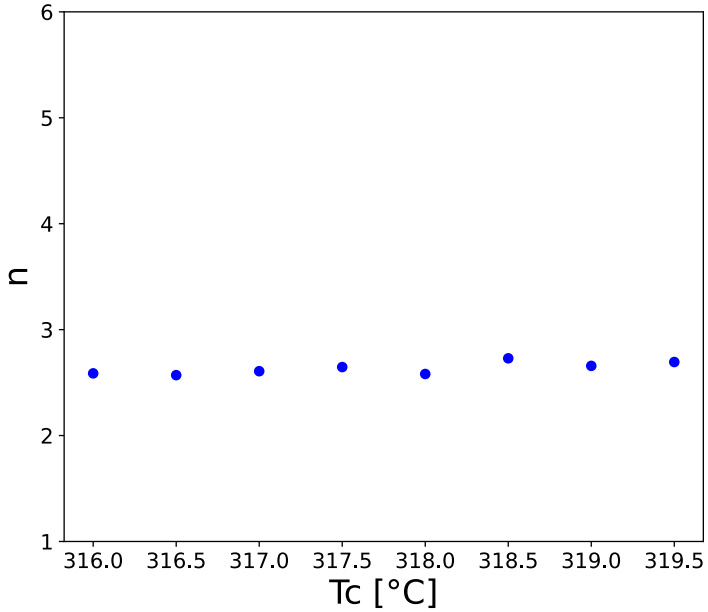

Fig. 67: Avrami index following isothermal crystallisation from SN for PEEK neat.

From $1/\tau^{G}_{50\%}$ trend it is possible to apply the LH model. As it is always the same material, the parameters can refer to Tab. 3.

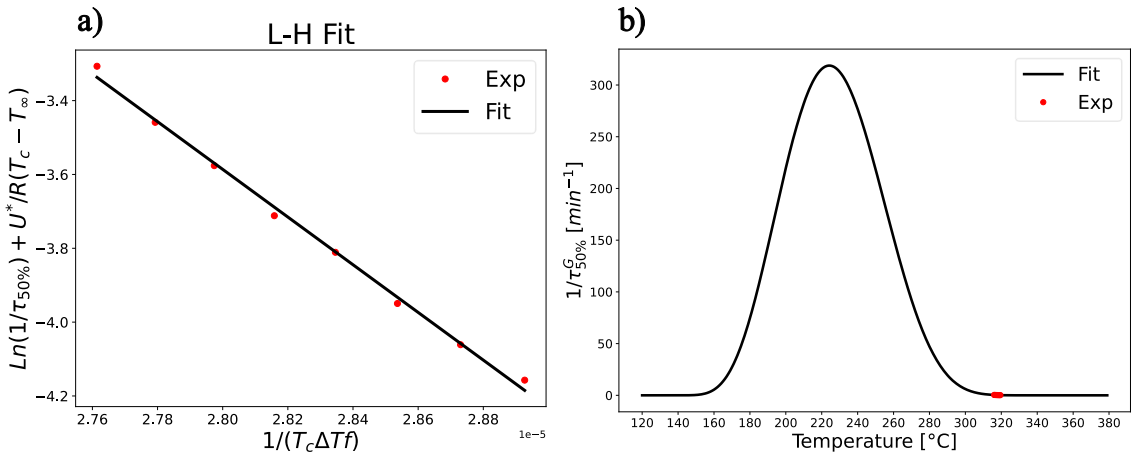

Fig. 68: a) LH fitting and b) LH fitting in the full range, from SN, for PEEK neat.

The results are shown in Fig. 68. These results will be important when comparing with the PEEK CF specimens, as a comparison will reveal whether the carbon fibres also directly influence the growth phase alone or not.

2.3.11 Analysis of the crystalline phase growth of PEEK CF and comparison with PEEK neat from SN

To complete the discussion of the effect of carbon fibres on crystal growth alone, which can be observed by means of the self-nucleation technique, the results of isothermal crystallisation from $T_{s,ideal}$ for PEEK CF are presented below.

The analysis is the same as in the previous paragraph, with the first difference being the temperature range. In fact, in the case of PEEK CF, the $T_{c,min,SN}$ is 308 °C, which is why the temperature range analysed goes from 308 to 311.5 °C in steps of 0.5 °C in order to obtain 8 experimental points.

By subtracting the baseline and applying the Single Avrami model, the trend of the parameter $1/\tau^G_{50\%}$ and the Avrami index were calculated. As already mentioned in the previous paragraphs, the parameter $1/\tau^G_{50\%}$ in this case refers only to the growth of the crystalline lamella (as indicated by the superscript G).

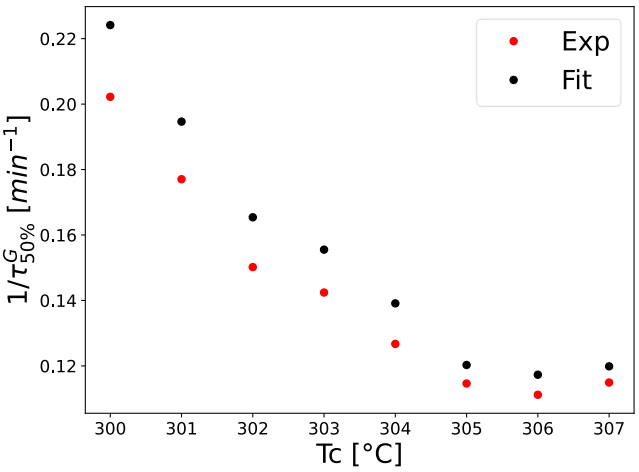

Fig. 69: Experimental and calculated trend with Avrami model for the term $1/\tau^{G}_{50\%}$ from SN for PEEK CF.

The trend in Fig. 69 follows that of PEEK neat in contrast to the values that are lower here. In addition, from the graph in Fig. 70, the trend of the Avrami index in comparison with that of PEEK neat can be observed. Again, the values are close to 3, indicating that the mode of self-nucleation does not vary.

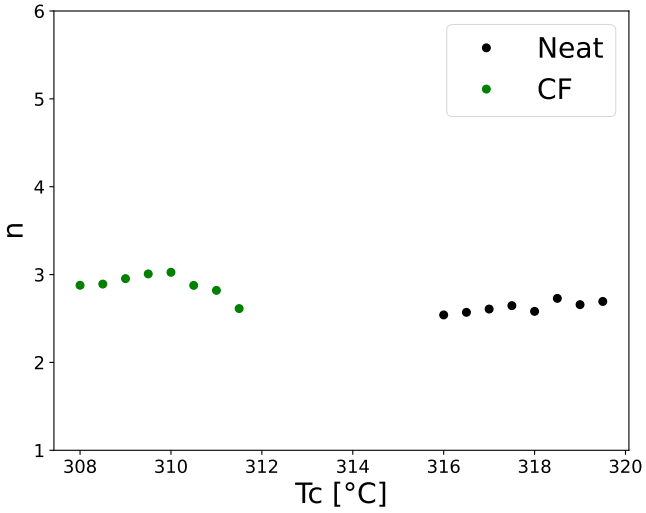

Fig. 70: Avrami index trend in both PEEK neat and PEEK CF.

By applying Avrami linear fitting, it is possible to calculate the entire crystallisation curve (in this case, of lamellae growth) and make a direct comparison between the growth rates of PEEK neat and PEEK CF. From Fig. 71 the difference in speed between PEEK neat and PEEK CF can be observed. Indeed, as with global crystallisation, even in the case of crystal growth alone, the presence of carbon fibres affects the velocities, slowing down the process considerably.

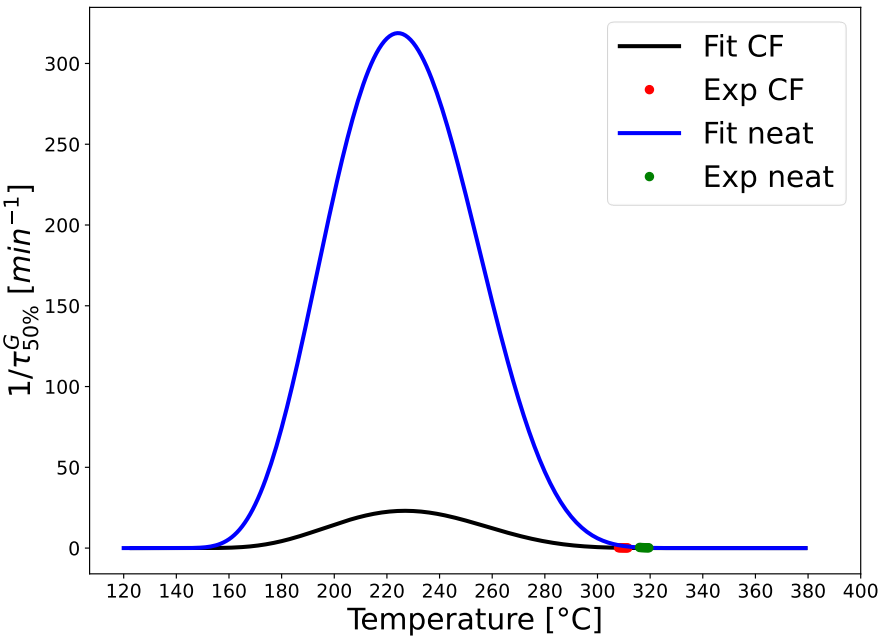

Fig. 71: Global growth rate trend, LH fitting between PEEK neat and PEEK CF.

This effect of slowing down the growth process of crystalline lamellae is easily observed by concentrating on the area of the curve near the experimental points and choosing a reference temperature to observe the corresponding growth rate.

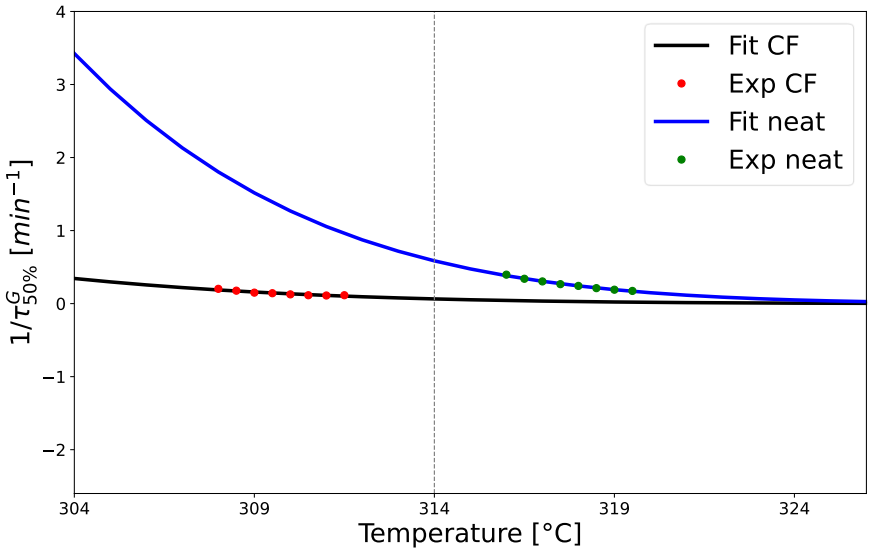

Fig. 72: Effect of slowing down the growth of crystalline lamellae in PEEK CF at a temperature of 314 °C.

Observing the Fig. 72, choosing 314 °C as comparison T_s, for PEEK neat the velocity $1/\tau^{G}_{50\%}$ is 0.58 min^{-1}, while for PEEK CF it is 0.065 min^{-1}. There is practically an order of magnitude difference between the two velocities, which is a clear sign that even in the case of crystalline lamellae growth alone, following the process of self-nucleation at $T_{s,ideal}$, the carbon fibres actively influence, producing a slowing down of the process.

2.3.12 Nucleation efficiency of the presence of carbon fibres

To calculate the nucleation efficiency of carbon fibres in PEEK, Eq. (24) was used. The $T_{c,max}$ can be calculated from the analysis of the SN ideal temperature of PEEK neat. In fact, the maximum crystallisation temperature that the polymer has, that corresponding to the maximum of the crystallisation peak after cooling from $T_{s,ideal}$, agreeing to the temperature at which the maximum amount of material crystallises. This temperature $T_{c,max}$ is equal to the temperature of the peak obtained in the curve of the equivalent step 6 of paragraph 2.2.3.3 when considering the actual $T_{s,ideal}$ calculated in the previous paragraphs. It is equal to 297.8 °C.

$T_{c,NA}$ and $T_{c,pol}$ can be calculated from the non-isothermal cooling peak as shown in Fig. 73.

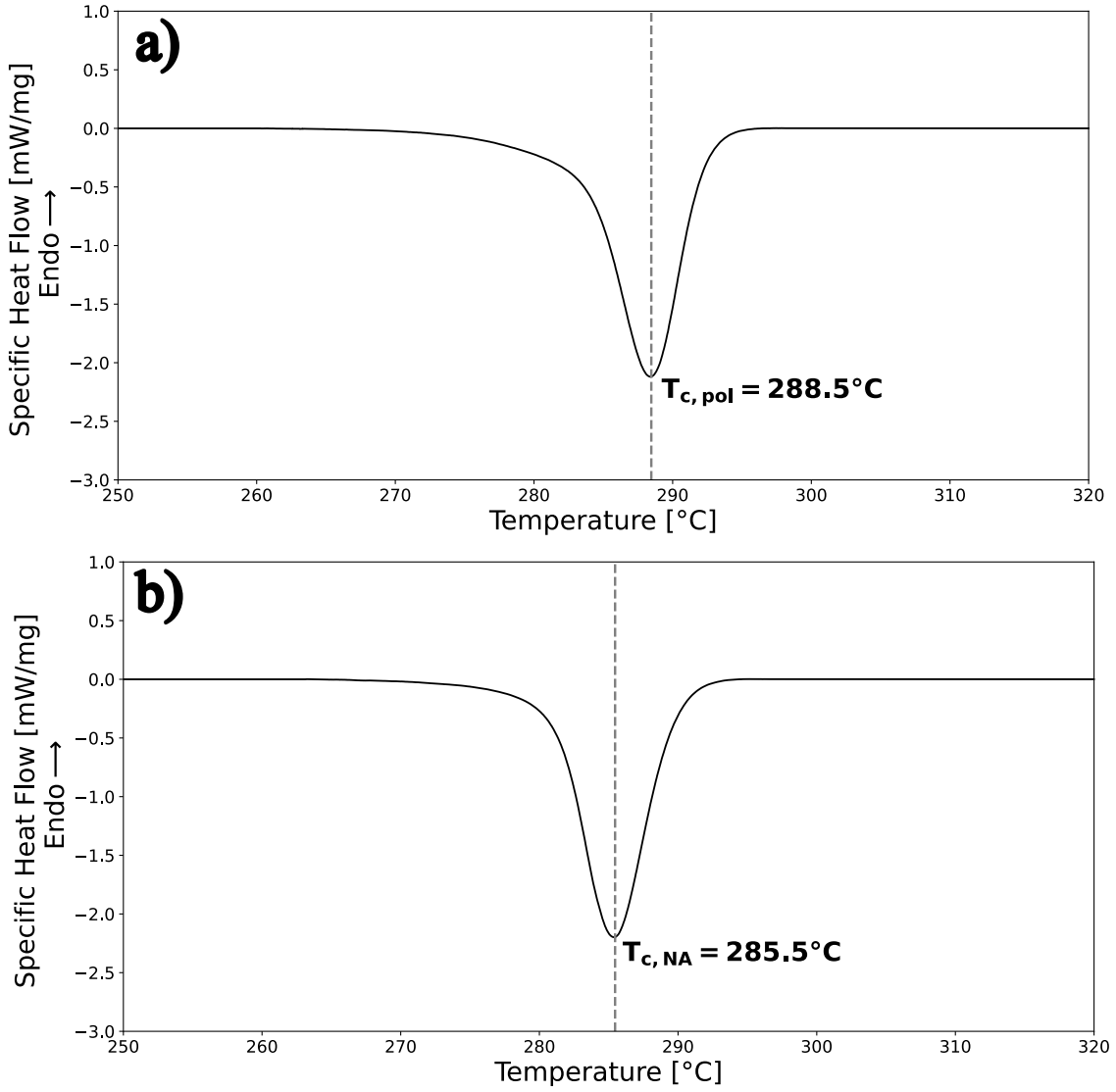

Fig. 73: Non-isothermal crystallisation temperature - a) PEEK neat; b) PEEK CF.

As shown in Fig. 73 $T_{c,NA}$ = 285.5 °C and $T_{c,pol}$ = 288.5 °C.

Applying Eq. (24) NE = -32.2% was obtained, i.e., the presence of the carbon fibres generates a negative nucleation efficiency, confirming that they can be defined as an anti-nucleating agent.

2.3.13 Successive self-nucleation and annealing (SSA) analysis: PEEK neat vs CF

Applying the protocol for thermal fractionation explained in section 2.2.3.6 the SSA process for PEEK neat and CF can be examined, to evince how the carbon fibres can influence the annealing process and thus the thickening of the crystalline lamellae. Looking first at the results of the PEEK neat, it can be observed that in the chosen T_s range, 8 peaks related to the annealing of the crystalline phase are obtained (Fig. 74). The temperatures chosen, also considering $T_{s,ideal}$, were 9, but 8 peaks are present precisely because $T_{s,ideal,}$ being exactly between regime II and III, is the first temperature not to present the annealing phenomenon.

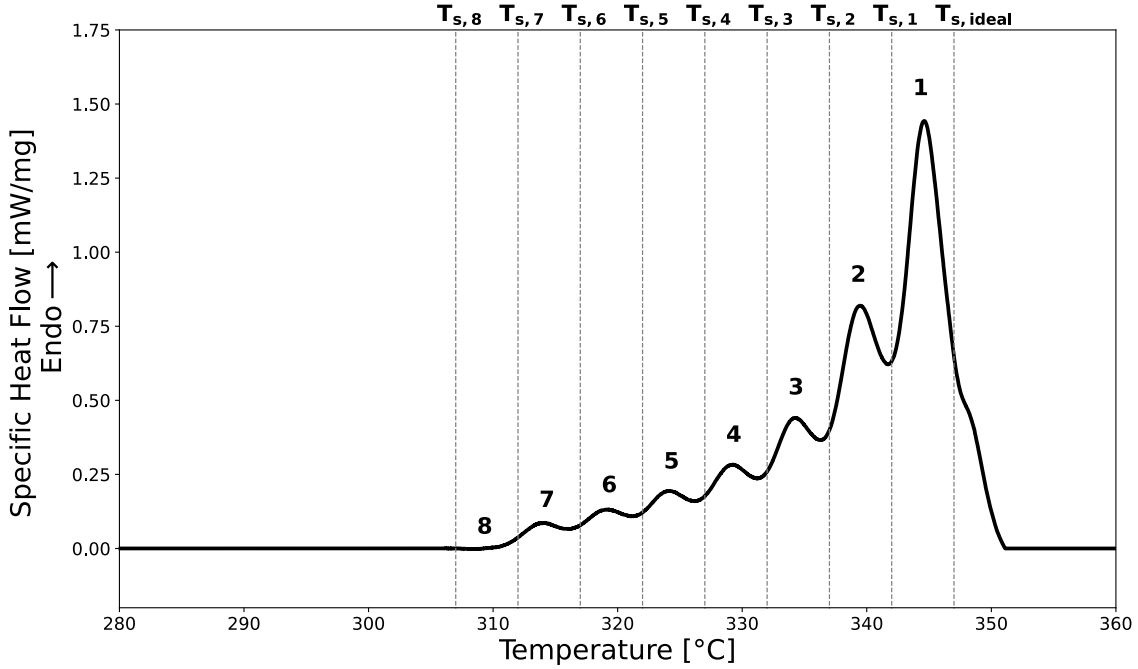

Fig. 74: Last heating step of the SSA process for PEEK neat.

In Fig. 74 the last heating ramp of the PEEK neat after undergoing the SSA protocol it is illustrated. Each peak corresponds to the thermal fractionation of the material, and the various heights are related to lamellae with increasing thickness from 8 to 1. Furthermore, as can be easily observed, each peak corresponds to the given T_s; thus, peak 1 corresponds to the crystalline phase grown during the 5 minutes held at $T_{s,1}$ and so on. For $T_{s,8}$, and thus peak 8, is practically not visible due to the low temperature to which the material is brought. The peak of greatest interest is peak 1, considering that it refers to the lamella most thickened during annealing.

To verify that the method was applied correctly and according to the guidelines proposed by Müller et Al. [84] it is possible to create a graph by placing the T_s chosen in the abscissas and the T of the corresponding peaks in the ordinates. Observing the graph in Fig. 75 the set of points forms a straight line, so it can be said that the method has been applied correctly.

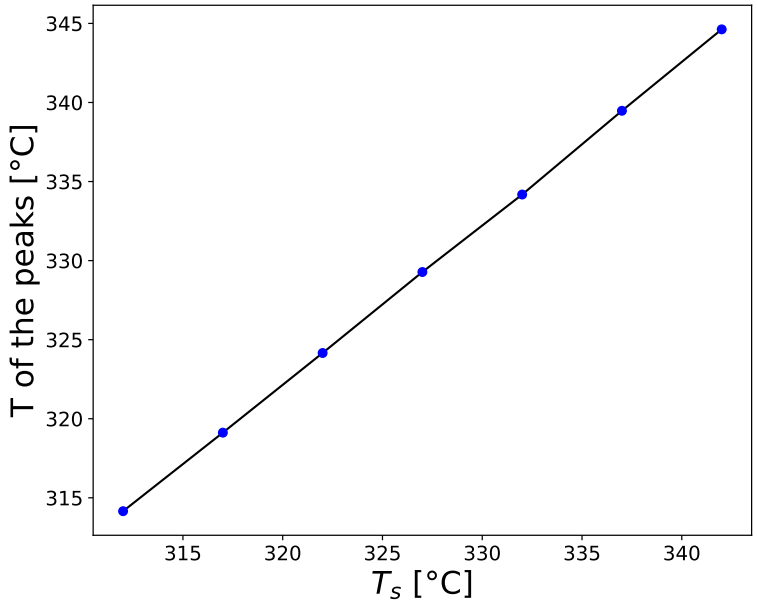

Fig. 75: T_s vs. T of the corresponding peak for verifying the correct application of the SSA protocol.

Returning to the application of the SSA protocol, by applying it to PEEK CF with the same values for the protocol, a direct comparison can be made as to whether the carbon fibres influence the annealing process.

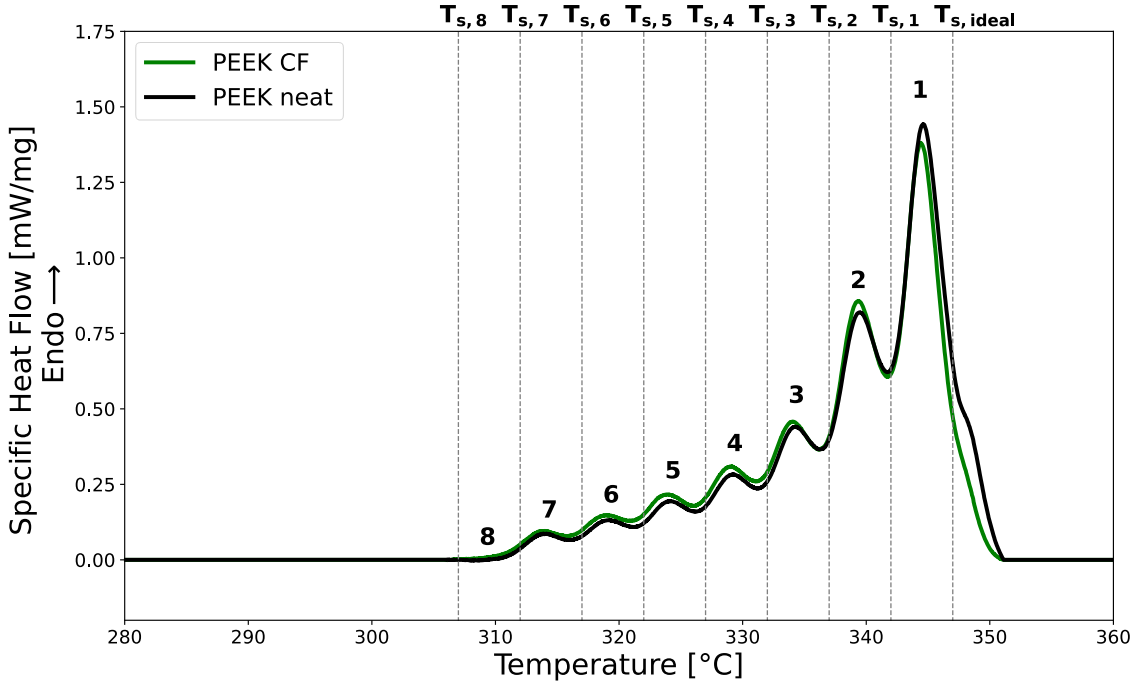

Fig. 76: Comparison of the last heating curves of SSA in PEEK neat and PEEK CF.

Observing Fig. 76 there is a difference in peak 1. In fact, the curve referring to PEEK CF presents a peak that is smaller than that of PEEK *neat*, confirming the fact that, in this case too, the presence of the carbon fibres has a negative influence on the crystallisation process of PEEK. Also in the annealing phase, the presence of the carbon fibres limits the growth of the crystalline lamella, thus creating a less thickened lamella than that formed with PEEK neat.

This finding is also confirmed by a direct comparison of the enthalpy related to peak 1 in both PEEK neat and PEEK CF. Considering the enthalpy of fusion of the crystalline phase of PEEK neat for peak $T_{s,1}$, it is 19.85 J/g. Comparing it with the corresponding figure for PEEK CF, which is 16.98 J/g, it can be deduced that, being smaller, the crystalline lamella is less thick.

2.3.14 Domain analysis in the self-nucleation of PEEK neat and CF

As a final analysis to complete the discussion on the crystallisation of PEEK, an extensive measurement campaign to identify all domains of self-nucleation was developed. Following the theory, the material's self-nucleation can be divided into three different domains, and depending on the temperature (T_s) analysed, the material's behaviour can be completely different. In domain I, i.e., at the highest temperatures, the crystalline phase is completely melted and thus the material is amorphous; in domain II, the material is in its state of self-nucleation, whereby crystalline phase is generated from the “memory” of crystals previously present; in domain III, the material exhibits both self-nucleation and annealing of crystals that have not completely melted, precisely because of the low temperature.

To identify the various domains, the protocol in section 2.2.3.7 was applied to obtain all possible material behaviours at varying T_s.

First, the reference curves (REF), i.e., non-isothermal heating and cooling, must be analysed, which in this work were carried out at 20 °C/min. In particular, the cooling curve is very important because the temperature value of its crystallinity peak indicates the transition between domain I and II. To best describe the various material behaviours, the results obtained for PEEK neat are shown in Fig. 77.

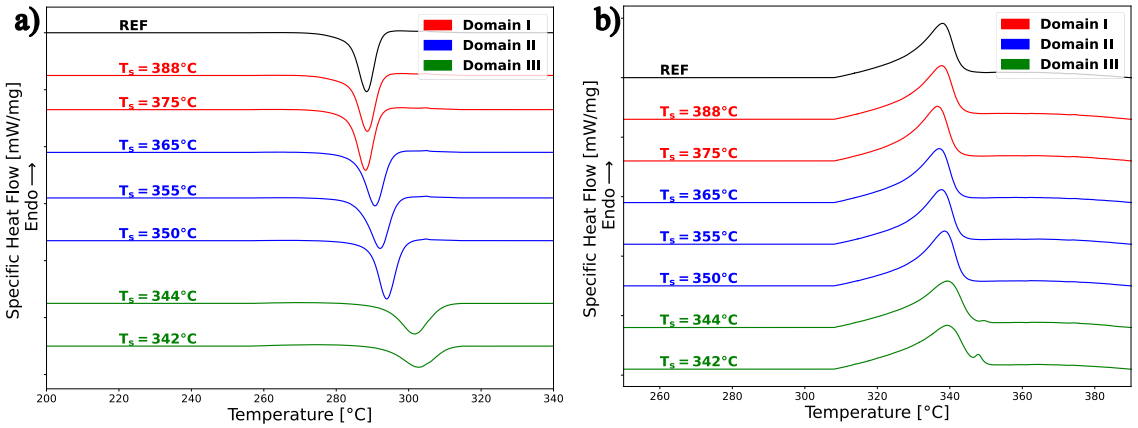

Fig. 77: Analysis of self-nucleation domains at varying T_s for PEEK neat- a) cooling curves; b) heating curves.

From Fig. 77a the difference between domain I and II are illustrated. From the literature [80] the transition between the first two domains occurs when the temperature of the crystallisation peak during cooling at T_s, is equal to that during non-isothermal cooling (i.e., REF). Considering the blue curves in Fig. 77a the peak temperatures are different from the reference temperature, so these temperatures are in the middle of domain II. Arriving at T_s of 375 °C, it can be observed that its peak temperature of 288.2 °C is practically equal to that of the REF peak, which is 288.5 °C (a deviation of up to 0.5 °C is acceptable and refers to the accuracy of the instrument), which is why the temperature of 375 °C marks the transition from domain I to domain II.

The heating curves (Fig. 77b) are needed to observe the comparison between domain II and III, and the process is identical to that was done for the identification of $T_{s,ideal}$ (already calculated in the previous paragraphs and equal to 347 °C for both PEEK *neat* and CF). As can be seen, the curves at 342 °C and 344 °C in the heating have a small second peak that is proper to annealing, so these two temperatures are fully contained in domain III. From these analyses, it is therefore possible to identify the three domains for PEEK neat, which are shown overall in Fig. 78.

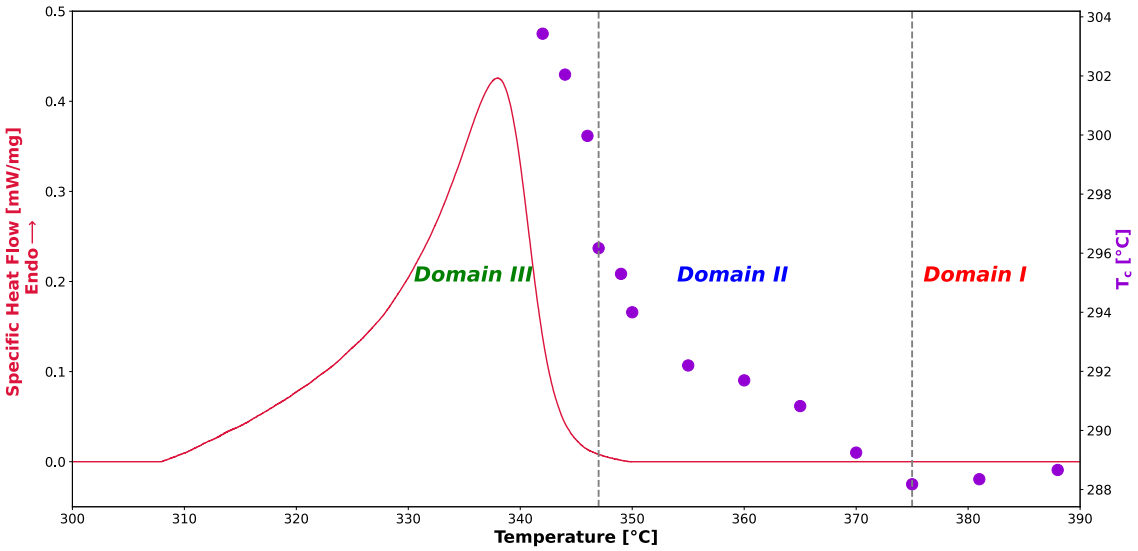

Fig. 78: Identification of the three domains for PEEK neat as the T_s and the peak temperature (T_c) of each T_s change.

From Fig. 78 the global crystallisation temperature trend of the cooling curves as a function of the T_s correlated to the reference heating curve can be observed, so as to find in which zone of the crystalline phase melting process, the various domains are positioned, beginning with the third, present on the right side of the peak, up to the first where the material can be considered completely melted and amorphous.

For PEEK CF, the results are shown in Fig. 79 e Fig. 80.

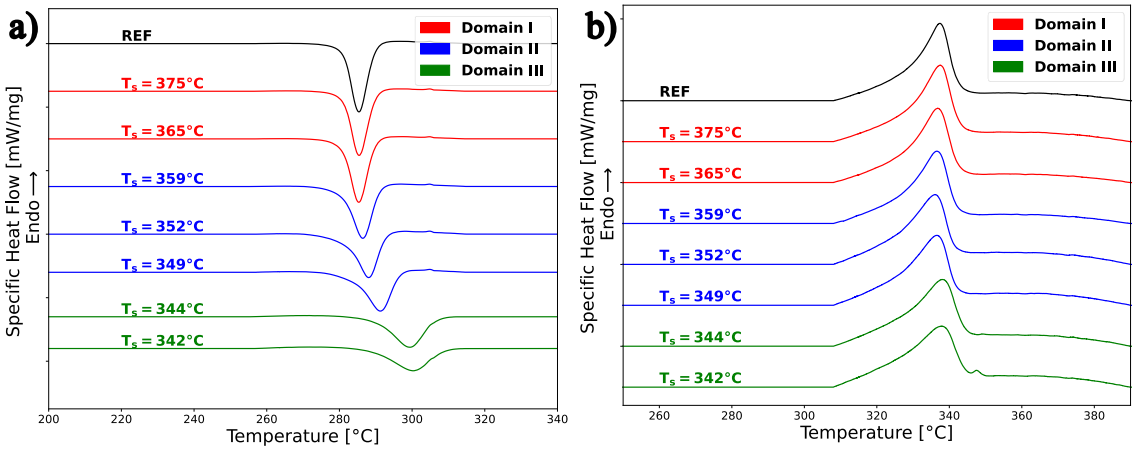

Fig. 79: Analysis of self-nucleation domains at varying T_s for PEEK CF- a) cooling curves; b) heating curves.

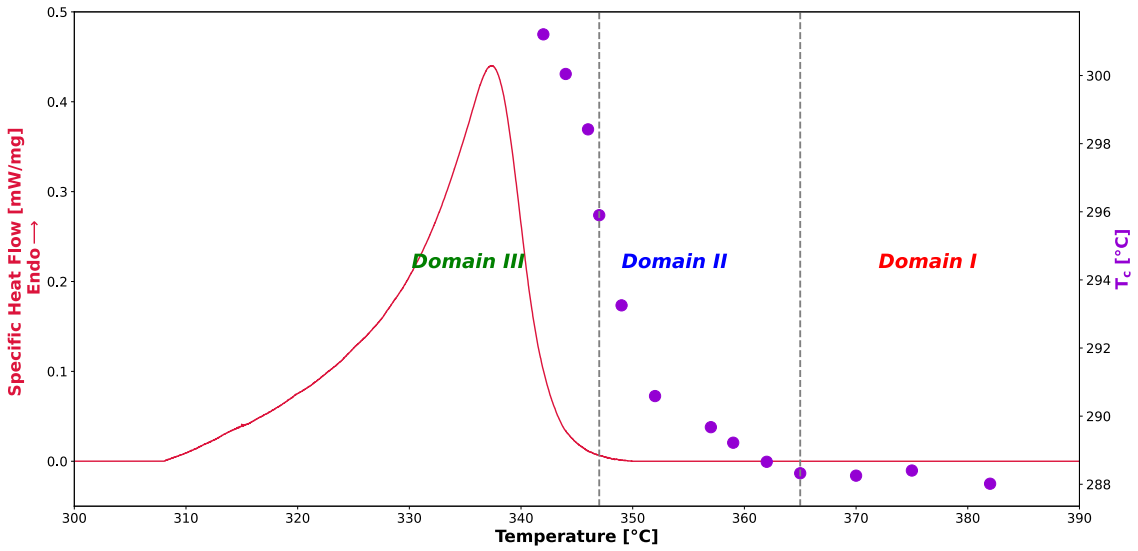

Fig. 80: Identification of the three domains for PEEK CF as the T_s and the peak temperature (T_c) of each T_s change.

The behaviour of PEEK CF is slightly different from PEEK neat, particularly regarding domains I and II. III is the same since, as explained in the previous paragraphs, $T_{s,ideal}$ is the same, and this can also be observed from the Fig. 79b where, from the green curves, the presence of the annealing peaks can be observed.

About the transition from domain I to domain II, in the case of PEEK CF the peak temperature equal to the reference temperature (285.5 °C) is obtained from a T_s of 365 °C, i.e., 10 °C less than PEEK neat.

2.3.15 Mechanical results

After all the studies on the kinetics of crystallinity and the influence of carbon fibres on the crystallisation of PEEK, tensile tests were carried out at varying crystallinity values. Due to the difficulty of controlling the exact temperature of the sample in the hot press, only three crystallinity values were evaluated. The first is the maximum degree of crystallinity, 27%, relative to a crystallisation temperature of 266°C (i.e., the temperature at which the sample was removed from the hot press and immersed in fresh water). The second is the minimum value of 0% crystallisation, obtained in a temperature range in which the material certainly retains its amorphous state. The last is a value in the range between the minimum and the maximum, i.e., 22%, corresponding to a crystallisation temperature of 276°C.

The results of the tensile strength and Young's modulus are showed in Fig. 81 and Fig. 82, respectively.

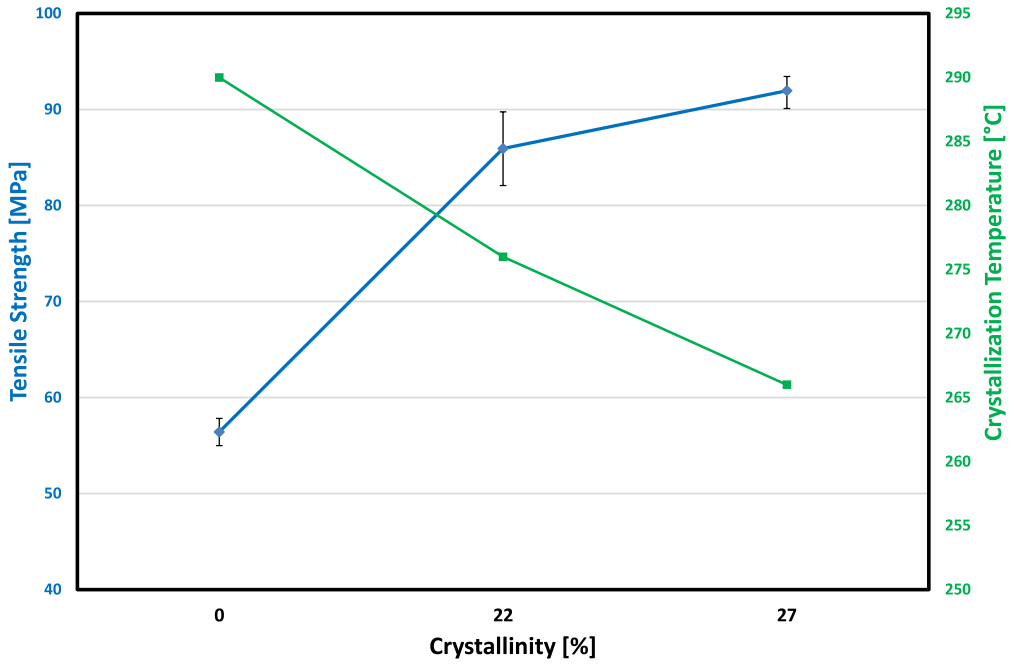

Fig. 81: Tensile strength varying the crystallinity and the crystallization temperature.

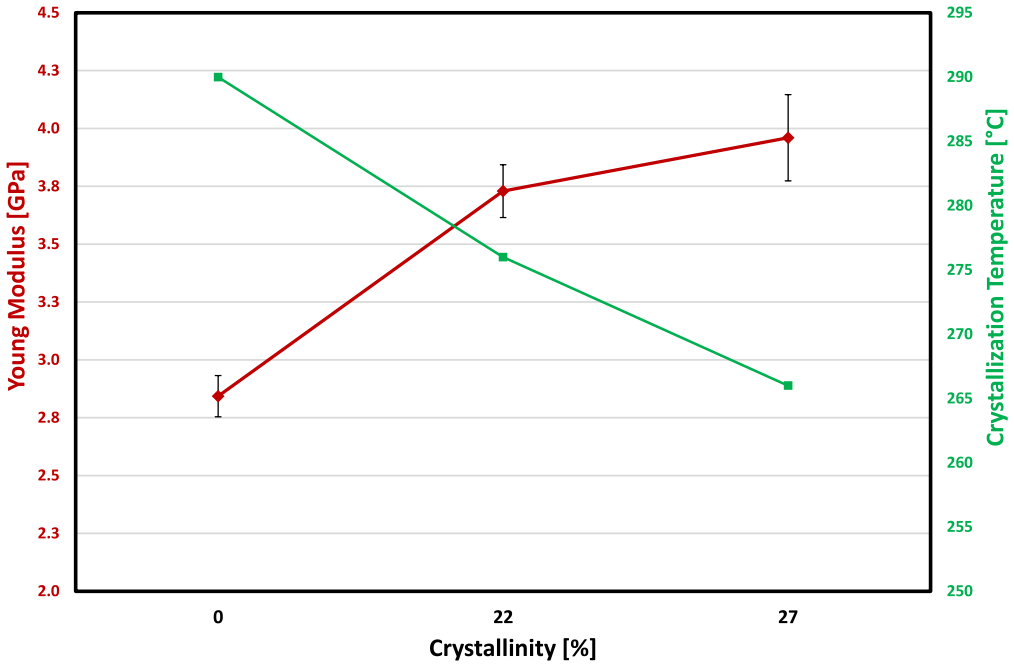

Fig. 82: Young's modulus varying the crystallinity and the crystallization temperature.

The modulus increases from 2.8 GPa to 4 GPa from 0% to 27% crystallinity, and the tensile strength from 56 MPa to 89 MPa. From 0% to 27% the tensile strength increases of +38.6% and the modulus of +28.2%. As the crystallinity value increases, the crystallisation temperature should decrease, while the mechanical properties of the material improve. As expected, crystallinity influences the mechanical properties of the material, so it is important to have these types of interpolated curves, because they can be

used in the same Abaqus model, seen in the previous paragraphs, by varying the crystallinity, a specific mechanical property can be linked to the crystallinity value.

2.4 Summary of the first part

In this first part of the PhD project, the crystallisation of the semi-crystalline PEEK, here considered as a matrix of the composite, was analysed in detail. This process directly influences the mechanical properties of the material, so it is important to analyse the process in detail to obtain its best performance. The PEEK crystallisation process was studied using a differential scanning calorimeter (DSC) by applying different temperature protocols to bring the material to those conditions favourable to developing crystalline lamellae. The entire process was studied, starting with nucleation and followed by growth, also applying indirect methods to assess the latter stage. In addition, all the various experiments were applied to both PEEK neat and PEEK CF, to assess the influence of carbon fibres (in the form of a bi-directional fabric) on the crystallisation process.

Once all the necessary experimental data had been obtained, it was decided to apply theoretical models, such as the Avrami model, to make a quantitative comparison on the ability of this material to form crystalline phase and on how carbon fibres could influence the process. Along with this model, a modification of it, the Dual Avrami, was applied to recreate, according to a theoretical equation, the curve of the material's total crystallinity as the isothermal crystallisation temperature and time varies.

This was done with the aim of creating a model in Abaqus capable of making a prediction of the crystallinity value after an isothermal process for given crystallisation temperature and time. Using Python scripts, the model was developed and, using a subroutine written in Fortran, imported into an Abaqus model (also written in Python).

The results reported here show that following the identification of the minimum crystallisation temperature and isothermal crystallisation for PEEK neat and PEEK CF, a significant slowdown in the crystallisation phase is observed in samples containing carbon fibres. Applying the Avrami model and calculating the overall crystallisation rate ($\tau_{50\%}$), a considerable decrease in the values in PEEK CF is observed at the same temperature. This is also evident in the subsequent application of the Lauritzen-Hoffman model, where by means of the parameters obtained from fitting the model, values of K_G^{τ} and σ_e were greater in PEEK CF ($7.724 \cdot 10^5\ K^2$ e $202.83\ \frac{erg}{cm^2}$), than the same in PEEK neat ($5.027 \cdot 10^5\ K^2$ e $132.11\ \frac{erg}{cm^2}$), and that was an indication that indeed the presence of the carbon fibres contributes to slowing down the overall crystallisation process.

Moreover, observing the anti-nucleating influence of the carbon fibres, the continuation was the studies on the crystal growth phase alone. To do this, the property of self-nucleation was exploited, by calculating the $T_{s,ideal}$, i.e., the temperature at which the maximum number of crystals is formed and thus all subsequent isothermal processes lead to the growth of already nucleated crystals alone. For both PEEK neat and CF, the $T_{s,ideal}$ was found to be 347 °C and analysis of the isotherms following self-nucleation shows that even in the growth of the crystalline phase alone, the presence of the carbon fibres slows down the process. Furthermore, by applying a thermal fragmentation of the crystal formation (SSA), less crystal growth is observed in the PEEK CF specimens.

In support of the tests on the anti-nucleating behaviour of carbon fibres, the calculation of the nucleation efficiency between PEEK neat and PEEK CF was performed, and it is equal to -32.2%, a clear indication that the presence of the carbon fibres in the specimens causes an anti-nucleating effect.

Finally, the entire self-nucleation process was analysed to obtain the complete picture of the various domains of both PEEK neat and PEEK CF.

As far as the model for predicting crystallinity is concerned, since the Single Avrami does not reproduce very accurate curves, the Dual Avrami model was applied, which approximates very well the experimental trend of the crystallinity value as a function of time. Thanks to this equation, it was possible to create a model on Abaqus that faithfully reflects the trend over the range of crystallisation temperatures investigated, a sign of the model's reliability.

The mechanical properties as the crystallinity value changes were analysed to determine the behaviour of them with the crystallinity value. These curves are useful due to the possibility of entering them into the Abaqus model and linking the crystallinity value obtained to the exact value of the mechanical properties. As expected, as the crystallinity value increases, the crystallisation temperature should decrease, while the mechanical properties of the material improve. By moving from PEEK in the amorphous state to the maximum crystalline form, the tensile strength increases by +38.6% and the Young's modulus by +28.2%.

In conclusion, it can be stated that thanks to this extensive experimental campaign, it was possible to evaluate the entire crystallisation process of the composite matrix, so as to obtain all the information relating to the formation of the crystalline phase and also how the presence of the carbon fibres affects the process, so as to recreate a predictive model in Abaqus that can more accurately reflect the reality of the process and in addition predict the mechanical characteristics of the material as the crystallinity changes.

Chapter 3: Second Part - Metal-Composite Interface

3.1 Literature analysis of the second part

3.1.1 Fibre Metal Laminates

Fibre metal laminates (F*ML*) are special hybrid materials composed of alternating metal sheets and polymer matrix composite material. They have been devised since the 1980s with the aim of enhancing the advantages of each component and mitigating its defects. Compared to monolithic metals and traditional composite materials, FMLs have several advantages, including high specific strength and stiffness, high strength-to-density ratio, flame and corrosion resistance, and excellent fatigue strength [80-84].

FMLs are classified primarily according to the type of fibre reinforcement of the composite substrate and metal:

- ARALL - Aramidic Reinforced ALuminium Laminates.
- GLARE - GLAss REinforced laminates.
- CARALL - CArbon Reinforced ALuminium Laminates.

However, the classification can be considered broader, as the characteristics vary depending on many other factors, such as surface treatments, layering of materials, orientation of the fibres in the composite and the choice of fibre and matrix.

ARALL was historically the first FML to be produced by Delft University. It consists of aircraft-grade aluminium alloy sheet and epoxy matrix composite reinforced with aramid fibres. Thanks to its constituents, it has a high resistance to impact and torsional and tensile stresses, as well as high hardness, low thermal conductivity, and high dimensional stability. On the other hand, it presents considerable processing difficulties and high costs.

CARALL is a FML obtained from the layering of epoxy matrix composites reinforced with carbon fibres and aluminium alloy sheets. The main peculiarity of this FML is its excellent impact resistance due to the combined effect of ductility conferred by the aluminium layer and rigidity given by the carbon reinforcement. However, one of the main disadvantages of this material is the possibility of obtaining galvanic corrosion. Due to the electrical conductivity of the carbon fibres, even though the presence of the epoxy matrix acts as an insulator, if the fibres met the aluminium alloy, electrical contact would occur, leading to very dangerous localised corrosion phenomena. For this reason, treatments must be carried out on the metal layer to prevent this phenomenon. [97].

GLARE is the best known and most widely used FML in the aviation industry, thanks to its application in the Airbus A380 aircraft on two large sections of the fuselage and on the leading edges of the horizontal tailplane (Fig. 83) [98].

Fig. 83: Materials used on Airbus A380-800 [98].

Commercial GLARE are classified into six categories according to the thickness of the metal substrate, the type of metal alloy (whether 7-series or 2-series aluminium) or the orientation of the reinforcing fibres in the composite substrate.

The reinforcement fibre used is structural glass (S2-Glass). Unlike other types of glass fibre (e.g., E-Glass), it has a high tensile strength and elastic modulus. The acronym *S2* indicates that the fibre has high strength, but unlike simple S-glass it has a lower cost.

All these FMLs now commonly used in the aircraft industry have a limitation related to the maximum operating temperature. In fact, both the use of aluminium alloys, but the use of epoxy matrix, cannot withstand high values.

For this reason, a possible solution could be to substitute the metal substrate with titanium alloys and the composite side with thermoplastic matrices such as PEEK, to achieve high thermal resistance and increase the applicability range of these materials.

3.1.2 Titanium and its alloys

Titanium was discovered in 1791 by the British chemist William Gregor, who detected its presence in ilmenite, a mineral found in lava rocks. A few years later, the German chemist M.H. Klaproth succeeded in isolating the same metal from rutile ores and inspired by Greek mythology, named it as the Titans because of its extraordinary mechanical properties. However, 99.9% pure titanium was first prepared at the beginning of the 20th

century, but it did not become industrially widespread until the end of the Second World War.

In nature, titanium does not exist in a pure state [99] It must therefore be extracted from ores; the most common method of doing it is the so-called Kroll process: this is a pyrometallurgical process that, starting from the ore (ilmenite or rutile), yields $TiCl_4$, titanium tetrachloride and, subsequently, by means of an oxidation-reduction process with magnesium, titanium sponge is obtained, which is then converted into molten metal by vacuum processes.

Titanium is the fourth most abundant structural element in the Earth's crust, preceded only by aluminium, iron and magnesium [99] , and owns the following properties:

- Low density: equal to 4500 kg/cm^3.
- High mechanical strength.
- Elastic modulus of 115GPa.
- High melting temperature (1668°C).
- High resistance to corrosion and erosion.
- Low thermal and electrical conductivity.
- High resistance to cavitation and shocks.
- Biocompatibility.

It is an allotropic element with two crystallographic forms:

- Phase α → from room temperature up to 882°C, it has a compact hexagonal structure (EC) that gives it limited ductility.
- Phase β → from 882°C up to the melting temperature, it possesses a body-centred cubic structure (CCC) that gives it high ductility.

The temperature of 882°C is called β-transus, defined as the lowest equilibrium temperature at which 100% β-phase occurs.

It is possible to distinguish between commercially pure titanium and titanium alloys. There are four types of commercially pure titanium classified according to the number of impurities. They are referred to as "grades" and have high corrosion resistance [100,101]. Grade 1, specifically, is the one with the lowest level of impurities.

From grade 5 onwards we speak of titanium alloys. They are classified according to microstructure and alligators (*Fig. 84*).

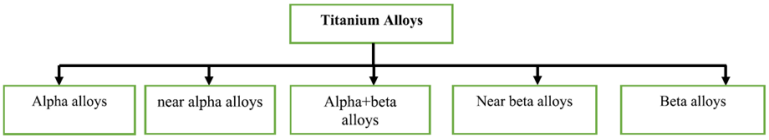

Fig. 84: Titanium alloy classification.

α-alloys contain *α*-stabilising elements, such as aluminium, nitrogen and oxygen, which increase the transformation temperature from the α phase to the β phase, making the α phase stable even at temperatures higher than the transition temperature.
Conversely, β-stabilising elements, such as vanadium, chromium, and molybdenum, make the β-phase stable even at lower temperatures than the β-transus.
Finally, elements such as tin and zirconium behave almost neutrally, causing only a slight decrease in β-transus temperature.
Near α-alloys contain less than 5% β phase; they are less corrosion-resistant than unalloyed titanium; however, they exhibit excellent ductility and good weldability. Near α-alloys contain small amounts of β-phase, which confer high creep resistance and good fracture toughness.
β and near β alloys have β-phase percentages of more than 20 per cent; they are rich in β-stabilising elements, which is why they have higher densities than their predecessors. They also exhibit excellent forgeability and high hardenability.
α+β alloys contain both stabilising α-elements and stabilising β-elements. Compared to α-alloys, they are characterised by higher mechanical strength, are heat-treatable, but have lower creep resistance and formability [100,102].

3.1.2.1 Alloy Ti-6Al-4V

To the α+β category belongs the Ti-6Al-4V alloy (Grade 5), consisting of titanium (90%), aluminium (6%) and vanadium (4%); the aluminium stabilises the α phase that contributes to the high strength; the vanadium stabilises the β phase that is responsible for the good ductility and fracture toughness. This alloy has an excellent combination of impact, fracture, and fatigue strength, with impressive ductility and weldability. It also enjoys good thermal and electrical conductivity and excellent corrosion resistance. This alloy possesses strength equal to that of steel and twice that of aluminium and has a density half that of steel itself [103].
These characteristics make Ti-6Al-4V alloy the most widely used alloy in aerospace and it is finding ever-increasing applications; it is used in fuselage, to prevent the propagation of fatigue cracks, in aircraft thrusters, in helicopters and even in space applications [104].

3.1.3 Aluminium and its alloys

Aluminium is one of the most widespread elements on earth and is often found combined with other elements. It is produced industrially from an ore called bauxite by the Bayer

process. Its basic characteristics, which have enabled its large-scale production and use, are:

- Low density, about one third that of steel.
- High electrical and thermal conductivity.
- High ductility, which is maintained even at low temperatures due to its face-centred cubic crystalline structure (CFC).

Its mechanical characteristics are considerably improved by adding alloying elements or alligators. There are various types of aluminium alloys, categorised in 8 series according to the type of main alloying element (*Tab. 5*).

Tab. 5: Main alligators and series of aluminium alloys.

Series	Composition
1XXX	Aluminium with a minimum purity of 99.00%.
2XXX	Al-Cu alloys
3XXX	Al-Mn alloys
4XXX	Al-Si alloys
5XXX	Al-Mg alloys
6XXX	Al-Mg-Si alloys
7XXX	Al-Zn alloys
8XXX	Al alloys with other elements (e.g., Lithium)

The alloys mainly used in aerospace are those of the 2000, 6000 and 7000 series, but those of the 5000 series also find some uses.

- 2xxx Series (Avional): These are alloys that need heat treatment (solution heat-treatment, hardening and ageing) to have adequate mechanical properties. They have poor corrosion resistance and therefore require protective systems. They are used in structural applications where a high strength-to-weight ratio is required.
- 5xxx series (Peraluman): these alloys can only increase their mechanical properties by hardening, as magnesium is very soluble, second only to zinc, so for concentrations below 7% it does not precipitate. The presence of magnesium also provides excellent corrosion resistance, even in a marine environment, so they are widely used in that sector. In addition, they own high ductility, which is why they are easily machined by plastic deformation, and excellent weldability, although they have lower mechanical properties than the 2xxx series.

- 6xxx series (Anticorodal): this series has intermediate mechanical properties, but still below the 2000 series. It has good weldability, corrosion resistance and can increase its mechanical characteristics through heat treatment. In addition, the presence of silicon decreases the intergranular corrosion that is typical of this alloy.
- 7xxx Series (Ergal): the presence of zinc in the alloy gives it the highest tensile strength of all aluminium alloys. This characteristic allows it to be used in highly stressed structures, even though it may be exposed to stress corrosion, because of which specific treatments are necessary. Finally, its mechanical properties can be enhanced through heat treatment.

Aluminium alloys can achieve rather higher mechanical properties than pure aluminium (i.e., aluminium series 1) since the alloying elements generate intermetallic particles capable of blocking the movement of dislocations. Thus, while the use of aluminium alloys is preferable to pure aluminium, they have worse corrosion resistance. The presence of intermetallic particles, indeed, plays a double role, since, depending on their chemical nature, they have different equilibrium potential values than those of aluminium, thus triggering localised corrosion phenomena, such as intergranular corrosion. Furthermore, the presence of intermetallic particles does not allow, unlike aluminium, the formation of a homogeneous and electrically insulating passive Al_2O_3 film of about 1-2 nm, which provides good corrosion resistance. For this reason, aluminium alloys are not used without a coating to increase their corrosion resistance. One of the strategies is anodising, a process that allows the growth of a coating consisting of an anodic barrier oxide layer (in the order of hundreds of nm thick) and a porous layer (in the order of microns) with the aim of protecting the underlying metal substrate. The anodising processes are followed by post-anodising processes such as hot water sealing to cover the pores and further increase corrosion resistance. [41].

3.1.3.1 Aluminium alloy 7075

This alloy, part of the 7-series, is widely used in aerospace, especially in structural parts requiring high strength. It was historically the first to be developed around the 1940s and the most widely used is 7075-T6, i.e., the one that has undergone an artificial solution hardening and ageing treatment. It contains zinc as the major alligant, followed by magnesium and copper, and it is thanks to the combination of these alligants that it possesses the highest mechanical strength values among aluminium alloys. On the other hand, it possesses a lower resistance to crack advancement than, for example, alloy 2024,

so that over the years various new alloys have been developed to improve this behaviour, such as aluminium alloys with the addition of lithium.
It has applications in a variety of aerospace components such as wings and fuselage, aircraft supporting structures, missile parts, gears, shafts, etc. [94-98].

3.1.4 Joints

Complex shapes and the search for high performance in modern structures lead to an increase in the use of different materials and constant changes in geometry, making the use of monolithic parts difficult. For this reason, the use of joints between the various parts is indispensable, even if they become the weakest element of the system. This may be the case with FMLs, which are not true joints, but suffer from the same weaknesses.
In general, joints can be divided into two types:

- Bonded joints: stress is exchanged at the surface where the adhesive is present and are mostly shear stresses.
- Mechanical joints: the stress is transmitted through a third element (rivet, bolt, etc.) and the stress is usually compressive on the latter.

There are also so-called mixed (adhesive-mechanical) joints that combine the two types.

3.1.4.1 Bonded joints

Bonded joints are formed by a polymer adhesive that joins two substrates. There are many different types of adhesives. In the structural field, adhesives must be used that allow for proper load transfer between the two substrates, and among the most common are epoxy-based adhesives. They are often used to join thin substrates or when the addition of rivets or bolts makes the structure too heavy. They are also widely used in composite repairs.
Of course, the main advantage is that they offer an even load distribution without any stress concentration, the joints are lighter than mechanical ones, resist fatigue crack propagation well, and stiffen the jointed area so that the buckling resistance of the structure increases by 30-100%.
On the other hand, they are permanent joints, proper surface treatment is essential, adhesives are susceptible to atmospheric conditions, and must be stored according to the manufacturer's specifications before being used, thus increasing running costs.
The stress to which the bonded joint is subjected is shear. The distribution has a constant trend along most of the bonded zone and then increases with a peak in the extreme zones (Fig. 85) [110].

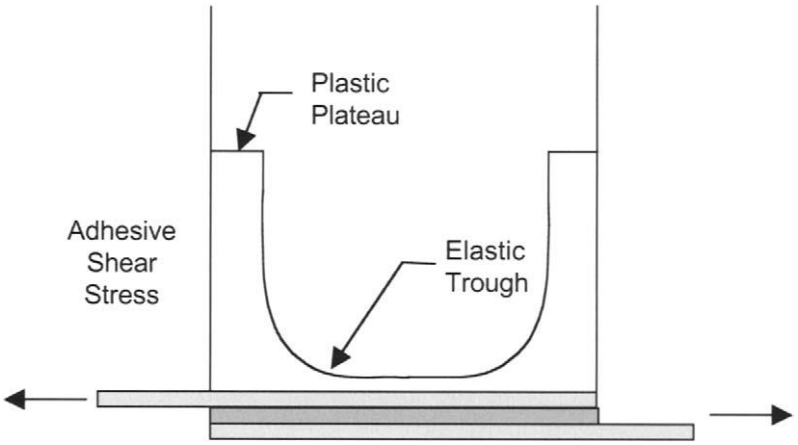

Fig. 85: Typical shear stress distribution along the bond.

Bonded joints can fail in several ways, some of which are acceptable and others to be avoided. Certainly, the most common are cohesive failure, when fracture occurs within the adhesive; adhesive failure, when fracture occurs at the interface between adhesive and substrate (to be avoided because it means that adhesion has not taken place in the best way); and, finally, fracture of one of the two substrates. The latter mode of fracture is the one to be pursued when designing and constructing a joint. In Fig. 86 the most common failure modes of bonded joints are schematised.

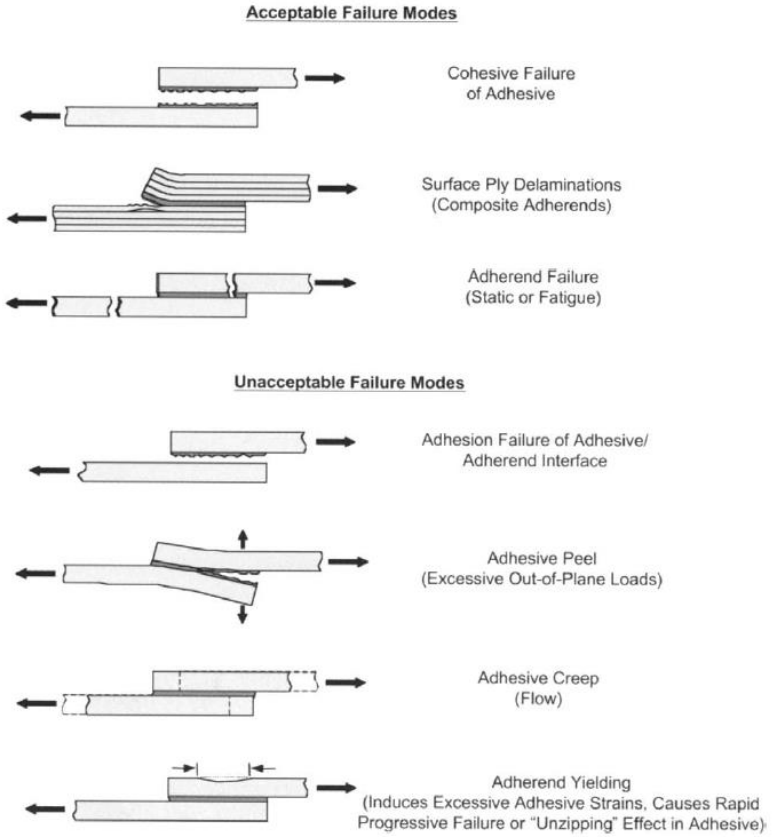

Fig. 86: Typical failure modes of bonded joints.

The adhesive to perform the bonding can be a third element, especially when the substrates are metallic, or it can be the matrix of the composite itself, the latter case is called co-cured joint. This type of bonding certainly involves an increase in complexity during the manufacture of the structure, which increases its cost, but it results in a structure with fewer joints, lesser discontinuities, and smaller number of parts. FMLs can also be considered as co-cured bonded joints.

3.1.5 Surface treatments

The most important part of the FML to consider improving the mechanical performance of the material is the interface between metal and composite. By their conformation, as mentioned in the previous paragraphs, FMLs are true *co-cured* bonded joints where the composite matrix also acts as an adhesive. For this reason, surface treatments, especially on metal, play a fundamental role in guaranteeing high material performance.

They can be divided into three macro categories: mechanical, chemical or electrochemical.

Mechanical abrasion is the simplest, only increasing the surface roughness by abrasive paper or sandblasting. The increase in surface roughness extends the effective bond length and promotes mechanical interlocking with the adhesive. Mechanical treatments also include those in which the surface modification is carried out by laser.

Laser treatments consist of modifying the surface by means of a texture created with the laser itself. An example is given by Romoli et al. [111] who studied different textures, modifying the depth of the groove excavated by the laser, and showed that creating grooves that are too deep worsens the strength compared to shallower grooves. This is because, if the groove is too deep during adhesive deposition, trapped air remains and becomes embedded in the resin, decreasing its mechanical characteristics. Therefore, it is preferable to create grooves whose ridges are higher than the valleys, to increase the surface roughness, and therefore the strength of the joint, and to avoid air being trapped.

Chemical treatment can be carried out by immersing the substrate in an acid solution (acid etching) to obtain a surface that is both rough and with pores of microscopic size, which are useful for *interlocking* with the resin. The most used acid baths are Forest Product Laboratory (FPL) and sulpho-ferric (P2) etching. It has been demonstrated in literature that these treatments alone do not guarantee good joint strength or durability [112]. Therefore, they are usually combined with an electrochemical treatment known as anodising, which will be discussed in detail below.

Chemical treatments include the ones with silane coupling agents. These are carried out by spraying or soaking the substrate in a solution of ethanol, water, and silane. The most commonly used are silanes that have an amine or epoxy functional group at one end, such as (3-Aminopropyl)trimethoxysilane *and* (3-glycidyloxypropyl)trimethoxysilane. The solution in which the silane is found is made acidic to promote the hydrolysis of the methoxy groups of the silane (OCH_3), which become siloxanes (Si-OH), so that they are reactive towards the substrate to be treated (aluminium, titanium, glass, or carbon fibres, etc.). On the other hand, the functional groups at the ends (e.g., amine-NH_2, epoxy or a C=C double bond) remain free to form bonds with the polymer matrix (or adhesive), increasing the tensile strength of the joint. In Fig. 87 a typical reaction between an amine silane, a basalt fibre substrate and a polymer matrix is shown [102-104].

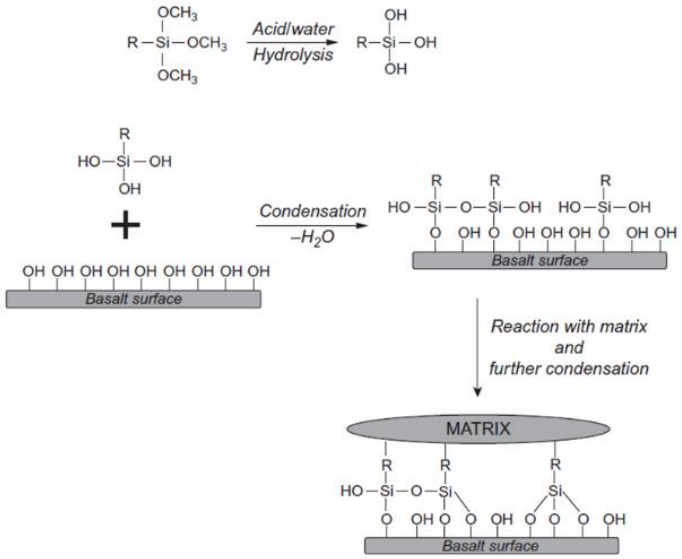

Fig. 87: *Chemical reaction of silane in solution, post fibre immersion and matrix deposition.*

As far as electrochemical treatments are concerned, the most used are anodising. Anodising is a process through which it is possible to thicken the oxide film on the surface of a metal, such as aluminium, titanium, zirconium, and others. This process involves the use of a galvanic cell consisting of an anode, i.e., the metal to be anodised, and a suitable counter-electrode or cathode that can be made of platinum, aluminium, or steel.

The properties of the oxide film obtained are a function of the bath composition and of three fundamental factors: time, temperature, and potential.

For aluminium alloys, among the most widely used electrochemical anodising treatments is chromic acid anodising (CAA), which guarantees high joint strength and excellent corrosion resistance, although efforts are now being made to abolish it due to the carcinogenicity of chromium VI.

A viable alternative to chromic acid anodising is phosphoric acid anodising (PAA). It guarantees high joint strengths, so much so that the process has been standardised [116], but provides the substrate with low corrosion resistance.

There are also others anodising in different acid solutions such as sulphuric acid (SAA), boric sulphuric acid, boric sulphuric-phosphoric acid, or tartaric sulphuric acid (TSA) or phosphoric sulphuric acid (PSA) [106-108].

As far as titanium alloys are concerned, the peculiarity of their anodic oxidation also lies in the possibility of imparting different colours to the surface, which are a function of the oxide thickness and the potential applied, colour variations from violet to blue, yellow, and finally bronze are observed [120,121].

In addition, by a solution containing fluorides in the anodic oxidation process, it is possible to obtain a surface consisting of titanium oxide nanotubes. The electrolytic solution contains a mixture of deionised water and ethylene glycol, the anion can be fluoride, bromide, chloride with different concentrations. The process can be potentiostatic, galvanostatic, potentiodynamic or galvanodynamic.

In the case of the potentiostatic process, a uniform and organised surface of nanotubes is obtained. The nanotube accretion process can be divided into three stages:

- formation of titanium oxide.
- dissolution of the oxide due to the application of the electric field.
- chemical dissolution of the oxide and titanium due to the presence of the fluoride ion.

Nanotubes grow perpendicular to the surface, from the bottom to the top.

As shown in Fig. 88, each nanotube is composed as follows: a titanium substrate, a fluoride-rich layer (FRL), an inner shell containing electrolyte elements (IST) and a compact outer oxide zone (OST). It is evident that the nanotubes do not have a uniform thickness: as can be seen from the figure, the zone called IST becomes thinner towards the top of the nanotube, because the fluoride ion attacks the walls and reduces its thickness [122,123].

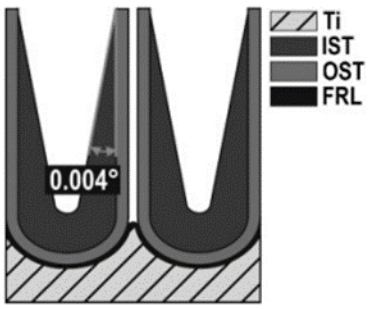

Fig. 88: Schematic representation of titanium nanotubes.

In general, anodic oxidation, in the case of a porous structure, but also in the case of a nanotube structure, provides a microstructural change that gives the material better resistance to corrosion and greater wettability with the adhesive.

3.1.5.1 Wettability and adhesion

Wettability is the ability of a liquid to spread effectively on a solid surface. As a preliminary step in assessing the wettability of a surface, contact angle tests can be performed, which give an indication of the surface tension of a solid.

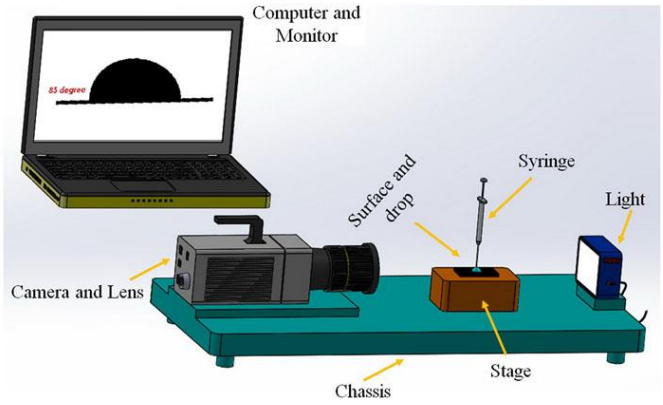

Fig. 89: Instrumentation for contact angle measurements [124].

The instrumentation in Fig. 89 uses the sessile drop method, it consists of: a light source, a support on which the sample is placed (stage), a syringe for depositing the drop of liquid and an image acquisition system (camera and lens), which is then analysed by dedicated software.

The contact angle is a quantity that estimates the wettability of a surface and can therefore be used as an index to assess the adhesion between, for example, a polymer and a metal during the production of the adhesive joint.

When a drop of liquid is released onto the surface of a metal, a zone is created where three surfaces coexist in three different states: the solid material, the liquid in the drop and the gas surrounding the two. Young was the first to discover the balance between these three phases by producing the so-called Young's equation (Eq.(29))

$$\gamma_{SV} = \gamma_{SL} + \gamma_{LV} \cos \theta_Y \tag{29}$$

Where γ_{SV} is the interfacial tension between solid and gas, γ_{SL} is the interfacial tension between solid and liquid and γ_{LV} between liquid and gas. θ_Y is Young's contact angle.

The greater the contact angle, the greater the wettability of the system. It can vary between 0°, when there is perfect wettability, and 180° when there is no wettability. The greater the wettability, the greater the hydrophilic behaviour of the material; conversely, it can be defined as hydrophobic behaviour (Fig. 90) [125].

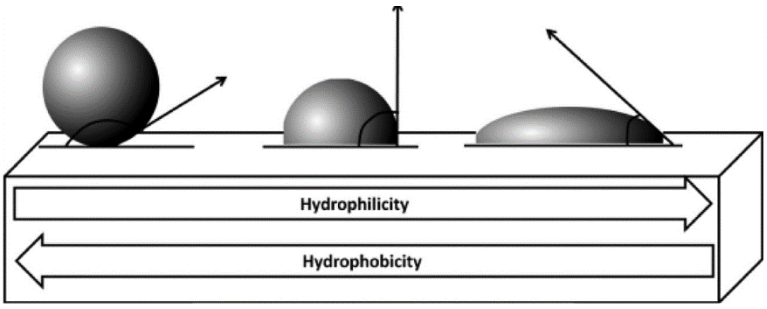

Fig. 90: Contact angle variations on a surface.

After confirming whether the wettability between the two substrates is good or not, to ensure good adhesion is important to consider what type of bond is established between the molecules of the liquid and the solid surface. Thus, three main types of bonds can be distinguished:

- Mechanical bonding: i.e., due to the surface roughness of the solid and the viscosity of the liquid. The higher the surface roughness, the more places the liquid can enter and thus increase adhesion, obviously this must be allowed by a viscosity that is not too high.
- Electrical bonding: this is the weakest bond, due for example to dipoles creating electrostatic interactions.
- Chemical bonding: presence of chemical elements that enable the bonding between the molecules of the liquid and the substrate.

For example, when different surface treatments are considered, adhesion will depend on all these factors, and therefore the morphology of the substrate and its chemical conformation must always be considered to have complete information on the wettability of the material [126]. Looking at this concept from another point of view, when designing a new surface treatment, to achieve the best treatment these concepts should be evaluated. For example, it is possible to modify the chemistry of the surface with a silane treatment or chance the surface morphology with anodising treatments, improving the mechanical interlocking.

3.1.6 Anodising

Anodising is an electrochemical process by which an oxide layer can be increased on the surface of metals such as aluminium, zirconium, titanium, tantalum, etc., known as valve metals. These, due to their low electrochemical potential, react easily with water or oxygen to form a dense, protective film of passivity. The name, valve, comes from early electronic researchers who observed the ability of the enhanced oxide layer to convert alternating current into direct current.

In general, the anodising process consists of circulating current within an electrolytic cell, where the metal to be anodised acts as the anode (positive pole). Negative ions, mainly from the dissociation of oxygen, migrate towards the anode, oxidising it and thus forming the metal oxide on the surface. The characteristics of the oxide, such as thickness or crystalline or amorphous nature, are easily controlled by process parameters (such as time, temperature, and voltage), while the type of solution affects the composition of the oxide, such as the introduction of chemical species into the layer. Another key factor is the pH of the solution, which determines whether the oxide layer will be a compact or porous layer [127].

3.1.6.1 Growth of a compact anodic film

A compact anodic film, called a barrier film, is ideally non-porous, uniform in thickness, characterised by high ionic and electronic conductivity and high electric field strength. The growth of the barrier film occurs mainly through the migration of metal ions and oxygen within the layer, which is only made possible by the presence of a high electric field. Many researchers during the last century have studied models to calculate the ionic current density within the film [128].

Guntherschulze and Betz [129] in 1934 showed that the ionic current density is exponentially related to the electric field strength according to Eq.(30).

$$i = i_0 e^{\beta E} \tag{30}$$

Where i_0 and β are material-dependent constants and E is the electric field strength in the oxide, dependent on the potential drop and film thickness (Eq.(31))

$$E = \frac{\Delta U}{D} \tag{31}$$

Eq.(30) defines the so-called high-field pattern of oxide layer formation in valve metals. The potential difference is guaranteed by an external circuit, which can: keep the current constant (galvanostatic), make the potential difference grow linearly over time (potentiodynamic), or keep the potential difference constant (potentiostatic). In the galvanostatic and potentiodynamic case, during the growth of the layer, the potential difference increases to keep the electric field strength constant. It increases until the so-called breakdown potential is reached (U_e), i.e., the value that leads to the oxide layer breaking down, with the formation of visible sparks, fractures or burns. The breakdown potential depends on the properties of the metal and the composition of the bath and can be calculated using Eq.(32).

$$U_e = A + B \log \rho_e \tag{32}$$

A and B are constants that depend on the composition of the bath and the metal, and ρ_e is the resistivity of the electrolyte.

In accordance with Pringle's study [130], during the growth of the oxide layer, the metal and oxygen from the electrolyte are separated from their reaction products. For them to react, it is necessary for the ions, M^{z+} and O^{2-} , to move within the oxide layer, according to the high field mechanism described by Eq.(30). There are five possible ways in which the two species can react to form the oxide:

1. Only metal cations migrate and increase the oxide at the film/electrolyte interface.
2. Only oxygen anions migrate, increasing the oxide at the interface with the metal.
3. They both migrate, cations and anions, and the oxide grows simultaneously at both interfaces.
4. They both migrate and grow from within the layer.
5. They both migrate and growths 3 and 4 occur simultaneously.

Anodising, and thus also the migration of ions, occurs through the passage of current within the cell using an external current and voltage source and mediated by the three possible modes described above: galvanostatic, potentiostatic, potentiodynamic.

The total current can be calculated with the sum of the ionic current (i_{ion}), electronic current (i_{el}) flowing within the oxide layer, and the dissolution current (i_{diss}) of the oxide layer depending on the pH of the solution.

$$i_{tot} = i_{ion} + i_{el} + i_{diss} \tag{33}$$

Furthermore, an efficiency η can be defined (Eq. (34)) that for many valve metals reaches almost 100 %, due to the high electrical isolation of the oxide layer ($i_{el} \approx 0$) and due to the thermodynamic stability of the oxide even in large pH ranges.

$$\eta = \frac{i_{ion}}{i_{tot}} = \frac{i_{ion}}{i_{ion} + i_{el} + i_{diss}} \tag{34}$$

3.1.6.2 Growth of a porous anodic film

Porous anodic films are composed of a thin barrier layer and a much thicker, but porous layer; the pores are cylindrical and evenly distributed over the surface (Fig. 91). For such a film to be produced, the nature of the bath must be altered. For example, for aluminium, an acidic or alkaline electrolyte is required, while for other valve metals, fluoride ions must be present (as for titanium). The porous layer can be described by structural parameters such as pore diameter, layer thickness, barrier film thickness and pore spacing. These characteristics can be controlled by changing process parameters such as solution temperature, immersion time, potential and current density.

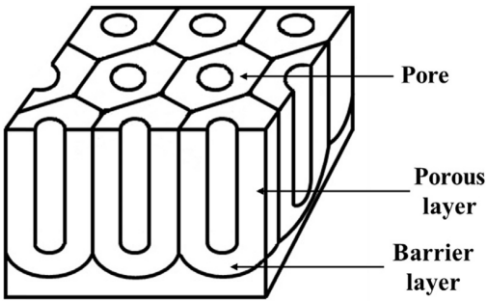

Fig. 91: Structure of a porous anodic film.

The barrier layer grows on the surface of the metal in a hemispherical shape, and from it all the pores whose diameter is closely related to the anodising potential. Usually, the application of the current in the electrolytic cell occurs in a potensiostatic manner, as the structural characteristics thus have a linear dependence on the process parameters.

To date, there is no universally accepted theory on the growth of porous anodic films, but several hypotheses have been validated over the past 50 years. The most accepted theory is that of "field-assisted" oxide dissolution. According to this model, the thickness of the barrier layer is initially non-uniform, due to the presence of an aggressive electrolyte that causes a dissolution current (i_{diss}), which lowers the yield of the process. For example, in aluminium, cracks form in the first moments of formation, the electrolyte penetrates them, causing them to become a current storage area and thus increasing their electric field strength, thus creating a 'field-assisted' dissolution pathway, i.e., the regular pore. Stationary pore formation is the result of barrier film accretion at the metal surface and "field-assisted" dissolution at the surface in contact with the electrolyte [127].

3.1.7 Corrosion

Corrosion is an electrochemical phenomenon that leads to the gradual deterioration of a metal when exposed to an aggressive environment. It can develop on the metal surface in a diffuse, localised, or selective manner. When referring to uniformly distributed attack, it is possible to calculate the rate of mass loss per unit area exposed to the aggressive environment (Eq.(35)):

$$v_m = \frac{\Delta W}{St} \tag{35}$$

Where ΔW is the mass loss in kg, S is the surface area in m^2 and t is the time in years. Eq.(35) when divided by the density, γ, of the material expresses the thickness lost from the metal (Eq.(36)).

$$v_{corr} = \frac{\Delta W}{\gamma St} \tag{36}$$

There are two types of corrosion, dry corrosion, where the metal is exposed to a gaseous environment at high temperatures, and wet corrosion, where the metal is in contact with aqueous solutions. The distinction is important because the mechanisms governing the phenomenon change markedly. In wet corrosion, the phenomenon is electrochemical in nature, i.e., corrosion arises from an anodic process of dissolution of the metal and a cathodic process of reduction of a chemical species present in the environment. In the case of dry corrosion, the process is chemical in nature, i.e., governed by thermodynamic laws and chemical kinetics [131].

3.1.7.1 Wet corrosion

This type of corrosion is the result of two electrochemical reactions:

- Anodic reaction: oxidation of the metal that makes electrons available in the metal phase.
- Cathodic reaction: subtracts electrons from the metal phase to reduce one or more chemical species in the environment. The most common cathodic reactions are oxygen and hydrogen reduction reactions (dependent on the pH of the solution).

There are also two other fundamental reactions, the transport of electrons from the anode, where they are produced, to the cathode, where they are consumed, and ion transport, i.e., an ionic current between anode and cathode.

In a nutshell, the wet corrosion process consists of four processes that occur at the same rate, which can be expressed as I_{corr}.

In general, for a chemical reaction to take place, the change in Gibbs free energy must be negative (Eq.(37)):

$$\Delta G < 0 \tag{37}$$

It can be calculated known the cathodic and anodic equilibrium potentials via Eq.(38).

$$\Delta G = -zF\left(E_{eq,c} - E_{eq,a}\right) \tag{38}$$

Where z is the equivalence of the reaction and F is Faraday's constant.

According to Eq.(38), a necessary condition for the corrosion reaction to occur spontaneously is that $E_{eq,c} > E_{eq,a}$. The equilibrium potentials were calculated using a Standard Hydrogen Electrode (SHE) and tabulated according to the possible reactions at the electrode (Fig. 92).

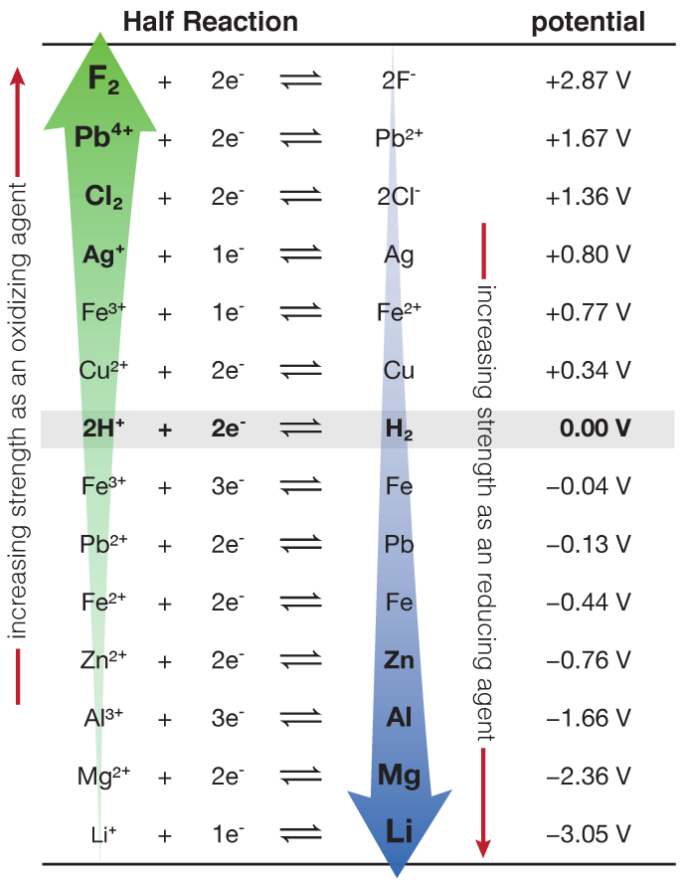

Fig. 92: Standard potentials.

When reactions do not take place under standard conditions, it is possible to use the Nernst equation (Eq.(39)):

$$E_{eq} = E^0 + \frac{RT}{zF} \ln \frac{a_C^c \cdot a_D^d \ldots}{a_A^a \cdot a_B^b \ldots} \tag{39}$$

Where E^0 is the potential under standard conditions, R is the universal gas constant, T the temperature expressed in Kelvin, and in the argument of the natural logarithm are the activities of the reactants in the denominator and the products in the numerator, raised by their stoichiometric coefficients.

3.1.7.2 Electrochemical Impedance Spectroscopy (EIS)

Corrosion phenomena on a metal are electrochemical in nature. There are several techniques for analysing how a material can resist to the corrosion. The simplest is certainly the visual one, i.e., placing the sample to be analysed inside an aggressive atmosphere (be it a salt spray chamber or an area exposed to sea spray) and observing the deterioration of the material over time. However, this process is very expensive, both in terms of time and cost. For this reason, a viable alternative, which should in any case be carried out alongside 1:1 test, is EIS. Thanks to this investigation technique, it is possible

to observe the ability of a system, subjected to corrosion, to withstand the process in a short time.

An electrochemical system can have several elements that oppose the passage of current, such as charge transport resistance, the capacity of the electrical double layer at the interface, etc. Each of these elements can be modelled as part of an equivalent circuit, thus making it possible to measure the impedance of the system, which will be directly related to the ability of the element studied to resist the corrosive phenomenon (Eq.(40) and (41)).

$$Z(\omega) = \frac{E(t)}{I(t)} \tag{40}$$

$$Z = Z_{re} + iZ_{im} \tag{41}$$

The impedance of the system is always composed of the sum of a real resistive (ohmic) part and a non-resistive part, which contains all inductive and capacitive phenomena.

The operation of the EIS technique is based on applying a small-amplitude alternating potential to the sample over a wide frequency range (100kHz to 100mHz). The sample responds by supplying an alternating current as the frequency varies, and from the relationship between potential and current, the overall impedance of the system as a function of frequency can be traced (Eq.(42) and (43)).

$$E(t) = E_0 sin(\omega t) \tag{42}$$

$$I(t) = I_0 sin(\omega t + \theta) \tag{43}$$

Where $\omega = 2\pi f$ and θ is the phase angle between potential and current.

When performing the EIS, the results are reported in three specific graphs: the Bode diagram of modulus and phase and the Nyquist diagram.

In the Bode diagram, the values of modulus and phase of the impedance are plotted as a function of frequency, on a logarithmic scale, while in the Nyquist diagram, the value of Z_{im} is plotted on the ordinates, changed by a sign (because it is almost always negative, and therefore plotted as positive in the graph), and on the abscissae, Z_{re}.

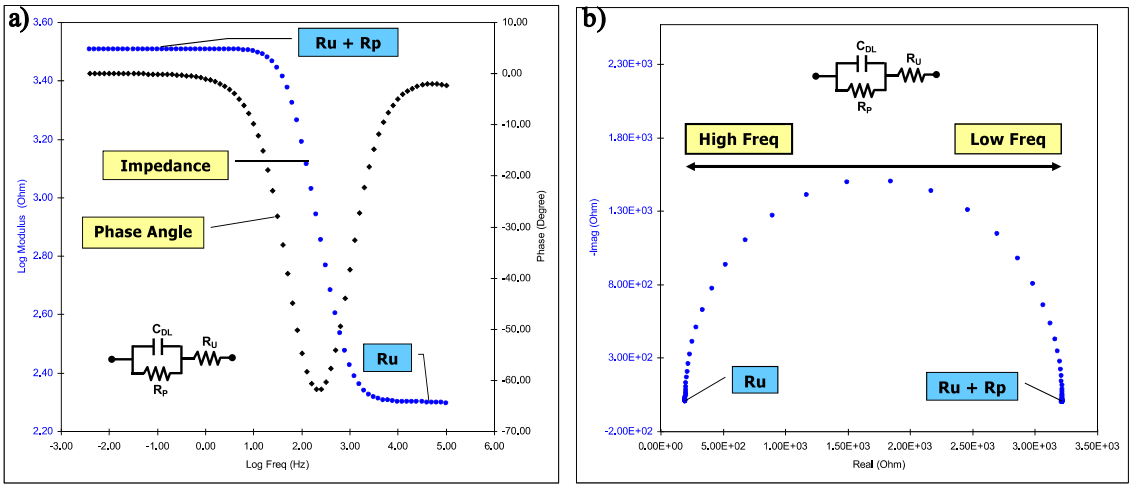

Fig. 93: a) Bode diagram module and phase; b) Nyquist diagram [132].

As can be seen from Fig. 93b, the Nyquist diagram is a semicircle. As mentioned above, the electrochemical system can be approximated to an equivalent electrical circuit and in Fig. 93 is shown the simplest of the circuits used, consisting of: the polarisation resistance of the element under consideration (R_p); the capacitance of the electrical double layer at the metal-electrolyte interface (C_{DL}); and the resistance of the electrolyte (R_u). In the Nyquist diagram, the frequency increases from right to left. At very high frequencies, the capacitance becomes a short circuit; therefore, the current flows through that side of the circuit and encounters only R_u, which can then be evaluated on the x-axis. On the other hand, at low frequencies, the capacitance acts as a circuit breaker, because the current can be regarded as almost constant and does not pass through the capacitance. For this reason, the current passes through R_p creating a series of resistors R_p+R_u. Therefore, when analysing the Nyquist semicircle, its diameter is the polarisation resistance of the material, a fundamental fact that serves as an index for the corrosion resistance of the material, which increases as the value of R_p increases.

Depending on the experimental data and the shape of the Nyquist diagram, different and much more complicated equivalent circuits can be used to fit the curve and to derive other electrochemical constants of the material that may be important in its characterisation [133].

3.2 Experimental of the second part

3.2.1 Materials

In this part of the project, aluminium alloy 7075-T6 and titanium alloy Ti-6Al-4V (grade 5) were chosen as metal substrates. Both metals have a thickness of 0.6 mm and were

supplied by Goodfellow Cambridge Ltd. (UK), whose mechanical and thermal properties are shown in *Tab. 6*.

Tab. 6: Tensile and thermal properties of alloy 7075-T6 and Ti6Al4V.

Properties from data sheet	AA 7075-T6	Ti6Al4V
Young's modulus [GPa].	71.7	106-114
Stress at break [MPa].	510-538	>895
Strain at break [%].	5-8	>10
Coefficient of thermal expansion [K^{-1}]	24.4-10^{-6}	8-10^{-6}
Thermal conductivity [W/mK] @20-23 °C	130	580

The composite part of the FML is the same for both metal substrates. It consists of a stacking film of PEEK and carbon fabrics. The sequence to produce the composite consists of 4 sheets of PEEK with a thickness of 0.2 mm and 3 layers of bi-directional carbon plain fabric with a grammage of 200 g/m^2 (HexTow AS4 - Hexcel, USA). The PEEK sheets were thermoformed from the pellets and then stacked in the chosen sequence. The PEEK used is the same as that analysed in the previous chapter.

3.2.2 Manufacture

FMLs with both metals were produced in the same way. The CARVER Autofour/3012-PLH hot press was used to thermoform the material by compression moulding. The composite substrate and the metal substrate, positioned according to the diagram in Fig. 94, were gradually heated to 385°C with a maximum pressure of 41 bar. The detailed process is shown in Fig. 95.

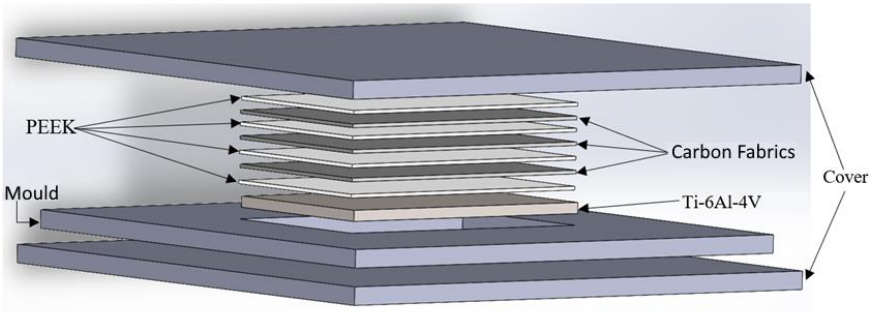

Fig. 94: Stacking sequence to produce FMLs.

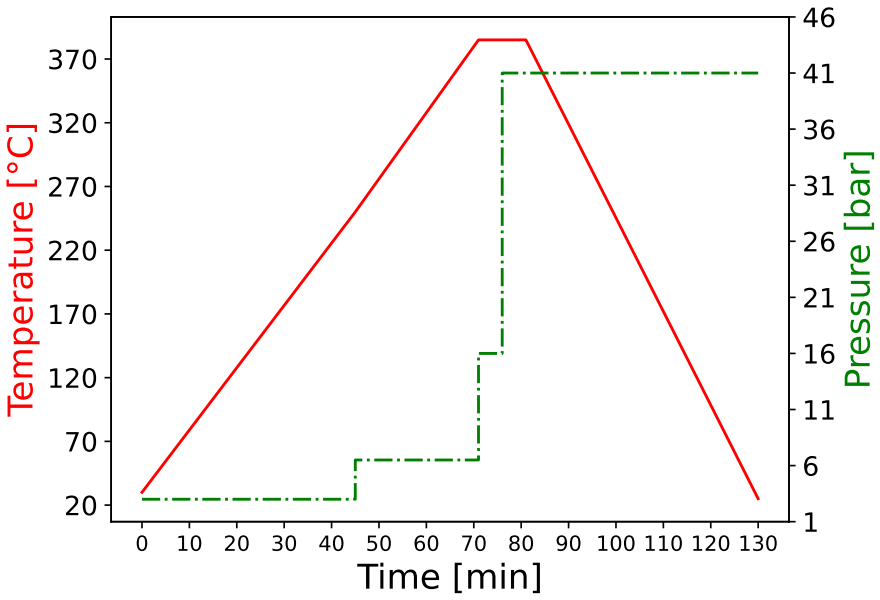

Fig. 95: FML thermoforming cycle in hot-press.

The surface dimensions of the FMLs were 100x150 mm with a thickness of 1.8 mm. In the case of aluminium, once the FML had been obtained, the test specimens for mechanical testing were cut using a Bosch GMC 800 SJ radial cut-off machine. On the other hand, for FML with titanium alloy, the titanium sheets were cut before thermoforming, according to the dimensions required for the mechanical test specimens. In fact, due to the hardness of the material, traditional cutting methods were too aggressive, thus damaging the FML.

3.2.3 Surface treatments

Different surface treatments were studied for both metals. The mechanical treatment is the same for both and serves as a reference; the electrochemical treatments are different specific anodising for the two metals; and finally, a chemical treatment with silane coupling agents was also chosen only for the titanium alloy substrate.

3.2.3.1 Surface treatment on aluminium alloy 7075-T6

Two anodising baths were mainly chosen: TSA (tartaric-sulphuric acid) and PSA (phosphoric-sulphuric acid). Before the electrochemical treatments, the samples are sanded with sandpaper up to #2000 and then washed by ultrasound in an acetone bath. After this, they are immersed in a 10%wt NaOH aqueous solution to carry out etching, which is used to remove impurities and the oxide layer naturally formed on the surface of the material. The process takes 30 seconds, and the solution is at a temperature of 60 °C. Subsequently, the samples are rinsed in deionised water and immersed for 15 seconds in an aqueous solution at room temperature containing 30%v/v HNO_3.

The innovative process that was carried out in this PhD project involves a two-step process consisting of an anodising in TSA followed by an anodising in PSA or vice versa, to engineer the surface of the metal, creating a porous morphology, with varying pore diameters along the thickness.

TSA anodising is carried out in an aqueous solution containing 40g/l sulphuric acid and 80g/l tartaric acid at 37 ± 2 °C. The immersed samples are subjected to a potential difference of 14V for 20 minutes.

PSA anodising is carried out using an aqueous solution with 110 g/l phosphoric acid and 80 g/l sulphuric acid at 27 °C. The immersed specimens remain for 23 minutes at a potential difference of 18V.

The innovative bi-step process consists of first anodising in one of the two baths, following its own process parameters, but with half the anodising time, and then, the other half of the time, immersing it in the other bath with its own parameters. TSA-PSA is performed by immersing the sample in the TSA solution at 37 °C, 14V for 10 minutes, then rinsed in deionised water and immersed in the PSA solution at 27 °C, 18V for 11.5 minutes. PSA-TSA is the reverse treatment, starting with PSA and continuing with TSA (Fig. 96).

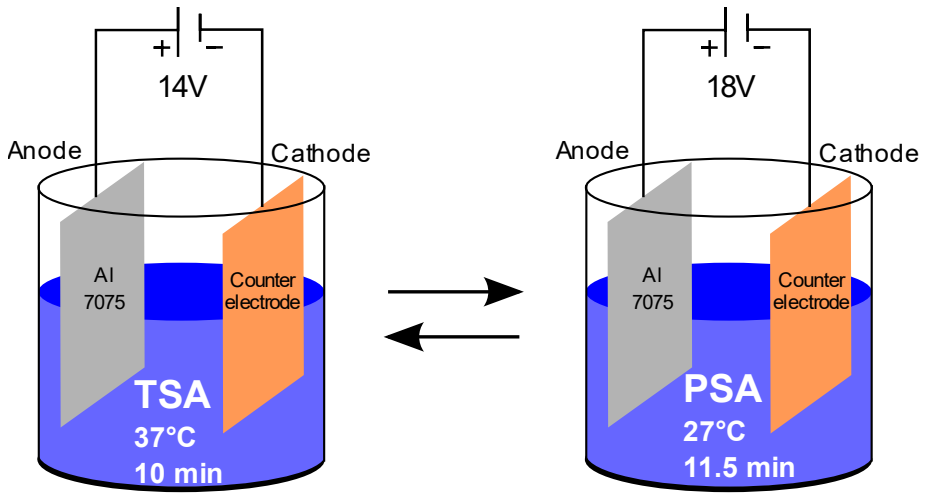

Fig. 96: Two-step anodising scheme.

Fig. 97 shows the experimental setup applied for anodising aluminium foil 100x150x0.6 mm.

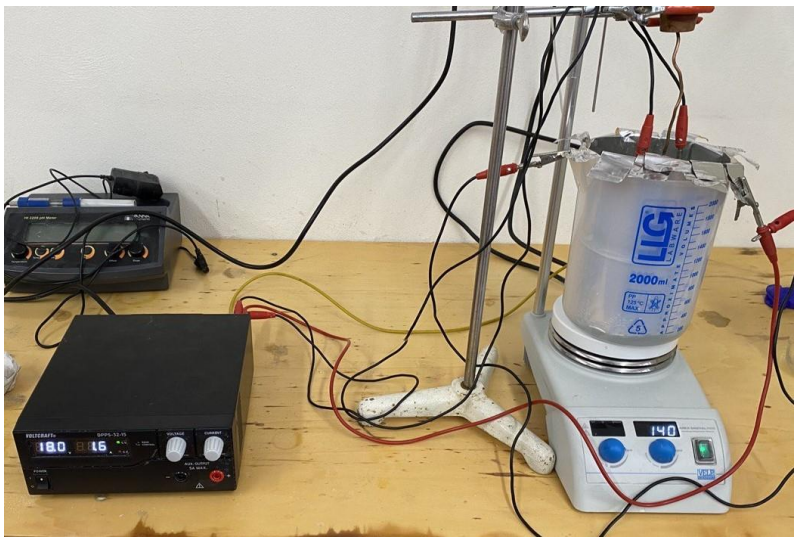

Fig. 97: Experimental setup for the anodising process of aluminium alloy 7075-T6.

In addition to these treatments, a process resulting from the modification of anodising in TSA was also applied, i.e., what so called pore widening by post-immersion of the TSA-treated samples in a 0.1 M NaOH solution at room temperature for 15 seconds (TSA-NaOH). Finally, the mechanical treatment produced by an orbital sander equipped with #80 abrasive paper was used as a reference to compare the innovative electrochemical treatments with the mechanical standard (MT).

3.2.3.2 Surface treatments on Titanium alloy Ti6Al4V

As already mentioned in previous sections, certain electrochemical processes for anodising titanium alloys lead to the formation of titanium oxide nanotubes. In this work, it was decided to analyse these electrochemical processes, varying the process parameters, to assess how these modifications influence the morphological properties of the nanotube layer. This surface conformation was chosen to create greater interlocking with the composite substrate, as, in fact, was the choice of anodising aluminium alloys to produce the porous surface.

First, the samples were ultrasonically cleaned in an acetone bath for 5 minutes and then rinsed in deionised water. After this, each sample was pre-treated in an etching solution consisting of hydrofluoric acid (39.5% v/v), nitric acid (69% v/v) and deionised water, in a volume proportion of 1:4:5 respectively. The duration of pre-treatment was 60 seconds, and the solution temperature was room temperature. Subsequently, the etched sample is washed in an ultrasonic bath of deionised water for 10 minutes and dried at room temperature.

The anodising solution generally consists of ethylene glycol, deionised water, and ammonium fluoride (NH_4 F). The amount of the latter remains unchanged for all samples

and is 0.5%wt. While the volume of water varies, as this is one of the parameters that is modified to assess the effect. This was chosen as: 5% v/v, 20% v/v, 50% v/v. Consequently, the volume of ethylene glycol varies according to the changes in water content.

In addition to the water content, the potential difference applied to the samples also varies. Two values were chosen for analysis, namely 30 V and 50 V. Finally, for each water volume content and each applied potential, the last changing parameter is the anodising time, which was varied in: 10, 30 or 60 minutes.

All the solutions produced were kept at room temperature. After completion of the anodising process, the samples were washed in deionised water for 15 minutes and then subjected to heat treatment in a muffle furnace for 60 minutes at 450 °C to consolidate the crystalline structure obtained (Fig. 98).

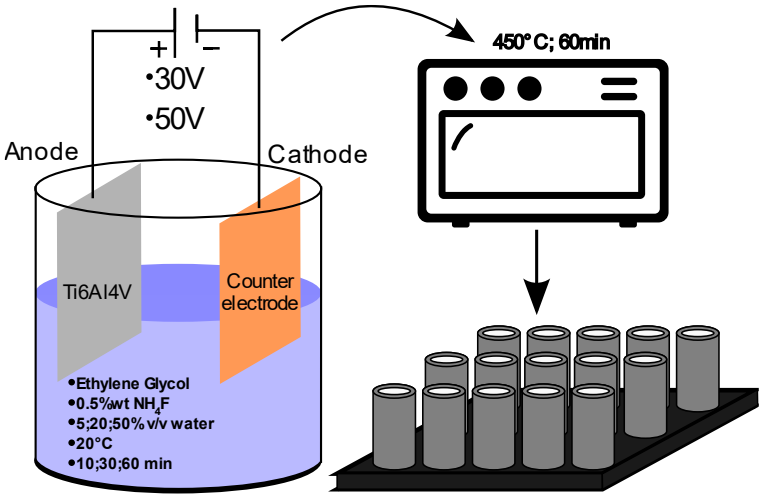

Fig. 98: Schematic illustration of the electrochemical treatment of the Ti6Al4V alloy.

In addition to the electrochemical treatments, a classic mechanical abrasion treatment and a chemical treatment using silane coupling agents were carried out. The mechanical treatment is the same as that carried out with the aluminium alloy, i.e., using an orbital sander with #80 paper.

For chemical treatment, a commercial silane, *(3-Aminopropyl)trimethoxysilane,* was applied. It was added at 5% v/v in a solution consisting of 90% v/v ethanol and 5% v/v deionised water. The solution was prepared by automatically stirring it with a magnetic stirring rod for 24 h to hydrolyse the silane molecules to form the siloxane groups. Before stirring, acetic acid was added to lower the pH of the solution to a value of 4.3. Once the solution was ready, the titanium sheets were soaked for 2 hours and then dried in an oven at 80 °C for 24 hours.

3.2.4 Morphological characterisation

Scanning electron microscopy (SEM) methods were used for both FMLs to observe the surface morphology, especially that following electrochemical treatments, which in the case of the aluminium alloy produces a porous oxide layer and in the case of the titanium alloy a layer of oxide nanotubes. The instrument used is FEI Quanta 200 EGF. Thanks to the images produced, it is possible to observe the correct production of the oxide layers and the conformation. Using an image analysis programme, ImageJ, it was possible to measure the average diameter of the pores or nanotubes. From each image, 20 random measurements were taken and then the average was calculated. The purpose of this characterisation is to verify how process parameters and the composition of the anodising bath could influence the formation of the surface layer.

Tests of the contact angle of a drop of water were also carried out for both metals, to measure the wettability of the metal surfaces as the applied treatment changed. The test was carried out by depositing a drop of water with a volume of 2 ml on the surface of the samples. Deposition of the drop and image acquisition of the contact angle were performed with the aid of the FTA2000 instrument, manufactured by First Ten Angstroms, Inc., while the angle value was calculated using the FTA32 software.

3.2.4.1 Additional characterisations for aluminium alloy: EIS

For the aluminium alloy samples, tests were conducted to assess their resistance to corrosion. This is because aluminium alloys are very susceptible to corrosive phenomena and therefore anodising is very useful to create a protective oxide layer, performing the dual function of protection and improved interlocking with the polymer matrix. The same tests were not carried out on the titanium alloy, since the oxide produced has very good corrosion resistance and therefore the only thing worth analysing is its ability to enhance interlocking.

Returning to the EIS tests on the aluminium alloys, the open circuit potential (OCP) was measured for 30 minutes in a cell consisting of the sample, the Ag/AgCl reference electrode (or *reference)* (0.197 V vs. SHE) and the electrolyte, i.e., seawater, at 3.5%wt aqueous solution of NaCl. Subsequently, a platinum counter electrode was added to the cell and the impedance measurement was performed using the Parstat 4000. The current in the circuit, whose potential is the OCP, was measured by varying the frequency from 100 kHz to 100mHz. The cell was exposed to room temperature.

3.2.4.2 Additional characterisations for titanium alloy: Raman and XRD

Titanium oxide can present up to five different crystal forms. For this reason, Raman and XRD tests were carried out to identify the crystal forms produced in the titanium oxide layer grown as nanotubes after anodising treatments.

The Raman spectrum was collected by a Raman microscope Renishaw Invia combined with a Leica DMLM microscope camera and CCD detector. The laser was focused on the sample with a 5x magnification lens to obtain an analysis diameter on the sample of ~50mm and a maximum laser power of 133mW. Only 10% of the maximum power was used for these measurements (reduced using holographic filters). A 532nm laser coupled with 2400 lines per millimetre grating was used, with a spectral resolution of 0.5cm^{-1}. Each measurement consists of two accumulations.

X-ray diffraction (XRD) patterns were collected with a RIGAKU model D-MAX 25600 HK. The analysis was performed through a copper anode (Cu Kα radiation, λ = 0.15405 nm, with Ni filter). The tube voltage was set at 40 kV, the current at 40 mA, the scan speed at 2°min^{-1} and the sampling at 0.02°. XRD patterns were recorded at an angle of 2θ between 10° and 90°.

3.2.5 Mechanical characterisation

Short Beam Shear (SBS) tests were performed to compare the mechanical performance at different treatments on the two metals in the FMLs. Five samples for each treatment were tested according to ISO 14130 [134] using a WANCE model ETM-C electromechanical testing machine equipped with a 50 kN load cell. The span was 10 mm. The speed of the moving crosshead was set at 1 mm/min. The test specimens were 20 mm long and 10 mm wide. Fig. 99 shows the diagram and the tool used to perform the SBS tests.

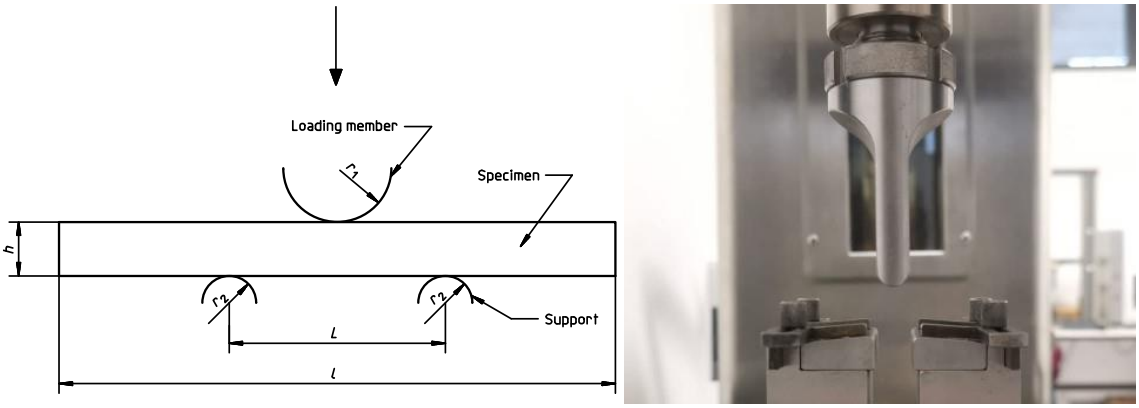

Fig. 99: Load application diagram in the SBS test.

The apparent interlaminar shear strength (ILSS) was calculated according to Eq.(44):

$$\tau = ILSS = \frac{3F}{4bh} \quad (44)$$

Where F is the breaking load in N, b is the specimen width in mm and h is the total thickness in mm.

The Double Cantilever Beam (DCB) tests were performed to estimate the contribution of surface treatments to interface fracture toughness. The tests were performed according to ASTM D5528 [135] with a Zwick-Roell universal testing machine model Z005, equipped with a 5kN load cell. To create an initial delamination, a layer of PEEK-specific liquid release agent was applied at the interface with the metal, creating an initial crack length at t_0 = 50mm. For each type of treatment, three samples were tested, each 150mm long and 20mm wide.

Crack growth was assessed in visual mode, using a graduated scale glued onto the specimen and taking a set of photographs during crack opening with a Nikon D5100 SLR camera equipped with macro lenses (Fig. 100). The movement speed of the moving crossbar was set at 10 mm/min.

Fig. 100: Experimental DCB test setup.

The energy release rate varying treatments was calculated using the equation from the modified beam theory (MBT) according to Eq.(45):

$$G = \frac{3}{2}\frac{P\delta}{B(a + |\Delta|)} \quad (45)$$

Where P and δ are the load in N and displacement in mm respectively. B is the width of the samples and a is the total crack length. Δ is a corrective term that can be calculated

from the linear regression between the cube root of compliance (C) and the total crack length. C is equal to δ/F.

3.3 Results and discussions of the second part: FMLs with aluminium alloy

In the following discussion of the results for the specimens formed from the aluminium alloy, a nomenclature related to the treatment applied will be used: MT for the mechanical treatment; TSA and PSA for the TSA-anodised and PSA-anodised specimens respectively; TSA-PSA and vice versa which will be the bi-step anodising and the TSA-NaOH which will be the TSA-anodised specimens with post-immersion in NaOH.

3.3.1 Surface morphology of treated aluminium alloy

The evaluation of the contact angle was performed as a preliminary test to assess which of the treatments considered had the best wettability with water. The latter is determined by the balance of adhesion and cohesion forces between the solid and liquid surfaces. The tendency of a liquid to spread over the solid surface, and thus the prevalence of adhesive forces, results in a decrease in the contact angle. Conversely, when cohesive forces prevail, the contact angle increases. The images shown in Fig. 101 were acquired by a camera aligned with the sample surface and show the results of the test.

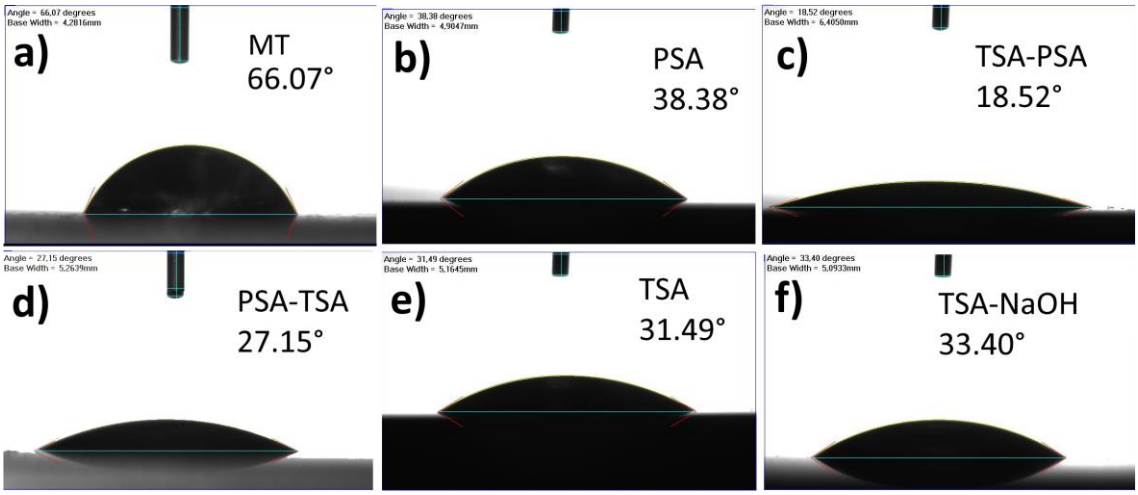

Fig. 101: Contact angle with a drop of water by varying aluminium alloy treatments - a) MT; b) PSA; c) TSA-PSA; d) PSA-TSA; e) TSA; f) TSA-NaOH.

Fig. 101 shows that the mechanical treatment (MT) has the worst wettability, i.e., the highest contact angle, followed by PSA, TSA-NaOH and TSA. When considering the two innovative bi-step treatments, TSA-PSA has the best wettability in comparison with PSA-TSA. However, wettability information alone is not sufficient to determine which of these treatments can generate optimal *interlocking* with the matrix. For this reason, SEM

images were also evaluated to observe the actual surface conformation of the specimens (Fig. 102).

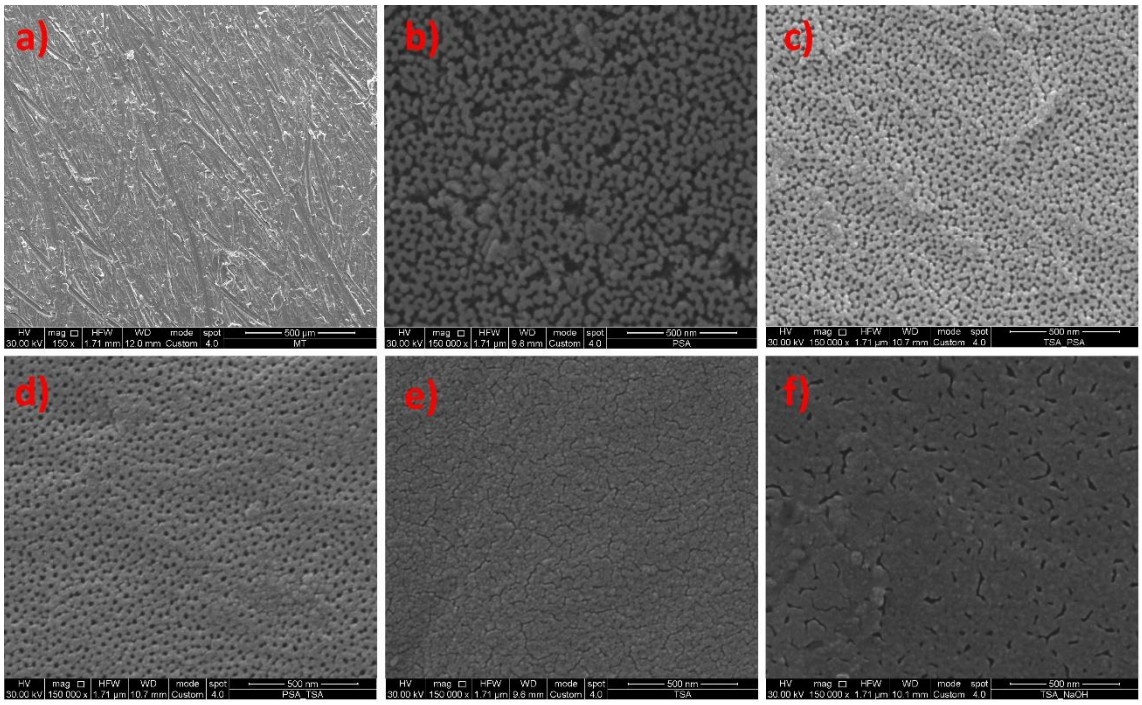

Fig. 102: SEM images of treated aluminium alloy specimens - a) MT; b) PSA; c) TSA-PSA; d) PSA-TSA; e) TSA; f) TSA-NaOH.

From Fig. 102 the first thing that can be observed is the substantial difference in morphology between MT and the rest of the treatments. The mechanical treatment is based on increasing the wettable surface by creating a macroscopic morphology formed by a set of ridges and valleys. On the other hand, anodised samples present porous structures composed of an ordered distribution of nano pores. Furthermore, focusing on anodised samples, PSA samples are composed of a larger pore structure, followed by PSA-TSA and TSA-PSA, which maintain the same pore structures. TSA and TSA-NaOH have a different structure with linear pores, and it is possible to observe how the pore enlargement treatment with NaOH works, considering that the linear pores of the Fig. 102f are larger than those in Fig. 102e. The pore diameter was measured from the images of Fig. 102. In the case of TSA and TSA-NaOH, the "diameters" refer to the minimum linear pore distance.

Tab. 7: Average pore diameter for anodised aluminium alloy specimens.

PSA [nm]	TSA-PSA [nm]	PSA-TSA [nm]	TSA [nm]	TSA-NaOH [nm]
26.68 ± 6.22	**16.81 ± 3.99**	**20.72 ± 5.17**	**8.33 ± 2.33**	**20.48 ± 6.36**

Tab. 7 shows numerically the differences between the treatments. Although PSA has poor wettability, it also has the largest pore size, which may allow for better interlocking with the matrix during thermoforming of the FMLs. In addition, TSA has the lowest value, as expected, because this treatment is designed to protect the substrate from corrosion. Pore widening in NaOH solution increases the pore size, creating a TSA more suitable for adhesion with the matrix. Furthermore, TSA-PSA has a smaller diameter than PSA-TSA but has the best wettability. The structure of TSA-PSA should be as shown in Fig. 103 with small-diameter pores on the outside and larger pores on the inside. This may allow the matrix to penetrate the pores and increase interlocking, while solidifying in the larger pores. The structure of PSA-TSA is the opposite, with larger pores on the outside and smaller on the inside. These assumptions are confirmed by the diameter data and subsequent corrosion and mechanical tests.

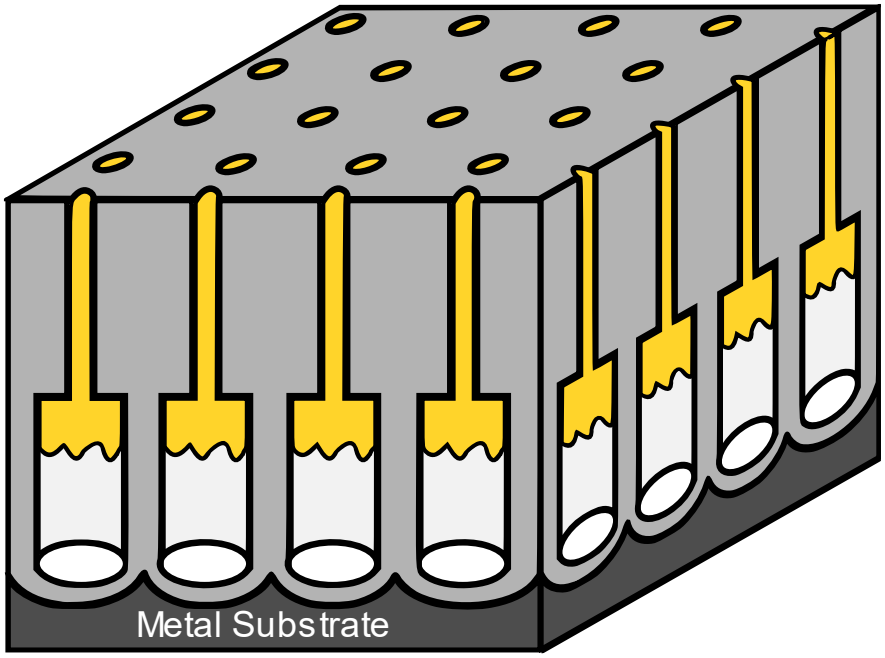

Fig. 103: Schematic illustration of the internal structure of the TSA-PSA with the matrix inside (yellow part) to simulate interlocking.

3.3.2 Corrosion resistance of treated aluminium alloy

The corrosion resistance of the samples was studied using the electrochemical technique of EIS. The open circuit potential (OCP) was calculated prior to impedance spectroscopy tests. All measurements were conducted in an aggressive environment recreating seawater to assess the ability of the surface treatment to protect the material even under the most extreme conditions. OCP values are shown in Fig. 104.

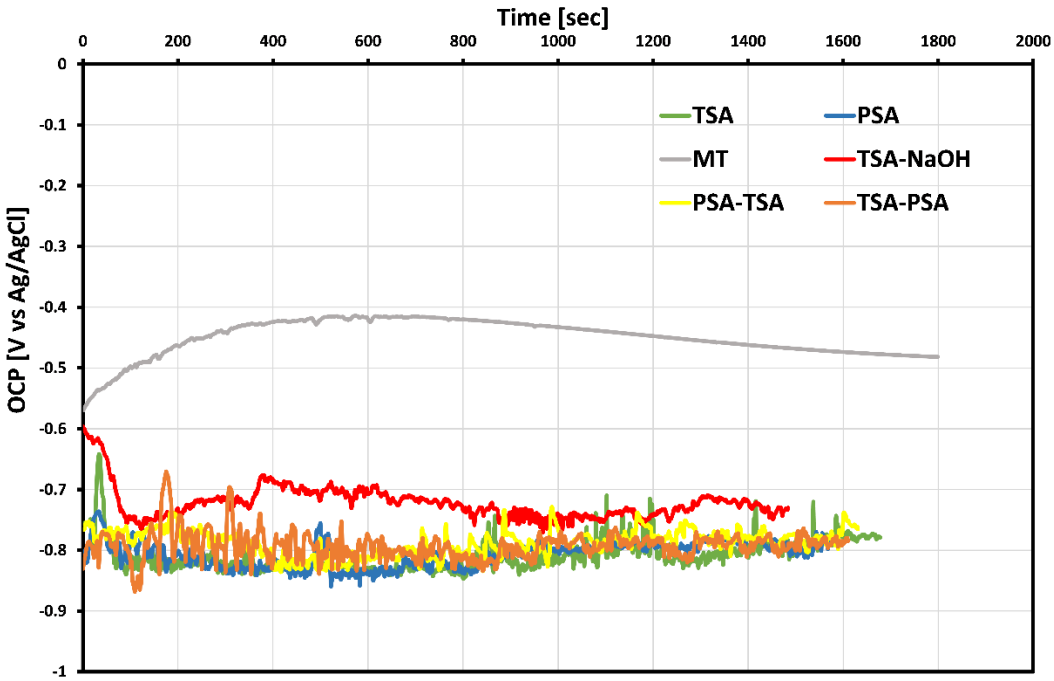

Fig. 104: OCP vs time at varying surface treatments on aluminium alloy.

EIS measurements were carried out around the OCP value, and the results are shown as a Nyquist diagram in Fig. 105.

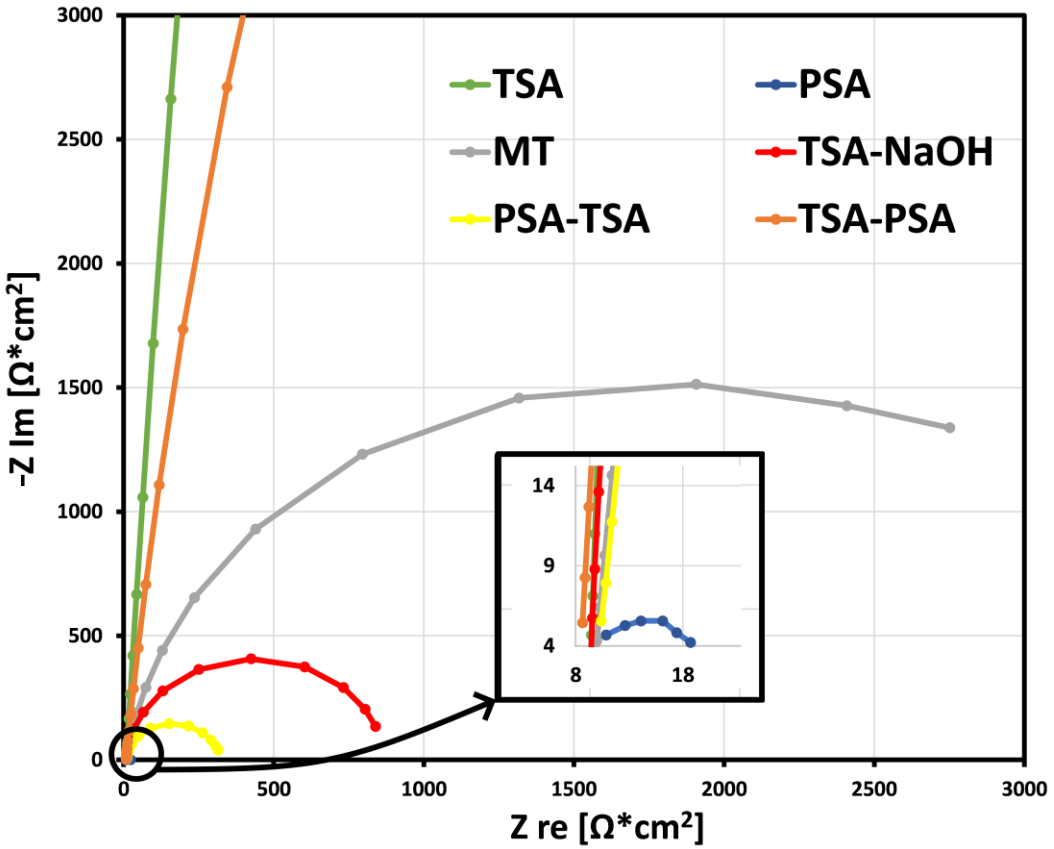

Fig. 105: Nyquist diagram for treated aluminium alloys.

The Nyquist diagram gives immediate information on the corrosion resistance of the material. The geometric shape that is represented during the measurement is a semicircle.

As already mentioned in the previous paragraphs, the diameter of this semicircle represents the polarisation resistance of the material being analysed, which can be associated with its corrosion resistance, the larger this value, the larger the semicircle, the higher the corrosion resistance under varying treatment. In this context, TSA anodising shows the highest value of corrosion resistance, as expected, because this treatment produces a small-diameter pore that allows only a small portion of the aluminium alloy to be exposed. On the other hand, despite the increase in pore diameter, TSA-PSA shows very high corrosion resistance, comparable to that of TSA; therefore, with bi-step anodising in this order (TSA-PSA), larger pores and high corrosion resistance can be achieved. On the other hand, by changing the order to PSA-TSA, the corrosion resistance decreases, which is mainly due to the increased pore diameter and a thinner compact oxide layer at the base of the porous layer. Furthermore, Fig. 105 shows that TSA and PSA have exactly opposite behaviour. The semicircle of PSA should be zoomed to be compared with the others, which means that the corrosion resistance of this treatment is very low. Therefore, it is possible that, when combining these treatments, different behaviour is encountered by varying the order in which the anodising is carried out. In this case, the best combination is TSA-PSA, which offers high corrosion resistance, a large pore diameter and good wettability. In addition, the pore widening of TSA, i.e., TSA-NaOH, shows a decrease in corrosion resistance, mainly because the larger the pores, the more easily the aggressive solution penetrates in contact with the underlying base metal. Finally, MT shows good corrosion resistance due to the natural barrier layer that forms immediately in this 7075-aluminium alloy.

3.3.3 Short beam shear test for aluminium alloy specimens

The short beam shear test (SBS) was performed to compare the mechanical performance of specimens with different treatments. The SBS test calculates the interlaminar shear strength (ILSS - Eq. (44)); in this case, with two materials of different nature, such as metal and composite, the weak part of the FMLs is the interface between them; therefore, the ILSS is directly related to the improvement in mechanical performance that the treatment gives to the samples. The higher the value, the greater the strength that the treatment given to the FMLs.

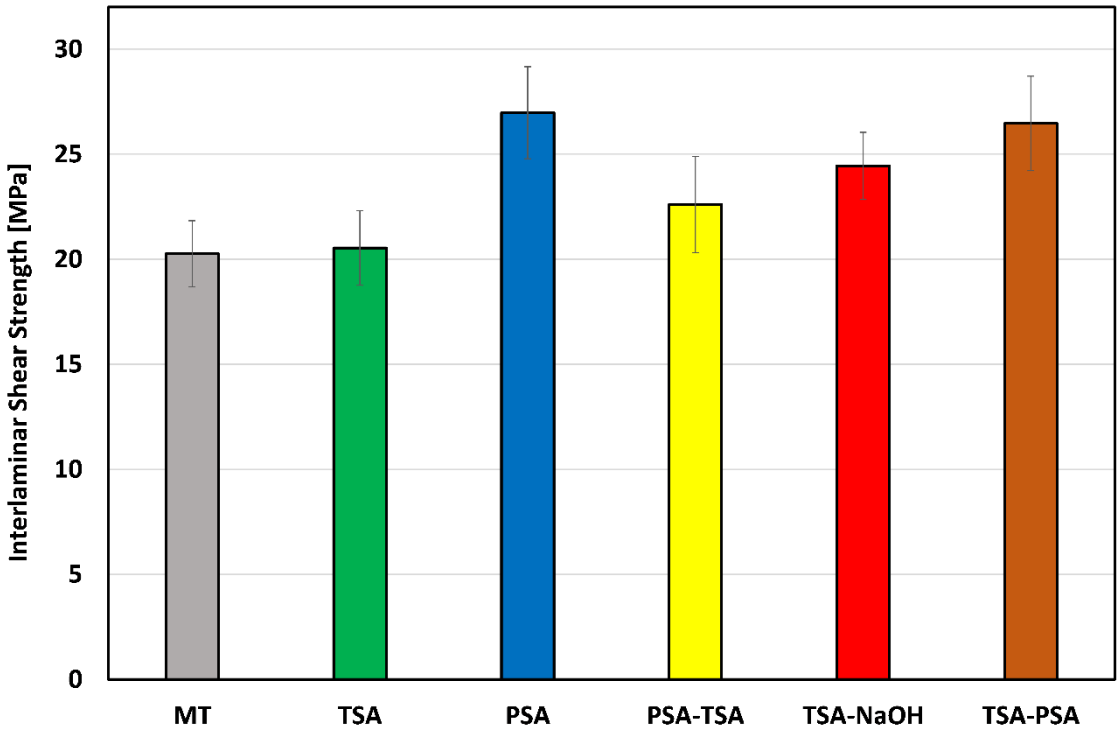

Fig. 106: ILSS calculated after the SBS test varying surface treatment on the aluminium alloy.

Fig. 106 shows the ILSS of the various treatments. The results show that TSA-PSA has a high strength, comparable to that of PSA (+32% for TSA-PSA and +33% for PSA compared to MT), which is a treatment specifically developed to improve the performance of the adhesive joint. This value is followed by TSA-NaOH, which could be considered a good treatment to use in an adhesive joint (+21% compared to MT). MT and TSA show the lowest values, as expected. TSA has small-diameter pores, which are useful to protect the material from corrosion, but does not work well when it comes to adhesion, especially with a thermoplastic matrix. MT has a different surface morphology, with ridges and valleys. This form is worse than the surface morphology formed by pores, which is typical of anodised samples. Therefore, MT with its morphology is not a suitable treatment to improve the mechanical performance of the material. Finally, PSA-TSA did not achieve the results of TSA-PSA (+12% compared to MT), so PSA anodising followed by TSA is not a suitable treatment to improve the properties of thermoplastic metal fibre laminates.

In Fig. 107 the typical failure mode after the SBS test can be observed. As mentioned earlier, the weak part of the FML is the interface, so that part will fail, detaching the composite from the metal from the outermost part to the midpoint of the specimen.

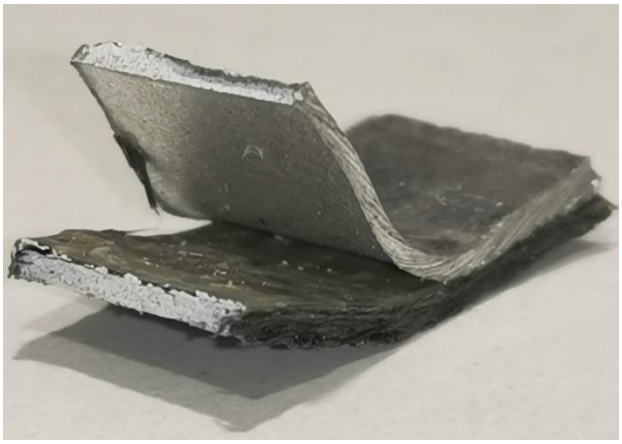

Fig. 107: Typical fracture mode for aluminium alloy SBS test specimens.

3.3.4 Double cantilever beam test for aluminium alloy specimens

The DCB test was evaluated to obtain a comparison of the various treatments when there is an I-mode crack-opening stress. Being more precise, the system is not subjected to a pure mode I stress, due to the asymmetry of the material (metal-composite junction), there will be spurious stress components that distort the pure mode I opening strength. However, the purpose of this work is not to find the absolute value of the energy release rate of the specimen, but to make a comparison at varying treatment under the same loading conditions. For this reason, even if spurious stresses are present, all specimens will still be subjected to the same loading setup and the comparison can therefore be made.

The mode I opening test proceeded as in Fig. 108.

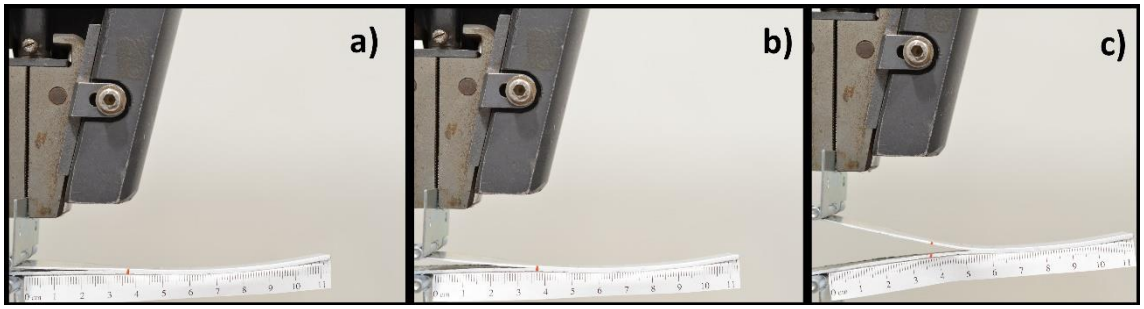

Fig. 108: DCB test execution mode - a) pre-existing crack opening at t_0; b) crack initiation value, the G_0; c) crack propagation.

As can be seen from Fig. 108, the moving crosshead goes at a constant speed opening the crack that already exists. Subsequently, the point is reached where the bonding between metal and composite begins, and at that point an increasing load begins to occur, which will reach a maximum when the crack starts to propagate. That is the point of the initial energy release rate or G_0 and can be considered as the parameter that the material has in

terms of opposition to crack opening. In Fig. 109 a typical force-displacement trend for this test is shown.

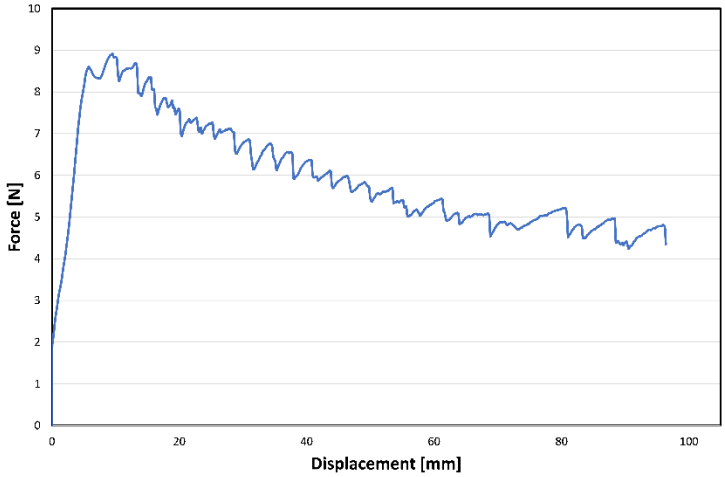

Fig. 109: Example of force-displacement curve during DCB test.

In this work, G_0 was chosen as the parameter to compare the various surface treatments.

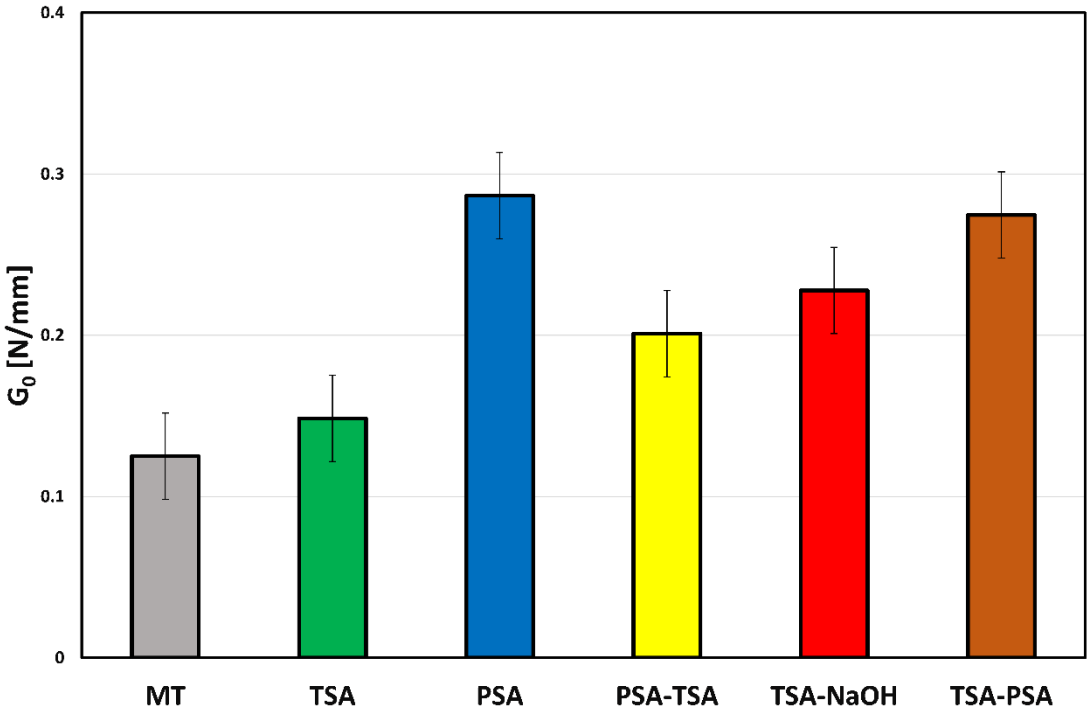

Fig. 110: Initial energy release rate calculated after DCB tests on aluminium alloy test specimens varying surface treatment.

In Fig. 110 are shown the results of G_0 calculated using Eq. (45). As expected, the mechanical treatment does not perform well, followed by TSA, which shows similar crack-opening resistance. The best result was achieved by PSA, producing a 129% increase in G_0 compared to MT. The most interesting fact is that the bi-step TSA-PSA treatment is also comparable to PSA, producing an increase over MT of 120%. Thus, placing it on a par with one of the best treatments used in the industry to date for adhesive junctions. Another treatment that showed an interesting result is TSA-NaOH, which has

a slightly lower G_0 value than TSA-PSA (+82% compared to MT). Again, PSA-TSA shows no interesting results, +60% compared to MT.

These data, together with the SBS results, confirm that PSA is the best treatment in terms of mechanical strength, but TSA-PSA provides totally comparable strengths, both in terms of interlaminar strength and Mode I crack opening.

3.4 Results and discussions of the second part: FMLs with titanium alloy

As far as FMLs formed from titanium alloy are concerned, the nomenclature below is defined as follows: MT, mechanical treatment and SIL, chemical treatment with silane coupling agents. As far as electrochemical treatments are concerned, the following rules are followed: the first number indicates the potential at which the treatment was carried out followed by a V (30V or 50V); the second number corresponds to the percentage by volume of water used in the solution followed by a P (5P, 20P or 50P); the last term indicates the anodising minutes chosen. An example is 30V50P_60min, i.e., the sample anodised at 30V for 60 minutes with a solution containing 50%v/v water.

3.4.1 Morphology of anodised titanium alloy surfaces

The morphological analyses for the samples with the titanium alloy metal substrate consisted of extensive visual inspection by SEM microscopy to observe the surface changes obtained when the anodising process parameters were varied. The treatment is, for simplicity's sake, divided into two large groups: the samples subjected to an anodising potential of 30V and those subjected to 50V. For each potential, the percentages of volume of water contained in the solution and the anodising time were varied. At Fig. 111 the results of the specimens anodised at 30 V are shown.

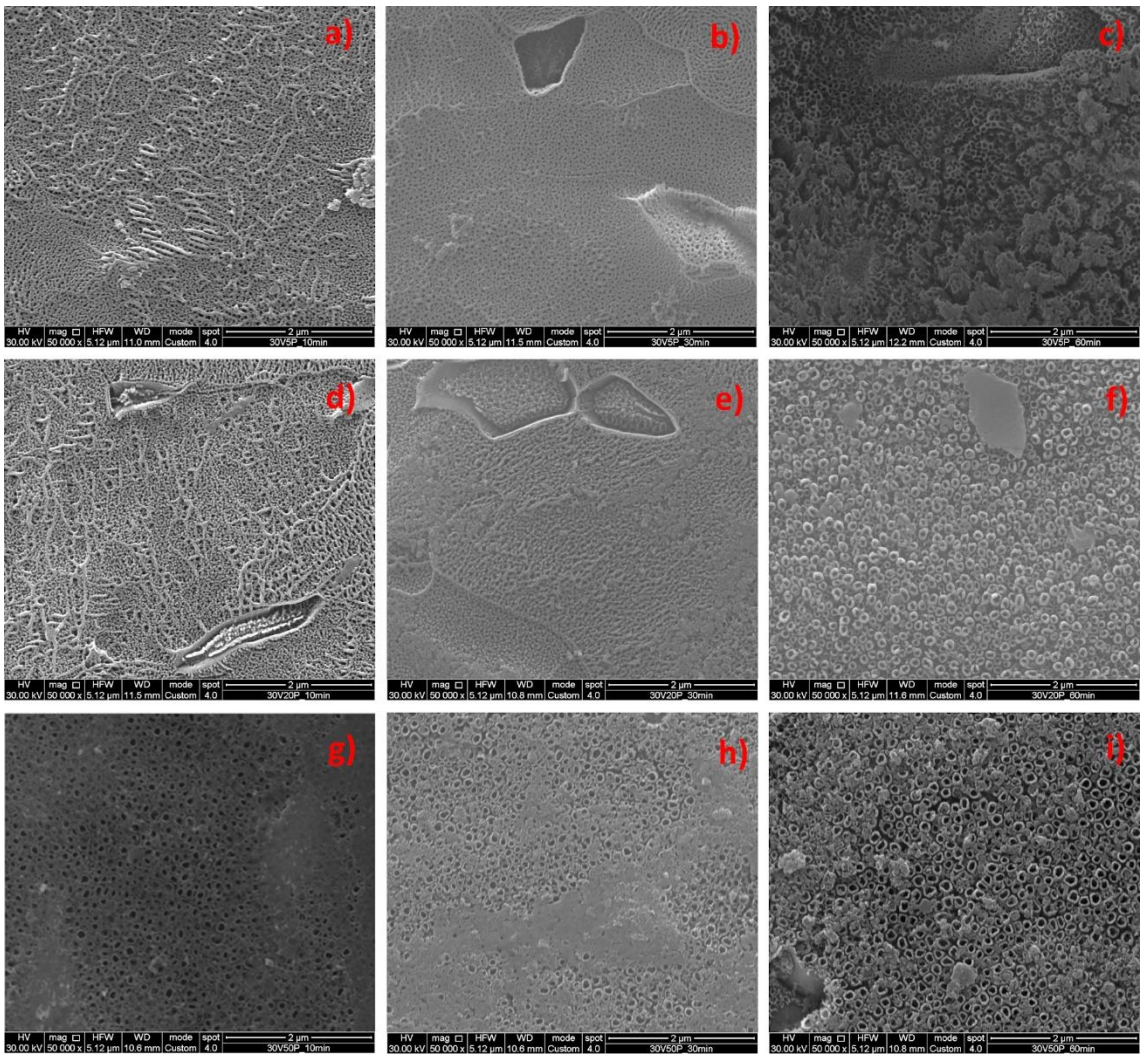

Fig. 111: SEM images of 30 V samples by varying the volume of water and anodising time. a) 30V5P_10min; b) 30V5P_30min; c) 30V5P_60min; d) 30V20P_10min; e) 30V20P_30min; f) 30V20P_60min; g) 30V50P_10min; h) 30V50P_30min; i) 30V50P_60min.

From Fig. 111 it can be seen that samples with 5%v/v water with an anodising time of 10 and 30 minutes (Fig. 111a and b), show a nanotube surface that is not well developed. A porous layer is visible, which can be assumed to be a preliminary structure that later leads to the production of the nanotubes. The various pores are proto nanotubes that have not yet been well formed. In fact, it can be seen from Fig. 111c that after 60 minutes the nanotubes are perfectly formed and separated from one another. The same behaviour can be observed by increasing the volume of water in the solution from 5% to 20% (Fig. 111d-f). After 10 and 30 minutes, only the porous pattern develops, but increasing the anodising time to 60 minutes (Fig. 111f), a well-formed nano-tubular structure can be observed, with large diameters and also thick walls, especially when compared to 5%.

By further increasing the water content to 50%, well-defined nanotubes begin to be observed even at 10 and 30 minutes (Fig. 111g and h). But it is after 60 minutes that well-

defined nanotubes with very large external diameters are obtained, which are obviously preferable in this context since interlocking with the thermoplastic matrix composite is to be increased. In Tab. 8 shows the average values of the diameters measured from the images with the ImageJ software, of the only specimens that showed the best nanotube formations, i.e., all those anodised at 30 V for 60 minutes.

Tab. 8: Average diameter of anodised samples at 30 V for 60 minutes, varying the percentage of water in the solution.

30V5P_60min [nm]	**30V20P_60min [nm]**	**30V50P_60min [nm]**
61.4 ± 6.8	**59 ± 9.8**	**101.67 ± 12.6**

As shown in Tab. 8 the treatment that generates the largest diameters corresponds to 30V50P_60min. In this context, larger diameters mean more interlocking with the matrix, thus increasing the mechanical performance of the FML [136,137]. Furthermore, another important detail is the space between the nanotubes, as this also acts as an area where the matrix can fit. Therefore, when comparing with the surfaces formed by the porous proto structure, the one with separate nanotubes is preferable.

As for the specimens subjected to 50 V, the SEM images are shown in Fig. 112.

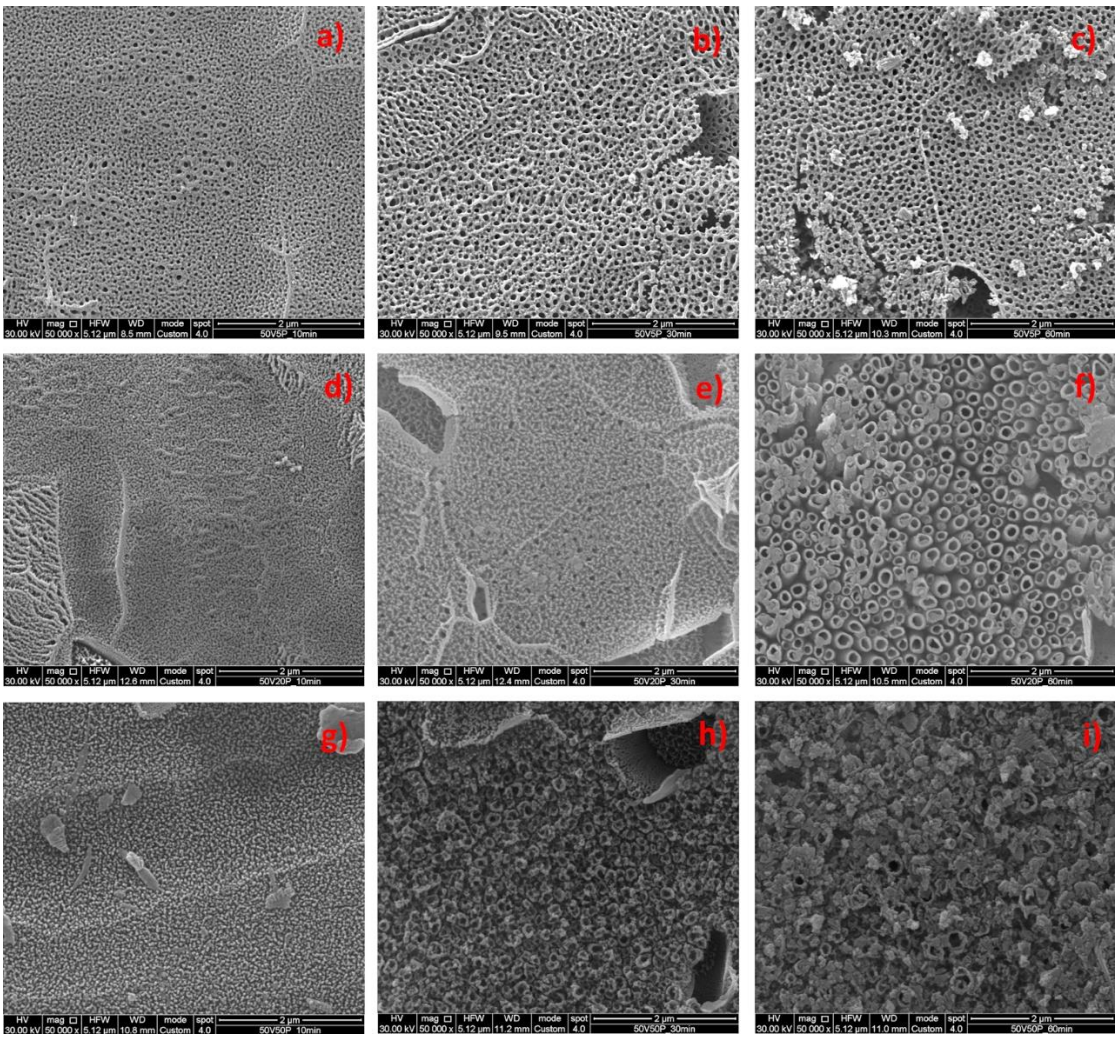

Fig. 112: SEM images of the 50 V samples by varying the volume of water and anodising time. a) 50V5P_10min; b) 50V5P_30min; c) 50V5P_60min; d) 50V20P_10min; e) 50V20P_30min; f) 50V20P_60min; g) 50V50P_10min; h) 50V50P_30min; i) 50V50P_60min.

The SEM images presented in Fig. 112 clearly show that the only set of parameters useful for producing a surface containing well-structured nanotubes is 50V20P_60min (Fig. 112f). In the case of samples with 5% volume of water, only a porous proto structure is formed, even after 60min of anodising (Fig. 112a-c). The same result was obtained by increasing the volume of water to 20% but only at times 10 and 30 minutes. Very different results compared to 30 V were obtained with 50% volume of water, particularly at high anodising times (30 and 60 minutes). From Fig. 112h and Fig. 112i, it can be seen that the nanotube structure is strongly damaged, in fact for these values of potential and water content the nanotubes are not chemically stable and the dissolution rate exceeds the formation rate, creating this destroyed structure.

The average diameter of the only specimen to have formed a good nano-tubular structure for the 50 V specimens is 113.5 ± 19.3 nm.

These experimental results show that the 30V50P_60min and the 50V20P_60min samples are the only ones that show a well-structured surface with titanium oxide nanotubes and, moreover, with large diameters of similar value. In accordance with the morphology, these two types are the most promising for generating good interlocking with the composite. These two treatments will later be used, together with the mechanical and chemical treatment, in mechanical tests to verify the mechanical strength of the interface. Since both are carried out with 60-minute anodising times, for simplicity's sake, this information will be omitted from the nomenclature in the following, so they will simply be referred to as 30V50P and 50V20P.

For both the 30V and 50V samples, it was observed that the amount of water plays a fundamental role. In the case of the 30V samples, as the amount of water increases, the external diameter of the nanotubes increases; in the case of the 50 V samples, the role played is the same, only that being coupled with a higher potential value, excessive dissolution of the layer is generated. This effect of enlarging the pore diameter has also been reported in the literature by other authors [138,139].

To further verify the nature of the nanotubular oxide layer formed, Raman and XRD investigations were carried out. For both 30V50P and 50V20P, the results are similar, so for sake of simplicity only the results of 30V50P are shown.

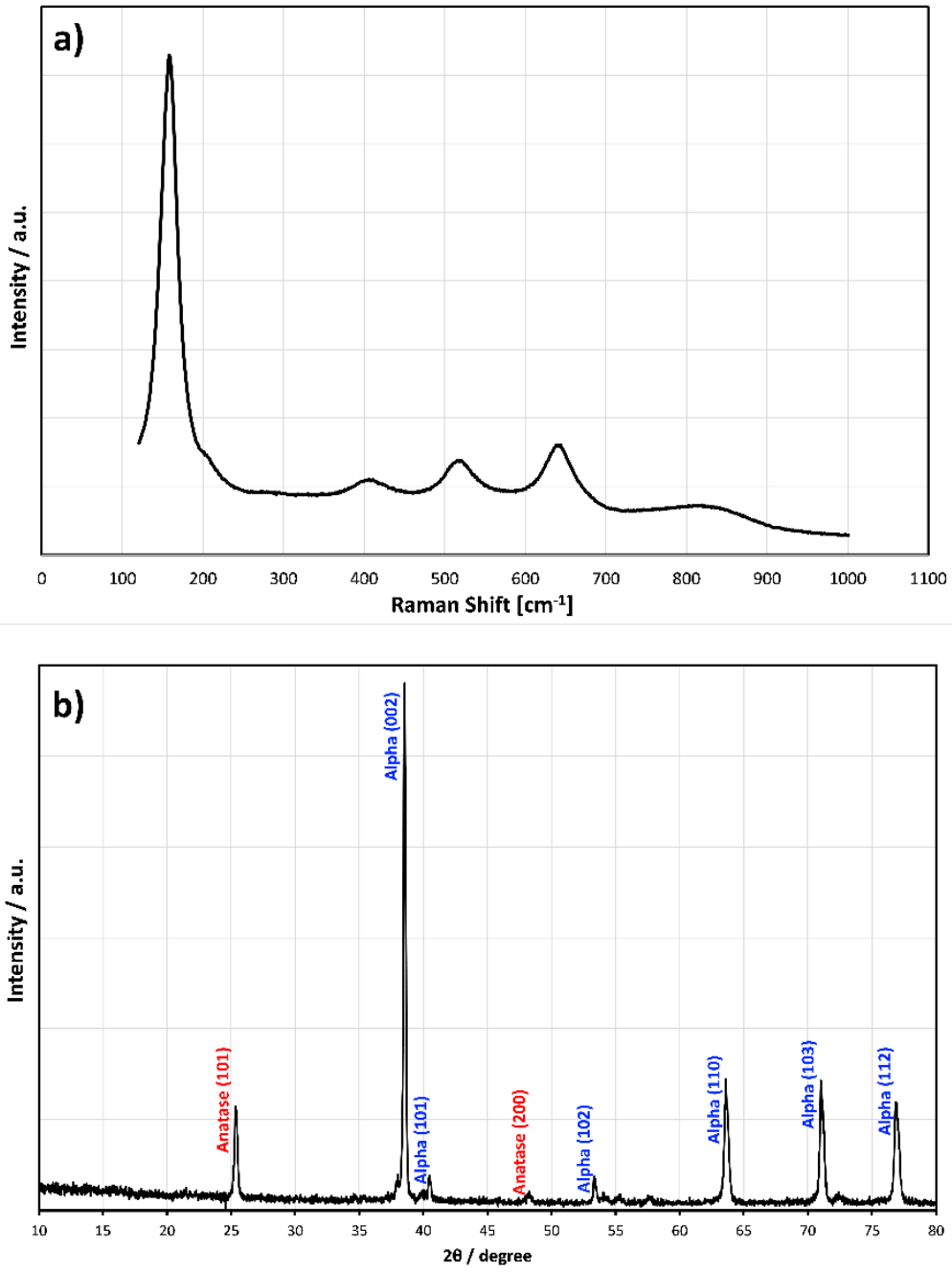

Fig. 113: (a) Raman spectrum and (b) XRD pattern for sample 30V50P.

In Fig. 113a Raman spectrum is shown. The tetragonal structure of anatase belongs to the D4h space group and has six formula units per primitive cell, corresponding to six active Raman protons: 3Eg (wavenumber 144, 196 and 638 cm^{-1}), 2B1g (wavenumber 398 and 519 cm^{-1}) and 1A1g (wavenumber 513 cm^{-1}) [140]. As shown in Fig. 113a, the main Eg peak appears at 155 cm^{-1} (which is shifted to a higher wave number than 144 cm^{-1}), followed by two lower intensity Eg peaks at 200 and 640 cm^{-1} , respectively. The shift in frequency could be attributed to phonon confinement and non-stoichiometric defects in the nanotubular titanium oxide [141]. Another active mode for anatase is the B1g corresponding to a wave number of 398 cm^{-1}.

The XRD graph of the 30V50P specimen after anodising treatment followed by heat treatment is shown in Fig. 113b. there are peaks related to the alpha phase of the base metal and two diffraction peaks (101) and (200), which are characteristic of anatase. Thus, in agreement with the Raman spectrum results, the crystal structure of the titanium oxide of the nanotube-formed surface is anatase.

3.4.2 Contact angle for titanium alloy samples

For the titanium alloy samples, measurements of the contact angle of the water droplet were also carried out to assess the wettability of the surface under varying treatment. The results are shown in Fig. 114.

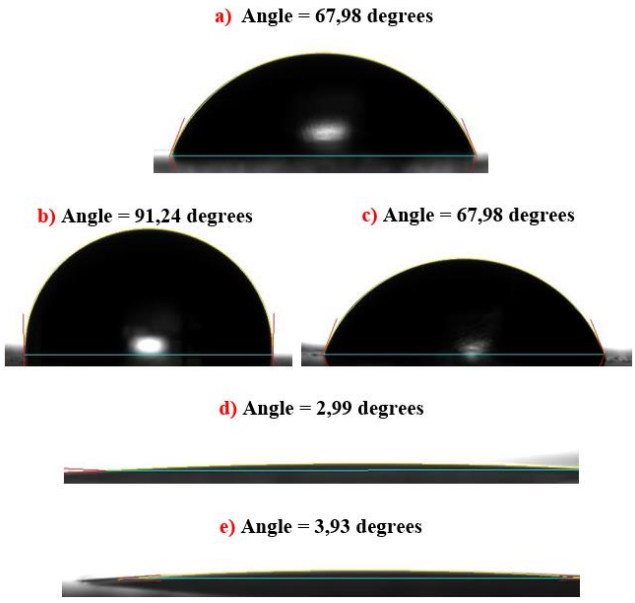

Fig. 114: Contact angles of the water droplet varying surface treatments - a) smooth base metal without treatments; b) mechanical treatment (MT); c) chemical silane coupling agent treatment (SIL); d) 30V50P; e) 50V20P.

Fig. 114b shows the contact angle of the metal that has undergone mechanical abrasion (MT): it has a contact angle ϑ of 91.24°, which is higher than that of the smooth base metal; this phenomenon occurs since the mechanical treatment increases the roughness of the surface, and the liquid is unable to adapt to the surface roughness.

Chemical silane treatment, in Fig. 114c, does not cause a substantial change in the contact angle with respect to the base metal, since it does not produce a morphological change in the surface, but rather generates a film on it that acts as a chemical bridge with the polymer matrix of the composite substrate.

This test showed unequivocally that electrochemical treatment is the best solution for increasing the wettability of a surface: Fig. 114d and e illustrate the results of the 30V50P and 50V20P tests respectively. Regarding these two anodic oxidation treatments, the test

returned very similar results, the contact angles assuming values between 2° and 5°: this indicates very high wettability, the surfaces are therefore perfectly hydrophilic.

3.4.3 Short beam shear test for titanium alloy specimens

The SBS test was used to experimentally evaluate the interlaminar shear strength of FML. Given the repeatability of the results, in Fig. 115 are reported examples of force-displacement curves for each treatment performed, in which the first peak corresponds to the interface failure.

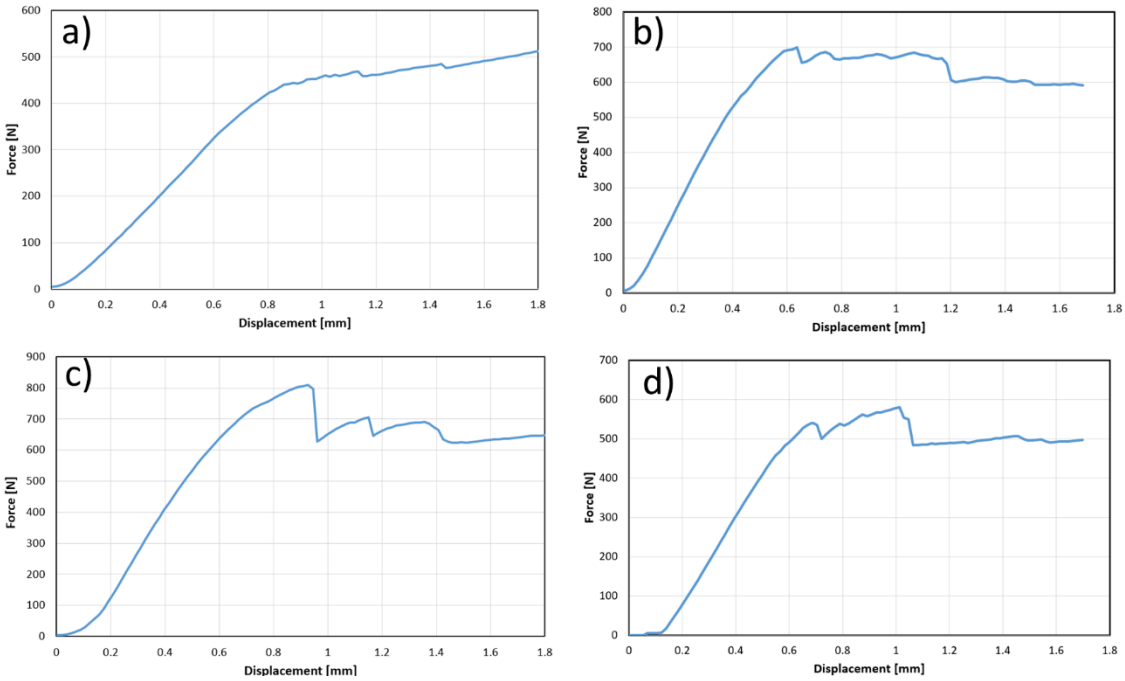

Fig. 115: Examples of force-displacement curves in the SBS test - a) MT; b) SIL; c) 50V20P; d) 30V50P.

failure occurs from the outer lateral edge and continues to the centre of the specimen, forming the failure mode at the interface observed in Fig. 116.

Fig. 116: Typical fracture of FML specimen with titanium alloy subjected to SBS test.

Calculating the ILSS via Eq.(44) from the force of first interface failure, the graph in Fig. 117 is plotted.

The best mechanical result was obtained with the 30V electrochemical treatment followed by the 50V treatment. These treatments achieved a 49% and 37% improvement over the

mechanical treatment (MT). In addition, the silane coupling agent showed an improvement in strength, achieving 22% more than the MT result.

These results demonstrate that electrochemical treatments with titanium oxide nanotubes provide a viable alternative as a surface treatment in adhesive joints. In this case, a treatment to improve the performance of FML.

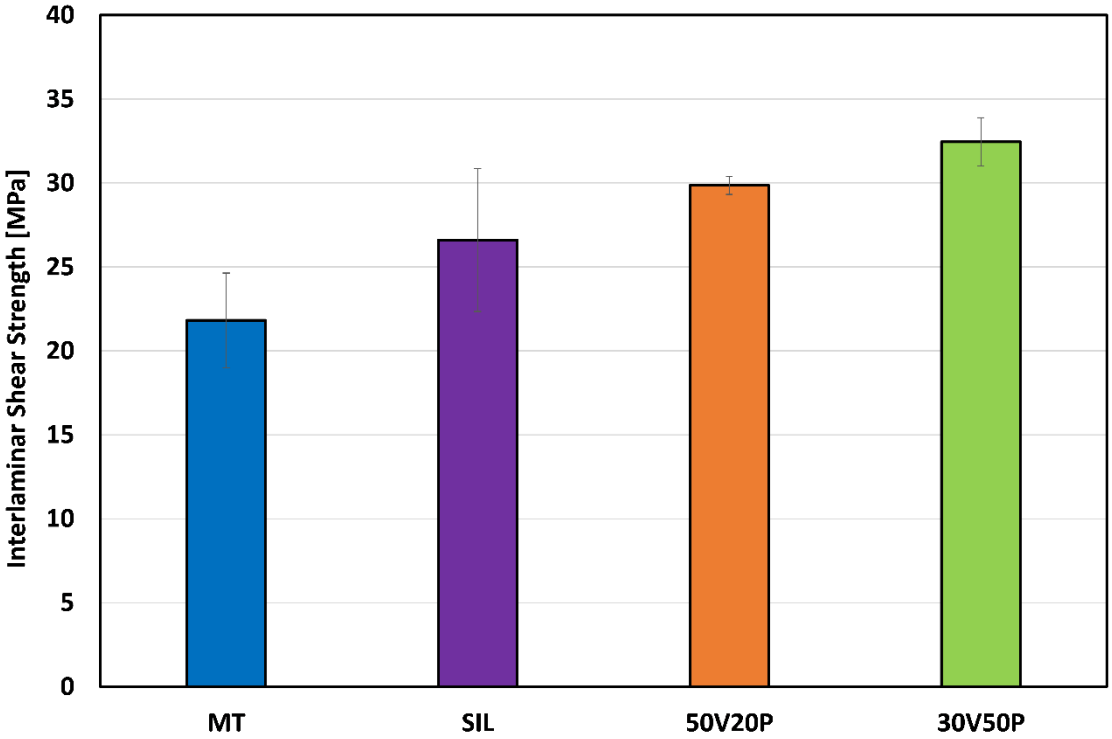

Fig. 117: ILSS calculated after the SBS test varying surface treatment on the titanium alloy.

3.4.4 Double cantilever beam test for titanium alloy specimens

For the FMLs obtained with the titanium alloy, fracture mechanics tests were also carried out to assess how, with varying surface treatments, the material opposes crack advancement. Again, it should be remembered that the purpose of this discussion is to evaluate the different treatments and not to calculate the absolute value of energy release rate.

The R-curves were derived by averaging the values of G (calculated with Eq.(45)). Given the repeatability of the results, in Fig. 118 a diagram for each treatment is shown.

As expressed in ASTM D5528, in the DCB test, as the crack length increases, a resistive behaviour develops, in fact, from the Fig. 118 it is evident that G_{Ic} first grows monotonically and then stabilises with further crack advancement.

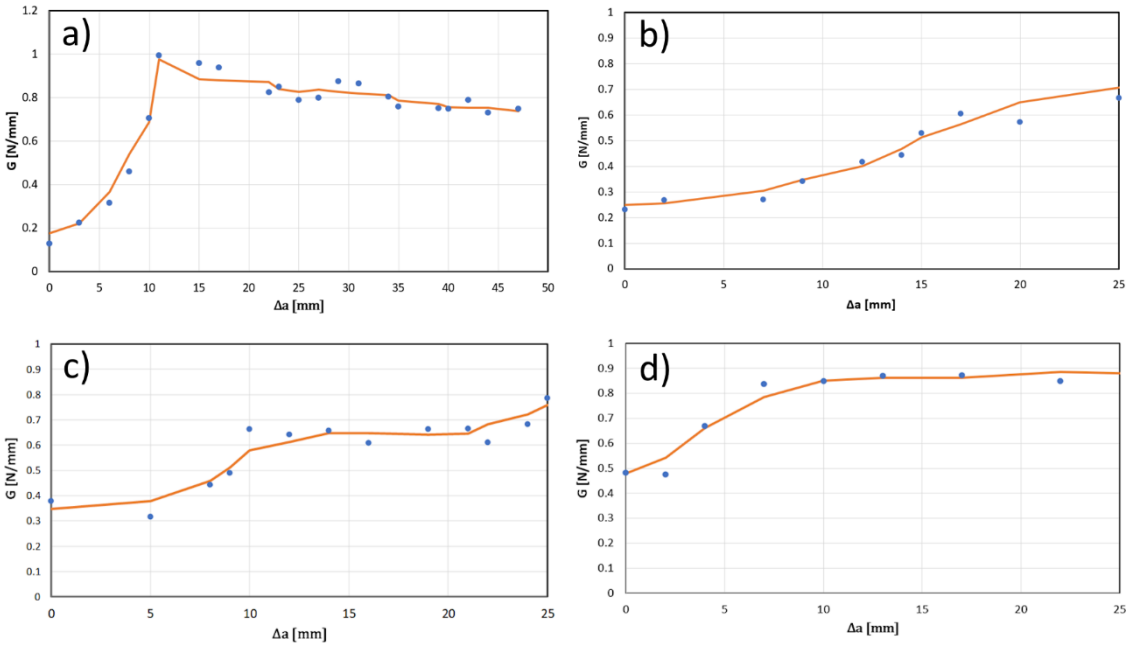

Fig. 118: R-curves (G vs Δa) for the various treatments on titanium alloy - a) MT; b) SIL; c)50V20P; d) 30V50P.

By comparing the values of G_0, it is possible to make a direct comparison of the crack advancement resistance as the surface treatment changes. The results are shown in Fig. 119. Specimens treated by silane show an average initial G value 56% higher than the mechanical treatment; however, they perform less than those treated electrochemically. The anodic oxidation treatments, show a much higher average value of initial energy release rate than that obtained from the samples subjected to abrasion, in particular: anodising at 50V returns G_0 values 144.5% higher than the mechanical treatment, while anodising at 30V provides values 260% higher. The results referring to the samples treated by abrasion also show a greater standard deviation: this phenomenon may be justified by the fact that it is more difficult to obtain a homogeneous surface by sanding then with electrochemical treatments. This test confirms what has already been said, namely that electrochemical treatment with a layer of nanotubes generates a significant improvement in the mechanical performance of the FML. This is also demonstrated by the visual analysis of the fracture surface. In Fig. 120 it can be seen that for MT the fracture is totally adhesive, no matrix remains on the surface (Fig. 120b), while for the samples with nanotubes the fracture is partially cohesive with much matrix remaining adhered to the surface of the titanium alloy (Fig. 120a). The silane coupling agent has an intermediate behaviour between all treatments (Fig. 120c). There is not much difference in the fracture surface between 30V50P and 50V20P, so for simplicity in the Fig. 120 only the surface of 30V50P has been shown.

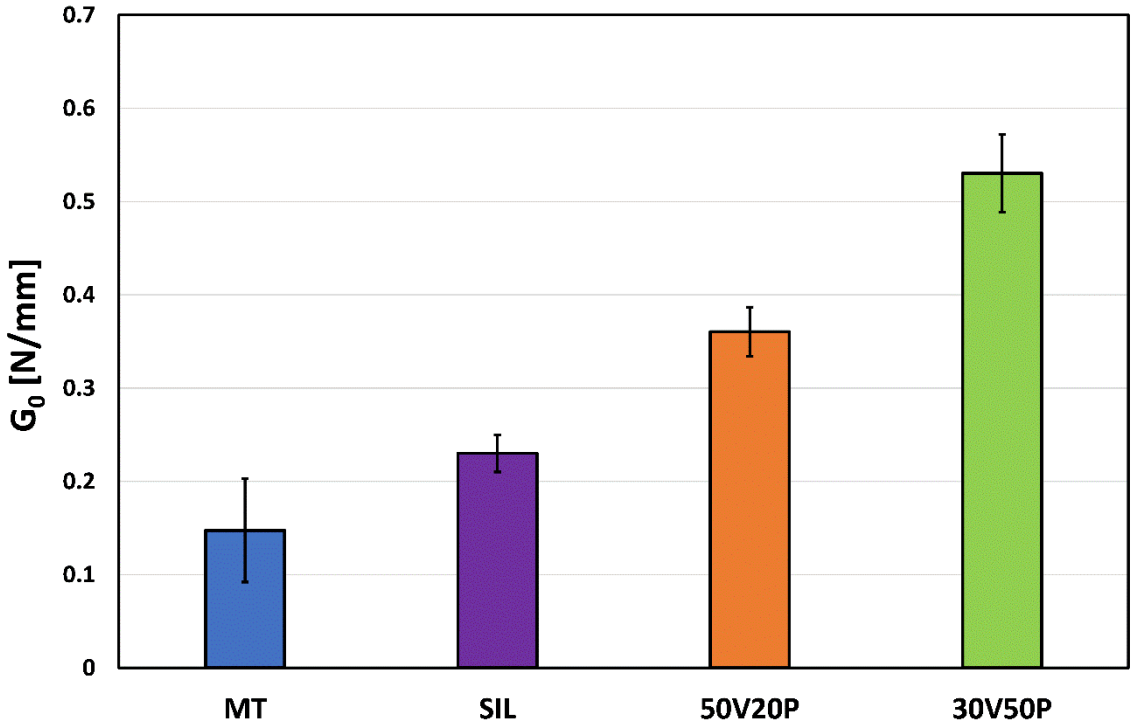

Fig. 119: Initial energy release rate calculated after DCB tests on titanium alloy specimens varying surface treatment.

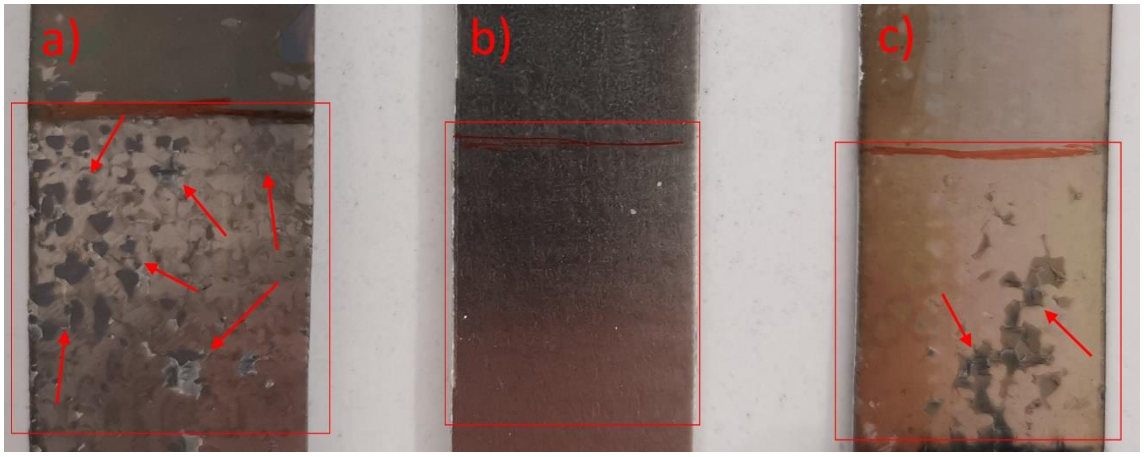

Fig. 120: Fracture surface after DCB test with varying surface treatments - a) 30V50P; b) MT; c) SIL.

3.5 Summary of the second part

In this part of the work, the interfaces of FMLs formed from a PEEK/carbon composite (analysed in Chapter 2) and a metal substrate, either aluminium alloy 7075 or titanium alloy Ti6Al4V, were evaluated.

For FMLs with aluminium alloy, PSA was considered as the electrolyte for the first treatment. This treatment, in the present work, was the reference as the best treatment, as it is used in some applications in the aerospace industry. In terms of damage resistance and interlaminar shear strength, the PSA-anodised FML samples were, as expected, the best, but in terms of corrosion resistance they returned low values. The second

electrochemical treatment consisted of using TSA as an electrolyte. In this case, the corrosion resistance was the best. Anodising in TSA returned oxides with very small pores, which is probably why the resin, despite the pressure applied during the hot-press cycle, was unable to enter the pores effectively. This resulted in low values for energy release rate and interlaminar shear strength, slightly higher than mechanically treated aluminium. This was followed by the two bi-step treatments, PSA-TSA, and TSA-PSA, anodised with the same solutions but in a different order. The aim of treating the aluminium with different solutions and different parameters was to obtain pores with varying diameters. The TSA-PSA treatment showed excellent results in all types of tests, showing good surface wettability, excellent corrosion resistance and critical G and shear strength values comparable to those obtained with PSA. The excellent performance of this treatment is attributable to the oxide structure obtained. The pores have a smaller external diameter than the internal one, protecting the aluminium substrate from corrosion and at the same time favouring the interlocking of the resin inside. The PSA-TSA treatment returned intermediate but unsatisfactory values for both energy release rate and interlaminar shear strength. Regarding corrosion resistance, the PSA-TSA-treated samples did not show good results, justified by the fact that theoretically the oxide structure obtained is opposite to that of the TSA-PSA treatment, showing a larger external pore diameter than the internal diameter. The last treatment investigated involved anodising in TSA with subsequent immersion in NaOH. The aim of this post-treatment was to modify the external structure of the pores, increasing their dimension. This resulted in energy release rate and shear strength values close to the best treatments, with acceptable corrosion resistance. Moreover, this treatment is among the simplest and least expensive in economic terms.

About FMLs with titanium alloy, three types of processes were compared: mechanical abrasion, carried out using a sander with #80 grit sandpaper, chemical treatment, carried out by silane coupling agent, and electrochemical treatment, carried out by anodising. In the latter case, the results of anodising performed at two different potential values: 30V and 50V were also evaluated. For each case, it was studied how the variation of the percentage of water in solution and the variation of the anodic oxidation time caused the formation of different nanotube structures: specifically, the three variations of water chosen were 5%, 20% and 50%, and the three variations of process time were 10 min, 30 min and 60 min.

In the case of anodic oxidation at 30V, the increase in the percentage of water, at the same potential and process duration, favoured the formation of nanotubes, also causing an

increase in the size of the average diameter. In the case of anodic oxidation at 50V, there is similar behaviour only up to 20% water, in fact in the last case (50% water) the structure collapses due to the high dissolution.

The results of this characterisation made it possible to select two ideal configurations: the first 30V, 50% water and 60 min (30V50P), and the second 50V, 20% water and 60 min (50V20P), which present average nanotube diameters of 101.67nm and 113.54nm respectively and extremely low contact angles, indicative of very high surface wettability.

Subsequently, fracture toughness was assessed by means of the DCB test, which yielded the following results:

- the samples subjected to silane treatment showed a fracture toughness 56% higher than the mechanical treatment.
- Samples subjected to 50V20P anodic oxidation showed 144% higher G_0 values compared to mechanical treatment.
- 30V50P samples showed the highest fracture toughness with a G_0 of 260% higher than the mechanical treatment.

The results of the SBS test show that:

- the highest interlaminar shear strength (ILSS) value was obtained from the samples (30V50P): they had an ILSS value 48.78% higher than the mechanical treatment.
- 50V20P samples outperformed mechanical treatment by 36.86%.

Samples treated by silanes show a 22% increase in ILSS compared to mechanical treatment.

In conclusion, it can be stated that, for both aluminium alloy and titanium alloy FMLs, electrochemical anodising treatments are always the best in terms of mechanical performance and corrosion resistance (when required). Therefore, from this study it can be assumed that applying these treatments to metal surfaces, in applications such as FMLs, is a viable alternative to increase the overall performance of these materials, in future aerospace applications.

Chapter 4: Final Considerations

4.1 General Conclusions

This PhD project aims to improve the performance of thermoplastic fibre metal laminates composed of a carbon-fibre reinforced PEEK composite substrate and an aluminium or titanium alloy metal substrate. To realise this improvement, several material performance aspects were analysed. The work was divided into two parts, namely the analysis of the composite part and the study of the interphase between metal and composite. Regarding the first part, reported in chapter 2 of this work, the influence of crystallinity on the properties of PEEK was evaluated. Extensive experimental work was conducted to evaluate the crystalline kinetics of PEEK. In addition, the influence of the presence of the carbon reinforcement fabric was estimated. Furthermore, the model equations used during these calculations were translated into an Abaqus model, using Phyton and Fortran scripts, to predict the degree of crystallinity by simulation. Finally, the mechanical performance of the PEEK was estimated by varying the degree of crystallinity, to assess how this parameter affects the properties and to create a useful interpolating curve dataset to be included in future mechanical models in Abaqus to link the predicted crystallinity value with the specific mechanical result.

In the second part, reported in chapter 3, the focus shifted to the interphase between the composite and the metal substrate. In this case, different surface treatments were applied to both metals and the modification of these surface treatments was analysed using different investigation techniques.

The overall results for both parts of this work show that in the composite part, the presence of the carbon fibre acts as an antinucleating species, so this aspect should be investigated more in future work. On the other hand, the mechanical properties of PEEK are substantially influenced by the crystalline presence, which shows how important it is to control this parameter, also by predicting it through simulation models.

On the other hand, this work shows that the treatment of the interphase between metal and composite plays an important role in the strength of the FML, demonstrating that electrochemical treatments produce the best mechanical performance.

In conclusion, this work demonstrates how complex a material such as metal fibre laminates can be, creating the basis for future research work exploring in more detail all the parameters that can influence the performance of these materials.

References

[1] Graver B, Zhang K, Rutherford D. CO 2 emissions from commercial aviation, 2018. 2018.

[2] Bachmann J, Hidalgo C, Bricout S. Environmental analysis of innovative sustainable composites with potential use in aviation sector—A life cycle assessment review. Sci China Technol Sci 2017;60:1301–17. https://doi.org/10.1007/s11431-016-9094-y.

[3] Roeseler WG, Sarh B, Kismarton MU. 6 TH INTERNATIONAL CONFERENCE ON COMPOSITE MATERIALS COMPOSITE STRUCTURES: THE FIRST 100 YEARS. 2007.

[4] Vogelesang LB. Development of a New Hybrid Material (ARALL) for Aircraft Structure. Ind Eng Chem Prod Res Dev 1983;22:492–6.

[5] Salve A, Mache A, Kulkarni R. A Review: Fiber Metal Laminates (FML's)-Manufacturing, Test methods and Numerical modeling. INTERNATIONAL JOURNAL OF ENGINEERING TECHNOLOGY AND SCIENCES (IJETS) 2016;6. https://doi.org/10.15282/ijets.6.2016.10.2.1060.

[6] Etri H El, Korkmaz ME, Gupta MK, Gunay M, Xu J. A state-of-the-art review on mechanical characteristics of different fiber metal laminates for aerospace and structural applications. International Journal of Advanced Manufacturing Technology 2022;123:2965–91. https://doi.org/10.1007/s00170-022-10277-1.

[7] Asundi A, Choi AYN. Fiber Metal Laminates: An Advanced Material for Future Aircraft. J Mater Process Technol 1997;63:384–94.

[8] Sinmazçelik T, Avcu E, Bora MÖ, Çoban O. A review: Fibre metal laminates, background, bonding types and applied test methods. Mater Des 2011;32:3671–85. https://doi.org/10.1016/j.matdes.2011.03.011.

[9] Thirukumaran M, Siva I, Jappes JW, Manikandan V. Forming and drilling of fiber metal laminates – A review. Journal of Reinforced Plastics and Composites 2018;37:981–90. https://doi.org/10.1177/0731684418771194.

[10] U SA, Remanan M, Jayanarayanan K. Comparison of Properties of Carbon Fiber Reinforced Thermoplastic and Thermosetting Composites for Aerospace Applications. Mater Today Proc 2020;24:453–62.

[11] Peters EN. Engineering Termoplastics-Materials, Properties, Trends. Applied Plastics Engineering Handbook: Processing, Materials, and Applications: Second Edition, Elsevier Inc.; 2017, p. 3–26. https://doi.org/10.1016/B978-0-323-39040-8.00001-8.

[12] Mallick PK. Thermoplastics and thermoplastic-matrix composites for lightweight automotive structures. 2010. https://doi.org/10.1016/B978-1-84569-463-0.50004-3.

[13] Parker D, Bussink J, van de Grampel HT, Wheatley GW, Dorf E-U, Ostlinning E, et al. Polymers, High-Temperature. Ullmann's Encyclopedia of Industrial Chemistry, Wiley-VCH Verlag GmbH & Co. KGaA; 2012. https://doi.org/10.1002/14356007.a21_449.pub4.

[14] Siraj N, Hashmi SAR, Verma S. State-of-the-art review on the high-performance poly (ether ether ketone) composites for mechanical, tribological and bioactive characteristics. Polym Adv Technol 2022;33:3049–77. https://doi.org/10.1002/pat.5795.

[15] Chu XX, Wu ZX, Huang RJ, Zhou Y, Li LF. Mechanical and thermal expansion properties of glass fibers reinforced PEEK composites at cryogenic temperatures. Cryogenics (Guildf) 2010;50:84–8. https://doi.org/10.1016/j.cryogenics.2009.12.003.

[16] Kyriacos D. High-Temperature Engineering Thermoplastics. Brydson's Plastics Materials: Eighth Edition, Elsevier Inc.; 2017, p. 545–615. https://doi.org/10.1016/B978-0-323-35824-8.00021-9.

[17] Lai YH, Kuo MC, Huang JC, Chen M. On the PEEK composites reinforced by surface-modified nano-silica. Materials Science and Engineering A 2007;458:158–69. https://doi.org/10.1016/j.msea.2007.01.085.

[18] Sarasini F, Tirillò J, Ferrante L, Sergi C, Sbardella F, Russo P, et al. Effect of temperature and fiber type on impact behavior of thermoplastic fiber metal laminates. Compos Struct 2019;223:110961. https://doi.org/10.1016/j.compstruct.2019.110961.

[19] Kazemi ME, Shanmugam L, Yang L, Yang J. A review on the hybrid titanium composite laminates (HTCLs) with focuses on surface treatments, fabrications, and mechanical properties. Compos Part A Appl Sci Manuf 2020;128. https://doi.org/10.1016/j.compositesa.2019.105679.

[20] He P, Huang M, Fisher S, Yue CY, Yang J. Effects of primer and annealing treatments on the shear strength between anodized Ti6Al4V and epoxy. Int J Adhes Adhes 2015;57:49–56. https://doi.org/10.1016/j.ijadhadh.2014.10.004.

[21] Zamani Zakaria A, Shelesh-nezhad K, Navid Chakherlou T, Olad A. Effects of aluminum surface treatments on the interfacial fracture toughness of carbon-fiber aluminum laminates. Eng Fract Mech 2017;172:139–51. https://doi.org/10.1016/j.engfracmech.2017.01.004.

[22] Gonzalez-Canche NG, Flores-Johnson EA, Cortes P, Carrillo JG. Evaluation of surface treatments on 5052-H32 aluminum alloy for enhancing the interfacial adhesion of thermoplastic-based fiber metal laminates. Int J Adhes Adhes 2018;82:90–9. https://doi.org/10.1016/j.ijadhadh.2018.01.003.

[23] Molitor P, Barron V, Young T. Surface treatment of titanium for adhesive bonding to polymer composites: a review. vol. 21. 2001.

[24] Droździel-Jurkiewicz M, Bieniaś J. Evaluation of Surface Treatment for Enhancing Adhesion at the Metal–Composite Interface in Fibre Metal-Laminates. Materials 2022;15. https://doi.org/10.3390/ma15176118.

[25] Ji C, Wang B, Hu J, Zhang C, Sun Y. Effect of different preparation methods on mechanical behaviors of carbon fiber-reinforced PEEK-Titanium hybrid laminates. Polym Test 2020;85. https://doi.org/10.1016/j.polymertesting.2020.106462.

[26] Ji C, Hu J, Wang B, Zou Y, Yang Y, Sun Y. Mechanical behavior prediction of CF/PEEK-titanium hybrid laminates considering temperature effect by artificial neural network. Compos Struct 2021;262. https://doi.org/10.1016/j.compstruct.2020.113367.

[27] Xu Y, Li H, Yang Y, Hu Y, Tao J. Determination of residual stresses in Ti/CFRP laminates after preparation using multiple methods. Compos Struct 2019;210:715–23. https://doi.org/10.1016/J.COMPSTRUCT.2018.11.090.

[28] Rans CD, Alderliesten RC, Benedictus R. Predicting the influence of temperature on fatigue crack propagation in Fibre Metal Laminates. Eng Fract Mech 2011;78:2193–201. https://doi.org/10.1016/J.ENGFRACMECH.2011.04.005.

[29] Cortes P, Cantwell WJ. The Impact Properties of High-temperature Fiber-Metal Laminates. Http://DxDoiOrg/101177/0021998306065291 2007;41:613–32. https://doi.org/10.1177/0021998306065291.

[30] Van Drongelen M, Van Erp TB, Peters GWM. Quantification of non-isothermal, multi-phase crystallization of isotactic polypropylene: The influence of cooling rate and pressure. Polymer (Guildf) 2012;53:4758–69. https://doi.org/10.1016/j.polymer.2012.08.003.

[31] Tardif X, Pignon B, Boyard N, Schmelzer JWP, Sobotka V, Delaunay D, et al. Experimental study of crystallization of PolyEtherEtherKetone (PEEK) over a large temperature range using a nano-calorimeter. Polym Test 2014;36:10–9. https://doi.org/10.1016/j.polymertesting.2014.03.013.

[32] Bonmatin M, Chabert F, Bernhart G, Djilali T. Rheological and crystallization behaviors of low processing temperature poly(aryl ether ketone). J Appl Polym Sci 2021;138:1–13. https://doi.org/10.1002/app.51402.

[33] Batista NL, Olivier P, Bernhart G, Rezende MC, Botelho EC. Correlation between degree of crystallinity, morphology and mechanical properties of PPS/carbon fiber laminates. Materials Research 2016;19:195–201. https://doi.org/10.1590/1980-5373-MR-2015-0453.

[34] Yaghini N, Peters GWM. Modeling Crystallization Kinetics and Resulting Properties of Polyamide 6. Macromolecules 2021;54:1894–904. https://doi.org/10.1021/acs.macromol.0c02588.

[35] Felder S, Vu NA, Reese S, Simon JW. Modeling the effect of temperature and degree of crystallinity on the mechanical response of Polyamide 6. Mechanics of Materials 2020;148. https://doi.org/10.1016/j.mechmat.2020.103476.

[36] Dusunceli N, Colak OU. Modelling effects of degree of crystallinity on mechanical behavior of semicrystalline polymers. Int J Plast 2008;24:1224–42. https://doi.org/10.1016/j.ijplas.2007.09.003.

[37] Spina R, Spekowius M, Dahlmann R, Hopmann C. Analysis of polymer crystallization and residual stresses in injection molded parts. International Journal of Precision Engineering and Manufacturing 2014;15:89–96. https://doi.org/10.1007/s12541-013-0309-2.

[38] Avrami M. Kinetics of phase change. I: General theory. J Chem Phys 1939;7:1103–12. https://doi.org/10.1063/1.1750380.

[39] Seo J, Gohn AM, Dubin O, Takahashi H, Hasegawa H, Sato R, et al. Isothermal crystallization of poly(ether ether ketone) with different molecular weights over a wide temperature range. Polymer Crystallization 2019;2. https://doi.org/10.1002/pcr2.10055.

[40] Seo J, Zhang X, Schaake RP, Rhoades AM, Colby RH. Dual Nakamura model for primary and secondary crystallization applied to nonisothermal crystallization of poly(ether ether ketone). Polym Eng Sci 2021;61:2416–26. https://doi.org/10.1002/pen.25767.

[41] Smith WF, Hashemi J. Foundations of Materials Science and Engineering. McGraw-Hill; 2006.

[42] Clyne TW, Hull D. An Introduction to Composite Materials. Cambridge University Press; 2019.

[43] Berthelot J-M, Ling FF. Composite materials: mechanical behavior and structural analysis. vol. 435. Springer; 1999.

[44] Mallick PK. Composites Engineering Handbook. CRC Press; 1997. https://doi.org/10.1201/9781482277739.

[45] Harper L, Clifford M. Design and Manufacture of Structural Composites. Elsevier; 2023. https://doi.org/10.1016/C2018-0-05165-8.

[46] Mallick PK. Fiber-Reinforced Composites. CRC Press; 2007. https://doi.org/10.1201/9781420005981.

[47] International Union of Pure and Applied Chemistry. Subcommittee on Polymer Terminology., Jones RG, International Union of Pure and Applied Chemistry. Commission on Macromolecular Nomenclature. Compendium of polymer terminology and nomenclature : IUPAC recommendations, 2008. Royal Society of Chemistry; 2009.

[48] Sawyer LC, Grubb DT, Meyers GF. Polymer microscopy: Third edition. Springer New York; 2008. https://doi.org/10.1007/978-0-387-72628-1.

[49] Gedde U. Polymer Physics. First edition. Chapman & Hall; 1995.

[50] Benedetti L, Brulé B, Decreamer N, Evans KE, Ghita O. Shrinkage behaviour of semi-crystalline polymers in laser sintering: PEKK and PA12. Mater Des 2019;181:107906. https://doi.org/10.1016/j.matdes.2019.107906.

[51] Britnell DJ, Cain RL, Coates R, Goodship V, Hulme A, Johnson MR, et al. An introduction to automotive composites. 2002.

[52] Grigorescu RM, Grigore ME, Iancu L, Ghioca P, Ion RM. Waste electrical and electronic equipment: A review on the identification methods for polymeric materials. Recycling 2019;4. https://doi.org/10.3390/recycling4030032.

[53] Levine H, Slade L. Influences of the Glassy and Rubbery States on the Thermal, Mechanical, and Structural Properties of Doughs and Baked Products. Dough Rheology and Baked Product Texture, Springer US; 1990, p. 157–330. https://doi.org/10.1007/978-1-4613-0861-4_5.

[54] Dargazany R, Khiêm VN, Poshtan EA, Itskov M. Constitutive modeling of strain-induced crystallization in filled rubbers. Phys Rev E Stat Nonlin Soft Matter Phys 2014;89. https://doi.org/10.1103/PhysRevE.89.022604.

[55] Dargazany R, Khiêm VN, Poshtan EA, Itskov M. Constitutive modeling of strain-induced crystallization in filled rubbers. Phys Rev E 2014;89:22604. https://doi.org/10.1103/PhysRevE.89.022604.

[56] Jiang X, Reiter G, Hu W. How Chain-Folding Crystal Growth Determines the Thermodynamic Stability of Polymer Crystals. Journal of Physical Chemistry B 2016;120:566–71. https://doi.org/10.1021/acs.jpcb.5b09324.

[57] Cavallo D, Müller AJ. POLYMER CRYSTALLIZATION. Macromolecular Engineering, vol. 2nd edition, Wiley; 2019.

[58] Young RJ, Lovell PA. Introduction to Polymers. Springer US; 1991. https://doi.org/10.1007/978-1-4899-3176-4.

[59] Pérez-Camargo RA, Liu GM, Wang DJ, Müller AJ. Experimental and Data Fitting Guidelines for the Determination of Polymer Crystallization Kinetics. Chinese Journal of Polymer Science (English Edition) 2022;40:658–91. https://doi.org/10.1007/s10118-022-2724-2.

[60] QIPENG G. POLYMER MORPHOLOGY. Wiley; 2016.

[61] Lorenzo AT, Arnal ML, Albuerne J, Müller AJ. DSC isothermal polymer crystallization kinetics measurements and the use of the Avrami equation to fit the data: Guidelines to avoid common problems. Polym Test 2007;26:222–31. https://doi.org/10.1016/j.polymertesting.2006.10.005.

[62] Lauritzen JI, Hoffman JD. Extension of theory of growth of chain-folded polymer crystals to large undercoolings. J Appl Phys 1973;44:4340–52. https://doi.org/10.1063/1.1661962.

[63] Li CY. The rise of semicrystalline polymers and why are they still interesting. Polymer (Guildf) 2020;211:123150. https://doi.org/10.1016/j.polymer.2020.123150.

[64] Sadler DM, Gilmer GH. PHYSICAL REVIEW LETTERS Rate-Theory Model of Polymer Crystallization. vol. 56. 1986.

[65] Hu W, Frenkel D, Mathot VBF. Intramolecular Nucleation Model for Polymer Crystallization. Macromolecules 2003;36:8178–83. https://doi.org/10.1021/ma0344285.

[66] Strobl G. From the melt via mesomorphic and granular crystalline layers to lamellar crystallites: A major route followed in polymer crystallization? The European Physical Journal E 2000;3:165–83. https://doi.org/10.1007/s101890070030.

[67] Kundagrami A, Muthukumar M. Continuum theory of polymer crystallization. J Chem Phys 2007;126:144901. https://doi.org/10.1063/1.2713380.

[68] Cheng SZD, Lotz B. Enthalpic and entropic origins of nucleation barriers during polymer crystallization: The Hoffman-Lauritzen theory and beyond. Polymer (Guildf), vol. 46, Elsevier BV; 2005, p. 8662–81. https://doi.org/10.1016/j.polymer.2005.03.125.

[69] Mark JE. Physical Properties of Polymers Handbook. New York, NY: Springer New York; 2007. https://doi.org/10.1007/978-0-387-69002-5.

[70] Thomas DG, Staveley LAK. A study of the supercooling of drops of some molecular liquids. Journal of the Chemical Society (Resumed) 1952:4569. https://doi.org/10.1039/jr9520004569.

[71] Velisaris CN, Seferis JC. Crystallization kinetics of polyetheretherketone (peek) matrices. Polym Eng Sci 1986;26:1574–81. https://doi.org/10.1002/pen.760262208.

[72] Verma R, Marand H, Hsiao B. Morphological Changes during Secondary Crystallization and Subsequent Melting in Poly(ether ether ketone) as Studied by Real Time Small Angle X-ray Scattering. 1996.

[73] Ko TY, Woo EM. Changes and distribution of lamellae in the spherulites of poly(ether ether ketone) upon stepwise crystallization. vol. 37. 1996.

[74] Seo J, Gohn AM, Dubin O, Takahashi H, Hasegawa H, Sato R, et al. Isothermal crystallization of poly(ether ether ketone) with different molecular weights over a wide temperature range. Polymer Crystallization 2019;2. https://doi.org/10.1002/pcr2.10055.

[75] Müller AJ, Michell RM, Pérez RA, Lorenzo AT. Successive Self-nucleation and Annealing (SSA): Correct design of thermal protocol and applications. Eur Polym J 2015;65:132–54. https://doi.org/10.1016/j.eurpolymj.2015.01.015.

[76] Lorenzo AT, Arnal ML, Sánchez JJ, Müller AJ. Effect of annealing time on the self-nucleation behavior of semicrystalline polymers. J Polym Sci B Polym Phys 2006;44:1738–50. https://doi.org/10.1002/polb.20832.

[77] Fillon B, Wittmann JC, Lotz B, Thierry A. Self-Nucleation and Recrystallization of Isotactic Polypropylene (α Phase) Investigated by Differential Scanning Calorimetry. J Polym Sci B Polym Phys 1993;31:1383–93.

[78] Blundell DJ, Keller A, Kovacs AJ. A new self-nucleation phenomenon and its application to the growing of polymer crystals from solution. Journal of Polymer Science Part C: Polymer Letters 1966;4:481–6.

[79] Fillon B, Lotz B, Thierry A, Wittmann JC. Self-nucleation and enhanced nucleation of polymers. Definition of a convenient calorimetric "efficiency scale" and evaluation of nucleating additives in isotactic polypropylene (α phase). J Polym Sci B Polym Phys 1993;31:1395–405. https://doi.org/10.1002/polb.1993.090311014.

[80] Pérez-Camargo RA, Cavallo D, Müller AJ. Recent applications of the Successive Self-nucleation and Annealing thermal fractionation technique. Frontiers in Soft Matter 2022;2. https://doi.org/10.3389/frsfm.2022.1003500.

[81] Muller AJ, Hernandez ZH, Arnal ML, Sanchez JJ. Successive self-nucleation/annealing (SSA): A novel technique to study molecular segregation during crystallization. vol. 39. 1997.

[82] Müller AJ, Arnal ML. Thermal fractionation of polymers. Progress in Polymer Science (Oxford) 2005;30:559–603. https://doi.org/10.1016/j.progpolymsci.2005.03.001.

[83] Pérez-Camargo RA, Saenz G, Laurichesse S, Casas MT, Puiggalí J, Avérous L, et al. Nucleation, Crystallization, and Thermal Fractionation of Poly (ε-Caprolactone)-Grafted-Lignin: Effects of Grafted Chains Length and Lignin Content. J Polym Sci B Polym Phys 2015;53:1736–50. https://doi.org/10.1002/polb.23897.

[84] Müller AJ, Michell RM, Pérez RA, Lorenzo AT. Successive Self-nucleation and Annealing (SSA): Correct design of thermal protocol and applications. Eur Polym J 2015;65:132–54. https://doi.org/10.1016/j.eurpolymj.2015.01.015.

[85] Blundell DJ, Osborn BN. The morphology of poly(aryl-ether-ether-ketone). Polymer (Guildf) 1983;24:953–8. https://doi.org/10.1016/0032-3861(83)90144-1.

[86] Bassett DC, Olley RH, Ai IAM, Thomson RJJ. On crystallization phenomena in PEEK*. 1988.

[87] Doumeng M, Makhlouf L, Berthet F, Marsan O, Delbé K, Denape J, et al. A comparative study of the crystallinity of Polyetheretherketone by using density, DSC, XRD, and Raman spectroscopy techniques 2021. https://doi.org/10.1016/j.polymertesting.2020.106878ï.

[88] Zhang RC, Sun D, Lu A, Zhong M, Xiong G, Wan Y. Equilibrium melting temperature of polymorphic poly(L-lactide) and its supercooling dependence on growth kinetics. Polymers (Basel) 2017;9. https://doi.org/10.3390/polym9110625.

[89] Zhang RC, Lu A, Xu Y, Min M, Xia JQ, Zhou JH, et al. Equilibrium melting temperature and spherulitic growth rate of poly(phenylene sulfide). Eur Polym J 2009;45:2867–72. https://doi.org/10.1016/j.eurpolymj.2009.06.026.

[90] Seo J, Zhang X, Schaake RP, Rhoades AM, Colby RH. Dual Nakamura model for primary and secondary crystallization applied to nonisothermal crystallization of poly(ether ether ketone). Polym Eng Sci 2021;61:2416–26. https://doi.org/10.1002/pen.25767.

[91] Hay JN, Kemmish DJ, Langford JI, Rae AIM. STRUCTURE OF CRYSTALLINE PEEK. Polymer Communications (Guildford, England) 1984;25:175 – 178.

[92] Meola C, Boccardi S, Carlomagno G maria. Composite Materials in the Aeronautical Industry. Infrared Thermography in the Evaluation of Aerospace Composite Materials, Elsevier; 2017, p. 1–24. https://doi.org/10.1016/b978-1-78242-171-9.00001-2.

[93] Pethrick RA. Composite to metal bonding in aerospace and other applications. Welding and Joining of Aerospace Materials, Elsevier; 2012, p. 277–303. https://doi.org/10.1016/b978-0-12-819140-8.00009-2.

[94] Mouritz AP. Introduction to aerospace materials. Introduction to Aerospace Materials, Elsevier; 2012, p. 1–14. https://doi.org/10.1533/9780857095152.1.

[95] Bieniaś J, Jakubczak P, Surowska B. Properties and characterization of fiber metal laminates. Hybrid Polymer Composite Materials: Properties and Characterisation, Elsevier Inc.; 2017, p. 253–77. https://doi.org/10.1016/B978-0-08-100787-7.00011-1.

[96] Salve A, Kulkarni R, Mache A. A Review: Fiber Metal Laminates (FML's) - Manufacturing, Test methods and Numerical modeling. International Journal of Engineering Technology and Sciences 2016;3:71–84. https://doi.org/10.15282/ijets.6.2016.1.10.1060.

[97] Khan F, Qayyum F, Asghar W, Azeem M, Anjum Z, Nasir A, et al. Effect of various surface preparation techniques on the delamination properties of vacuum infused Carbon fiber reinforced aluminum laminates (CARALL): Experimentation and numerical simulation. Journal of Mechanical Science and Technology 2017;31:5265–72. https://doi.org/10.1007/s12206-017-1019-y.

[98] Shivi Kesarwani. Polymer Composites in Aviation Sector. International Journal of Engineering Research And 2017;V6. https://doi.org/10.17577/IJERTV6IS060291.

[99] Leyens C, Peters M. Titanium and Titanium Alloys. Wiley; 2003. https://doi.org/10.1002/3527602119.

[100] Donachie MJ. Titanium: A Technical Guide. 2nd ed. ASM International; 2000.

[101] Inagaki I, Takechi T, Ariyasu YSN. Application and Features of Titanium for the Aerospace Industry, 2014.

[102] Pushp P, Dasharath SM, Arati C. Classification and applications of titanium and its alloys. Mater Today Proc 2022;54:537–42. https://doi.org/10.1016/j.matpr.2022.01.008.

[103] Uwanyuze RS, Alpay SP, Schafföner S, Sahoo S. A first principles analysis of oxidation in titanium alloys with aluminum and vanadium. Surf Sci 2022;719:122026. https://doi.org/10.1016/j.susc.2022.122026.

[104] Peters M, Kumpfert J, Ward CH, Leyens C. Titanium Alloys for Aerospace Applications. Adv Eng Mater 2003;5:419–27. https://doi.org/10.1002/adem.200310095.

[105] Raj R, Selvam P, Pughalendi M. A Review of Aluminum Alloys in Aircraft and Aerospace Industry 2021.

[106] Rambabu P. and Eswara Prasad N and KVV and WRJH. Aluminium Alloys for Aerospace Applications. In: Prasad N. Eswara and Wanhill RJH, editor. Aerospace Materials and Material Technologies : Volume 1: Aerospace Materials, Singapore: Springer Singapore; 2017, p. 29–52. https://doi.org/10.1007/978-981-10-2134-3_2.

[107] Heinz A, Haszler A, Keidel C, Moldenhauer S, Benedictus R, Miller WS. Recent development in aluminium alloys for aerospace applications. Materials Science and Engineering: A 2000;280:102–7. https://doi.org/10.1016/S0921-5093(99)00674-7.

[108] Heinz A, Haszler A, Keidel C, Moldenhauer S, Benedictus R, Miller WS. Recent development in aluminium alloys for aerospace applications. Materials Science and Engineering: A 2000;280:102–7. https://doi.org/https://doi.org/10.1016/S0921-5093(99)00674-7.

[109] Sankaran KK, Mishra RS. Chapter 4 - Aluminum Alloys. In: Sankaran KK, Mishra RS, editors. Metallurgy and Design of Alloys with Hierarchical Microstructures, Elsevier; 2017, p. 57–176. https://doi.org/https://doi.org/10.1016/B978-0-12-812068-2.00004-7.

[110] Campbell FC. Adhesive Bonding and Integrally Cocured Structure: A Way to Reduce Assembly Costs through Parts Integration. Manufacturing Processes for Advanced Composites 2004:241–301. https://doi.org/10.1016/b978-185617415-2/50009-5.

[111] Romoli L, Moroni F, Khan MMA. A study on the influence of surface laser texturing on the adhesive strength of bonded joints in aluminium alloys. CIRP Ann Manuf Technol 2017;66:237–40. https://doi.org/10.1016/j.cirp.2017.04.123.

[112] Park SY, Choi WJ, Choi HS, Kwon H, Kim SH. Recent trends in surface treatment technologies for airframe adhesive bonding processing: A review (1995-2008). Journal of Adhesion 2010;86:192–221. https://doi.org/10.1080/00218460903418345.

[113] Valenza A, Fiore V, Fratini L. Mechanical behaviour and failure modes of metal to composite adhesive joints for nautical applications. International Journal of Advanced Manufacturing Technology 2011;53:593–600. https://doi.org/10.1007/s00170-010-2866-1.

[114] Ferreira DP, Cruz J, Fangueiro R. Surface modification of natural fibers in polymer composites. Elsevier Ltd; 2018. https://doi.org/10.1016/B978-0-08-102177-4.00001-X.

[115] España JM, Samper MD, Fages E, Sánchez-Nácher L, Balart R. Investigation of the effect of different silane coupling agents on mechanical performance of basalt fiber composite laminates with biobased epoxy matrices. Polym Compos 2013. https://doi.org/10.1002/pc.22421.

[116] Conshohocken W. Standard Guide for Preparation of Aluminum Surfaces for Structural Adhesives Bonding (Phosphoric Acid Anodizing). Astm International 2014;98:1–5. https://doi.org/10.1520/D3933-98R10.2.

[117] Zhang J-S, Zhao X-H, Zuo Y, Xiong J-P. The bonding strength and corrosion resistance of aluminum alloy by anodizing treatment in a phosphoric acid modified boric acid/sulfuric acid bath. Surf Coat Technol 2008;202:3149–56. https://doi.org/10.1016/j.surfcoat.2007.10.041.

[118] van Put MA, Abrahami ST, Elisseeva O, de Kok JMM, Mol JMC, Terryn H. Potentiodynamic anodizing of aluminum alloys in Cr(VI)-free electrolytes. Surface and Interface Analysis, vol. 48, John Wiley and Sons Ltd; 2016, p. 946–52. https://doi.org/10.1002/sia.5919.

[119] Curioni M, Skeldon P, Koroleva E, Thompson GE, Ferguson J. Role of Tartaric Acid on the Anodizing and Corrosion Behavior of AA 2024 T3 Aluminum Alloy. J Electrochem Soc 2009;156:C147. https://doi.org/10.1149/1.3077602.

[120] Delplancke J-L, Degrez M, Fontana A, Winand R. Self-colour anodizing of titanium. Surface Technology 1982;16:153–62. https://doi.org/10.1016/0376-4583(82)90033-4.

[121] Gaul E. Coloring Titanium and Related Metals by Electrochemical Oxidation. J Chem Educ 1993;70:176–176.

[122] Batool SA, Salman Maqbool M, Javed MA, Niaz A, Rehman MAU. A Review on the Fabrication and Characterization of Titania Nanotubes Obtained via Electrochemical Anodization. Surfaces 2022;5:456–80. https://doi.org/10.3390/surfaces5040033.

[123] Albu SP, Ghicov A, Aldabergenova S, Drechsel P, LeClere D, Thompson GE, et al. Formation of double-walled TiO2 nanotubes and robust anatase membranes. Advanced Materials 2008;20:4135–9. https://doi.org/10.1002/adma.200801189.

[124] Chen H, Muros-Cobos JL, Amirfazli A. Contact angle measurement with a smartphone. Review of Scientific Instruments 2018;89:035117. https://doi.org/10.1063/1.5022370.

[125] Singh MK, Singh A. Chapter 16 - Contact angle and surface wettability measurement. In: Singh MK, Singh A, editors. Characterization of Polymers and Fibres, Woodhead Publishing; 2022, p. 359–85. https://doi.org/https://doi.org/10.1016/B978-0-12-823986-5.00013-0.

[126] Wypych G. 2 - MECHANISMS OF ADHESION. In: Wypych G, editor. Handbook of Adhesion Promoters (Second Edition), ChemTec Publishing; 2023, p. 5–62. https://doi.org/https://doi.org/10.1016/B978-1-77467-018-7.50005-0.

[127] Di Franco F, Zaffora A, Santamaria M, Di Quarto F. Anodization and anodic oxides. Elsevier Inc.; 2018. https://doi.org/10.1016/B978-0-12-409547-2.11704-4.

[128] Lohrengel MM. Thin anodic oxide layers on aluminium and other valve metals: high field regime. Materials Science and Engineering: R: Reports 1993;11:243–94. https://doi.org/10.1016/0927-796X(93)90005-N.

[129] Guntherschulze A, Betz H. Die Elektronenstromung in Isolatoren bei extremen Feldstarken. Zeitschrift Fur Physik 1934;91:70–96. https://doi.org/10.1007/BF01340550.

[130] Pringle JPS. Transport Numbers of Metal and Oxygen during the Anodic Oxidation of Tantalum. J Electrochem Soc 1973;120:398. https://doi.org/10.1149/1.2403466.

[131] Pedeferri P. Corrosion Science and Engineering. Cham: Springer International Publishing; 2018. https://doi.org/10.1007/978-3-319-97625-9.

[132] Mussini PR. https://sites.unimi.it/ECEA/0910Impedenza.pdf n.d.

[133] Lazanas ACh, Prodromidis MI. Electrochemical Impedance Spectroscopy–A Tutorial. ACS Measurement Science Au 2023;3:162–93. https://doi.org/10.1021/acsmeasuresciau.2c00070.

[134] International Standard UNI ISO 14130: Fibre-reinforced plastic composites-Determination of apparent interlaminar shear strength by short-beam method 1997.

[135] ASTM D5528 - Standard Test Method for Mode I Interlaminar Fracture Toughness of Unidirectional Fiber-Reinforced Polymer Matrix Composites. 2002.

[136] Xu D, Yang W, Li X, Hu Z, Li M, Wang L. Surface nanostructure and wettability inducing high bonding strength of polyphenylene sulfide-aluminum composite structure. Appl Surf Sci 2020;515. https://doi.org/10.1016/j.apsusc.2020.145996.

[137] Dong L, Li Y, Huang M, Hu X, Qu Z, Lu Y. Effect of anodizing surface morphology on the adhesion performance of 6061 aluminum alloy. Int J Adhes Adhes 2022;113. https://doi.org/10.1016/j.ijadhadh.2021.103065.

[138] Berger S, Kunze J, Schmuki P, Valota AT, LeClere DJ, Skeldon P, et al. Influence of Water Content on the Growth of Anodic TiO2 Nanotubes in Fluoride-Containing Ethylene Glycol Electrolytes. J Electrochem Soc 2010;157:C18. https://doi.org/10.1149/1.3251338.

[139] Valota A, LeClere DJ, Skeldon P, Curioni M, Hashimoto T, Berger S, et al. Influence of water content on nanotubular anodic titania formed in fluoride/glycerol electrolytes. Electrochim Acta 2009;54:4321–7. https://doi.org/10.1016/j.electacta.2009.02.098.

[140] Santamaria M, Conigliaro G, Franco F Di, Quarto F Di. Photoelectrochemical Evidence of Cu2O/TiO2Nanotubes Hetero-Junctions formation and their Physicochemical Characterization. Electrochim Acta 2014;144:315–23. https://doi.org/10.1016/j.electacta.2014.07.154.

[141] Šćepanović MJ, Grujič-Brojčin MU, Dohčević-Mitrović ZD, Popović Z V. Effects of confinement, strain and nonstoichiometry on Raman spectra of anatase TiO2 nanopowders. Materials Science Forum, vol. 518, Trans Tech Publications Ltd; 2006, p. 101–6. https://doi.org/10.4028/www.scientific.net/MSF.518.101.